PARTICLE ENGINEERING – NOVEL STRATEGIES TO ENHANCE THE EFFICIENCY OF DRY POWDER INHALER FORMULATIONS

Doctoral Thesis

submitted in partial fulfilment of the requirements for
the degree of doctor of natural sciences
of the Faculty of Mathematics and Natural Sciences

at Kiel University, Germany

by

Simon Stefan Bock

Kiel, 2022

Printed with the permission of the Faculty of Mathematics and Natural Sciences of Kiel University.

This work was carried out from April 2018 until March 2022 at the Department of Pharmaceutics and Biopharmaceutics at Kiel University, Kiel, Germany. The thesis was prepared under supervision of Prof. Dr. Regina Scherließ.

1st Referee:	Prof. Dr. Regina Scherließ
2nd Referee:	Prof. Dr. Dr. Dr. Thomas Rades
Submission of the PhD Application:	01.08.2022
Date of examination:	05.10.2022

Dean: Prof. Dr. Frank Kempken

Dedicated to my family

„ *I never think of the future. It comes soon enough.* “

Albert Einstein

Publications

The dissertation contains textual materials and figures from the below listed author's publications. The relevant publications are referenced in the text.

Review articles

- *Additive Manufacturing in respiratory sciences – Current capabilities and future prospects* by Simon Bock, Thomas Rades, Regina Scherließ and Jukka Rantanen in *Advanced Drug Delivery Reviews* (Volume 186, July 2022, 114341)

- *Particle Engineering in dry powders for inhalation* by Regina Scherließ, Simon Bock, Nicholas Bungert, Anna Neustock, Lena Valentin in *European Journal of Pharmaceutical Sciences* (Volume 172, May 2022, 10658)

Poster presentations

- *Artificial dispersing aids and carriers for DPI formulations - Proof of Principle* by S. Bock and R. Scherließ at Drug Delivery to the Lungs 2019 (Edinburgh, UK)

- *Modifying particle surface of model Dry Powder Inhalation (DPI) carriers* by S. Bock and R. Scherließ at PBP World Meeting 2022 (Rotterdam, The Netherlands)

Oral presentations

- *Particle engineering for Dry Powder Inhalation (DPI): Modifying drug-to-carrier interactions in adhesive mixtures* by S. Bock and R. Scherließ at Nordic POP conference 2019 (Oslo, Norway)

- *Additive manufacturing in respiratory drug delivery: Dispersing aids in Dry Powder Inhalation (DPI) formulations* by S. Bock and R. Scherließ at Nordic POP conference 2020 (Copenhagen, Denmark)

- *Dry Powder Inhalation – Additive Manufacturing and Numerical Simulation for formulation development* by S. Bock at DPhG Annual PhD and Postdoc Meeting 2022 (virtual)

Patent

- *Powder formulations for inhalation (WO2021115877A1)* –R. Scherließ, S. Bock

The absence of a special marking or a corresponding reference to a trademark, utility model or patent protection does not allow the conclusion to be drawn that the items specified in this work can be freely disposed of.

Table of contents

Introduction

Promoting and maintaining peoples' health status is the primary objective of healthcare systems and the measures they provide. This includes administration of medicines that have principally been recognised to increase life expectancy and improve quality of life. An administration of drugs via the lungs is an important part of current therapeutic measures to treat local and systemic diseases. For this therapeutic route, a variety of pharmaceutical dosage forms exist, whose clinical outcomes are influenced by unique biological, behavioural and environmental characteristics. Those dosage forms, namely orally inhaled and nasal drug products (OINDP), involve various formulation strategies, inhaler designs and delivery mechanisms. Drug delivery and deposition in the respiratory tract are affected by material characteristics of the formulation ingredients, airflow and particle collision in the inhaler as well as patient-individual factors such as anatomy, physical constitution and inhalation profile.

Both formulation ingredients and inhalation devices are mass-produced, which fails an adequate tailoring to the diversity of individual medical need. Consequently, device development and formulation engineering strive to optimise product performance to be independent of the individual patient characteristics. Developing an OINDP characterised by patient-independent performance specifically requires identifying the product attributes which require refinements and exploring how they could be optimally designed. Product attributes have been scientifically studied through a variety of device and formulation engineering variations, well-knowing that all components continuously influence each other. Theoretical and practical research on improvements of OINDPs is increasingly based on computational technologies. One of these technologies is Additive Manufacturing (AM), which allows to fabricate tailored objects. Refinements in AM steadily open up novel approaches in pharmaceutical research. Such advances particularly apply to respiratory sciences, as numerous technological developments are enabling research at both device and formulation levels. Likewise, progress in computational modelling of airflow and particle trajectories provides insights into the fate of aerosols during inhalation. With the help of such computational methods, data can be generated and analysed in a structured and objective way. At best, such data provide insights into aerosol mechanisms that were previously hidden. Detailed insights can therefore accelerate and streamline the OINDP development process, allowing refinement of formulation and device design.

Although formulation techniques are becoming increasingly diverse and complex, it is not yet feasible to discretely explore the fundamental influencing factors in respiratory drug

delivery. This is particularly true for dry powders for inhalation (DPI) as an example of a formulation strategy for OINDP whose performance depends on an extensive array of influencing factors. In the field of DPI formulation development, emerging technologies such as AM and Numerical Simulation (NS) have so far received relatively little attention. This indicates a need to explore their potential applications in the field of respiratory drug delivery in the future.

Objectives

The purpose of this thesis is to present a strategy for DPI product development that combines the use of Additive Manufacturing (AM) and Numerical Simulation (NS). As an overarching objective, this exploratory thesis aims at identifying gaps in research on respiratory drug delivery that could potentially be bridged with the help of these technologies.

One of the objectives is to describe general weaknesses of DPI formulations in terms of delivery performance, with a focus on carrier-based blends. This thesis aims at identifying the limitations of engineering common carrier material to improve their performance. The main hypothesis of this work is that the use of AM can be applied as an alternative approach to improve the performance of OINDPs. To identify key particle characteristics that drive the performance, a further objective is to investigate the applicability of NS. Moreover, this thesis aims at discussing the combinatorial use of both technologies as an approach for particle engineering of DPI carriers.

Beyond an introduction in respiratory drug delivery (Chapter 1), this thesis comprises an experimental particle engineering approach (Chapter 2), the assessment of complex 3D-printed (3DP) accessories to promote dispersion (Chapter 3), numerical models to simulate particle-wall collision (Chapter 4), and an outlook on next level DPI carrier engineering (Chapter 5). Each of these chapters is introduced with theoretical background before providing a description of the conducted methodology. Then, the observations obtained with each method are presented and interpreted accordingly. At the end of each chapter, the key findings are summarised. Chapter 6 concludes the findings of this thesis with a summarising discussion and conclusion including prospects for future developments.

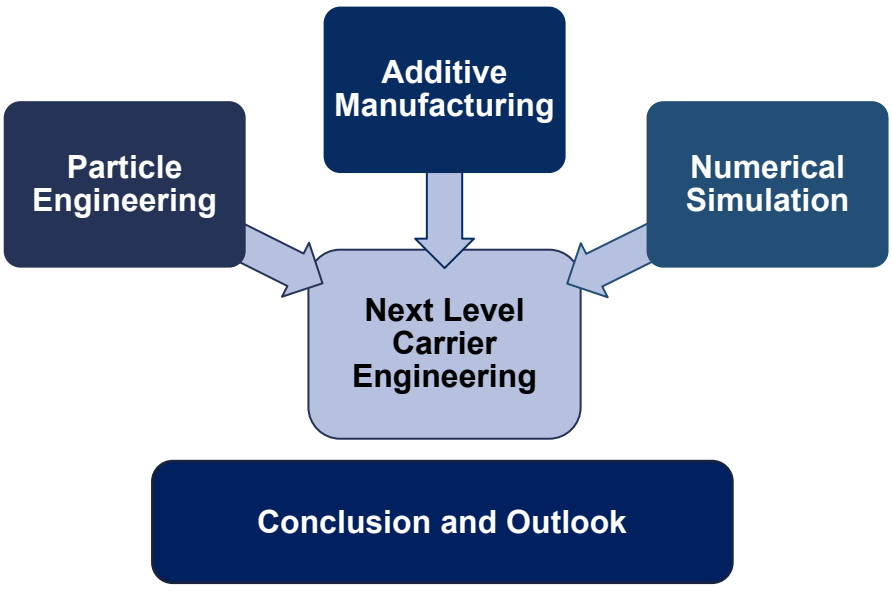

Chapter 1 Respiratory drug delivery

1.1 Anatomy of the respiratory tract

Breathing is a vital process for the human body as physiological functions essentially rely on continuous gas exchange of oxygen with carbon dioxide. The breathing process involves repetitive cycles of inhalation and exhalation through the respiratory system, which leads from the nasopharyngeal chamber to the alveoli. This system is divided into upper, conducting and alveolar airways (Figure 1.1). Mouth, nose and pharynx are responsible for conducting air towards the larynx, including humidification of the inspired gas as well as filtration of large, airborne particles. Once the air passes the larynx, gas and entrained particles enter the conducting airways. This region comprises multiple segments from the trachea to the terminal bronchioles, characterised by gradual tapering of the airway diameter [1].

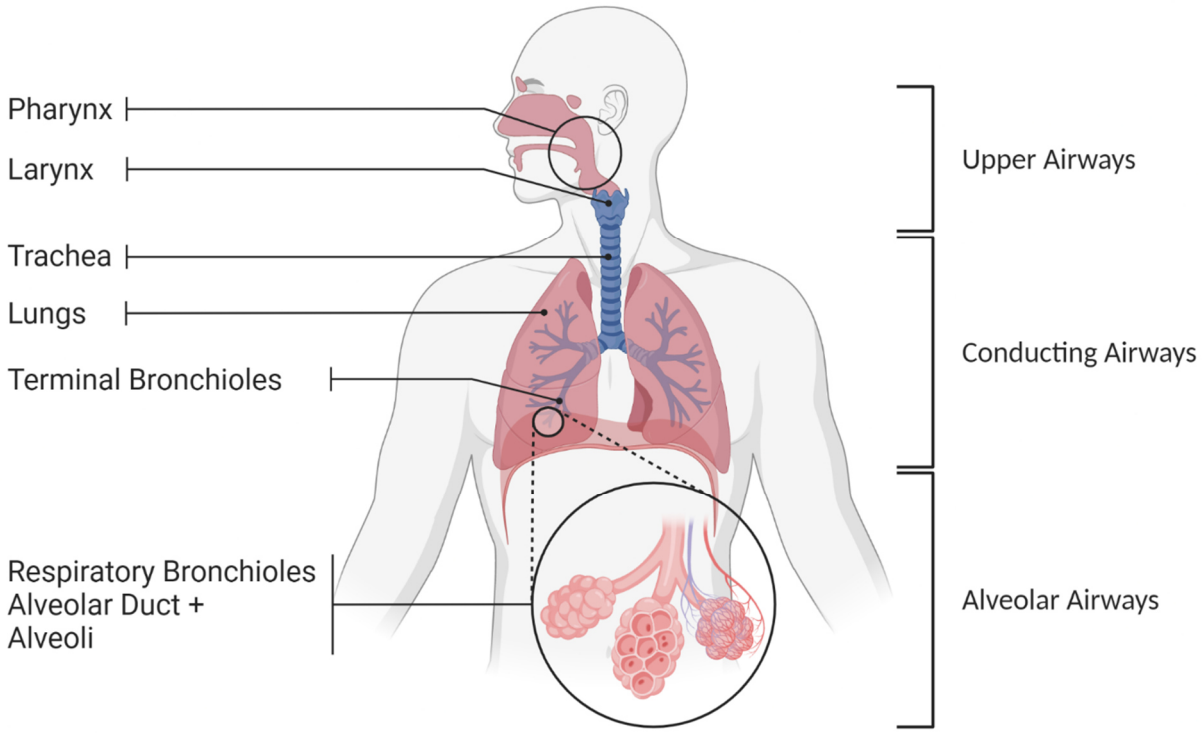

Figure 1.1: The anatomy of the respiratory tract.

Distal from the trachea the airway divides about 23 times [2]. By that, the cross-sectional area increases whereas the gas velocity decreases with each branching generation. Terminally, the pulmonary acini, made up of respiratory bronchioles, multiple alveolar ducts and alveoli, are the regions of the lungs in which the gas exchange takes place. In this respiratory zone, rapid oxygen uptake is determined by the total number of about 300-400 million alveoli in an adult lung [1].

1.2 Particle deposition in the airways

Airway dimensions and histology as well as breathing patterns influence both gas exchange and particle deposition in the lungs. Depending on their aerodynamic particle size, airborne particles are deposited in different regions of the lung, whereby very small particles can reach the alveoli. The size of the particles not only influences their deposition in the various areas of the respiratory tract but also their possible passage into the bloodstream [3,4].

The deposition of drug particles in the lungs principally bases on five different mechanisms: Inertial impaction, sedimentation and diffusion are the most important, while interception and electrostatic deposition are of less relevance (Figure 1.2) [5].

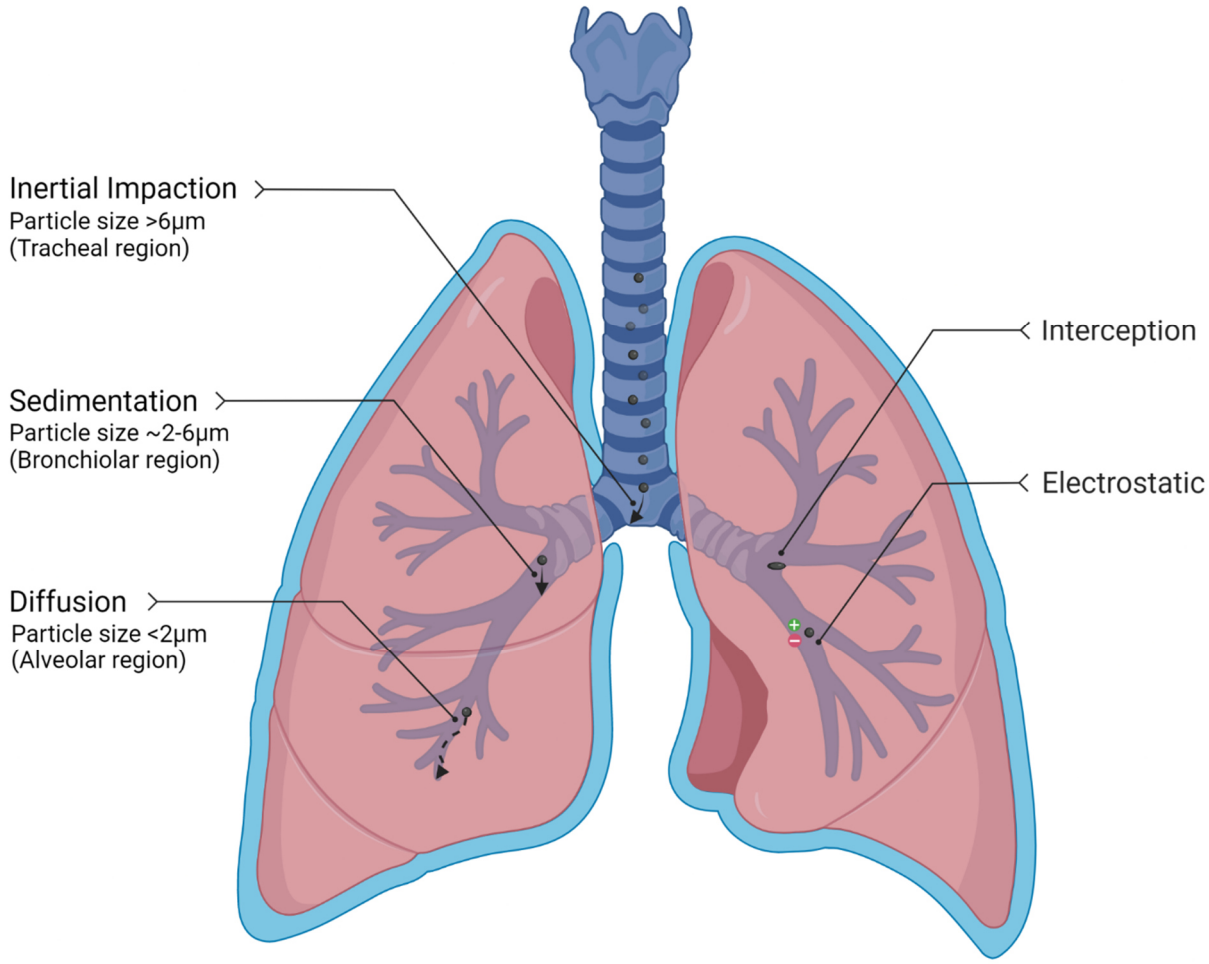

Figure 1.2: Particle deposition in the tracheobronchial and alveolar region. Modified from [5].

Impaction occurs when airborne particles fail to follow the streamlines of the inhaled air into the gradually branching segments of the respiratory tract. Due to their inertia, which is increased with higher air velocity (η_a), greater particle radius (r_p) and density (ρ_p), the particles impact at the bifurcations of the airways. As seen in Equation 1.1, the viscosity of air (η_a) and the airway radius (r_A) further influence the probability of particle impaction,

described by the Stokes number (Stk) [6]. As a result, airborne particles with a diameter > 6 µm are prone to impact in the upper airways or the tracheal region.

$$Stk = \frac{2}{9} * \frac{\rho_p * r_p^2 * v_a}{\eta_a * r_A} \qquad \text{Equation 1.1}$$

Besides impaction, the fate of particles in the airways is also determined by time-dependent, gravitational sedimentation and terminal settling velocity (v_{ts}), respectively [6]. According to Stokes-Cunningham equation (Equation 1.2), the sedimentation rate of particles is, in simple terms, greater the larger the radius (r_p) of the particles and the density difference of disperse and dispersed phase ($\Delta\rho$). Here, g is the acceleration of gravity, A is a dimensionless factor and λ is defined as the median free path length of gas molecules. Mainly through sedimentation processes, particles with a diameter of 2 - 6 µm settle in the distal, bronchiolar region, in which the airflow velocity steadily decreases.

$$v_{ts} = \frac{2 * \Delta\rho * r_p^2 * g}{9 * \eta_a} * (1 + A * \frac{\lambda}{r_p}) \qquad \text{Equation 1.2}$$

Particles with diameters below 2 µm are subject to Brownian molecular motion of the surrounding gas molecules (Equation 1.3). Deposition by diffusion, defined as the diffusion coefficient (D), also depends on the velocity and diameter of the particles. Only small particles reaching the terminal bronchioles and the alveolar regions, where the velocity of airflow becomes negligible, are considerably affected by diffusion. In contrast to the latter mechanisms, diffusion velocity and particle diameter are inversely proportional, as the diffusion coefficient increases with decreasing diameter. Here, k is the Boltzmann constant and T is the temperature, which in this case corresponds to the physiological temperature.

$$D = \frac{k * T}{3 * \pi * \eta_a * d_p} \qquad \text{Equation 1.3}$$

The mechanisms of interception and electrostatic deposition of particles play a subordinate role. Anisometric, especially fibrous particles exhibit interception, which results in deposition through contact with the lung mucosa, although the particle centre of gravity could still follow the airflow. During aerosol formation and passage through the respiratory tract, airborne particles are often electrostatically charged. Therefore, electrostatic forces contribute to particle deposition in the airways.

Inhaled particles further encounter multiple factors, such as moist environment, histological and active metabolic barriers. The respiratory tract is lined with epithelium which contains cilia and secretes mucus. Due to the movement of the cilia, particles trapped in the

viscous mucus get cleared out of the airways. This intrinsic mucociliary clearance is followed by cellular und enzymatic barriers [1]. The presence of these barriers poses additional mechanisms of particle deposition and hence absorbance in the respiratory tract. Particles that are not deposited during a breathing cycle are exhaled again [7]. This predominantly applies to particles < 1 µm aerodynamic diameter (Chapter 1.4, Equation 4.6) due to a lack of deposition forces [6,7]. For particles > 5 µm, these forces, in turn, govern an impaction in the upper airways [7].

1.3 General considerations on respiratory drug delivery

The challenges in respiratory sciences are manifold, involving a broad spectrum of research and requiring a high degree of interdisciplinarity. A necessity of interdisciplinary research derives in principle from the human nature. Individual biological and socio-cultural determinants that are closely interwoven with each other, shape anatomical conditions. Thus, they influence the physiological behaviour of the respiratory tract across the human lifespan [8,9]. Age, gender and health conditions affect the diversity of inspiratory forces and patterns influencing a variation of mechanical properties of the lungs [9–14]. On these bases, environmental exposure, malignant genetic predisposition, smoking, and infectious diseases cause adverse effects on the respiratory tract. Lung diseases such as asthma, chronic obstructive pulmonary disease (COPD), cystic fibrosis, pneumonia, tuberculosis and lung cancer are among the most common diseases with partly increasing global prevalence [9,15–17]. Current strategies to prevent and control respiratory diseases have been recognised as important and highly cost-effective components of global healthcare [18] Within the healthcare system an ongoing improvement of diagnostics and medications appears to be indispensable [19].

The respiratory system is a route to treat airway disorders with locally acting inhalants; however, it is also well suited for systemic drug application. This is related to its relatively low metabolic activity and thin histological barrier, which allows local absorption and thus systemic distribution [7,9,20,21]. Recently, a growing interest has been recognised in preventive and therapeutic immunisation via the respiratory tract as an alternative route to invasive options [19,22]. In comparison with an oral administration, drug delivery to the lungs is associated with therapeutic benefits such as rapid onset of action at a lower total drug concentration [23]. This pharmacological difference has been mainly attributed to the bypassing of the first-past metabolism [24].

For the treatment and control of both respiratory and systemic diseases, a variety of active pharmaceutical ingredients (API) combined with suitable devices for inhalation purposes are

available. Such pharmaceutical dosage forms improve the patients' quality of life and reduce the risk of death. To meet the patient needs, public authorities, pharmaceutical industries, healthcare providers as well as researchers all over the world are concurrently challenged. The challenge arises from the complexity developing pharmaceuticals and medical equipment. To develop dosage forms and devices, comprehensive knowledge of physiology, pathology, diagnosis, pharmacology, clinical practice and data science is as crucial as technological expertise. Regulatory criteria for quality, safety and efficacy set high standards on the production of such products. For orally inhaled drug products (OIP), the criteria apply to formulation excipients, the design and manufacture of the device as well as the assembly of the final drug product [25].

The development of both low-cost and high-efficient as well as easy-to-use devices is in the focus of current efforts [26], because socio-economic aspects determine therapeutic success to a considerable extent [17]. Likewise, the development and global launch of new medicines entail high financial, labour, infrastructural and time expenditure. These prevailing circumstances suggest that a technology like AM has the potential to accelerate research and development (R&D) processes because it allows the rapid production of an almost unlimited variety of objects. Acceleration R&D process could further culminate in improved devices and formulations leading to better healthcare at lower costs.

1.4 Orally Inhaled Drug Products

The pulmonary route is a well-established way to treat various diseases. Application of API through the airways is usually achieved by aerosols. From a pharmaceutical perspective, aerosols comprise a wide spectrum of drug formulations that are basically dispersed as droplets (wet aerosol) or solid particles (dry aerosol) in a carrier gas (typically air or propellants) for administration. Specifically, an appropriate therapeutic effect matures from three fundamental aspects: (1) a well-dispersed distribution of the drug particle in the gas phase, (2) its behaviour in the inspiratory as well as expiratory airstream and (3) its deposition profile in the airways. For inhalable drug particles, it is desirable to avoid deposition in the oropharyngeal area, as this prevents the API from reaching the targeted site. The deposition in that area is due to impaction, which principally increases with particle size and velocity. An aerodynamic particle size between 1 and 5 µm is considered to be decisive for reaching the lungs based on mathematical evaluation [27–31], pharmacokinetic [30,32–34] and imaging [6] studies. The aerodynamic particle size distribution (APSD) is a parameter that describes how the corresponding API particles behave in an air stream (Equation 4.6). It is commonly derived from *in vitro* impaction analysis and aerodynamic

particle sizing, respectively, or laser diffraction [35]. In turn, this parameter depends particularly on particle shape (X), which is challenging to determine, and geometric diameter (D_{eq}) as well as density (ρ_p). As density affects particle deposition, geometrically large particles with a low density are more likely to reach deep lung regions than relatively small particles with a higher density [36]. As a relativising reference value, an equal-volume sphere with a density of 1 g/cm³ is defined (ρ_0). Effective drug deposition therefore requires good control over these particle characteristics.

$$D_{ae} = D_{eq}\sqrt{\frac{\rho_p}{\rho_0 * X}} \qquad \text{Equation 1.4}$$

In addition, how the particles are emitted out of the device affects their velocity and movement in the airflow. Device design determines internal airflow patterns and outlet velocity, which influences the dispersion efficiency and thus the generated aerosol particle size. The velocity of the emitted aerosol poses the localisation of particle deposition and thus the degree of pulmonary delivery. With regard to the patient administering an OIP, individual inspiratory pressure drops influence the fate of the aerosol throughout the oral cavity and the branches of the respiratory tract [14]. To a limited extend, the velocity can be controlled through appropriate device engineering, e.g. by a specific mouthpiece or a critical orifice. When evaluating whether a device is amenable for a specific treatment by aerosol inhalation, the characteristics of the device as such are inextricably linked to the formulation it contains. There are numerous publications excellently reviewing the various drug delivery systems that are commercially available [19,22,25,26,37,38].

At present, only a handful of technological principles exist which are capable of appropriate dispersion for drug delivery via the pulmonary route. Basically, OIPs can be distinguished between nebuliser, pressurised and non-pressurised metered dose inhalers (MDI) and dry powder inhalers (DPI) [25,26,35,39]. Overall, the assessment of any type of device is governed by guidelines published by local authorities and incorporated into respective pharmacopoeias. Dose variability/uniformity testing, and aerodynamic particle sizing are standard pre-market validation criteria to be met for this type of pharmaceutical product to demonstrate reliability, repeatability and efficacy [25,40]. As an output parameter of APSD assessments, the mass median aerodynamic diameter (MMAD) is considered as a comparative attribute of orally inhaled formulations because it depends on dispersion characteristics of the formulation in the device and in the airstream [6]. Additionally, the amount of inhalable fine particles, given as the fine particle fraction (FPF) of either loaded or emitted dose from the respective device, can be calculated from aerodynamic

assessments such as impaction analysis [35]. The corresponding drug quantity, which is defined as the fine particle dose (FPD), is generally considered to be capable of penetrating the lungs during inhalation.

1.5 Challenges in drug delivery to the lungs

MDI and DPI formulations are the most used OIPs for the treatment of respiratory diseases. It has been shown that the doses of fine particles having been determined for several pulmonary dosage forms are considerably lower than the label claims [41]. Thus, far less than the designated doses reach the target tissues in the lungs. This finding clearly indicates that there still is ample space for improvements [19,23,41,42]. The lack of delivery efficiency can be ascribed to various device and formulation-specific reasons.

Numerous combinations of formulation and device are commercially available. MDI dosage forms typically consist of a canister that is inserted into a device, with which the dose release can actively or passively be actuated. The canister contains a solution, suspension or emulsion in which the API is incorporated. In case a propellant is added to ensure aerosol generation, the MDI is further classified as a pressurised metered dose inhaler (pMDI). Many parameters such as drug concentration and solubility of the API in the formulation affect the stability and delivery performance of metered OIPs. Further, the excipients added, water uptake of the formulation, storage conditions, but also valve components of the device influence the aerosol generation and overall performance [43–45].

DPI products are provided in prefilled reservoirs and capsules or blistered individual doses, from which powder is released during inspiration [25,41,42]. This powder typically contains the micronised API in the form of so-called interactive mixtures (mixture of API and carrier), soft agglomerates (controlled spheronisation of API, optionally with excipients) or engineered particles (typically spray-dried) [19,38,46]. These strategies of DPI formulation will be described in chapter 1.7. Generally, such formulation strategies are required because micronised particles are typically prone to uncontrolled agglomeration due to high cohesiveness, resulting in poor flowability (Chapter 1.6). Optimal performance, low adverse effects and thus therapeutic success of DPI formulations require an appropriate balance of adhesion and dispersion between the powder components [19,47].

The use of solid formulations is in many cases considered to be advantageous in comparison to MDI and nebuliser formulations. Avoidance of propellants, reduced risk of microbial contamination, high drug stability and high dose carrying capacity account technically for DPI formulations. When using MDIs, a temporal mismatch between aerosol release and inhalation leads to an undesirably increased deposition of particles in the

oropharyngeal region and thus to a reduced therapy efficiency. Contrarily, coordination of actuation and inhalation is generally unnecessary with DPI formulations. However, the applicability of DPIs is counteracted by the dependence on the highly individual inspiratory pressure drop [14]. However, good delivery performance is shown, which is why DPI formulations have attracted rising interest in pulmonal drug administration in the recent decades [23,41]. This applies in particular to therapeutic approaches for which high doses are expedient [48]. In contrast, the coordination of actuation, which induces an immediate release of the formulation, and inhalation limits the efficiency of drug delivery of MDI formulations. In return, the release of the active ingredient is less dependent on the health status, the individual forced inspiratory strength and thus on the general condition of the patient.

Breath-actuated devices have been designed to circumvent the necessity of coordination. Nevertheless, the dispersion and storage of API in a liquid propellant leaves physical and chemical stability issues, making this kind of formulation unsuitable for sensitive drugs. Once the API is dissolved or suspended in liquid, or filled into a suitable form, the surrounding medium and external conditions affect its physicochemical stability and thus the behaviour of the aerosol. Both particulate and fluid-dynamic processes are involved in the release of the active ingredient out of inhaler devices. Moreover, physiological, anatomical and cognitive factors of the patient also play a role in appropriate drug delivery, which are beyond the control of the developer.

1.6 General considerations on Dry Powder Inhalation

Powders for inhalation, as the term implies, inevitably contain API powder particles that must be aerosolised to ensure drug deposition in the lungs. How the API particles are pharmaceutically formulated in bulk dictates their behaviour including flow and dispersion. This behaviour is principally the result of a multitude of interparticulate forces. The interaction of respirable particles featuring an aerodynamic diameter of 1 to 5 µm, is a complex interplay of physical forces. These forces are namely size-dependent van der Waals, charge-dependent electrostatic as well as capillary forces, that are dependent on particle size and surface tension of the medium in which the particle is dispersed. Additionally, mechanical interlocking arising from surface cavities and asperities influence the interaction between particles [49].

Due to their physical nature, microparticles such as API particles for inhalation exhibit relatively strong interparticulate forces cumulating in a high affinity to aggregate. Therefore, particles in the respirable size range are predominantly affected by adhesion and cohesion.

This tendency to form agglomerates, in turn hampers processability, dispersion and thus aerosolisation. The attributes influencing API particle handling and aerosolisation are manifold. Variable sizes and irregular shapes of the particles lead to heterogeneous surface properties and thus to varying interparticle forces [49]. Besides variability in particle morphology [50], density [51], hygroscopicity [52], moisture content and chemical composition affect powder processing and behaviour. The extent to which the API particles are ultimately aerosolised and delivered to the lungs is therefore directly determined by their physicochemical attributes [38,46].

A variety of techniques for preparation of API particles is documented in the literature, each resulting in products with different particulate properties [53]. Since the behaviour of the yielded products is primarily governed by forces previously mentioned in this chapter, micronised API particles require further processing and formulation into a suitable dosage form for pulmonary administration.

1.7 Formulation strategies for Dry Powder Inhalation products

Besides physicochemical properties of the API particles, its formulation and inhaler type as well as the patient who uses it, affect the clinical efficacy of DPIs. Ultimately, the intention in formulating DPI products is to ensure good bulk powder handling as well as appropriate dispersing during inhalation. Marketed DPI formulations are principally similar in their working mechanism but differ in their formulation strategy and exact mode of action of the device. In general, drug delivery of such formulations is enabled once the patient inhales actively. Depending on the DPI properties, appropriate inspiratory strength results in fluidisation of the bulk powder and aerosolisation of the drug particles.

There are currently three DPI formulation strategies available for dry power to be inhaled, namely interactive blends, softpellets (also named soft agglomerates) and engineered powders. In each of these formulation strategies, the API must be dispersed either from a particle aggregate or a carrier blend.

1.7.1 Interactive blends

Blending micronised API with carrier excipients, such as lactose or mannitol, is the most common formulation strategy for DPI products. Primarily demonstrated as ordered mixtures by Hersey in 1975 [54], this formulation strategy has commonly become referred to as adhesive mixture [55]. During blending, API particles adhere to the carrier particles, which is mainly governed by the mechanisms mentioned in section 1.6. Adding carrier excipients to the API improves processability in terms of flowability and dosing of the bulk. Moreover,

such interactive blends facilitate fluidisation and thus aerosolisation of the formulation ingredients (section 1.4). Prior to dispersion in the air stream whilst inhalation, the API particles need to detach again from the carrier which requires their adhesion forces to be overcome. Once the API particles are dispersed in the inspiratory air stream, they can follow the air towards the lower airways, whereas the carrier particles impact in the upper airways (Figure 1.3).

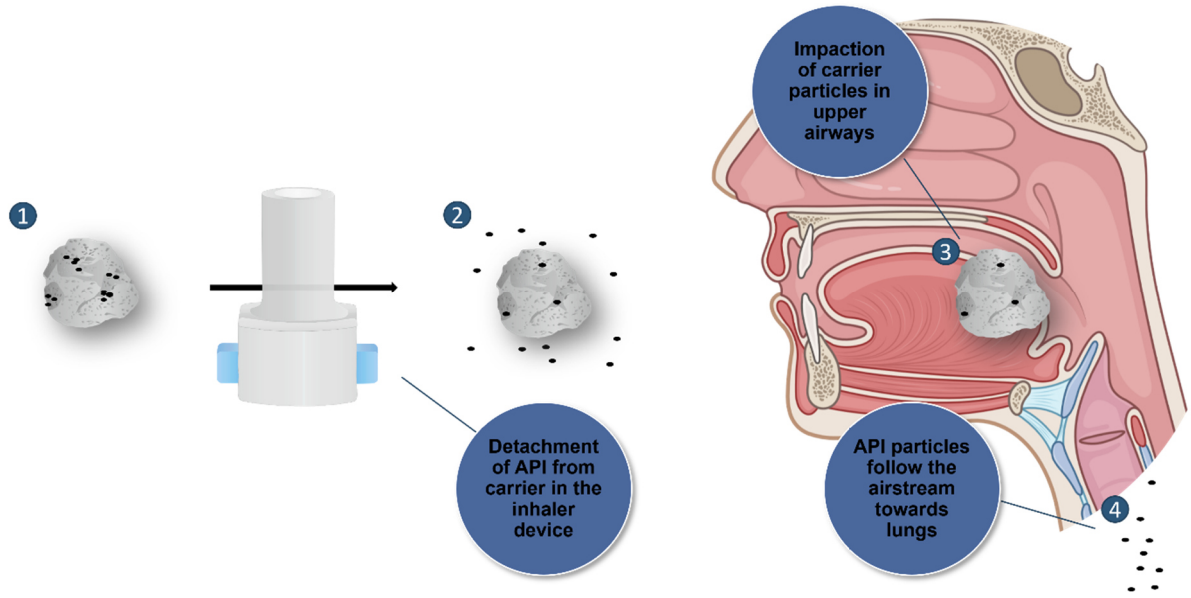

Figure 1.3: Mechanism of API release off the carrier during inhalation.

Typically, commercial products relying on interactive blends contain a binary combination of micronised API (section 1.2) and α-lactose monohydrate (Chapter 2.2.1.1) in the size range from 50 to 200 µm as carrier material [53]. Several strategies exist to improve the particle deagglomeration and hence the aerodynamic performance of this formulation type. Basically, these strategies involve adding fine portions of the carrier material, namely lactose fines, adding so-called force control agents (FCAs) [56] or carrier engineering (Chapter 2). The specific mechanism of the first two strategies, referred to as ternary blends, remains partly unclear, whereby several hypotheses exist for mechanism of fines (Table 1.1).

Adding FCAs as a ternary constituent is intended to alter particle interactions and thus to reduce drug-carrier adhesion and interparticle cohesion. As a results of lessened particle interactions, FCAs are reported to improve deagglomeration upon aerosolisation of the powder and thus its aerodynamic performance. FCAs compose of various compounds like amino acids, peptides, phospholipids, hydrogenated oils, and metal stearates, with magnesium stearate as the most frequently studied excipient [57].

Table 1.1: Hypothesis and working mechanism for the addition of fines to interactive blends (modified from [57,62]).

Hypothesis	Mechanism
Active sites	Fine particles saturate areas on the carrier surface with a high binding energy, so-called “active sites”, leaving less adhesive sites accessible for API particles to interact [58].
Agglomeration	Fines and API particles form mixed agglomerates, which possess higher mass than individual drug particles, resulting in stronger separation forces and facilitating detachment off the carrier [59].
Buffer	Fines serve as a buffer particles, preventing the API from excessive press-on forces onto carriers during the mixing process, which in turn facilitates detachment and aerosolisation during inhalation [60].
Fluidisation	Fines increase the internal tensile strength of the powder blend and thus the buoyancy forces required for fluidisation. Due to the enhanced minimum fluidisation velocity (MFV), the powder is thus dispersed more vigorously [61].
Case-dependent	Fine particles do not automatically improve the aerodynamic performance of a DPI, as it depends on the dispersion conditions and the formulation as such.

1.7.2 Softpellets

Micronised and thus cohesive particles tend to form agglomerates. Their forming process is driven by the interparticle interactions described in section 1.6. Controlled agglomeration of primary API particles allows the preparation of soft agglomerates, also referred to as softpellets. Depending on the preparation procedure and material used, softpellets are stable enough for processing and dosing, but loose enough to deagglomerate during inspiration. Principally, this formulation type can be prepared of API only, making this strategy particularly suitable for high dose inhalation [48].

At this point in time, softpellets are commercially available in Turbohaler® preparations, which are distributed by AstraZeneca. As an example, the Symbicort Turbohaler® 320/9 (Astra Zeneca, Sweden) contains softpellets consisting of budesonide, formoterol and lactose monohydrate. In comparison to interactive blends, the API to excipient ratio is much higher in softpellet formulations. However, adequate dispersion of the agglomerates was identified as a key challenge of this formulation strategy [63].

1.7.3 Engineered powders

Particle engineering comprises a wide range of techniques aiming at the formulation of dry powder that is optimally suited for pulmonary administration (see also Chapter 2) [64]. This involves an improvement of aerodynamic properties, increase of physicochemical stability, enhancement of drug absorption and the combination of naturally incompatible APIs. Researchers have studied various methods to improve these different properties, including milling, spray-drying, freeze-drying, spray-freeze-drying, supercritical fluid-drying, thin-film-freezing, particle replication in not-wetting templates, inkjet-printing and hot-melt extrusion [53].

At present, spray-drying is the most commonly used technique to engineer dry powders for inhalation. This technique principally yields spherical, porous and thus low-dense particles with good flowability and aerodynamic properties (see Chapter 2.1). Various spray-dried formulations have been marketed, such as Tobi® Podhaler® and Afrezza® [65,66]. The Tobi® Podhaler® contains a formulation, that consists of the antibiotic Tobramycin which is diluted in an O/W-emulsion prior to spray drying (PulmoSphere™) [67]. In contrast, Afrezza contains highly porous particles consisting of spray dried Fumaryl diketopiperazine, on which Insulin is loaded afterwards (Technosphere®) [68].

The pulmonary route is a well-established way to treat diseases.
For pulmonary treatment, various dosage forms exist.
Despite the variety in devices and formulations,
drug delivery to the lungs lacks efficiency.

This thesis focusses on refinements in dry powders for inhalation.
For DPI formulations, three strategies currently exist:
interactive blends, softpellets and engineered powders.

Chapter 2 Particle engineering for DPI carriers

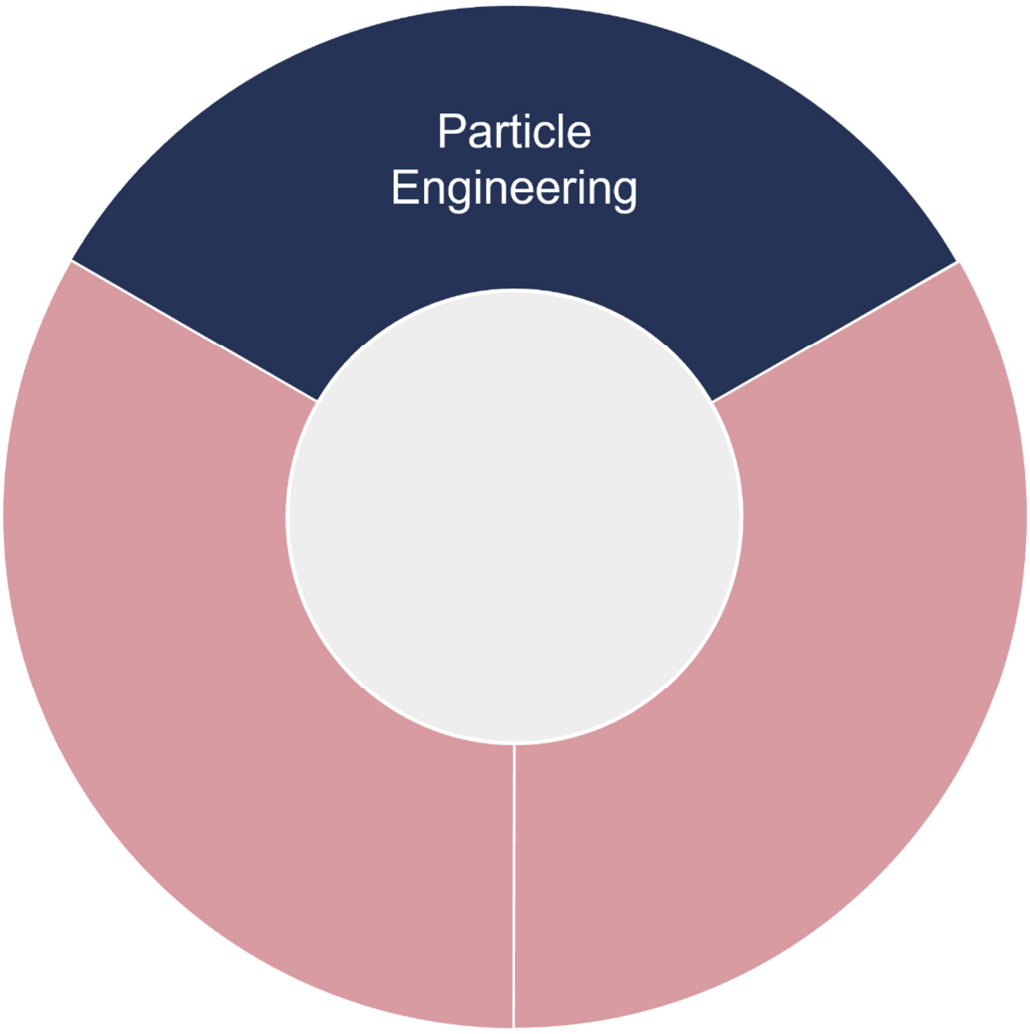

2.1 General considerations on particle engineering for DPI carriers

Various techniques exist to increase the performance of DPI formulations by engineering drug and excipient particles. Besides the engineering at the API particle level (Chapter 1.7.3), researchers also investigate the engineering of DPI carriers, which are used in interactive blends. For such carrier-based blends, numerous properties determine the suitability of a particular material as a carrier excipient (Chapter 1.7.1). These properties are particle size distribution, morphology, chemical composition including impurities, surface roughness, electrostatic behaviour and many more (Figure 2.1). Optimising particle properties essentially corresponds to an adjustment of the interparticle forces between carrier and API. Altering specific carrier characteristics principally allows for optimising DPI formulations but also help to understand the influence of individual particle properties. Therefore, scientists use techniques such as spray-freeze drying, supercritical fluid, supercritical or ultrasound assisted antisolvent and electrospinning [57]. This section provides a concise overview of spray drying and particle coating as the most common techniques for particle engineering of carrier materials.

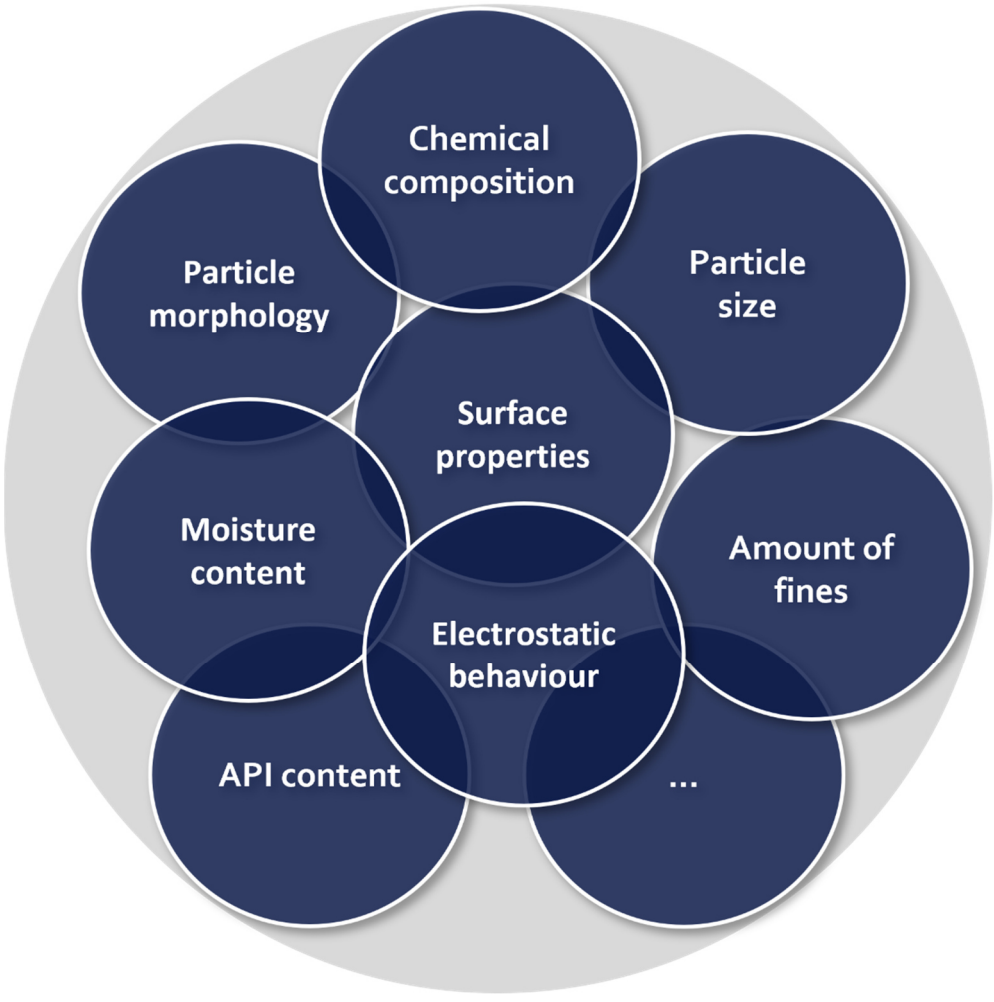

Figure 2.1: Exemplary attributes that effect aerodynamic performance of DPI formulations.

An established technique for both producing and modifying API or carrier particles is spray drying. This technique is generally employed in pharmaceutics as a method to produce spherical, highly porous particles with low density. Typically, spray-dried materials are amorphous, feature good dispersibility due to their sphericity and have a narrow particle size distribution. This technique allows for a formation of particles in the inhalable size range, but also in the size range of carriers. It has therefore been applied to research on the most common carrier materials lactose (section 2.2.1.1) and mannitol (section 2.2.1.2). With spray dried lactose being amorphous, it is physically instable and sensitive against humidity [69]. Adding excipients such as the amino acid leucine, which forms a hydrophobic shell on the surface, can principally decrease moisture uptake, prevent recrystallisation and thus enhance stability [70]. With spray dried mannitol instantly recrystallising, this material does not show the stability issues that were reported for lactose. It has therefore been extensively investigated as an alternative in carrier-based formulations [71]. In comparison to lactose crystals, which are considered to resemble tomahawks, spray-dried mannitol particles show a raspberry-like appearance.

Principally, spray-drying a composition of different materials affects the resulting particle attributes and thus particle-particle interactions. In addition, drying parameters determine morphology and surface roughness of the product. A change in particle morphology and roughness changes the contact area between adjacent surfaces or the propensity of surface charging [37], influencing both flow characteristics and aerodynamic performance [72].

Besides morphology and roughness, the interaction between particles is furthermore governed by the chemistry of the interacting surfaces. The chemistry determines the type and strength of the corresponding forces (Chapter 1.6). Altering the carrier chemistry has previously been conducted using wet or dry particle coating processes. Wet particle coating describes the application of an excipient solution onto carrier material. This has been conducted e.g. applying hydroxypropyl methylcellulose by a fluidised bed technique [73] or by modified spray-drying methods using ethyl cellulose and suspended lactose particles [74]. Coating with these cellulose derivatives led to an increase whereas the use of polyvinylpyrrolidone resulted in a decrease of aerodynamic performance [73,74]. Dry particle coating, in turn, includes methods with which FCAs can be applied onto the carrier particles without fragmentation. These excipients may be composed of numerous compounds such as amino acids or peptides, whereas metal stearates or derivatives thereof are the most common [57]. Using FCAs basically affects drug-to-carrier adhesion, thus

influencing deagglomeration upon aerosolisation. For dry particle coating, various mixing techniques or so-called mechanofusion were conducted [57,64].

Basically, the coating material layered onto a carrier surface determines the nature and magnitude of API-to-carrier interactions. Processing may further cause a smoothening of the particle surface and thus a reduction of surface roughness. The sum of these morphological and topographical properties defines the interaction forces and thus the aerodynamic performance of a DPI formulation. Besides these characteristics related to chemical composition and morphology, the technical process as such can affect other bulk properties like the particle size distribution. A change in the size distribution can be caused for example either by process-related particle fragmentation and attrition due to shear forces [75] or by particle growth due to nucleation and consolidation once a liquid is applied [76]. On the one hand, the size of the carrier determines the particle trajectories and thus the dispersion mechanisms in an inhaler depending on its design. On the other hand, relatively small particles, namely fines, impact API-to-carrier interaction (Chapter 1.7.1). Overall, a variation in particle size distribution influences the DPI performance in its entirety. Commonly used carriers, which consist of either lactose or mannitol, are commercially available in a variety of morphologies and sizes.

2.2 Materials

2.2.1 Carrier materials in DPI formulations

Previously described in Chapter 1.7, most of the DPI formulations contain a mixture of micronised API and slightly larger carrier material, which facilitates processability, fluidisation and aerosolisation. Since the aerodynamic performance of an interactive mixture (Section 1.7.1) is largely dependent on the carrier characteristics, their physico-chemical properties are highly relevant.

2.2.1.1 Lactose

Lactose is a disaccharide composed of glucose and galactose which are linked by a glycosidic bond (Figure 2.2). Traditionally, α-lactose monohydrate has been established as a typical carrier in interactive blends due to its comparatively material stability, general compatibility with many APIs and proven toxicological safety [70]. A drawback of lactose being a reducing sugar is that it potentially reacts with functional groups of amino acids (primary or secondary amines). This chemical mechanism, namely a Maillard reaction, can cause reactants such as proteins and peptides built on amino acids to become pharmacologically ineffective. Besides this disadvantage, lactose can potentially be a source

of chemical and microbial contamination because it basically originates from animals [77,78].

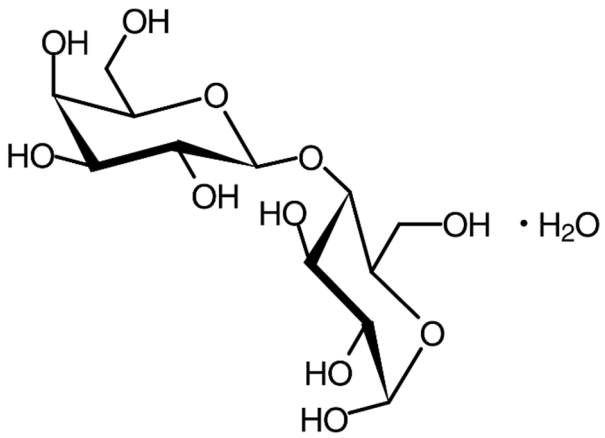

Figure 2.2: Structural formula of alpha-lactose monohydrate [35].

Different lactose grades are commercially available from various distributors. Technically, the lactose grades suitable and officially approved for pulmonary drug delivery are produced via crystallisation and subsequent sieving or milling. Lactose particles with different characteristics and particle size distributions depending on their production are commercially available. The respective size distribution and properties define the lactose particles to serve either as carrier material or fines as mentioned in Chapter 1.7.1 [37,77].

2.2.1.2 Alternative carrier excipients

Research on alternative carrier materials for dry powder inhalation has been of scientific interest for many years [57,79]. The investigation on alternatives has previously focused on several sugars such as glucose, sorbitol, maltitol, xylitol, sucrose, trehalose, raffinose and mannitol. The most promising candidate has been identified as mannitol [77], which, like lactose, has been classified by the FDA as a substance, which is generally recognised as safe [80]. In contrast to the previously excipient materials, this is a non-reducing sugar alcohol that has no animal but plant origin [81]. Due to its proven toxicity profile, it is already being utilised in many pharmaceutical products [82]. Recently, the suitability of mannitol as an alternative carrier material to lactose has been systematically proven, as it features comparable bulk properties as well as aerodynamic performance but lower chemical reactivity [71].

2.2.1.3 Microcrystalline cellulose pellets

Besides carrier chemistry, differences in particle morphology may have an effect on the propensity to deagglomerate, because drug to carrier interactions are driven by surface phenomena [37]. To eliminate the effect of heterogeneous particle morphology, in this work relatively uniform, spherical pellets composed of microcrystalline cellulose (MCC) served as

an alternative carrier material (Figure 2.3) for studies on aerodynamic performance. Basically, cellulose is the main constituent of plant fibres, with cotton being the purest natural form of the substance. According to the GRAS substances database, there is no evidence on MCC that indicates a risk to humans when used in appropriate quantities.

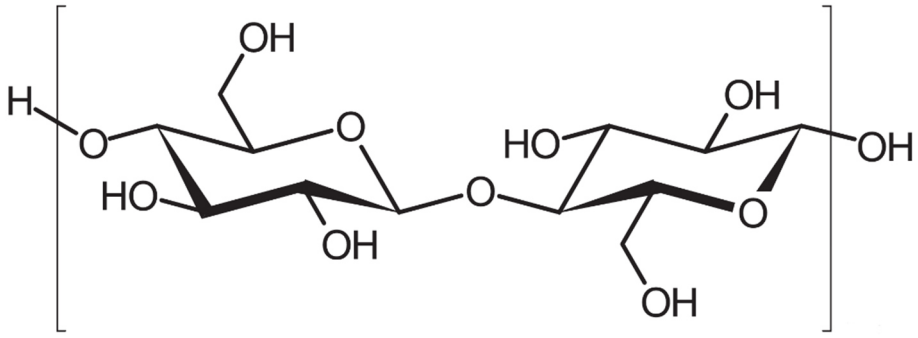

Figure 2.3: Structural formula of cellobiose, the cellulose monomer consisting of β-d-glucose units [35].

Hydrolysing the amorphous portions of purified cellulose sourced from wood yields a product with a higher degree of crystallinity, namely MCC. Enhanced crystallinity can also be achieved by reactive extrusion or steam explosion [83]. The product is nearly white, mechanically robust, chemically inert and insoluble in water. It is used in diverse pharmaceutical formulations due to its compressible, moisture binding, liquid thickening and bioadhesive properties [83]. MCC has also been used as an excipient in pharmaceutical additive manufacturing processes [84]. According to the supplier of the material utilised in this thesis, the various grades of Vivapur® MCC spheres (JRS Pharma, Germany) derived from different sieve fractions of pelletised, rounded and subsequently fluid bed dried bulk material.

2.2.2 Model drug – Salbutamol sulfate

The drug substance salbutamol sulfate (SBS) belongs to the pharmacological class of beta-2 adrenergic receptor agonists. Agents of this class act mainly on the smooth muscle of the vasculature and bronchial tree causing them to relax. SBS is further categorised in the therapeutic group of short-acting bronchodilators. Such therapeutic agents are used both in control of acute symptomatic episodes as well as chronic, long-term prevention and management of asthma. Administration of this API also prevents bronchospasm in patients suffering from bronchitis, COPD and other bronchopulmonary disorders [87]. SBS is a racemic mixture of R- and S-isomers (Figure 2.4). It is further a crystalline powder with white appearance. Whilst slightly soluble in water, it is practically insoluble to very slightly soluble in dichloromethane and in ethanol 96 % [35]. Micronised SBS was purchased from Lusochimica S.p.A., Italy.

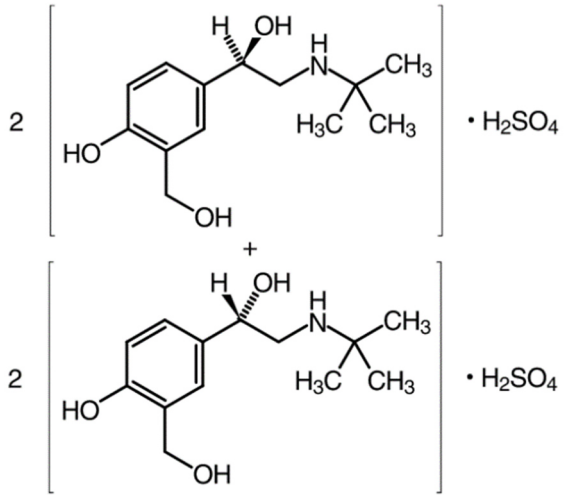

Figure 2.4: Structural formula of salbutamol sulfate (mixture of R- and S-isomers) [35].

2.2.3 Amino acids for carrier coating

To study the effect of surface alteration on aerodynamic performance, spherical and relatively uniform MCC particles were coated with three different amino acids. Principally, amino acids are endogenous molecules with a relatively low molecular weight. In the context of DPI formulations, L-leucine is the most frequently studied amino acid that basically serves as an amphiphilic FCA in ternary blends for inhalation (Chapter 1.7.1). This amino acid was utilised as a compound in multiple particle engineering approaches, principally revealing an improvement in aerosol performance [57].

In this thesis, the aromatic amino acids phenylalanine (Phe), tyrosine (Tyr) and tryptophan (Trp) were chosen as FCAs. Theses amino acids provide a variety of intermolecular interactions because of their chemical structure (Figure 2.5). These interactions include π-stacking, hydrogen bonds, van der Waals and electrostatic forces [88].

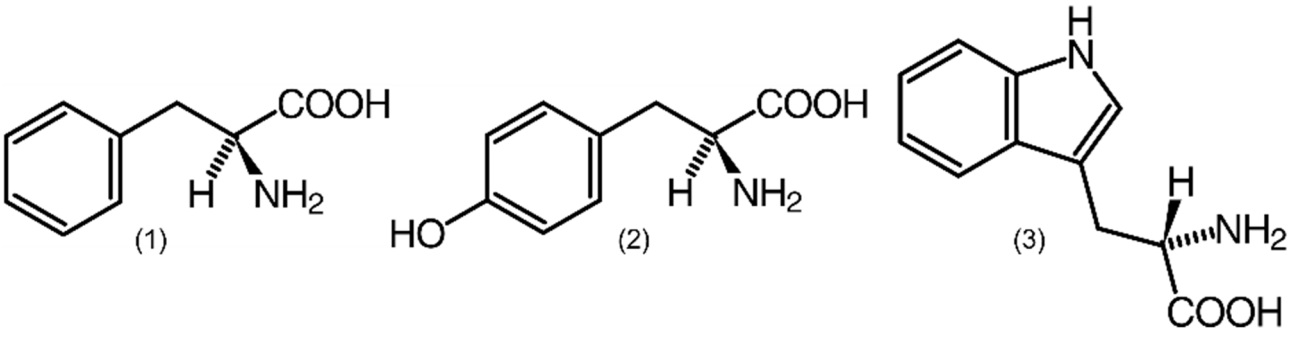

Figure 2.5: Structural formula of phenylalanine (1), tyrosine (2) and tryptophan (3) [35].

Phenylalanine has previously been utilised as a compound in spray-drying with positive effects on the resulting DPI product [89]. With reference to these effects, this thesis examines the influence of aromatic amino acids onto a carrier on the aerodynamic performance of an OIP. With the substances having a benzene ring, these compounds show

good UV absorption, which coincides with adequate quantification sensitivity and selectivity. Each amino acid was purchased from Sigma Aldrich (Germany).

2.2.4 Inhaler devices

In general, DPI products are commercially available in prefilled reservoirs and capsules or blistered individual doses, from which powder is released during administration. The aerodynamic assessments in this chapter base on the utilisation of both reservoir-based and capsule-based inhaler devices, that are commercially available. The latter type of device requires the insertion of a capsule into the designated chamber immediately before use.

The inhalers tested differ in their design and thus device resistance, powder storage and dispersion mechanism. In the following, they are presented regarding their handling and mode of operation.

2.2.4.1 HandiHaler®

Basically, the capsule-based DPI device HandiHaler® (Boehringer Ingelheim, Germany) consists of a capsule chamber and a mouthpiece (Figure 2.6). One powder-filled capsule can be inserted in a vertical position into the chamber. The capsule is perforated by two sharpened pins that are triggered once a button on the side is pushed. During inhalation, air flows into the inhaler and through the punched holes into the capsule, causing it to vibrate and thus releasing the powdered content. Subsequently, the fluidised powder streams through a grid, which borders the capsule chamber at the top, into a conically shaped tube. This tube, in turn, ultimately functions as the inhaler mouthpiece. In the studies described in this chapter, the inhaler was loaded with HPMC capsules of size 3 with an internal volume of 0.3 mL (Vcaps® Plus, Lonza Group, Switzerland).

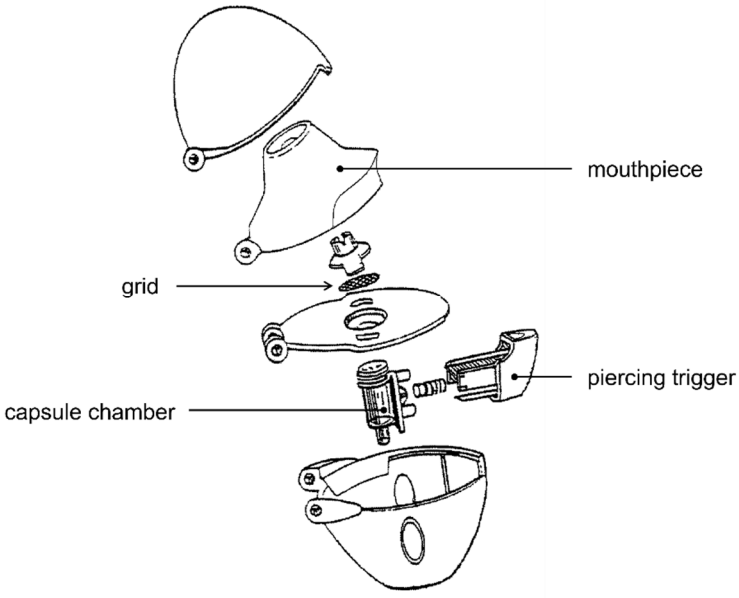

Figure 2.6: Technical drawing of the HandiHaler® device (modified from [90]).

2.2.4.2 Novolizer®

The Novolizer® (MEDA, Germany) inhaler is a reservoir-based inhaler, i.e., the powder is stored in bulk in a cartridge and is volumetrically metered into single doses by pressing the trigger. Once triggered, the powder falls into the indentation at the back end of a channel at the bottom of the inhaler. By inhalation, the powder is carried further through the channel into the air classifier, which is located vertically in the mouthpiece. Along its outer edge, this cyclonic classifier features several obliquely arranged baffle plates and a circular outlet in the centre (Figure 2.7).

This arrangement causes a circular flow upon inhalation that swirls the powder particles into a corresponding trajectory. The resultant centrifugal forces acting on the powder agglomerates cause them to impact against the plates, which leads to deagglomeration of the particles. In the case of interactive powder blends, this causes the API particles to detach from the carrier. The acting forces are driven by the velocity of the inspiration flow, but also by size and mass of the particles. Therefore, primarily particles on which relatively low centrifugal forces act and that have a relatively low inertia leave the inhaler via the central outlet.

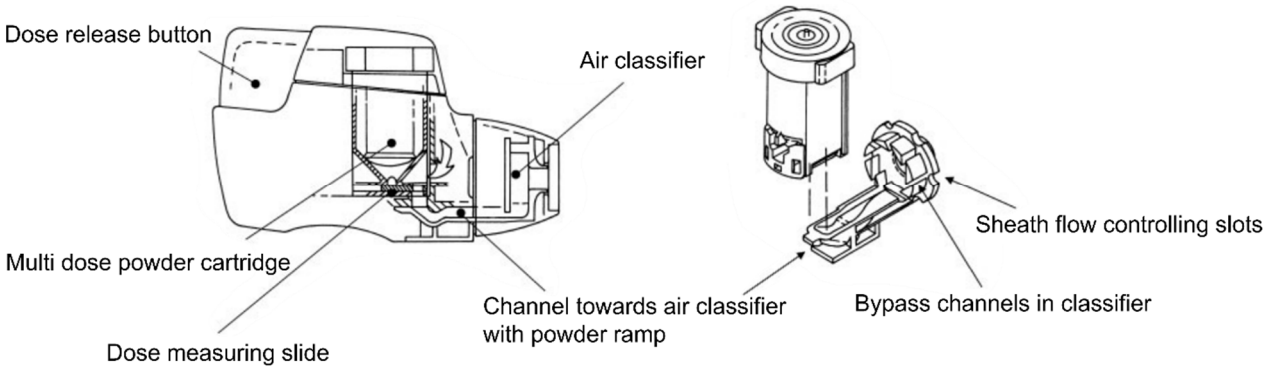

Figure 2.7: Technical drawing of the Novolizer (modified from [91]).

2.3 Methods

2.3.1 Characterisation of morphology and particle size distribution

To characterise the initial materials as well as the processed formulations, various methods were conducted. The following section will provide detailed information about the methods applied and their analytical principles.

Imaging of morphological characteristics of the samples mentioned in this thesis based on scanning electron microscopy (SEM), digital microscopy or dynamic image analysis. Besides imaging, these methods also allow sizing of particles, providing number-based (q1) particle size distributions. In contrast, laser diffraction analyses provide volume-based (q3*) particle size distributions. In principle, it is feasible to convert particle size data from one

distribution to another. However, this requires detailed information about the physical properties of a particle and its precise shape.

Interpreting results of particle size distribution (PSD) measurements require statistical measures of location and spread. Characteristic parameters for such measures are $x10$, $x50$ and $x90$, which represent the volume equivalent diameter at which 10%, 50% and 90% of the particles are smaller than the respective value. The span value indicates the distribution width and spread, respectively (Equation 2.1).

$$span = \frac{x_{90} - x_{10}}{x_{50}} \qquad \text{Equation 2.1}$$

2.3.1.1 Scanning electron microscopy

The SEM is a microscope whose measuring principal is based on an electron beam scanning a sample. An electron source emits electrons, which are accelerated depending on the applied voltage and focussed into a beam by magnetic lenses. The finely bundled beam then hits and thus scans the surface of the sample in a precise spot. Detectors collect the backscattered electrons, and the corresponding signals are then displayed as a topographic image of the specimen.

Collisions with gas molecules interfere with the signal which disturbs an appropriate measuring. Therefore, the measuring chamber is hermetically sealed and evacuated. Before non-conductive samples can be analysed with the SEM, such specimens are coated with a conductive layer. As all materials were non-conductive, the samples mentioned in this thesis were fixed onto carbon stickers which were placed on aluminium stubs (both Plano GmbH, Germany), and sputtered with BAL-Tec SCP 050 Sputter Coater® (Leica Microsystems, Germany) prior to microscopic visualisation. The sputtering process was carried out under argon atmosphere for 20 seconds with a pressure of 0.05 mbar at a sputter power of 60 mA.

Imaging of particle morphology was conducted with the Phenom XL® (Thermo Fisher Scientific Inc., USA) at an acceleration voltage of 5 kV to 15 kV and a vacuum of 10 Pa.

2.3.1.2 Digital microscopy

A digital microscope is an instrument that bases on an image sensor to display images of a specimen on a monitor. An image sensor, which is composed of photodiodes, detects light entering through a lens. The sensor converts the analogue signal into digital data which is then converted into an image of the analysing sample.

Digital imaging of the samples mentioned in this thesis was conducted with an VHX-500K® (Keyence Corp., Japan). This microscope has a depth composition function, which

allows extracting and stitching of focused pixels at different levels of magnification. With this function, a fully focused image of a sample can be captured. Moreover, the instrument was also used to determine the PSD. Digital microscopy yields two-dimensional images whereas the samples are generally three-dimensional objects. On this account, the resulting images only provide PSD based on the assumption of spherical objects. PSD analysis conducted with digital microscopy therefore provides a list of specimen diameter of the maximum length in one dimension. A corresponding distribution can then be determined from this listed data.

2.3.1.3 Dynamic imaging analysis

Capturing particle projections with high-speed image analysis was conducted using the QICPIC® system (Sympatec GmbH, Germany). This instrument uses a pulsed light source in combination with a high-speed camera capable of capturing up to 450 images/s. Resulting images of an analysed specimen provide information of the particles' shape and size between 1 and 20,000 µm.

To obtain the true morphology a size of the specimen, product-specific dispersion prior to imaging is necessary. For this purpose, modular equipment for dry and wet dispersion can generally be adapted to the QICPIC®. The samples in this thesis that refer to QICPIC® analyses were measured by coupling the GRADIS® module to the QICPIC®. This module is a freefall shaft containing deflector plates and adjustable outlet slits. These slits were set to 4 mm to ensure proper particle distance and thus proper sample imaging. Correct dosing to the measurement chamber was obtained applying the VIBRI® module, which enables computer-controlled feeding via a vibrating chute. This module was not applied in case of softpellet samples to avoid erroneous deagglomeration prior to imaging.

In addition to particle imaging, this method can also be used for PSD analysis. To assess the size of particles and softpellets, respectively, the area equivalent circle diameter (X_{EQPC}) was determined. This parameter is derived from the projection area of each particle. From this area the software WINDOX® (version 5.8, Sympatec GmbH, Germany) calculates a circle with the same area (A) and provides the diameter of it (Equation 2.2):

$$X_{EQPC} = 2\sqrt{\frac{A}{\pi}} \qquad \text{Equation 2.2}$$

2.3.1.4 Laser diffraction

Sizing of particles can principally be conducted using laser diffraction analyses. This methodology bases on light diffraction once a laser beam passes through a dispersed particulate specimen and is diffracted by the particles.

The morphology of the particles determines the intensity of the diffracted light and its angle, which in turn depend on the size and physical properties of the samples. Principally, small particles scatter light at large angles, whereas large particles scatter light at small angles relative to the incident light. In addition to the particle size, the particle shape also influences the scattering pattern. The diffraction pattern of spherical particles typically shows a ring structure. In contrast, non-spherical particles reveal diffuse diffraction patterns. To determine the total scattered intensity as a function of the scattering angle considering the direction of the incident light, different algorithms have been developed. In turn, detecting the angular and intensity variations with a photodetector enables the calculation of the particle size distribution.

For samples mentioned in this thesis, calculating the particle size by laser diffraction generally bases on the Fraunhofer theory. This theory only considers the diffraction at the contour of the particle on the assumption that the incident light waves propagate rectilinearly and parallelly. As a result of this simplification, the particle size distributions determined with this method relate to the equivalent diameter of spheres that have an identical diffraction pattern.

Laser diffraction was applied to determine the PSD of micronised drug particles as well as processed materials such as interactive blends and softpellets. For this, a Helium Neon Laser Optical System (HELOS®, Sympatec GmbH, Germany) system equipped with a RODOS® dry dispersing unit was used. Correct dosing to the dispersion chamber was obtained applying the VIBRI® module or the samples were fed manually into the inlet funnel. The samples were dispersed towards the measurement chamber by compressed air. PSD measurements given in this thesis are preceded by a dispersion pressure evaluation to ensure adequate deagglomeration of the individual particles as well as to exclude process-related particle fragmentation.

The measurements were performed to determine the particle cumulative frequency (Q3) and probability density function (q3*). In this thesis, particle sizing was conducted in triplicate for each sample and the shown data is the arithmetic mean. Data derived from laser diffraction measurements offers statistically higher validity than microscopy, because it is imaging large numbers of particles. At high optical concentrations, however, resolution can be impeded as particle overlap leads to erroneous results and seemingly larger particle sizes. The data given in this thesis principally rely on optical concentrations between 3 to 15 % as determined by the control and evaluation software WINDOX®.

2.3.2 Carrier coating

Spherical carrier particles consisting of MCC (see section 2.2.1.3) were coated with different amino acids. The MCC spheres served as model carrier because of their relatively uniform morphology and smooth surface. As illustrated in Figure 2.8, the coating was performed in a fluidised bed using a Mini-Glatt® equipped with a Wurster-inlet (Glatt, Germany).

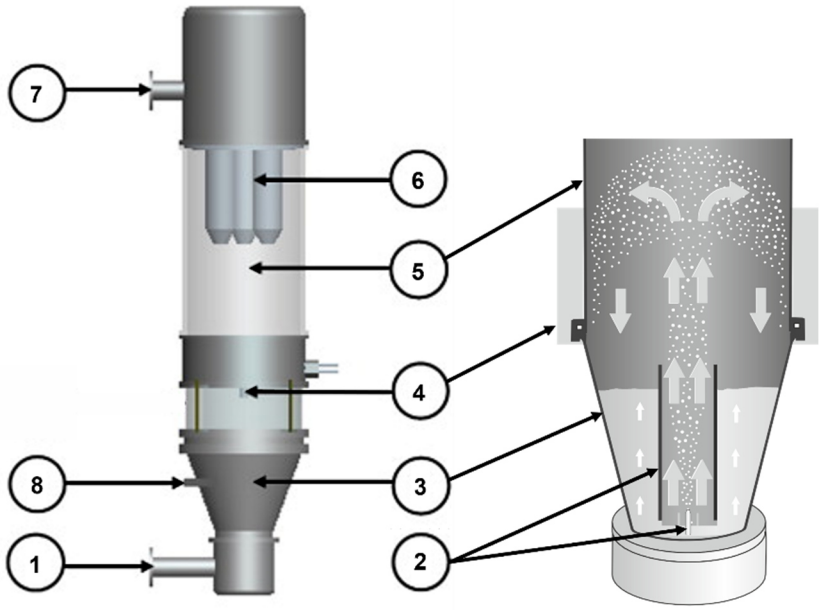

Figure 2.8: Schematic cross-section of the Mini-Glatt®: air inlet (1), bottom-spray nozzle and Wurster-inlet (2), product container (3), glass window (4), filter housing (5), filter (6), air outlet (7), temperature measuring port (8).

With a Wurster-inlet in the centre of the downwards conically tapered container combined with a bottom-spray inlet, a controlled particle movement and coating can be achieved. In bottom spray coating, spraying is done using nozzles that are directed from below up into the fluidised bed. At the bottom of the Wurster-inlet the particles are abruptly accelerated upwards and directed along the upper end of the spray nozzle. This ensures a consistent particle retention time in the spray zone and causes high kinetic energy in the upbed. On the one hand, the high kinetic energy prevents the particle from sticking to each other. On the other hand, the positioning of spray nozzles and Wurster-inlet prevents premature evaporation of the spray liquid. Therefore, this instrumentation is suitable for homogeneously adding functional coatings onto particles.

In this work, aqueous solutions containing the respective amino acids (section 2.2.3) were sprayed onto fluidised MCC spheres. For this purpose, 200 mg of amino acid were weighed into a 50 ml volumetric flask. To ensure proper dissolution, 5 ml of a 1 molar sodium hydroxide solution (4 g/100 ml, Sigma Aldrich, Germany) was added. Then, the flask was

filled to just below 50 ml, treated in a temperature-controlled ultrasonic bath for 5 minutes and then fully filled.

After 40.0 g of MCC spheres were filled into the product container (Figure 2.8), the fluidised bed system was completely assembled. The assembly involved connecting the volumetric flask to the bottom-spray inlet via a hose threaded into a peristaltic pump, which was set to a flow rate of 1 mL/min. Spraying was initialised once the particles flew in a stable fluidised bed, that was heated up to at least 40.0 °C. Supply air and sprayer pressure were monitored and, if necessary, adjusted. Corresponding process parameters are shown in Table 2.1. After complete spraying of the solution, the material was dried until the outlet air temperature corresponded to the inlet air temperature.

Table 2.1: Process parameters for coating of MCC spheres with the Mini-Glatt®.

Parameter	**Supply air [°C]**	**Supply air pressure [bar]**	**Sprayer pressure [bar]**	**Fluidised bed temperature [°C]**	**Outlet temperature [°C]**
Value	50 – 55	0.5 – 0.6	0.45 – 0.5	40 **–** 45	32 **-** 43

2.3.3 Preparation of interactive blends

Preparing adhesive mixtures was conducted with the high shear mixer module Picomix® (Hosokawa Alpine, Germany). Firstly, to break up agglomerates prior to blending, carrier and API bulk material were separately passed through a sieve. Depending on the particle size distribution of the used material, the sieve meshes ranged from 180 µm (API), 560 µm (MCC 200) and 800 µm (MCC 350 and 500). Then, the chamber of the Picomix® was separately filled with carrier and API using a double-sandwich procedure. The mixer was operated at a rotation speed of 500 rpm twice for 60 seconds with an intermediate sieving step (560 µm and 800 µm sieve, respectively). Each formulation was blended at ambient conditions (20 - 23 °C and 30 – 65 % rH).

Differences in morphological and physicochemical characteristics of particles in a bulk potentially result in segregation. For particles in the micrometre range, segregation is also driven by relatively strong interparticle adhesion and cohesion forces (Chapter 1.6). Therefore, processing two or more different components to an interactive powder blend is accompanied with a relatively high probability of non-homogeneous particle distribution. Accordingly, product quality testing is mandatory to monitor alterations upon powder handling and to ensure that each sample taken is representative of the source bulk material (section 2.3.3.1).

2.3.3.1 Quantification of API and amino acids

To test the coating quality (Section 2.2.4), the relative standard deviation of excipient content in ten sample increments was determined. For this purpose, the amino acid content of ten randomly sampled units was analysed in duplicate with UV-HPLC quantification (Waters Corp., USA) and an external standard calibration. Each amino acid required an appropriate analytical methodology, i.e. column type, wavelength, mobile phase and eluent flow (Table 2.2 and Appendix G). Data acquisition was carried out with Waters Empower® software (Waters Corp., USA).

Table 2.2: Analytical parameters for quantification of the coating excipients.

Substrate	Column type	Mobile phase	Flow [mL/min]	λ [nm]
Phenylalanine	RP-18	10 % Acetonitrile + 90 % buffer solution Buffer: 3.4 g/L Potassium dihydrogen phosphate in $_{dd}H_2O$. pH-value set to 3.0 by adding ortho-Phosphoric acid 85 %.	0.8	274
Tryptophan	RP-18		1.0	220
Tyrosine	RP-18		0.8	274

To test the blend quality (Section 2.3.3), the relative standard deviation of API content in sample increments was determined. For this purpose, the API content of ten randomly sampled units was also quantified by HPLC (Table 2.3). Another characteristic of a powder blend is the API recovery, which results from the substance mass quantified by HPLC analysis divided by the practically weighed and thus theoretically detectable API mass.

Table 2.3: Analytical parameters for quantification of the API salbutamol sulfate.

Substrate	Column type	Mobile phase	Flow [mL/min]	λ [nm]
Salbutamol sulfate	RP-18	22 % Acetonitrile + 78 % buffer solution Buffer: 2.87 g/l Sodium heptanosulfonate, 2.50 g/l Potassium dihydrogen phosphate. pH-value set to 3.65 by adding ortho-Phosphoric acid 85 %.	0.8	220

2.3.4 Aerodynamic assessment

Testing of the DPI formulations used in this thesis principally based on the method *preparations for inhalation: aerodynamic assessment of fine particles* according to the European Pharmacopoeia (Ph.Eur. 2.9.18) [35]. The Ph.Eur. provides a methodology to be used to determine the aerodynamic performance, expressed as the fine fraction of particles in an aerosol. According to this guideline, this comparative measure can be assessed with a handful of instruments. Each of these instruments relies on particle impaction due to

inertia, meaning that the particle can no longer follow the airflow. As a result of the APSD assessments aerodynamic size distributions can be determined (Chapter 1.4).

2.3.4.1 Next Generation Pharmaceutical Impactor

For the aerodynamic assessments examined in this thesis the Next Generation Pharmaceutical Impactor® (NGI, Copley Scientific, Nottingham, UK) was used (Figure 2.9). This instrument is composed of an induction port, a preseparator, a central unit and eight cups, namely stages. These parts are arranged in a specific order, directing sucked air from the induction port, through the preseparator into one stage of the central unit after another. The air leaves each compartment through connecting channels and nozzles, respectively, whereas the nozzles of the stages feature a progressively reducing jet diameter. In the same way, the distance between nozzle and cup is continuously reduced, both causing an acceleration of the airflow. As a result, the particles impact on the stage in dependency on their aerodynamic characteristics. The eighth stage, namely the micro-orifice collector (MOC) is designed to collect very fine particles. However, a microfiber filter (GE Healthcare, UK) was used as the final part of the NGI collecting particles that have not deposited earlier in this cascade impactor.

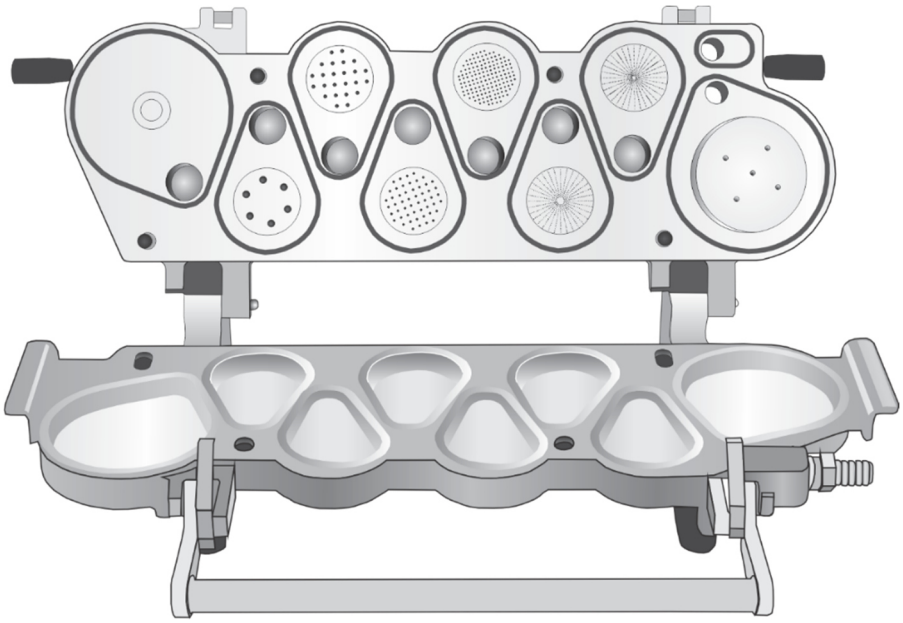

Figure 2.9: Next Generation Pharmaceutical Impactor (NGI).

For the analyses, the inhaler device of interest was connected to the induction port making use of an appropriate mouthpiece. A pump connected on the other end of the NGI enabled a flow rate to be applied resulting in an air flow through the instrument. The flow rates for each inhaler type used were adjusted to achieve a pressure drop of 4 kPa according to the Ph.Eur. [35]. The corresponding airflow rates and measuring time to obtain a flow volume of 4.0 L are listed in the following Table 2.4.

Table 2.4: Airflow rates and measuring time according to Ph.Eur. 2.9.18 [35].

Inhaler device	Airflow rate	Measuring time
Novolizer®	78.3 L/min	3.1 sec
Handihaler®	39.0 L/min	6.2 sec
Twister® (Chapter 3.6)	55.0 L/min	4.3 sec

To prevent particles from bouncing and re-entrainment in the air stream, the deposition plate inside the preseparator as well as each stage were coated with stage coating prior to each analysis. The respective solution consisted of Brij 35, ethanol 96 % (v/v) and glycerol (99 % w/w in the ratio 15:51:34 (w/w). After coating the solution was passively dried on air. Then, an inhaler containing the DPI formulation was plugged into the mouthpiece mounted on the induction port. Once properly assembled, triggering the vacuum pump for a certain time value (see previous Table) enabled the required volume of air to flow through the NGI. Each run was conducted in triplicate under controlled conditions in a climate chamber at 21 °C and 45 % rH.

After one run was finished, the instrument was dissembled and an appropriate volume of solvent was applied on the deposition plate and each of the stages, respectively. According to the solubility of salbutamol sulfate, $_{dd}H_2O$ served as solvent. The respective volume of $_{dd}H_2O$ required to dissolve each sample is displayed in Table 2.5.

Table 2.5: Solvent volume applied to samples of aerodynamic particle sizing via NGI.

Sample	Capsule	Device	Mouthpiece	Throat	Preseparator	Stages
Volume	5 ml	10 ml	10 ml	15 ml	20 ml	5 ml

Capsule, device and mouthpiece were transferred into beakers, rinsed with the solvent and then sealed with Parafilm® M (Bermis Company Inc., Wisconsin). The induction port and preseparator, in turn, were sealed with stoppers after filling with respective solvent volume. Once sufficient solvent was applied to the cups of each stage, the whole tray was covered with a plate to avoid evaporation. To ensure proper dilution, each sample was gently agitated for at least 60 seconds either manually or on a shaker plate. Afterwards the samples were filled into HPLC vials without further processing.

2.3.4.2 Quantification of API and evaluation aerodynamic assessment

HPLC equipped with UV detection (Waters, USA) served as the method of choice to quantify the samples' API concentrations derived from NGI testing. Each analyte required a specified analytical methodology, i.e., column type, wavelength, mobile phase and eluent

flow (Table 2.3 and appendices). Chromatographic grade solvents for all HPLC procedures were purchased from Honeywell Riedel-de Häen (Chromasolv™, Germany). Analytics were carried out using a linear calibration of a standard solution of each substrate. Each sample was analysed in duplicate. Data acquisition was carried out with a Waters Empower® software (Waters Corp., USA). Doubled distilled water ($_{dd}H_2O$) served as the solvent for SBS, which served as the model API in the studies of this chapter.

Evaluating the corresponding results to determine the aerodynamic performance of the formulations was conducted using the CITDAS® 3.1 software (Copley Scientific Limited, Nottingham, UK). This software allows calculating the MMAD, the FPF and FPD, known as comparative measures of OIPs (see Chapter 1.4). To calculate the FPF, the emitted dose of each run was defined as the amount of API incrementally quantified in each sample excluding capsule and device. For the Novolizer® only, the emitted dose derived from dose uniformity according to Ph.Eur. Moreover, the inhaler retention corresponds to the sum of the API masses quantified in the respective inhaler and in the capsule(s) used. The inhaler retention is expressed as a percentage of the total mass determined within the aerodynamic assessment. It thus represents the difference between the metered dose (MD) and the delivered dose (DD).

Besides these comparative measures, the recovery rate for each experiment was determined. As a qualitative attribute, the recovery rate indicates the extent to which theoretically detectable API concentrations were actually quantified within an experiment. Consequently, the recovery value gives an indication of whether the necessary work steps were carried out with sufficient care. In the case of a low value, it could be assumed, for example, that the experimental procedure was accompanied by a loss of API. It should be noted that the recovery should not be used as the sole decisive parameter for the assessment of a procedure due to several overlapping effects. Thus, an incorrect API quantification caused by poor analytics can falsely compensate for actual active ingredient losses.

2.4 Statistical analysis

For descriptive statistics, the arithmetic mean including the standard deviation was used for all multiple determinations. The corresponding calculations based on the equations for the arithmetic mean ($\bar{x}$; Equation 2.3), standard deviation (SD; Equation 2.4) and relative standard deviation (RSD; Equation 2.5)

$$\bar{x} = \frac{\sum_{i=1}^{n} x_i}{n} \qquad \text{Equation 2.3}$$

$$SD = \frac{\sqrt{\sum_{i=1}^{n}(x_i - \bar{x})^2}}{n-1}$$ Equation 2.4

$$RSD = \frac{SD}{\bar{x}} * 100\ \%$$ Equation 2.5

Unless stated differently, the graphical illustrations show the respective mean value from a series of measurements. These values also include the SD which is indicated by an error bar. In tables or in information in the text, the SD is listed with a '±' sign. Statistical significance was determined, where applicable, using one-way analysis of variance with Tukey's post hoc analysis and between groups using independent sample t-test using the software Sigma Plot (SYSTAT Software Inc., USA). Resultant p-values below 0.05 were considered statistically significant and labelled as follows: * for $p < 0.05$, ** for $p < 0.01$, and *** for $p < 0.001$.

2.5 Results – Chapter 2

This section provides the results of the study on the effects of chemical surface alterations on aerodynamic performance (Figure 2.10). To investigate this alteration specifically, this study based on a model carrier consisting of relatively uniform, spherical pellets. These pellets consisted of microcrystalline cellulose featuring relatively low abrasiveness. After alteration, the model carrier was characterised with regards to particle size, morphology, coating quantity and quality. Blending of both the initial and the altered carrier material with a model API, namely SBS, led to the formulation of interactive blends. Aerodynamic assessments of the different samples allowed for determining the aerodynamic performance thus investigating the API-to-carrier interactions.

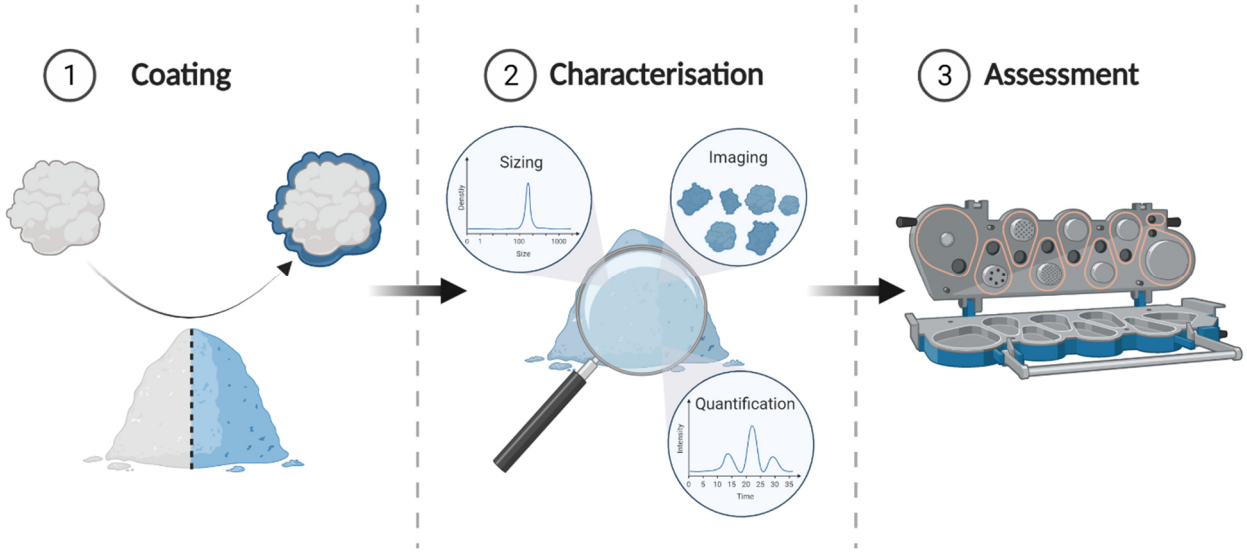

Figure 2.10: Three phases of particle engineering for DPI carriers: coating of carrier material (1), characterisation of initial and coated material (2) and aerodynamic assessment, which includes preparation of interactive blends and aerodynamic particle sizing (3).

2.5.1 Wet particle coating

Spherical carrier particles were coated with different amino acids (section 2.2.3) in a fluidised bed coating process (section 2.2.4). Figure 2.12 shows a representative image of three different grades of MCC spheres used as the initial material for particle coating, namely Vivapur® MCC 200, MCC 350 and MCC 500 (JRS Pharma, Germany). Previously mentioned in section 2.2.1.3, these grades are sieved fractions of the same production process including rounding and smoothening, respectively. Each row of this figure represents one of these grades with a series of different magnifications using SEM (section 2.3.1.1). These MCC grades served as model carriers because of their relatively uniform, spherical morphology and smooth surface in comparison to standard excipients. Representative images of the standard carrier particles composed of lactose (L; InhaLac® 70, Meggle GmbH, Germany) and mannitol (M; Parteck® M DPI, Merck KGaA,

Germany) are presented in Figure 2.11 for comparison. Lactose crystals show a tomahawk-like shape whereas mannitol particles show a raspberry-like appearance with relatively heterogeneous surface topography.

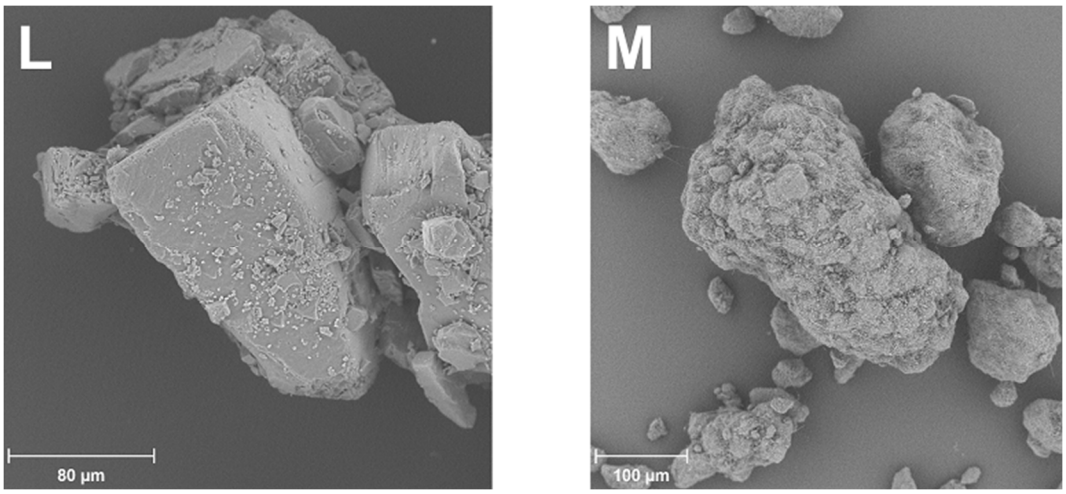

Figure 2.11: Representative images of carrier particles of lactose (L) and mannitol (M).

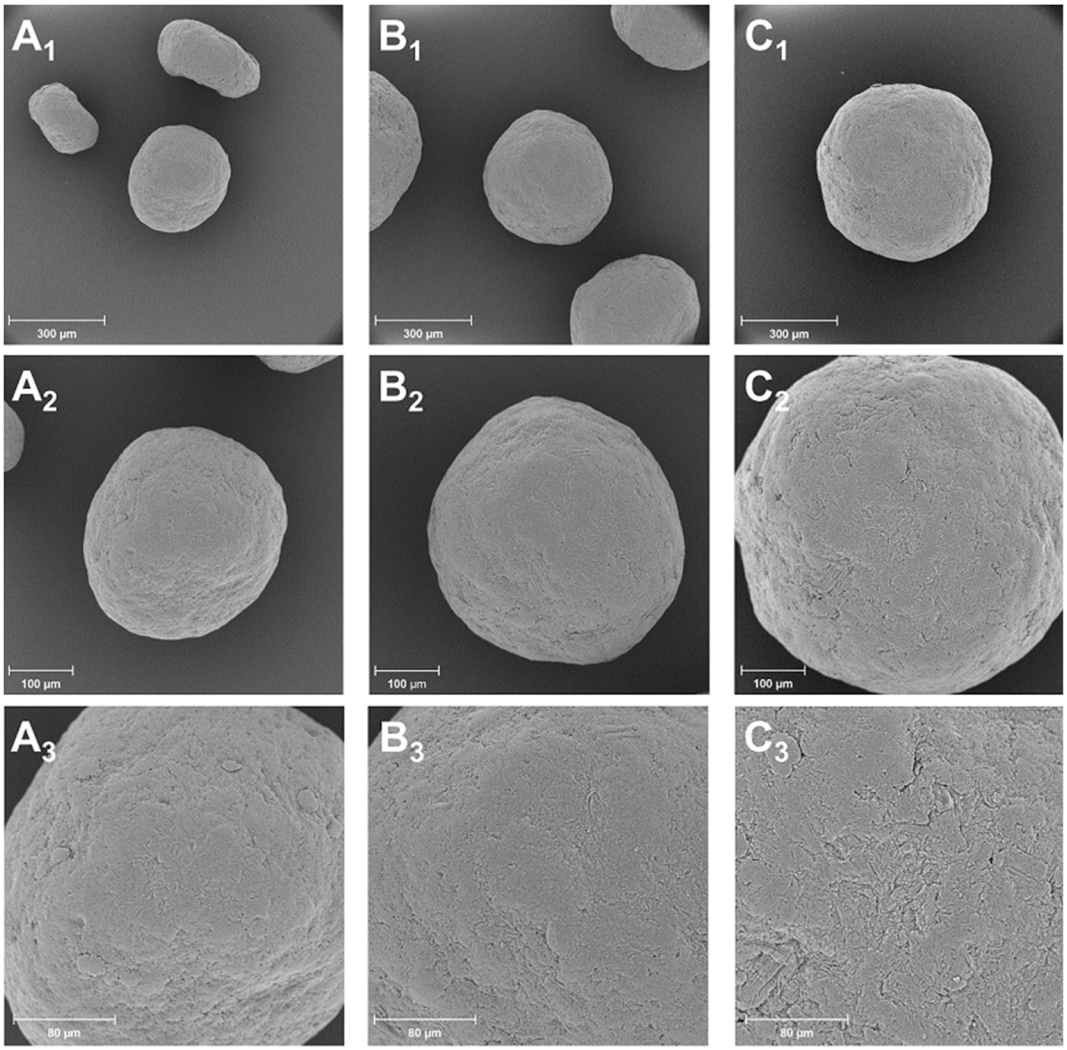

Figure 2.12: Representative images of MCC 200 (A), MCC 350 (B) and MCC 500 (C).

The PSD of each initial carrier material was measured using dynamic imaging analysis as described in section 2.3.1.3. For the different MCC grades, particle sizing revealed monomodal distributions mainly differing in median size (Figure 2.13).

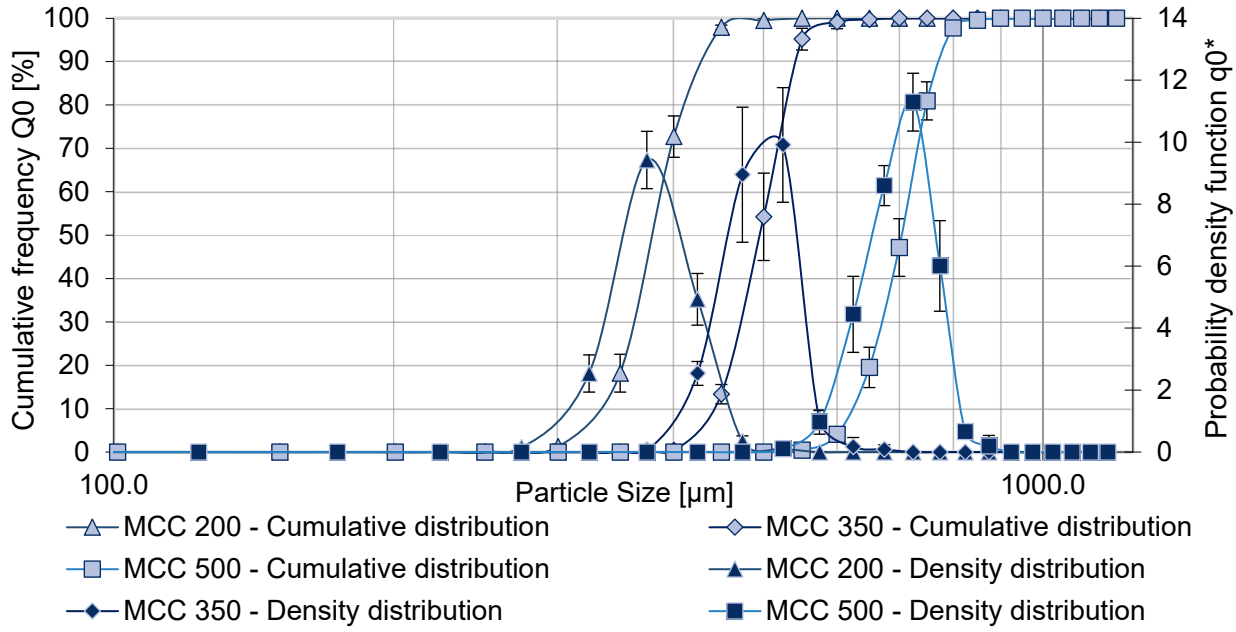

Figure 2.13: Graphical illustration of the PSDs for the starting material (MCC spheres); n = 3, error bars = SD.

MCC 200 contained particles in the size range of 327.8 ± 8.6 µm (x_{10}) to 434.5 ± 4.2 µm (x_{90}) with an x_{50} of 379.9 ± 3.3 µm. This differed from the PSD for MCC 350, which shows an x_{10} of 438.3 ± 6.3 µm, an x_{50} of 496.2 ± 9.9 µm and an x_{90} of 543.7 ± 4.3 µm. For MCC 500, particles in even larger size ranges were found with an x_{10} of 620.9 ± 8.5 µm, an x_{50} of 704.0 ± 9.5 µm and an x_{90} of 776.0 ± 7.6 µm (Table 2.6). According to section 2.5.1 and as presented in Table 2.8, the span values for each grade equated 0.28 ± 0.02 (MCC 200), 0.21 ± 0.01 (MCC 350) and 0.22 ± 0.01 (MCC 500), respectively.

Table 2.6: PSD of the starting materials; n = 3.

Material	x_{10} [µm]	x_{50} [µm]	x_{90} [µm]	span
MCC 200	327.8 ± 8.6	379.9 ± 3.3	434.5 ± 4.2	0.28 ± 0.02
MCC 350	438.3 ± 6.3	496.2 ± 9.9	543.7 ± 4.3	0.21 ± 0.01
MCC 500	620.9 ± 8.5	704.0 ± 9.5	776.0 ± 7.6	0.22 ± 0.01

Particle coating was conducted as described in section 2.2.4 using phenylalanine (Phe), tryptophan (Trp) or tyrosine (Tyr) that were introduced in section 2.2.3. During this process, the MCC particles turned slightly orange, whereby the colour and its intensity depended on the amino acid used. To determine changes in particle characteristics, post-coating analysis comprised both morphological and particle size analysis. In addition, quantifying the

respective amino acid applied by using HPLC analysis complemented particle characterisation (section 2.3.3.1).

Representative images of the processed samples derived from SEM are displayed in Figure 2.14. Each row of this figure represents one of the different grades, whereas each column shows a different amino acid. Comparing the processed with the initial material, the microscopic images indicate no substantial differences in morphology. On closer inspection, no abrasion in the form of small, fragmented particles is apparent on the surfaces. Like the starting material, the processed spheres also feature small crevices and edges. However, the coated particles show comparatively smooth topographies.

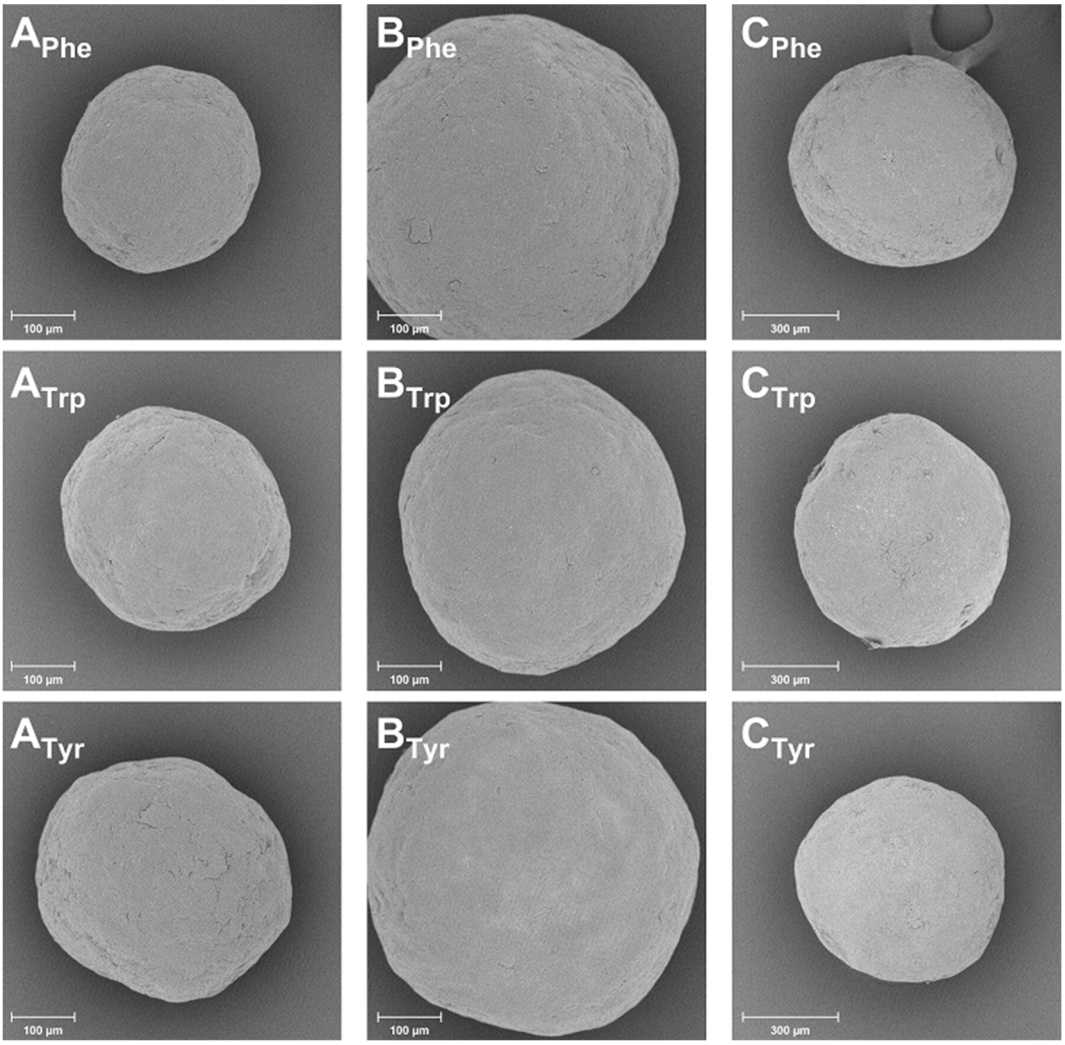

Figure 2.14 Representative images of coated MCC 200 (A), MCC 350 (B) and MCC 500 (C) with phenylalanine (Phe), tryptophan (Trp) and tyrosine (Tyr), respectively.

Determining the PSD of the coated carrier material was conducted in the same way as for the initial materials. Graphical illustrations of the different particle size distributions are given in Figure App. 1, (Appendix A), indicating a monomodal distribution for each processed grade independently on the amino acid used.

Table 2.7 summarises the measures of location and spread for each sample. Compared to the properties of the starting material (Table 2.6), the coating process led on average to a slight shift in particle size towards smaller values. This observation was due to mechanic abrasion as an effect of the fluidised bed coating process as verified with processed but uncoated pellets. However, process-induced fragmentation of the particles was apparently not detectable with dynamic imaging analysis which supported the microscopic findings. As a result of applying a fluidised bed process, particles in the size range of fines were removed, which would affect the aerodynamic performance of interactive mixtures (section 1.7.1). As an intermediate conclusion, the coating process had no major effect on morphological properties. Furthermore, initial material and the resulting product after coating do not substantially differ in particle size (Appendix A).

Table 2.7 Particle size distribution of the coated MCC spheres and respective standard deviation; n = 3.

Material	x_{10} [µm]	x_{50} [µm]	x_{90} [µm]	Span
MCC 200_{Phe}	298.2 ± 6.5	364.6 ± 5.1	422.7 ± 6.4	0.34 ± 0.00
MCC 200_{Trp}	311.2 ± 7.4	373.1 ± 4.5	431.5 ± 0.1	0.32 ± 0.02
MCC 200_{Tyr}	300.1 ± 12.8	367.2 ± 5.4	430.1 ± 7.7	0.35 ± 0.05
MCC 350_{Phe}	432.9 ± 5.2	498.9 ± 5.6	551.1 ± 8.7	0.25 ± 0.03
MCC 350_{Trp}	425.3 ± 12.7	494.2 ± 5.2	551.3 ± 9.2	0.26 ± 0.01
MCC 350_{Tyr}	422.4 ± 3.1	492.5 ± 8.5	545.5 ± 2.8	0.25 ± 0.01
MCC 500_{Phe}	610.3 ± 8.2	686.3 ± 18.0	757.3 ± 13.5	0.21 ± 0.03
MCC 500_{Trp}	603.9 ± 4.0	698.9 ± 9.5	773.8 ± 6.4	0.24 ± 0.00
MCC 500_{Tyr}	600.3 ± 4.2	687.2 ± 9.2	751.1 ± 7.8	0.22 ± 0.02

To prove successful coating of MCC spheres, the amount of amino acid coated onto the material was quantified using HPLC analysis as described in section 2.3.3.1. Specifically, testing the coating quality comprised determining the excipient content (in m/m) and its relative standard deviation (RSD; in %) for each sample. Optimally, 200.0 mg of excipient were coated on 40.0 g of carrier material, which equals 0.5%. As shown Table 2.8, the mass of excipient finally applied onto the particles was slightly different for the tested samples, although the same coating process parameters and conditions were chosen for each material grade (Appendix A). Content values varied most widely for the MCC 500 spheres, ranging from 0.41 % ± 2.11 % RSD (Phe) to 0.65 % ± 3.87 % RSD (Tyr). Accordingly, amino acid coating onto MCC 350 varied least, ranging between 0.44 % ± 2.37 % RSD (Phe) and

0.50 % ± 1.94 % RSD (Tyr). For coated MCC 200, the content ranged from 0.43 % ± 4.24 % RSD (Trp) to 0.56 % ± 3.47 % RSD (Tyr). From the results of coating homogeneity derived no causal relationship between the chemical composition of the excipient and the coating quantity.

Environmental conditions such as relative humidity (rH), temperature and electrostatics influence the coating process. These factors determine inter-particle and particle-wall adhesion as well as cohesive behaviour of the material in the fluidised bed. Further, relative humidity and moisture content of the spheres affected evaporation of the sprayed amino acid solution and thus the probability of solidification. Additionally, during each process, a random number of particles accumulated on the inner wall. Accumulated particles were thus unavailable for the coating as such and subsequently separated from the product batch. Despite processing with equal parameters, the coating processes therefore differed slightly from batch to batch resulting in varying excipient quantities. In turn, the respective RSD values evidenced low intra-batch deviation, indicating homogeneous coatings.

Table 2.8 Coating homogeneity of the engineered MCC spheres; n = 10.

Batch	Amino acid content (m/m)	Content RSD
MCC 200_{Phe}	0.51 %	3.04 %
MCC 200_{Trp}	0.43 %	4.24 %
MCC 200_{Tyr}	0.56 %	3.47 %
MCC 350_{Phe}	0.44 %	2.37 %
MCC 350_{Trp}	0.50 %	3.27 %
MCC 350_{Tyr}	0.50 %	1.94 %
MCC 500_{Phe}	0.41 %	2.11 %
MCC 500_{Trp}	0.65 %	3.87 %
MCC 500_{Tyr}	0.44 %	1.81 %

Wet particle coating in a fluidised bed served as an engineering technique to modify the chemical composition of model, spherical carrier particles.

2.5.2 Preparation of interactive blends

Each carrier batch, namely uncoated and coated MCC spheres of the three different grades, was blended with 2.0 % (m/m) of micronised salbutamol sulfate as described in section 2.3.3. Combining two or more components to form a powder mixture rarely leads directly to a homogeneous particle distribution in the material. Interparticle cohesion tendencies result in segregation tendencies. Therefore, the mixing quality of a bulk powder depends on particle properties such as shape, size, density, roughness, surface energy or residual moisture. To assess the quality of an interactive powder mixture on how the substances used are mixed with each other, the homogeneity serves as a quality attribute. Specifically, testing the blend homogeneity comprised determining the API content (in m/m) and its RSD (in %) for each sample (Appendix A). To prove carrier loading quality, the amount of API attached to the material was quantified using HPLC analysis as described in section 2.3.3.1.

As shown in Table 2.9, the blending homogeneity differed between the tested samples, although the same blending process was chosen for each material grade and batch. To prevent the samples from further energy input and thus potential particle fragmentation, no extra mixing step was conducted. Optimising the blending process was not within the scope of this work. Therefore, the criteria for homogeneity in this chapter were RSD below 10 % and a recovery of 75 – 125 %. For blends based on MCC 200 API contents ranged from 1.60 % with an RSD of 4.57 % (Trp) to 1.77 % with an RSD of 2.33 % (uncoated). Quantifying the API content for MCC 350 blends revealed a range from 1.38 % with an RSD of 3.57 % (Trp) to 1.77 % with an RSD of 1.28 % (uncoated). MCC 500 blends contained between 1.67 % API with an RSD of 4.57 % (Phe) and 1.92 % API with an RSD of 6.99 % (Tyr).

A loss of active ingredient due to the blending process was obvious because none of the samples contained the target concentration of 2% API per sample. However, substantial differences in the drug loading capacity depending on the carrier size are not evident. The API content of MCC 200 and 500 blends are on average in the same range. With the blend based on Trp-coated MCC 350 (Table 2.9,*) having an exceptionally low value, the respective subgroup shows on average relatively low API contents. Contrarily, MCC 500 blends showed considerable high RSD values in comparison to MCC 350 and MCC 200. This finding suggests that particle size is an influencing factor on the degree of drug content variation using MCC spheres as carrier material.

Table 2.9 Blend homogeneity of coated MCC spheres; n = 10.

Batch	API content (m/m)	Content RSD
MCC $200_{uncoated, blended}$	1.77 %	2.33 %
MCC $200_{Phe, blended}$	1.62 %	4.84 %
MCC $200_{Trp, blended}$	1.60 %	4.57 %
MCC $200_{Tyr, blended}$	1.76 %	4.93 %
MCC $350_{uncoated, blended}$	1.77 %	1.28 %
MCC $350_{Phe, blended}$	1.52 %	4.43 %
MCC $350_{Trp, blended}$	1.38 %*	3.57 %
MCC $350_{Tyr, blended}$	1.52 %	3.57 %
MCC $500_{uncoated, blended}$	1.72 %	8.07 %
MCC $500_{Phe, blended}$	1.67 %	7.32 %
MCC $500_{Trp, blended}$	1.87 %	7.93 %
MCC $500_{Tyr, blended}$	1.92 %	6.99 %

To verify whether drug attachment is localised rather than heterogeneously distributed on the carrier surface, characterising the blends comprised microscopic analyses by SEM imaging. Figure 2.15 shows representative images of the different blends based on uncoated material. Image A represents MCC 200, image B shows MCC 350, and image C represents MCC 500 blends with respective magnifications.

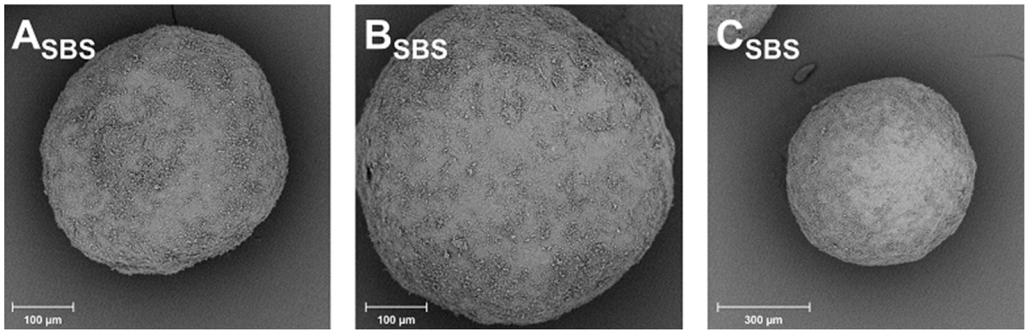

Figure 2.15: Representative images of MCC spheres blended with 2 % salbutamol sulfate (SBS).

Complementary, Figure 2.16 shows representative images of the different blends based on coated material. Each row of this figure represents one of the different grades, whereas each column shows a different amino acid. Comparing both the different grades and the coated with the uncoated carrier blends, the microscopic images revealed no substantial

differences in API distribution on the surfaces. On closer inspection, API particles accumulate randomly and some form agglomerates nearby edges and crevices.

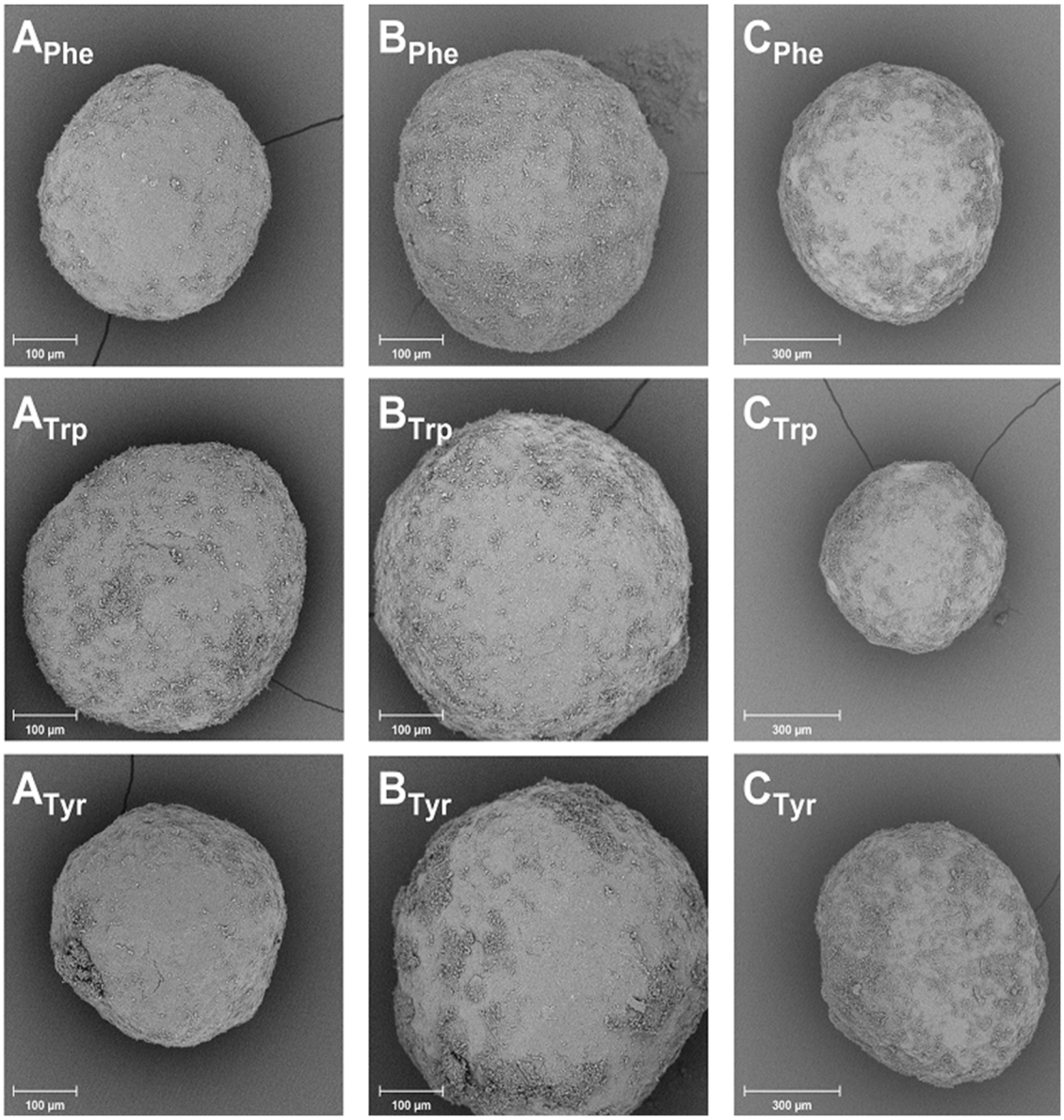

Figure 2.16: Representative images of SBS blends composed of MCC 200 (A), MCC 350 (B) or MCC 500 (C) coated with the amino acids Phe, Trp or Tyr.

To proof that the blending procedure as such affected particle size of the carrier material, characterising the blended batches additionally comprised dynamic imaging analyses (section 2.3.1.3). Determining the PSD of these batches followed the same procedure as of the starting and the coated material. The corresponding method was parametrically limited to particles larger than 100 µm. Due to these metrological limitations, micronised drug particles were not included in the PSD values, which thus solely represent the carrier material (Appendix A). Table 2.10 summarises the measures of location and spread for each batch. Compared to the properties of both the initial and the coated material (section 2.5.1), the terminal blending procedure did not significantly influence the PSD. The absence of

carrier fragments proofed mechanical robustness of the MCC spheres. A further finding was that the high-shear blending process had neither an effect on morphological properties nor on particle size, both characteristics, in turn, affecting the aerodynamic performance (Chapter 1.7.1). Overall, taking the coating homogeneity (section 2.5.1) into account, neither API content nor the respective deviation correlated with the previous coating quality.

Table 2.10: Particle size distribution of the uncoated and coated MCC spheres after blending; n = 3, SD.

Material	**x_{10} [µm]**	**x_{50} [µm]**	**x_{90} [µm]**	**Span**
MCC $200_{uncoated,\ blended}$	299.2 ± 7.0	367.4 ± 1.6	427.5 ± 3.6	0.35 ± 0.03
MCC $200_{Phe,\ blended}$	283.9 ± 5.0	362.6 ± 1.8	420.1 ± 5.0	0.38 ± 0.01
MCC $200_{Trp,\ blended}$	275.8 ± 6.1	350.9 ± 5.5	408.0 ± 4.7	0.38 ± 0.02
MCC $200_{Tyr,\ blended}$	285.1 ± 12.9	356.2 ± 11.7	417.7 ± 16.1	0.37 ± 0.02
MCC $350_{uncoated,\ blended}$	430.0 ± 12.2	495.9 ± 9.9	546.4 ± 3.8	0.24 ± 0.02
MCC $350_{Phe,\ blended}$	417.4 ± 4.8	486.8 ± 8.0	542.6 ± 2.2	0.26 ± 0.01
MCC $350_{Trp,\ blended}$	413.5 ± 3.8	480.5 ± 10.8	540.5 ± 3.6	0.26 ± 0.01
MCC $350_{Tyr,\ blended}$	425.3 ± 12.7	494.2 ± 5.2	551.3 ± 9.2	0.26 ± 0.01
MCC $500_{uncoated,\ blended}$	572.5 ± 8.8	676.8 ± 9.9	761.4 ± 18.9	0.28 ± 0.01
MCC $500_{Phe,\ blended}$	592.4 ± 10.2	677.5 ± 13.0	754.3 ± 7.0	0.24 ± 0.01
MCC $500_{Trp,\ blended}$	585.4 ± 20.7	681.1 ± 17.7	773.7 ± 7.2	0.28 ± 0.03
MCC $500_{Tyr,\ blended}$	601.1 ± 21.3	687.4 ± 17.2	780.4 ± 15.2	0.26 ± 0.02

Coated MCC particles served as model, mechanically stable carrier that were blended with SBS as a model API. The variation range in drug loading capacity apparently depended on the carrier particle size.

2.5.3 Aerodynamic assessment

To study the effect of carrier size and coating on the aerodynamic performance, impaction analyses allowed aerodynamic particle sizing of the interactive blends (section 2.3.4). As a result of this aerodynamic particle sizing, the FPF and FPD of API particles below 1, 3 and 5 µm aerodynamic diameter and the MMAD served as comparative measures. SBS served as a model API, which was blended with three different grades of MCC spheres. In addition, each grade was altered by changing the chemical composition of the particle surface. As a subsidiary outcome, this alteration allowed for studying the effect of chemical modification on particle adhesion and detachment.

For the aerodynamic assessment, the previously prepared blends were filled into either a reservoir of a Novolizer® device (section 2.2.4.2) or in capsules, which were then inserted into the HandiHaler® device (section 2.2.4.1). After filling, each batch was stored for at least 14 days at 20 – 25 °C and 45 % rH in a desiccator containing an oversaturated solution of potassium carbonate.

The following results derived from aerodynamic assessments making use of the HandiHaler® device and interactive blends based on uncoated MCC spheres. In each run, three capsules were used successively, each filled with 40.0 mg of the respective formulation. Figure 2.17 shows the deposition profile of the uncoated carrier materials.

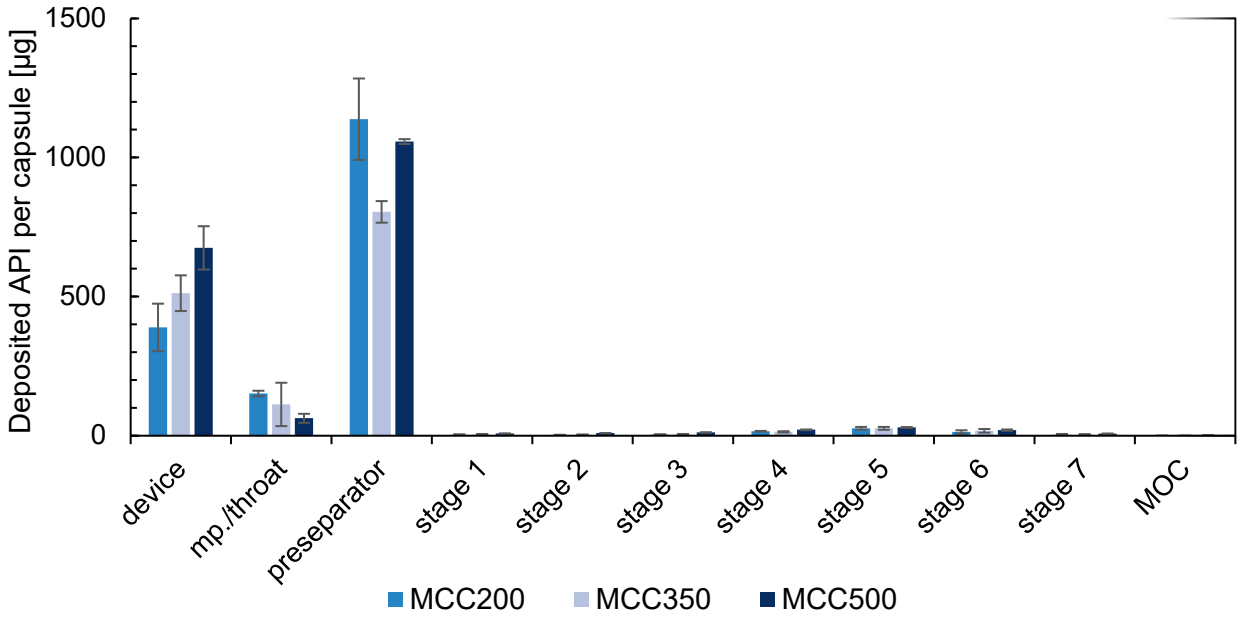

Figure 2.17: Deposition profile of interactive blends composed of non-coated (Uncoated) or coated MCC 200 as carrier material and SBS as a model API (HandiHaler®; n = 3, error bars = SD).

The highest amount of API was detected in the preseparator, followed by the device (Figure 2.17). The API concentrations of the samples taken from the NGI stages were partly below the limit of detection (particularly MOC samples). As shown in Figure 2.18 and

Appendix A, the resultant FPF < 5 µm ranged from 5.25 % ± 4.66 % (MCC 200) to 8.96 % ± 6.26 % (MCC 350). In addition, the FPD < 5 µm were between 20.8 µg ± 5.12 µg (MCC 200) and 29.6 µg ± 1.76 µg (MCC 500). The MMAD was 1.73 µm ± 0.12 µm (MCC 200), 1.65 µm ± 0.09 µm (MCC 350) and 1.88 µm ± 0.03 µm (MCC 500), respectively.

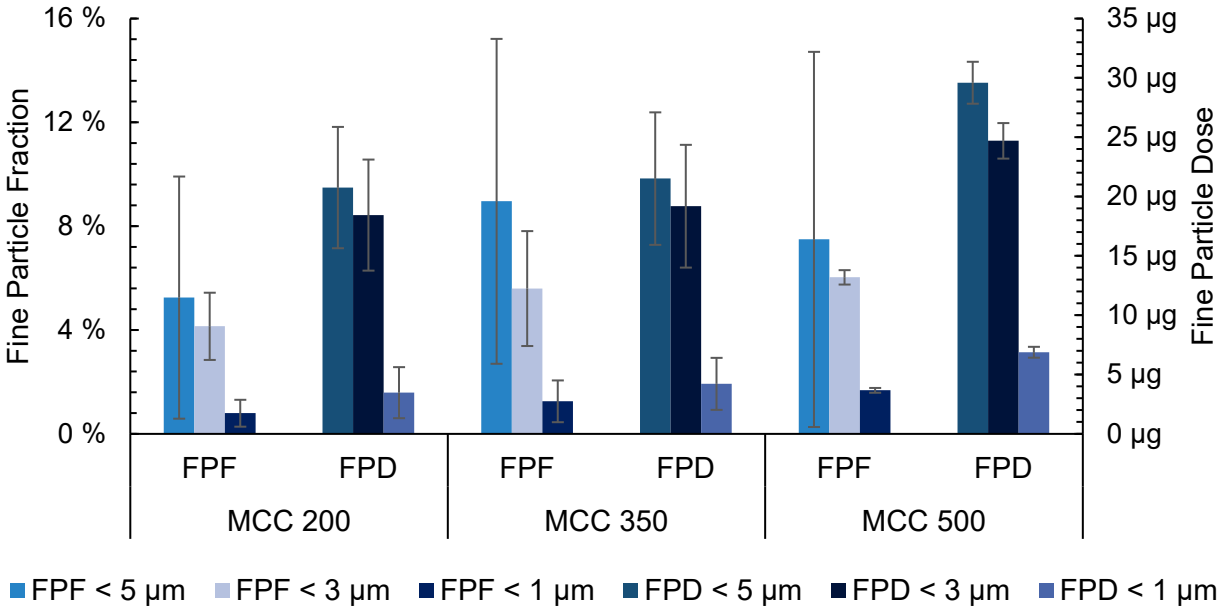

Figure 2.18: Fine Particle Fractions (FPF) and Fine Particle Doses (FPD) of the interactive blends using the HandiHaler® device; n = 3; error bars = SD.

Overall, the aerodynamic performance of the blends based on spherical MCC particles were low compared to data published in the literature. Regarding the different MCC carrier sizes, aerodynamic assessments indicated no significant difference in neither FPF nor FPD values. As an explanation, the dispersion mechanism of the capsule based HandiHaler® caused insufficient energy to disperse each DPI formulation. This device was thus considered unsuitable for further testing.

The following data resulted from aerodynamic assessments using the Novolizer® device and interactive blends based on both uncoated and coated carriers. Each NGI run comprised five separately delivered doses from the inhaler device. Figure 2.19 summarises the deposition profile for samples containing carrier based on MCC 200. For each of these samples, the highest amount of API was detected in the preseparator, while the API concentrations of the MOC samples were below the limit of detection. Comparing uncoated with coated carriers, the major finding of this aerodynamic particle sizing was a shift of API quantities towards stages with lower aerodynamic cut-offs.

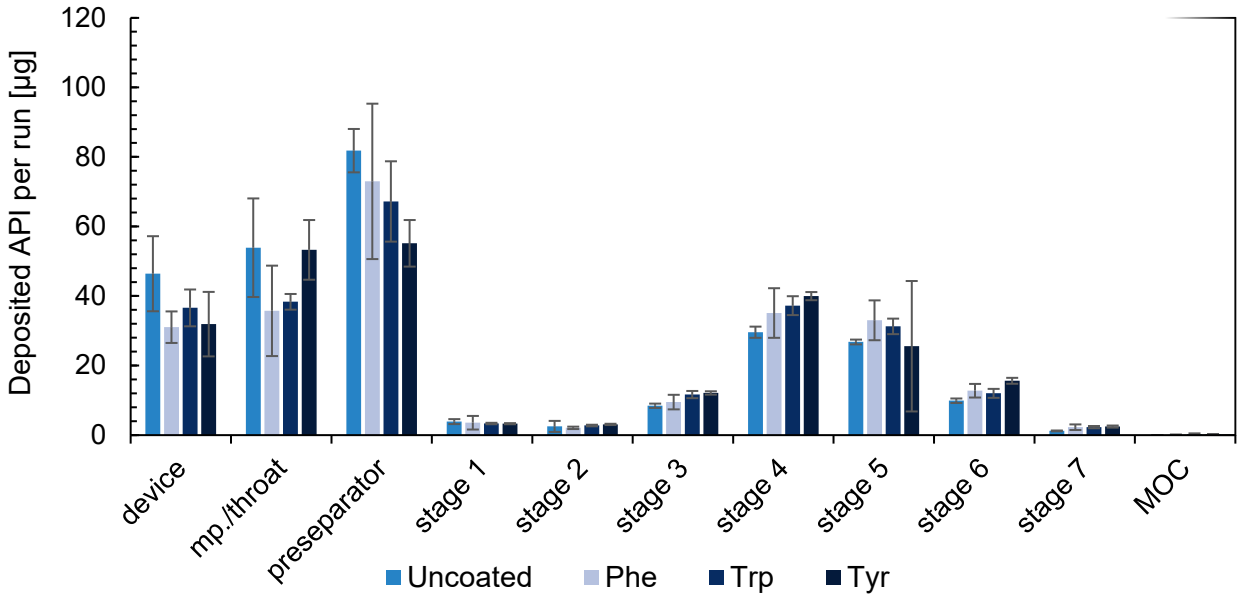

Figure 2.19: Deposition profile of interactive blends composed of non-coated (Uncoated) or coated MCC 200 as carrier material and SBS as a model API (Novolizer®; n = 3, error bars = SD).

Figure 2.20 shows the deposition profile of the different blends based on MCC 350 spheres. For each sample, the highest API quantity was detected in the mouthpiece/throat and preseparator, while API concentrations were lowest in the MOC samples. Similar to the results presented for MCC 200 samples (Figure 2.18), the major finding of this analysis was a shift of API quantities towards stages with lower aerodynamic cut-offs. Accordingly, this shift derived from a decrease in API quantity in the device and preseparator and, in turn, an increase particularly in stage 3 to stage 6 in comparison to the uncoated carrier.

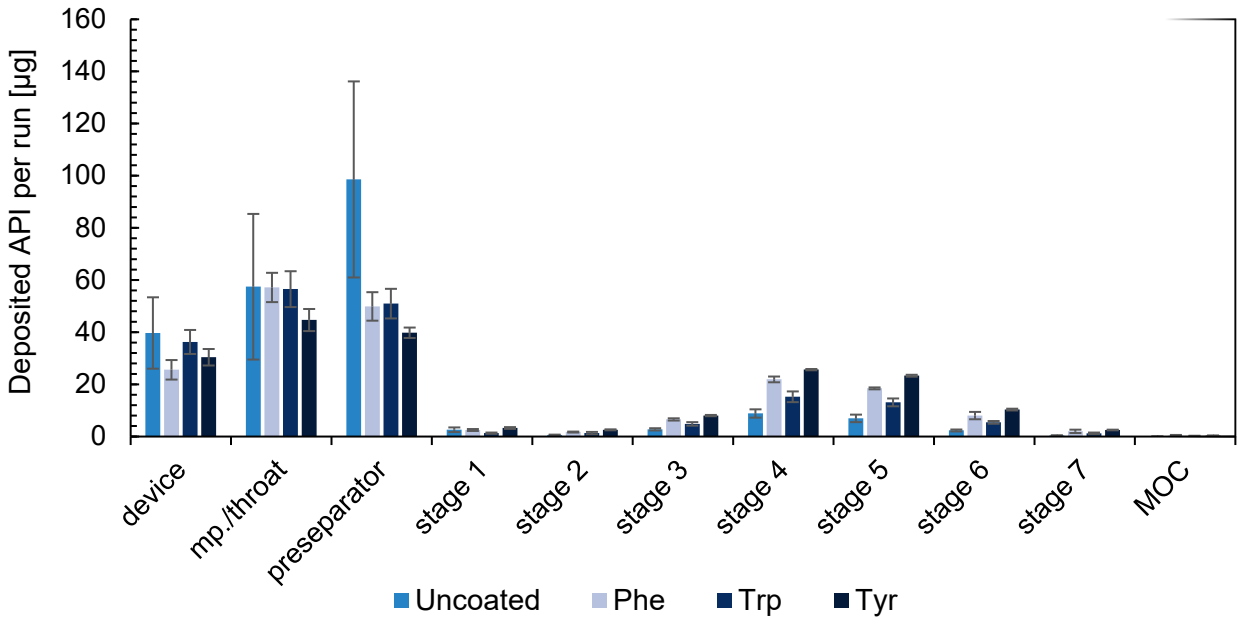

Figure 2.20: Deposition profile of interactive blends composed of non-coated (Uncoated) or coated MCC 350 as carrier material and SBS as a model API (Novolizer®; n = 3, error bars = SD).

Figure 2.21 shows the deposition profile of uncoated and coated MCC 500 spheres. For each sample, the highest amount of API was detected in the preseparator, while the API concentrations of the MOC samples were below the detection limit. In comparison to the uncoated material, the API quantities shifted towards stages with lower aerodynamic cut-offs. Basically, this shift based on differences in API quantity particularly in stage 3 to stage 6 compared to the uncoated carrier.

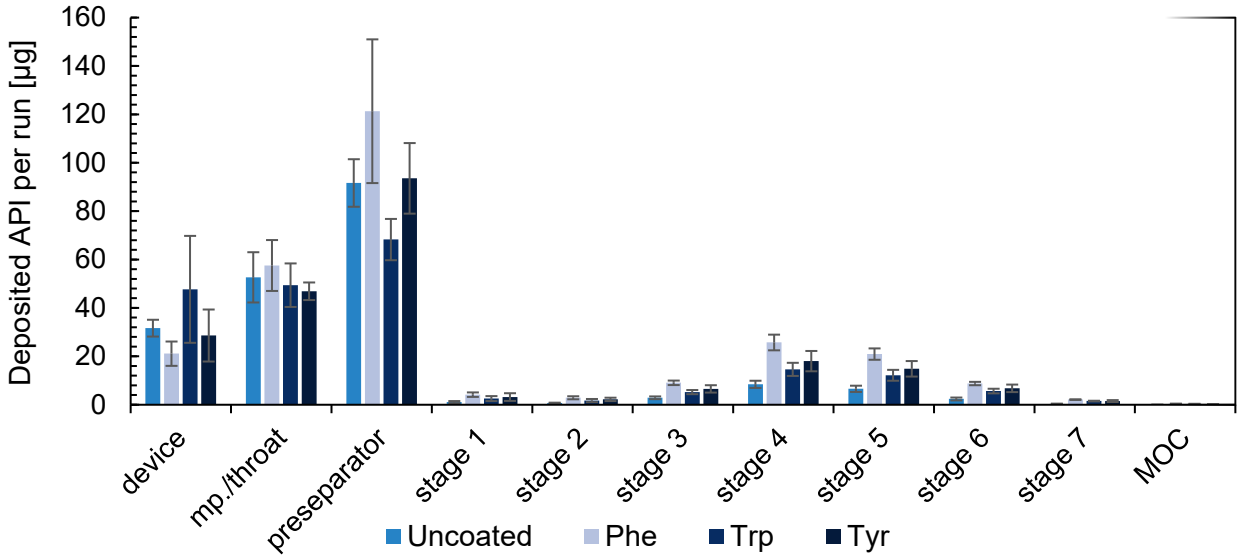

Figure 2.21: Deposition profile of interactive blends composed of non-coated (Uncoated) or coated MCC 500 as carrier material and SBS as a model API (Novolizer®; n = 3, error bars = SD).

Differences in the quantified API concentrations led to differences in FPF (Figure 2.22 and Appendix A) and FPD (Figure 2.23 and Appendix A) values (see also Chapter 1.4). As shown in Figure 2.22 and Figure 2.23, the coated material provided on average comparably high values for FPF and FPD compared to the uncoated material. This finding indicated a superior aerodynamic performance after coating. Of all carrier types tested, interactive blends containing MCC 200 had highest FPF and FPD values, respectively. Considering the FPF, formulations based on MCC 500 provided lowest values.

Using coated MCC 350 and 500 carriers resulted in different FPF values, but the data revealed no differences in corresponding FPD. This finding was a result of the variation in drug contents listed in Table 2.9. The MCC 500 blends contained relatively high amounts of drug, which consequently compensated for the low FPF compared to MCC 350 mixtures. This compensation derived from the comparably higher amount of API delivered to the NGI in each run. However, aerodynamic assessment of the blends showed no correlation between the amount of API adhered to the carrier and the FPF.

An increase in FPF and FPD values indicated that the coating process caused a change in aerodynamic performance. However, the presented results did not provide any indication

that this change is primarily influenced by one of the coating materials. Respective samples of the subgroups showed no significant differences among each other. Accordingly, the MMAD values of the tested blends remained similar (Figure 2.24).

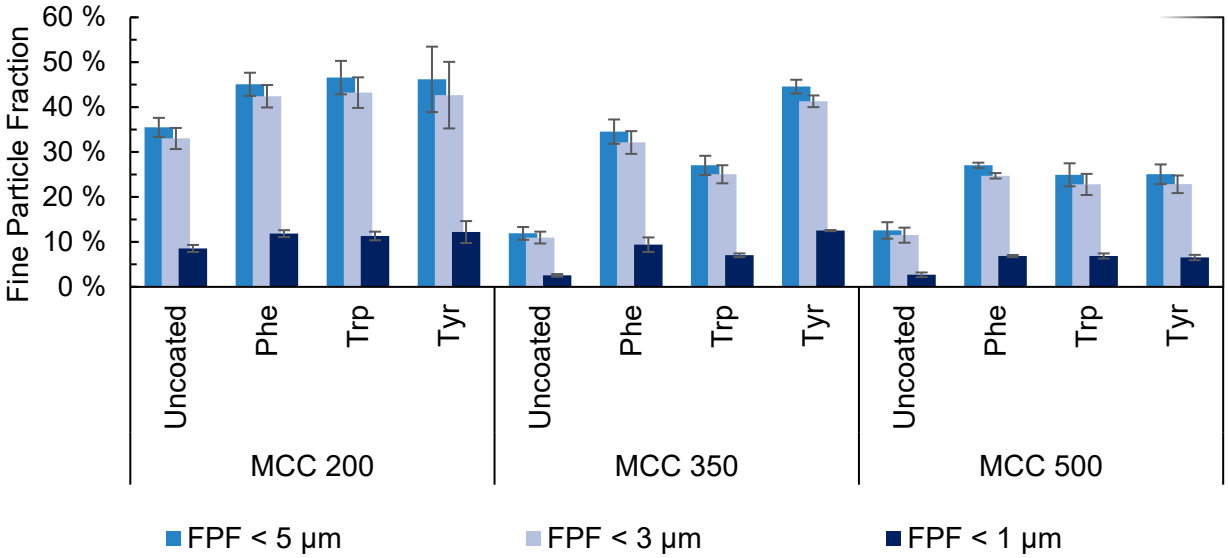

Figure 2.22: Fine Particle Fractions (FPF) of the interactive blends (Uncoated, Phe, Trp, Tyr); n = 3; error bars = SD.

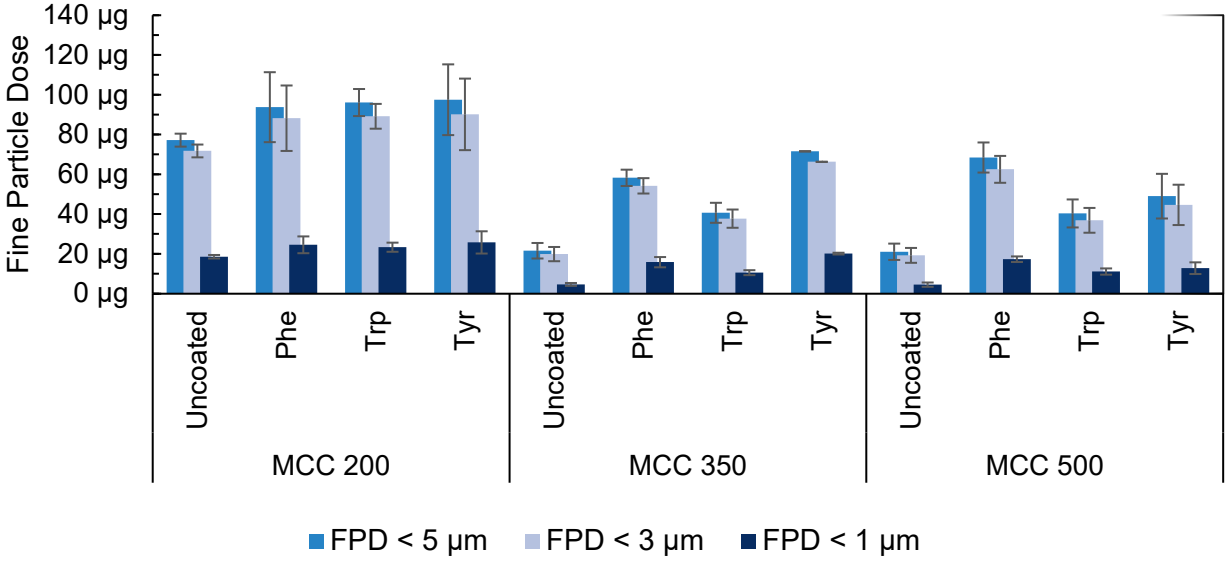

Figure 2.23: Fine Particle Doses (FPD) of the interactive blends (Uncoated, Phe, Trp, Tyr); n = 3; error bars = SD.

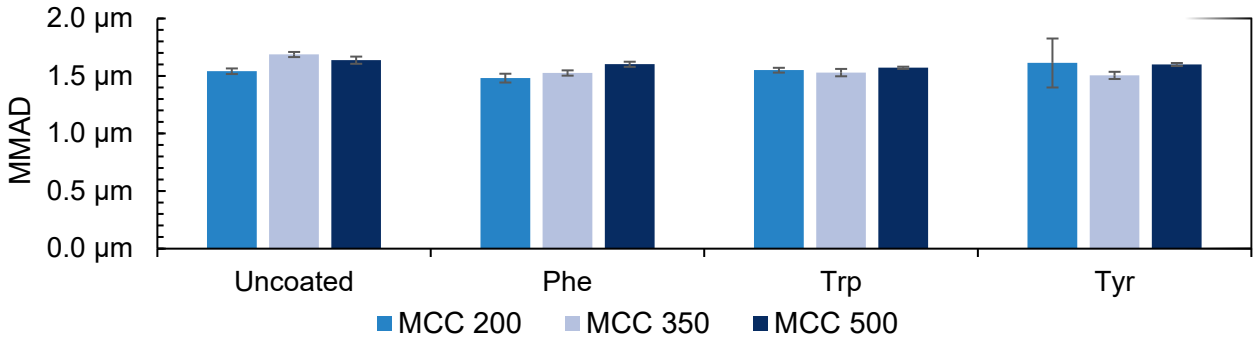

Figure 2.24: Mass Median Aerodynamic Diameter (MMAD) of each sample; n = 3; error bars = SD.

2.6 Conclusion and Discussion – Chapter 2

Spherical MCC particles served as alternative carriers for DPI formulations, namely interactive powder blends. These carriers proofed their suitability in the reservoir-based Novolizer® inhaler but did not disperse well in the capsule-based HandiHaler® device. Testing the formulation in the Novolizer® generally showed that the smaller the MCC carrier particles the higher the aerodynamic performance, i.e. FPF and FPD values.

To improve the aerodynamic performance, the initial carrier materials were coated with different amino acids using a wet-coating process in a fluidised bed. As a result of this engineering approach of DPI carriers, the chemical composition of the particle surface was changed without any significant change in particle size.

The different carrier materials were blended with a model API, namely SBS, in a high-shear process prior to aerodynamic assessment. Variations in drug loading capacity after blending apparently depended on the carrier particle size. The larger the spherical material the higher the relative deviation of the drug content. Measuring the particle size distributions gave no significant change in size after the blending process. This indicated adequate robustness of the carrier material for the conducted high-shear processes.

Compared to uncoated material, coating of the carriers led to an increase in the aerodynamic performance of corresponding mixtures. The presented results left unclear whether this increase was solely due to the coating alone or due to the processing as such. Thus, the extent of the enhancements in aerodynamic performance could not be directly attributed to the different amino acids. Moreover, aerodynamic assessment provided no indication that the drug content of the blends had an influence on the resultant performance.

Formulating interactive mixtures based on spherical MCC particles requires further optimisations in the future. An optimisation would address reducing the loss of API during processing, which affected the drug content variability. Nevertheless, the basis the presented work was primarily a standardised manufacturing process, i.e. coating and mixing procedures, rather than equal drug contents in each formulation. Standardising the drug content of each formulation could compensate for potential content-related effects on particle dispersion. To achieve a certain API content, the mixing process could be repeated or prolonged. However, repeating the mixing could risk enhanced particle fragmentation due to high-shear forces. Particle fragmentation would in turn affect the aerodynamic performance, which could mask the effect of the coating.

Coating the carrier and further processing to interactive powder blends could affect not only chemical composition but also influence surface characteristics of the carriers.

Differences in topography could, however, have been decisive for drug loading capacity and drug detachment of API particles. Studying the actual topography of the carrier particles would be necessary to distinguish effects of the coating process from effects of the type of coating. SEM imaging is, however, limited in detecting detailed topographical variations. In the present work, the particle roughness was not determined, even though known to impact aerodynamic performance. The coating process potentially influenced the roughness and thus the adhesive forces between API and carrier.

Conclusively, coating and blending procedures imply multiple changes in particle characteristics. Therefore, particle engineering by wet-particle coating does not allow for isolated particle modification of chemical composition and surface attributes. Nevertheless, MCC could principally serve as an alternative to lactose or mannitol as carrier in DPI formulations.

Spherical MCC particles served as carrier material
for interactive blends in DPI formulations.
The dispersion efficiency depended on the type of inhaler.
In a Novolizer® device, coated carriers resulted in
superior aerodynamic performance compared to uncoated MCC particles.

Chapter 3 Additive manufacturing of dispersing aids

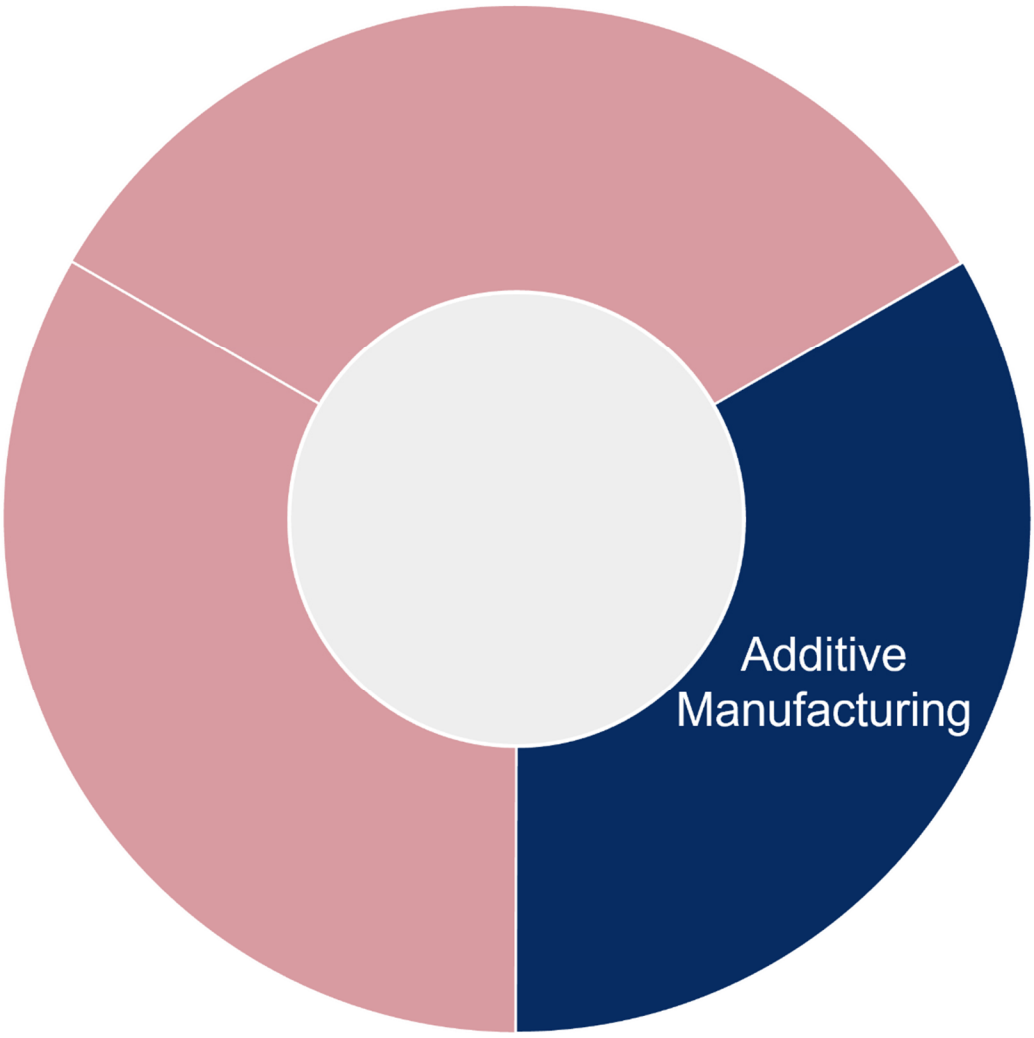

3.1 Additive Manufacturing in respiratory sciences

The following sections 3.1.1 to 3.1.5 are part of the review *Additive Manufacturing in respiratory sciences – Current capabilities and future prospects* that was published in the journal *Advanced Drug Delivery Reviews, Volume 186* by Simon Bock, Thomas Rades, Jukka Rantanen and Regina Scherließ in July 2022 [92].

3.1.1 Basic principles of Additive Manufacturing technologies

In the last four decades, AM technologies have been developing fast impacting various fields of engineering and manufacturing. In contrast to conventional fabrication methods, AM technologies allow the production and replication of an almost unlimited variety of object geometries, even with complex internal structures. This unprecedented design space is due to the digitalised process chain, which includes the construction of tailor-made objects on the computer.

As a starting point, a digital three-dimensional (3D) model is created either by geometric modelling from scratch or by reverse engineering based on an existing physical object. The structure of this 3D model can also be optimised with computer simulations of the performance of this object in its intended physical environment. From this digital model, a computer-aided design (CAD) file, construction patterns for the fabrication are compiled to an AM file format (e.g. STL, AMF, PLY). Then, this file is converted into the respective process parameters, defining for example the location of the energy focus (e.g. by means of a laser or electron beam) or the material or binder application (e.g. by means of an extruder nozzle) depending on the physical principle of the utilized AM technology. By solidifying the applied material, the digitally generated object is finally physically created. Fine finishing is the final step in the process chain. The entire workflow can thus be classified into three phases: pre-processing, fabrication, and post-processing (Figure 3.1).

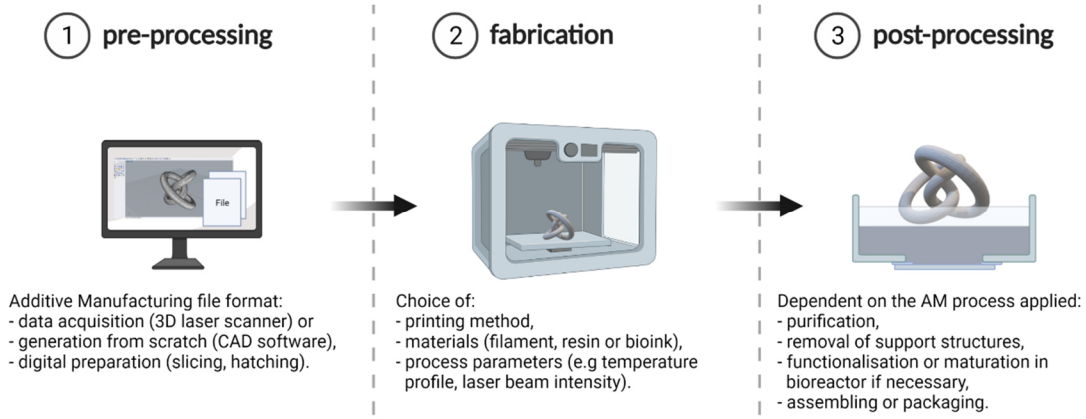

Figure 3.1: The process chain of AM comprises pre-processing, fabrication, and post-processing. From digital design, preparation of materials to a validated printing process including post-processing, such workflows are highly diverse.

3.1.2 Additive Manufacturing of pharmaceuticals

AM technologies ultimately yield a tailor-made object, where function and purpose are defined by its morphological design and structural composition. Each AM method has specific technical limitations and distinct requirements on the materials to be used. The respective methods can be divided into three main groups, namely extrusion, powder solidification and liquid solidification, and the general challenges related to each group of methods have been discussed [93,94]. Many of the methods are still at their infancy considering their direct use for respiratory sciences, and more basic engineering research is needed to make the full potential available. From a pharmaceutical perspective, the properties of the processable components eventually determine the applicability of the resulting product. Several AM techniques have been used in pharmaceutical and medical research, covering examples from printed drug delivery systems to tissue engineering, surgery training, implants or prostheses [94–97].

Seoane-Viaño et al. provided an overview on AM technologies in pharmaceutic applications and recent pre-clinical as well as clinical applications [94]. Most of these examples demonstrate the design of drug product prototypes, which are analogous in appearance to conventional drug delivery systems such as tablets. Conventional mass production of pharmaceuticals involves several powder-based unit operations in which excipients and active ingredients are processed together. However, this approach does not allow for straightforward customisation of the drug product. In contrast to mass production methods, the integration of AM processes envisages the preparation of personalised doses or multicompartmental drug filling with modulated release profiles [98]. In this context, mass customisation due to product modularisation has recently been proposed as a pharmaceutical concept to provide dosage form individuality [99]. Continuously operating manufacturing solutions have been identified as important for the transition from mass production towards mass customised products. Some of these technologies, such as pellets, are already well-established as technological platforms [100]. However, remaining challenges include the holistic integration into the healthcare ecosystem and the implementation within regulatory boundaries.

A medicinal product basically passes through various phases of research and development, production, quality assurance, distribution and therapeutic application. The same requirements that are imposed on classical dosage forms must principally also be met by AM-based products. In turn, this requires a highly controlled and validated workflow, which is not yet fully existing for AM based products.

In 2017, the U.S. Food and Drug Administration (FDA) published a guidance providing a regulatory framework for the additive manufacturing of medical devices [101]. Key questions concerning assurance of quality, safety and efficacy of printed pharmaceuticals on the other hand remain less clear. However, the approval of the ZipDose™ manufacturing process (Aprecia Pharmaceuticals), in which a binding fluid (ink) is iteratively applied to powdered drug-excipient layers, is considered the initial spark for AM-based mass production. Such AM application has so far been limited to a single FDA-approved product called Spiritam™ [95,102]. A further example is an extrusion-based process offered by the company Triastek, with which solid oral dosage forms with customisable release kinetics can be produced in an automated and real-time monitored process [103]. In part because the diversity of printing technologies continuously grows, this FDA guidance does not yet include either dosage forms or biological, cellular and tissue-based products. Generally described as bioprinting, the manufacturing of the latter products using AM technology demands additional production process and product life cycle monitoring considerations, as well as novel regulatory pathways [96,97].

Rapid advances in the development and fabrication of novel solid dosage forms haven taken place in the recent past. Although encouraging and promising, considerable scientific work is still needed to extend such advances to the manufacturing of highly functional, biomedical tools or even artificial organs. As an intermediate step, additively manufactured replicas, stents and functionalised cell cultures serve as precursors for 3D-printed organs. Furthermore, the criteria for customised objects for surgical or implantological purposes (such as durability or biodegradability) differ fundamentally from the criteria for prints that are utilised in *in vitro* studies or merely serve as prototypes of medical devices.

3.1.3 Current needs in respiratory sciences

For the treatment and control of both respiratory and systemic diseases via the lung a variety of active pharmaceutical ingredients (API) combined with suitable inhaler devices are available. To meet the patient needs, public authorities, pharmaceutical industries, healthcare providers as well as researchers all over the world are constantly and comprehensively challenged. The challenges arise from the complexity in developing pharmaceuticals and medical device. To develop dosage forms and devices comprehensive knowledge of physiology, pathology, diagnosis, pharmacology, clinical practice and data science is as crucial as pharmaceutical and technological expertise.

Regulatory criteria for quality, safety and efficacy set high standards on the production of such products. For orally inhaled and nasal drug products (OINDP), the criteria apply to

formulation excipients, the design and manufacture of the device, as well as the composition of the final drug product [25]. The development of both low-cost and highly efficient as well as easy-to-use devices is in the focus of current efforts [26], since socio-economic aspects determine therapeutic success to a considerable extent [17]. Likewise, the development and global launch of new medicines entail high financial, labour, infrastructural and time expenditure. These prevailing circumstances suggest that an emerging technology such as AM has the potential to accelerate research and development (R&D). Such an acceleration is attributed to AM, because it enables fast prototyping, product personalisation and the possibility to demonstrate and validate computer simulations. Such technological capabilities ultimately culminate in improved devices and formulations, which in turn may lead to better healthcare at lower costs.

3.1.4 Particle design

The application range of AM is determined by the different fundamental operating principles and corresponding print resolution as well as the composition of the material used. In contrast to the production of tablets or implants, the size distribution of individual particles needs to be typically lower in dosage forms for pulmonary administration. This is because in orally inhaled drug products (OIP) an aerodynamic particle size below five microns is associated with physiological effects of the API contained in the particle. To date, the production of comparably small objects with intricate details in the micron range remains a considerable challenge. With classical oral solid products, there are examples of AM based particle design, however, typically in the millimetre scale for proof-of-concept [104,105]. As recently reviewed by Hahn et al., only very few approaches, such as Two-Photon Polymerisation (TPP), Electron Beam Induced Deposition (EBID) and Direct Ink Writing (DIW), meet the criteria of submicron-size and resolution [106].

In respiratory sciences, TPP has been used as a method to fabricate well-defined morphologies for the investigation of particulate interactions. Particularly, utilisation of various printed ridges down to 1 µm in size provided general insights into the interplay of surface morphology on the one hand and adhesion, deposition and detachment of particles on the other [107]. In contrast to this high-resolution technique appears the methodological complexity, the printing speed as well as the non-pharmaceutical composition of the substrates or photoresins needed [106]. Therefore, it appears to be more feasible to engineer particles with lower level of detail but on the scale of carriers in dry powder inhaler (DPI) formulations.

On a formulation level with particle sizes in the single-digit micrometre range, López-Iglesias et al. introduced the production of porous particles via thermal inkjet printing followed by supercritical drying. In the latter process the printed polysaccharide-based aerogel yields microspheres with a relatively narrow particle size distribution but a strikingly rough topology. These particles loaded with a model substrate have already been tested in aerodynamic assessments, indicating a general suitability as DPI carriers [108]. At present, direct manufacturing of tailor-made particles in the sense of AM lacks methodological capabilities. Instead, particle design and production are currently based on moulding processes. As an example, the encapsulation of API in microdevices offers precise control over topology and size. As shown by McHugh et al., the underlying SEAL® technology features the assembly of pre-moulded, biodegradable lactide-glycolide copolymers in a layer-by-layer manner to form 3D structures. The authors demonstrated, that such container microparticles could potentially be useful for parenteral applications [109]. Such a micro drug delivery system can in principle be sensitised to certain environmental conditions such as pH value or enzymatic activity allowing specific drug release. From our point of view, the production of similar biodegradable DPI carrier particles would also be conceivable.

Torge et al. reported the fabrication and comparison of cylindrical and spherical shapes in the size range of API particles using a template-assisted and a spray-drying process, respectively. This enabled the investigation of nanoparticle-embedded drug delivery systems amendable for pulmonal administration. According to the authors, further progress in this technology allows fine-tuning of drug loading and disintegration behaviour, depending on particle size and morphology [110]. Another approach that provides precise control over the latter properties, with the help of moulding matrices, is the particle replication in non-wetting templates (PRINT®) technique [111]. Garcia et al. introduced this methodology in the fabrication of dry powder particles, that are principally suitable for aerosol generation [112]. Using this manufacturing process, it was further shown how the particle morphology and the shape factor, respectively, influence the aerodynamic diameter [113]. However, the morphology of the resulting objects with at least one flat surface suggests a high tendency to form agglomerates, which will be detrimental for particle dispersion in inhalation [112,113].

The abovementioned studies are mainly limited to inhalable API particles with sizes in the single-digit micrometre range. As complex geometries in this range become in principle accessible, Fromen et al. pointed out that new characteristic parameters for describing the aerodynamic behaviour need to be identified [113]. A simple transfer of the characteristics of such API particles to much larger DPI carrier particles seems implausible. Flat surfaces

would potentially counteract the suitability of microstructures as DPI carriers because “flat-on-flat” arrangements cause strong adhesive strength [114]. The resultant tendency to adhere and form aggregates could in turn hamper particle dispersion while inhalation.

Despite current methodological limitations, an implementation of AM on a DPI formulation level might just be a matter of technical progress and process acceleration. In a different size category, the insertion of additively manufactured geometries into DPI devices as free-levitating accessories for dispersion enhancement was presented. In the relevant proof of principle, a shift in mass median aerodynamic diameter (MMAD) was derived from the use of relatively large dispersing aids [115]. This principle derives from the finding by Buttini et al., that an add-on accessory, which contains an axial oscillating bead, improves the aerosol dispersion of a commercial DPI inhaler. Such an add-on device influences the airflow patterns within the unit and thus affects the device flow resistance [116]. Replacing the oscillating bead with complex, dispersion-promoting geometries has not yet been investigated. Therefore, considering the multitude of variations in accessory geometry and size, a novel strategy for enhanced particle deagglomeration behaviour was recently anticipated by us [115]. In this context, AM offers a wide design space for the oscillating object and allows fine-tuning of the entire internal structure of a device.

3.1.5 Rapid prototyping of inhaler devices

Established examples of AM are especially evident in the development and rapid prototyping of inhaler devices and enables the realisation of device concepts in small quantities for rapid *in vitro* evaluation. The variables include technical design features of an inhaler such as the arrangement of air inlets, mouthpiece, or grid characteristics [117–121]. Integrating *in silico* simulation models in the development process provides valuable information about fluid and particulate flow. In turn, numerical data allow refinements to be made on the device design [119–123].

To study the flow patterns within inhalers, computational fluid dynamics (CFD) has been used by Versteeg et al. for metered dose inhaler (MDI) [124] and by Coates et al. for DPIs [125]. Due to the enormous complexity of predicting how a multicomponent solid/gas/liquid system with complex inhalable particles behaves, simulations without assumptions and simplifications are currently not feasible [120–123,126]. This is especially challenging for DPI formulations with different size/shape distributions and bulk properties, inhomogeneous surface energy distributions as wells as potential deformations of the individual particles. Recently, Longest and Farkas demonstrated the applicability of CFD in combination with rapid prototyping to design high-performance DPI aerosolisation units. The presented

approach provides a blueprint for the development of future inhaler generations, even if this experimental setup is based on a principally well-dispersible powder [126]. A formulation with other properties in terms of aerosolisability may require a different dispersion mechanism.

Since CFD analysis simulates only the patterns of a fluid and does not account for particle-particle interactions, coupling with methods that can in turn incorporate such interplay is of relevance. By coupling CFD models with discrete element methods (DEM), thus including both air flow and particle interactions, a more comprehensive representation of the underlying effects is achieved [122,123,127,128].

Overall, the linkage of computational analysis and design with AM closes the loop of iterative testing procedures for the optimisation of inhalers (Figure 3.2) [121,123,126]. The intention of such design thinking processes is usually related to the development of both generic and innovative devices [123]. Corresponding detailed records are mostly undisclosed because such practices generally entail the preservation of intellectual property.

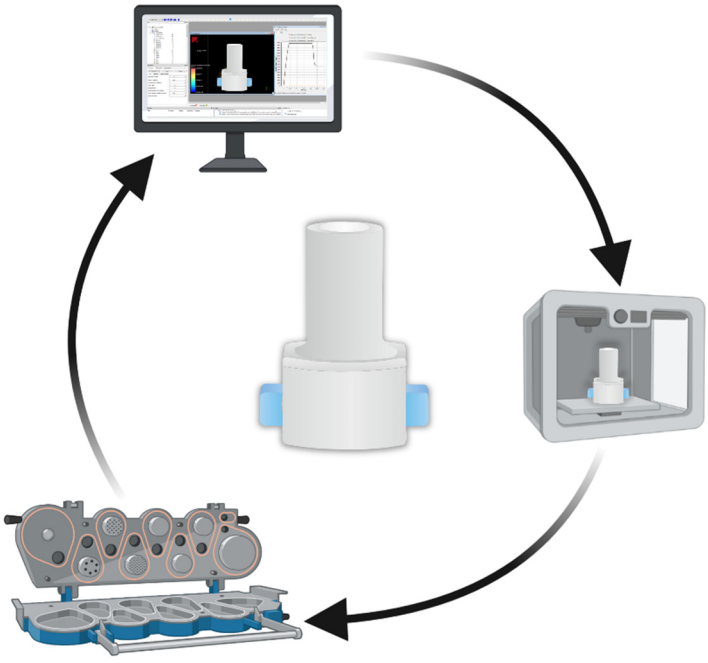

Figure 3.2: Iterative loop of device design, rapid prototyping and *in vitro* evaluation. Device designs derived from numerical data are rapidly fabricated using AM. The prototypes are then evaluated using standardised procedures (e.g. impaction analysis). Resulting *in vitro* data in turn facilitates optimisation of the product.

3.2 Enhancing dispersion in DPI devices

When inhaling DPI formulations, the patient needs to generate an adequate pressure drop to fluidise, disperse and hence aerosolise the powder within the inhaler. The ability of an individual to generate a sufficient flow rate further influences particle deposition throughout the respiratory tract (Chapter 1.4). Such influencing factors complicate inhaler

development, which basically aims at constant dose delivery independent of the patient. To achieve efficient and consistent drug delivery, a main consideration in DPI device design is to promote adequate dispersion.

Inserting spherical objects into the central unit of DPI devices to promote dispersion was patented multiple times in the recent decades. The patents WO1995/003846 A1 (1; unit 6) and US2001/0027790 A1 (2; unit 40) exemplarily describe the insertion of a bead into differently designed devices (Figure 3.3) [129,130].

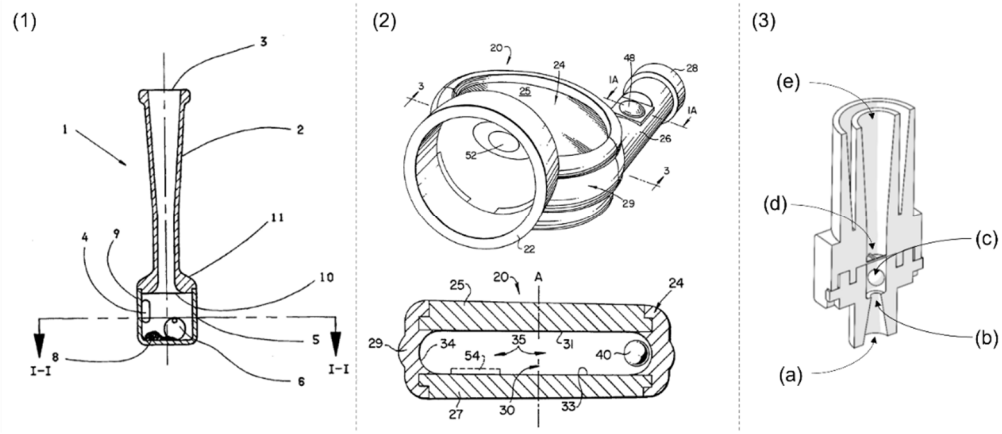

Figure 3.3:Technical drawings of DPI devices or add-ons in which spherical objects are inserted to promote dispersion. WO1995/003846 A1 (1), US2001/0027790 A1 (2) and AOS™ (3). The AOS™ consists of inlet funnel (a), inlet orifice (b), AOS™ bead (c), bead stop grid (d) and outlet funnel (e). Adopted from [129], [130] and modified from Respira Therapeutics, USA.

As specified in these patents, inserting beads is considered to separate the API particles from each other or the carrier particles more efficiently. This particle separation is ascribed to bead-to-particle collisions. Furthermore, the beads collide with the interior device surfaces, promoting a detachment of particles that remain stuck to the inner wall. In addition to placing beads in an inner device chamber, scientists also investigated placing spherical objects in the air stream towards the mouthpiece end. As previously described in section 3.1.4, such add-ons, which were mounted on or integrated in various DPI devices, were studied by Buttini et al. [116]. In this study, so-called AOS™ (Axial Oscillating Sphere™, Respira Therapeutics, USA) inserted into the add-on were reported to increase the aerodynamic performance of commercial drug products. Similar to the descriptions in the patents, the authors attribute this effect to improved dispersion of the powder through dynamic particle impaction with the bead (Figure 3.3). Considered as an additional dispersion mechanism, the dynamic particle impaction could complement other mechanisms such as friction, shear, and particle-particle or particle-wall collisions.

Based on this phenomenon, the following hypothesis could be derived: frequency and intensity of collisions with a dispersing aid (DA) determine the efficiency of particle

dispersion. Accordingly, an increase in the collision probability appears to be scientifically expedient. The use of DAs in the form of spheres is apparent in that such bodies are commonly available and easy to handle. However, truly rational substantiations for the use of spherical bodies are difficult to articulate and cannot be found in the literature. This raises the question of what size and morphology such inserts should optimally feature. To explore morphologically optimised DAs, the following sections elaborate on AM as a technique to fabricate highly complex geometries with improved dispersing capabilities.

This chapter explores the use of structurally complex dispersing aids in various DPI formulations. To investigate such aids, this thesis firstly assesses different AM methods and the resulting products for specified applicability. Secondly, the insertion of dispersing aids into model DPI devices is evaluated in terms of aerodynamic performance.

3.3 Materials

This section describes two different types of materials that were used in the subsequent studies. First, the materials used to prepare DPI formulations, namely various carrier materials and model agents. Second, the inhaler for the study of additively prepared DAs intended to promote particle deagglomeration. The applied DAs as such are described in section 3.4.2.

3.3.1 Carrier materials

As outlined in Chapter 1.7, basically three strategies exist for developing DPI formulations, namely interactive blends, softpellets and engineered particles. Formulating interactive blends commonly involves the use of lactose monohydrate as carrier material (Chapter 2.2.1.1). A number of lactose grades are commercially available varying in terms of PSD and other bulk characteristics. In the subsequent studies on interactive blends, two grades of lactose were used, namely InhaLac® 120 and InhaLac® 251. These grades were chosen as representative carrier materials covering a wide range of existing lactose grades intended for a use in DPI formulations (see also section 3.6.1.1).

3.3.2 Model drugs

The drug substances that were utilised in this chapter are common medications in the treatment of asthma bronchiale, COPD or tuberculosis. This section describes the different APIs, namely budesonide, isoniazid and rifampicin. Salbutamol sulfate was previously described in Chapter 2.2.2. Due to their chemical nature, the drugs feature different physico-chemical properties, e.g. logP and water solubility (Table 3.1). Each of the APIs used in the following studies was of micronised quality. Micronisation was provided by the respective supplier or by applying a milling technology as described in section 3.4.1.1.

Table 3.1: Physio-chemical properties of model drug substances [35,85].

API	Molecular weight, g/mol	Solubility in water	LogP
Budesonide	430.5	Insoluble	2.73
Isoniazid	137.1	Freely soluble	-0.70
Rifampicin	822.8	Very slightly soluble	2.77
Salbutamol sulfate	576.7	Slightly soluble	0.34

3.3.2.1 Budesonide

The drug substance budesonide (BUD, Figure 3.4) is a mix of 22R and 22S epimer and belongs to the pharmacological class of glucocorticoids. Agents of this class principally bind to cytosolic glucocorticoid receptors mediating changes in gene expression. This leads to

multiple downstream effects such as decrease of inflammation, vasodilation and permeability of capillaries. BUD is an API indicated for prophylactic therapy and management of respiratory and digestive disorders [86].

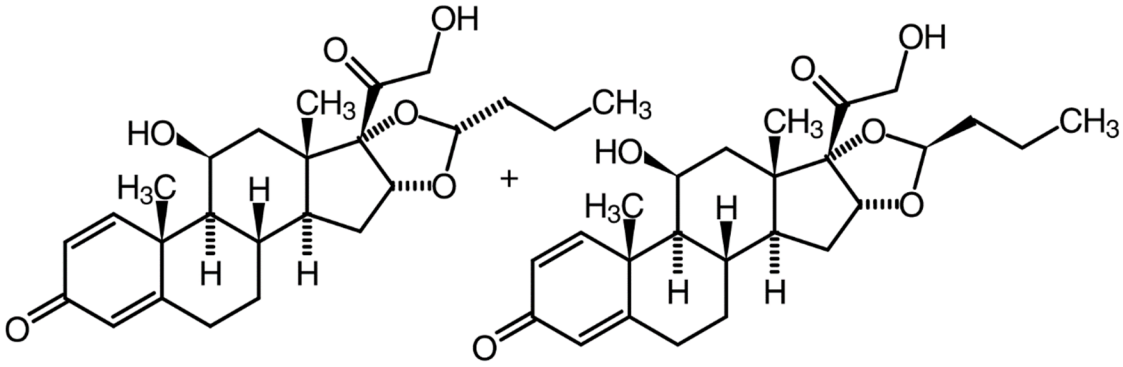

Figure 3.4: Structural formula of budesonide (22R and 22S epimer) [35].

Practically insoluble in water, the white to almost white crystalline powder is slightly soluble in dichloromethane and sparingly soluble in ethanol 96 % [35]. Micronised BUD was purchased from Farmabios S.p.A., Italy.

3.3.2.2 Isoniazid

The drug substance isoniazid (ISN, Figure 3.5) belongs to the class of antibiotics, that are highly specific against organisms of the genus Mycobacterium. It is therefore the treatment of choice for mycobacterial infections. To treat active or latent tuberculosis it is most commonly combined with other antimycobacterial agents. Being a prodrug, ISN must be activated by bacterial catalase. Once activated, the API inhibits the synthesis of essential components of the bacterial cell wall [131]. ISN is sparingly soluble in ethanol 96 %, whereas it is freely soluble in water [35]. ISN was purchased from Sigma-Aldrich (Merck KGaA), Germany.

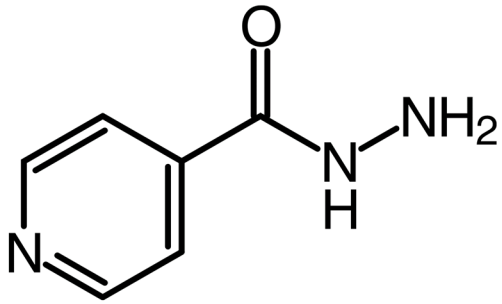

Figure 3.5: Structural formula of isoniazid [35].

3.3.2.3 Rifampicin

The drug substance RIF (Figure 3.6) is a semisynthetic, macrocyclic antibiotic, that belongs to the pharmacological class of DNA-dependent RNA polymerase inhibitors. In susceptible bacteria it forms a stable complex with the RNA polymerase, causing cell death

by suppression of RNA synthesis. Due to its pharmacological mechanism, this API has a broad antibacterial spectrum, but is, however, specifically indicated in the treatment of tuberculosis. Like ISN, it is mostly combined with other bactericidal agents [132]. RIF is a brownish red crystalline powder. It is very slightly soluble in water, acetone and ethanol 96 %, but soluble in methanol [35]. RIF was purchased from Caesar & Loretz GmbH, Germany.

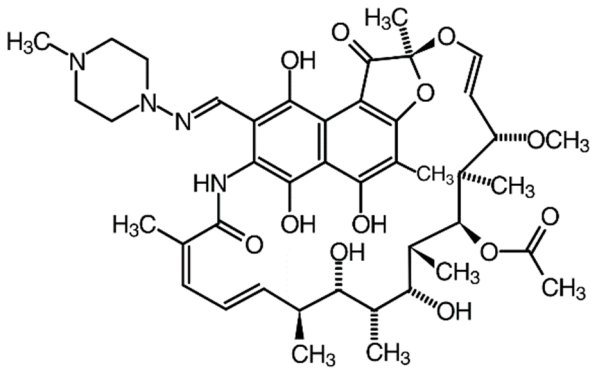

Figure 3.6: Structural formula of rifampicin [35].

3.3.3 Inhaler device - Twister®

To study the effect of DA on aerodynamic performance of a dry powder formulation, the capsule-based inhaler Twister® (AptarGroup Pharma, France) was used (Figure 3.7). This device has a twisting mechanism with which an inserted capsule of size 3 (Vcaps® Plus, Lonza Group, Basel, Switzerland) is pushed into the inner camber when twisted and is thus opened. Thereby, both halves of the capsule and the previously infilled powder lie relatively freely inside the inhaler. Compared to other DPI inhalers, the Twister® has a relatively voluminous chamber. To generate flow in this chamber upon inspiration, it features various holes on the top and bottom side. The fluid flow through these holes causes the capsule halves to spin arbitrarily and promotes deagglomeration of the powder formulation.

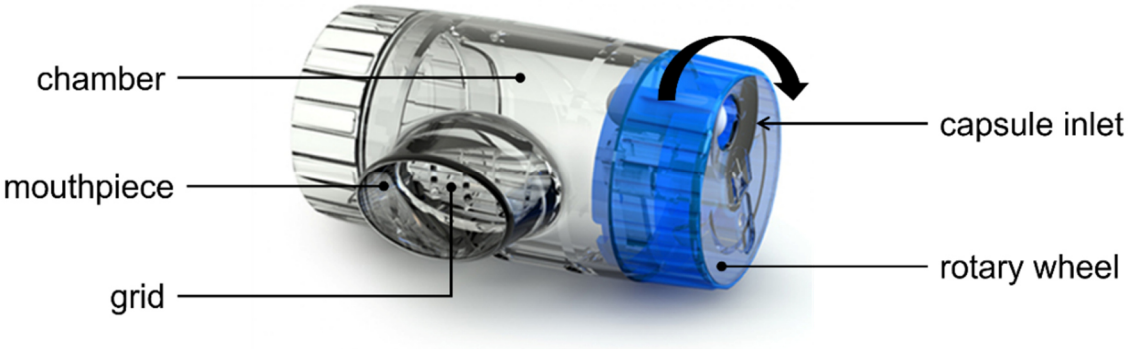

Figure 3.7: Illustration of the Twister® inhaler.

3.4 Methods

This chapter investigates the use of structurally complex DAs in various DPI formulations. For this, the following sections describe the methods used to obtain softpellet formulations (section 3.4.1), to create objects in different sizes and qualities (section 3.4.2) and to evaluate their suitability as DAs (section 3.4.3). The characterisation of particles, the preparation of interactive blends and the procedure of aerodynamic assessment were described in the previous chapter (Chapter 2.3).

3.4.1 Preparation of softpellet formulations

In the following studies on softpellets, the utilised drug substances were common APIs for treating tuberculosis, namely ISN and RIF (section 3.3.2). Both APIs were milled to obtain a micronised product quality suitable for inhalation. Then, the milled API particles were agglomerated to softpellets.

3.4.1.1 Milling

To obtain API particle sizes in the µm range suitable for inhalation [133], an air jet mill was used (Fluid Energy Jet, USA). In this dry grinding process, the starting material was fed through a feed hopper at the top of the mill and introduced into the milling chamber by a feed nozzle (Table 3.8). Inside this chamber the particles are accelerated into a circular motion by the carrier fluid, namely nitrogen. This acceleration results in interparticle and particle-wall collisions, which cause grinding of the feed into smaller particles [134]. As the nitrogen expands, the temperature in the gas stream drops, which offsets the heat generated during grinding. In turn, this avoids thermal degradation of the material.

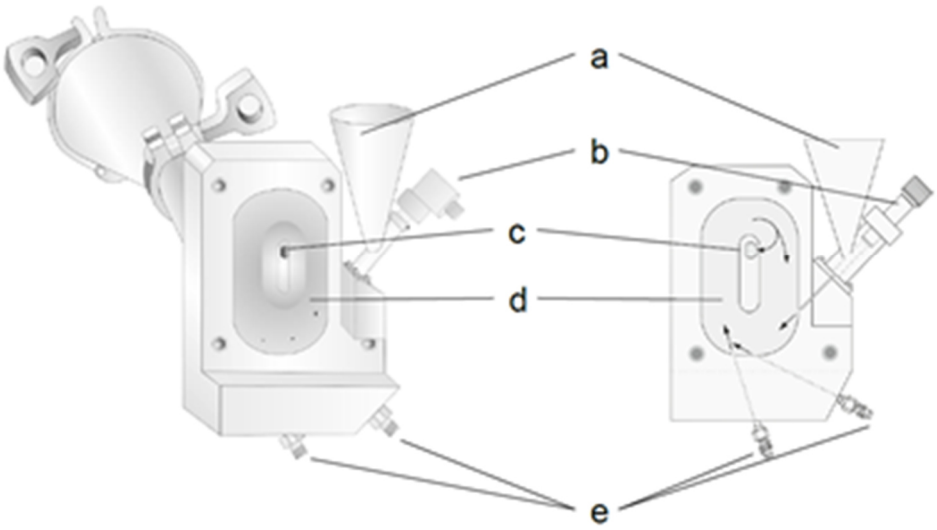

Figure 3.8: Schematic representation (left) and cross-section (right) of an air jet mill: a) sample inlet, b) conveying pressure, c) sample outlet, d) milling chamber, e) milling pressure (adopted from [63]).

The micronised particles escape from the grinding chamber through the central outlet, provided the centrifugal forces acting on them are small enough. A decrease in particle size and mass reduces the centrifugal forces, which causes them to follow the air flow into a filtering and collecting unit [134]. Typically, the PSD of the product is relatively narrow, because large particles remain in the milling chamber.

3.4.1.2 Controlled agglomeration

As described in Chapter 1.6, micronised particles tend to agglomerate due to cohesion. Provided, that this cohesion can be controllably regulated, it can be used to produce spherical agglomerates. Initially developed and patented by AstraZeneca [135], this production method yields powders suitable for respiratory drug delivery. Commercially, such a powder formulation is filled into DPI devices, e.g. Pulmicort® Turbohaler® (AstraZeneca, Cambridge, UK) [136]. This device features a formulation reservoir followed by a volumetric dosing mechanism moving a single dose into the inhalation channel. This dosing operation requires a good flowability of the powder, which is provided through the properties of softpellets.

Controlled agglomeration of micronised API to softpellets was achieved by an apparatus previously described by Etschmann [63]. This apparatus consists of a chute whose inclination angle can be steplessly adjusted and along which the particles can slide. The chute is mounted on an audio speaker (E-Series ML-1715E Power 8, Mac Audio, Germany), that is connected to an audio amplifier (RX V 365 5.1 AV-Receiver, Yamaha, Japan). This amplifier, in turn, is operated with the software Test Tone Generator V 4.0 (Esser-Audio, Germany) allowing the amplitude and frequency to be controlled. Due to resulting vibration of the chute, the particles deposited on it are set into a bouncing motion and, following gravity, are transported to the end of the slide into a collecting container.

Prior to the vibration procedure, the initial material was pre-agglomerated by pressing it through a sieve with a mesh size of 500 µm. Production of softpellets with smooth surface and adequate flowability were obtained by repeating the sliding process up to four times. For this purpose, the intermediate powder was reapplied on the starting point of the chute. Each iteration was preceded by a cleaning and drying step of the slide.

3.4.2 Fabrication of complex dispersing aids

As described in section 3.2, previous research on inserts to promote deagglomeration and DAs, respectively, lacks rational considerations of their optimal size and shape. To the best understanding of the author of this thesis, it is hypothesized that the following characteristics will promote their efficiency of dynamic particle impaction:

- low lifting resistance to enable levitation even at low airflow velocities,
- large contact area to ensure optimum transfer of energy,
- irregular motion in the airstream to increase the probability of collision.

Three geometries that were perceived to meet these criteria were selected from the designs listed in the patent *WO2021115877A1*, which is owned by the author of this thesis and Regina Scherließ [137]. The geometries studied in this thesis, namely *Pharmacone* (PC), *Rollingknot* (RK) and S*occerball* (SB), were either created using SketchUp Pro 2019 (Trimble Inc., Sunnyvale, USA), or were selected from open-source databases (Figure 3.9).

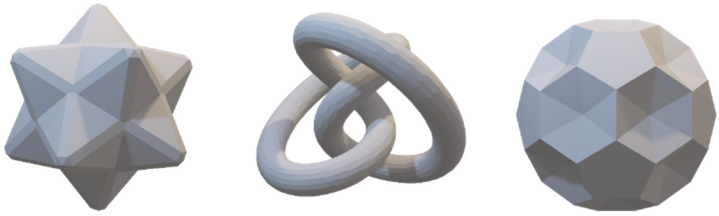

Figure 3.9: Digital design of tested geometries. From left to right: Pharmacone, Rollingknot and Soccerball.

The surface of the SB features alternating flat and recessed surfaces with sharp edges. Similar to the SB, the PC has edges but also conical and partly rounded extensions arranged in a triangle. Unlike the latter DAs, the RK has a single continuous structure with no edges. Instead, this geometry is intertwined and twisted.

Exploring such morphologically different DAs requires a process capable of creating and replicating these designs. AM is a technology that meets these general requirements. This technology is the formalised term for procedures that are used to create physical objects directly from digital data.

Popularly called 3D-printing (3DP), the term AM comprises a variety of different methods. Initially conceived by Charles Hull in 1984 [138], the basic idea of how these methods work is that objects are made by processing material in a layer-by-layer manner [93,94]. The various AM methods differ in their manufacturing principle, the materials applied, the solidification mechanism and the resulting product characteristics. Despite the methodological differences, the steps of each AM process chain are principally the same, involving digital design, manufacturing and post-processing.

Various distributors are available for every AM technology, each offering 3D-printers with slightly different features. The following chapter introduces the AM processes which were used to manufacture DAs: Fused Deposition Modeling bases on extrusion and layer-by-layer deposition of thermoplastic material (3.4.2.1), whereas Selective Laser Sintering

(3.4.2.2), Stereolithography and Two-Photon-Polymerisation (3.4.2.3) basically rely on solidification after light/laser exposure (Figure 3.10).

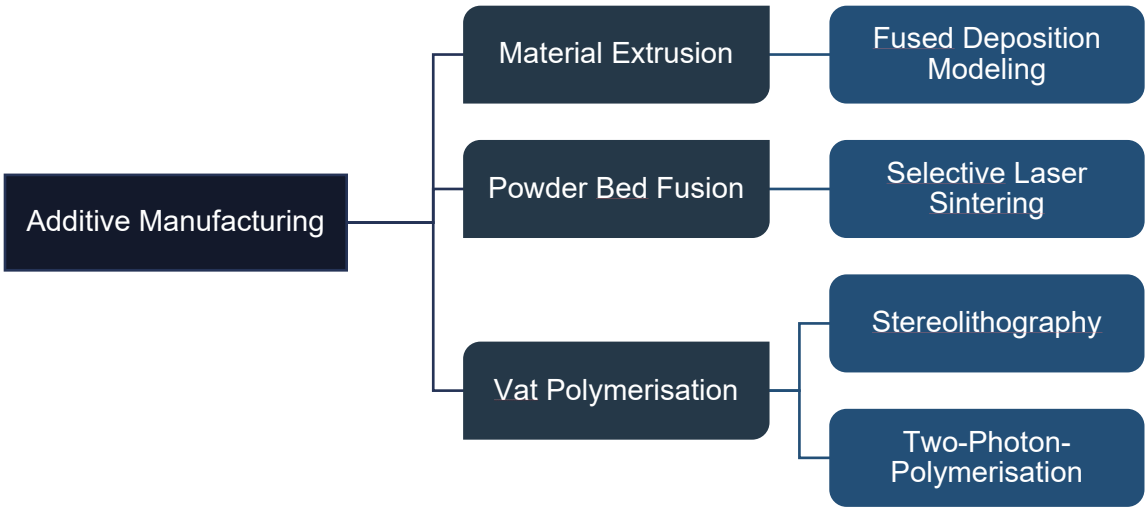

Figure 3.10: Fundamental AM principles and the corresponding techniques applied in this thesis.

3.4.2.1 Fused Deposition Modeling

Fused Deposition Modeling (FDM) is a type of AM processes that involves the extrusion and deposition of melted, thermoplastic filaments that re-solidify after cooling. The filament is mechanically guided through a nozzle orifice of a heated printhead in which the thermoplastic is melted. Melted filament is then applied in layers onto a vertically adjustable platform. Positioning of the printhead and the platform beneath ultimately results in a three-dimensional object which resolution depends on layer height. In addition, the resolution of an FDM method is dependent on the orifice diameter as well as the filament attributes such as melt viscosity and speed of solidification. For preparation of DAs made by FDM, the applied filaments composed of Ultimaker PLA Black (Polylactic acid) and Ultimaker PVA natural (Polyvinyl alcohol, both types Ultimaker B.V., Utrecht, The Netherlands). For printing the Ultimaker 3+ (Ultimaker B.V., The Netherlands) was used. After printing, the support structure made of PVA was manually removed.

3.4.2.2 Selective Laser Sintering

Solidifying powder by sintering or melting due to laser focus is called Selective Laser Sintering (SLS). This technology can be categorised to the group of Powder Bed Fusion. In this technological group, solid layers of thermoplastic, granular material are formed by heating slightly below melting temperature. When a layer is completely sintered, the build platform moves downwards followed by a new layer of powder to be spread and levelled upon. Then, a laser scans the contour of the next layer and selectively sinters the powder particles along the cross-section of the designated object. The speed and resolution of this

sintering process are basically dependent on the characteristics of the granular material as such, the powder refeeding and levelling as well as the laser accuracy.

The prints made by SLS consisted of powdered polyamide PA 2200® (EOS, Germany), which was sintered using the Formiga-P 100® (EOS, Germany) with a layer height of 0.10 mm. After printing, the objects were entirely embedded in the unsintered powder which was subsequently removed with compressed air.

3.4.2.3 Vat polymerisation

In vat polymerisation processes, a vat of photo-reactive liquid resin is selectively exposed to light inducing photo-polymerisation. The photo-polymerisation technologies used in this thesis differ in the light source and energy level of the light and laser beam, respectively. Guided and focused by mirrors and optics to a focal spot, the light initiates a cross-linking of the photoresin components. The volume of this spot ultimately determines the resolution of each method. In these techniques, the fabricated object is bound to a platform immersed in photoresin that, depending on the actual process, ascends or descends once a layer of photoresin is cured. Cross-linking polymerisation fundamentally requires appropriate light intensity, but also a photoinitiator to induce the polymerisation.

The technology named stereolithography (SLA) makes use of a UV laser to draw each layer of an object. Using two motor-driven mirrors called galvanometers, the laser beam is quickly steered across the print zone to solidify the resin as the beam moves. For fabricating prints based on this technology, either standard black resin was processed in the Form 2® (both Formlabs, USA) or Accura 60® resin was processed in the Viper Si2™ SLA printer (both 3D Systems, USA) in high-resolution mode with 0.05 mm layer height. Post-processing steps comprised the removal of supportive structures, if any, and surface finishing of the prints.

AM technologies that rely on two-photon absorption, as initially described by Maria Goeppert-Mayer [139], are referred to as Multiphoton polymerisation, Multiphoton lithography, Direct Laser Writing and, most commonly, Two-Photon-Polymerisation (TPP). The absorption of two photons by an atom or molecule implies a non-linear excitation into an energetically higher state. This physical mechanism occurs once a short-pulsed light, for which mostly a low energy level such as near-infrared (NIR) is applied, is focused tightly on a focal region in a photosensitive medium, namely a photoresin. Only inside this focal spot and voxel, respectively, an appropriate light intensity is obtained. Sufficient intensity and photon density induce the typically liquid photoresin to absorb the energy of two photons simultaneously. Sufficient photon density is achieved by combining an appropriate laser,

specifically a Ti: Sapphire femto-pulsed laser, with a high numerical aperture objective (Figure 3.11) [140]. The absorption of two photons, in turn, causes the components of the photoresin to polymerise and hence to solidify.

Besides the light source and power, the voxels' dimension is further dependant on the chemical and optical properties of the photoresin components, the optical system and scan speed. In summary, these parameters define the resolution of the printing technique. In comparison to FDM (section 3.4.2.1), SLS (section 3.4.2.2) and SLA, the vertical and lateral resolution of TPP is improved, which allows smallest features in the sub-micrometre range to be printed.

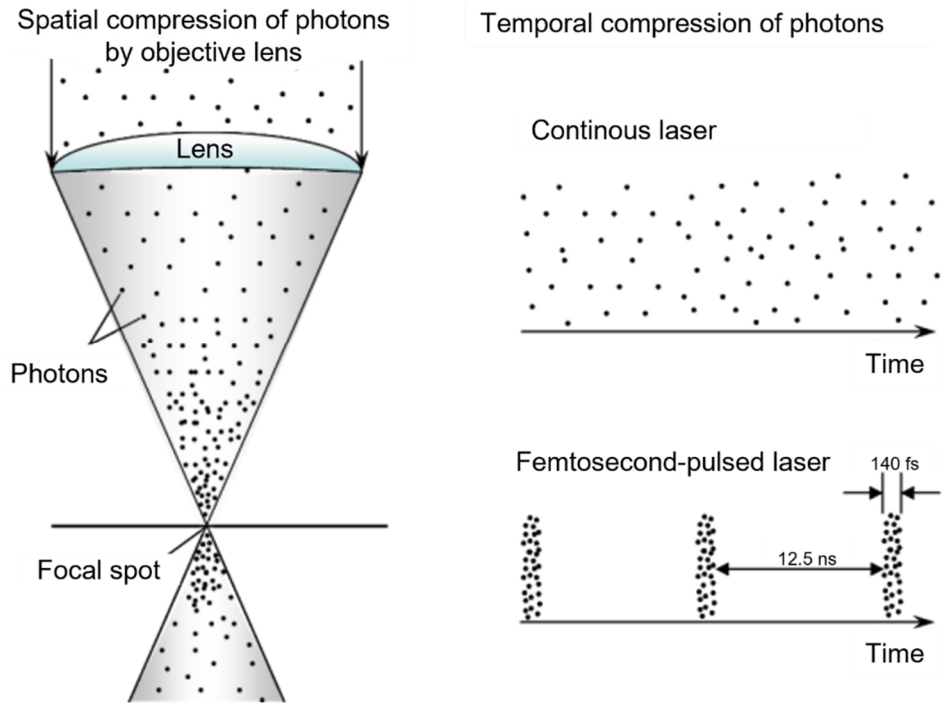

Figure 3.11: Schematic illustration of spatial and temporal compression to achieve appropriate photon density at the focal spot (adopted from [141]).

The TPP-prints used in this thesis were manufactured using the Photonic Professional GT2 (Nanoscribe GmbH & Co. KG, Germany) platform. For the printing process, IP-Q® served as the photoresin material. This material contains acrylate-monomers as a reactive group that cures upon free radical polymerisation. The print job was conducted in the Shell/Scaffold-mode using an objective with 10 x magnification. Once the print was finished the unpolymerised resin was removed. Post-processing of the prints included UV curing as well as removal from the preparation plate by heating for 5-10 seconds and immersion in isopropyl alcohol in an ultrasonic bath for 30 seconds.

3.4.3 Assessment of lifting pressure and trajectories

To investigate the levitation behaviour of additively manufactured geometries (section 3.3) in an air stream, a method was developed based on the Ph.Eur. 2.9.41 [35]. For this, prints based on SLS printing (section 3.4.2.2, Figure 3.13) were tested in an apparatus that consisted of an upright glass tube with an inner diameter of 24.3 mm, which was fixed to a tripod. Connected to compressed air supply, a sieve plate was mounted at the bottom of the tube. To monitor and adjust the air pressure and thus flow rate, a Bourdon tube pressure gauge (Kobold Messring, Germany) was connected to the air inlet (Figure 3.12). A camera was positioned on another tripod so that both the pressure gauge and the glass tube were in its field of vision.

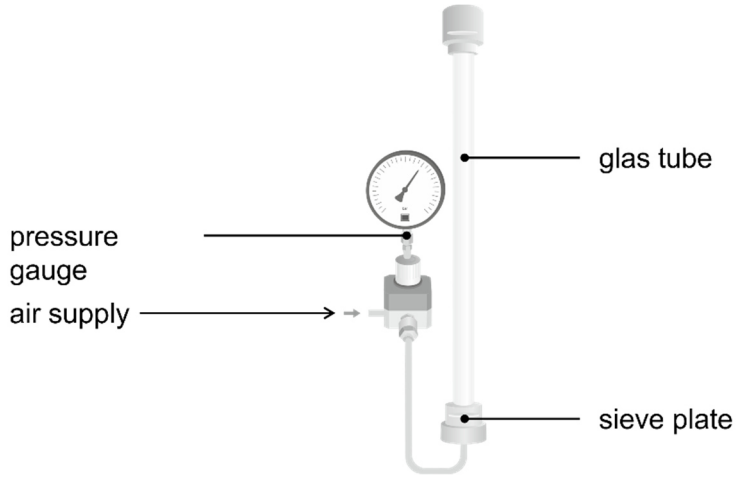

Figure 3.12: Test apparatus for levitation studies.

The air pressure was regulated by manually adjusting the pressure gauge. Both the pressure and the motion of the objects to be studied in the air stream were recorded by video (normal image speed and slow-motion). Recording the objects' trajectories at different pressures allowed to investigate how the objects behave in an air stream, considering their structural variety and respective weights. Furthermore, studies on the influence of the number of identical objects on the lifting pressure to be applied and on the objects' behaviour in the air stream were carried out.

3.5 Pre-evaluation of tailor-made dispersing aids

Assessing the required lifting pressure and the trajectories of different geometries in an airstream allowed for a pre-evaluation of their suitability as DAs. In selecting the morphologies shown in Figure 3.9 and Figure 3.13, respectively, a variety of different morphological features in terms of plane surfaces, edges and curves were considered.

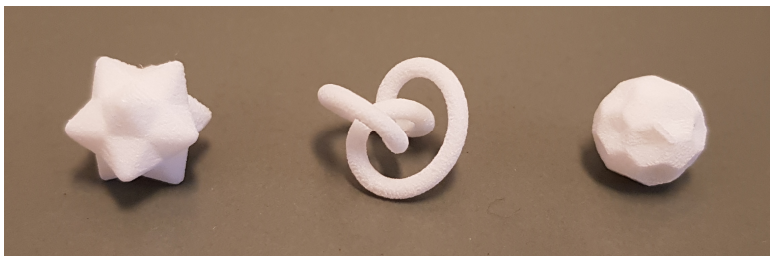

Figure 3.13: Additively manufactured geometries with 12 mm in diameter made by SLS printing (purchased from nobitec GmbH). From left to right: PC, RK and SB.

The tested geometries showed varying tendencies to fluidise and in their motion behaviour. Figure 3.14 shows the air pressures that were needed to lift the respective number of geometries. This critical lifting pressure (cLP) was smallest for the RK, followed by the SB and PC. With the RK (1: 0.07 bar, 2: 0.08 bar, 3: 0.1 bar), the pressure to be applied increased with the number (1 < 2 < 3) of geometries that were placed in the glas tube. In contrast, the pressure to be applied for the SB decreased with the number of geometries in the air stream (1: 0.34 bar, 2: 0.28 bar, 3: 0.28 bar). Testing the PC, no correlation between the pressure and the number of objects were found (1: 0.34 bar, 2: 0.38 bar; 3: 0.29 bar). Overall, the cLP was lowest for RK compared to SB and PC. However, this enhanced tendency to fluidise could be attributed to its lower weight.

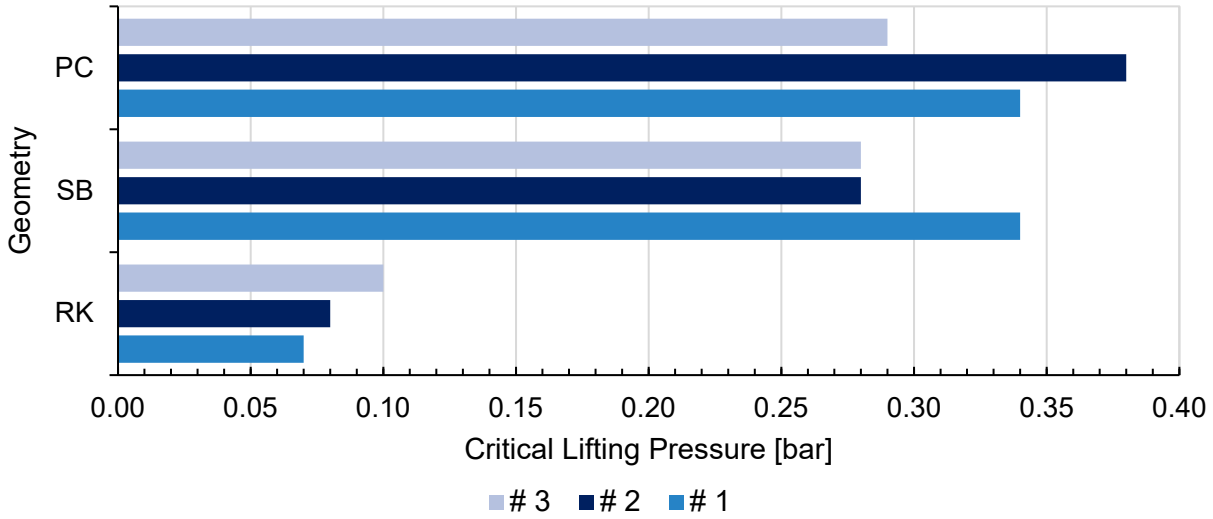

Figure 3.14: Critical lifting pressure to be applied to lift the respective objects (number of objects from top to bottom: 3, 2 and 1).

Dividing the cLP by the respective mass allows considering the morphological peculiarities. Basically, the mass is a decisive factor for lifting an object because the opposing gravitational forces on its weight. With given density, the volume of each object determines the specific mass. Based on this rationale, the median mass of the individual objects varied due to their morphological differences (Table 3.2). Consequently, when determining the fluidisation of the objects, their mass must also be considered.

Table 3.2: Median mass of the printed geometries used for DA pre-evaluation (n = 10).

Parameter	PC	RK	SB
Median Mass [mg]	480	147	388
SD [mg]	6.44	3.06	6.87

The corresponding results of cLP (in mbar) divided by mass (in mg) were in accordance with the previous finding in that the RK has the lowest mass-specific cLP (0.48 mbar/mg). Next, the PC showed a mass-specific cLP of 0.71 mbar/mg, followed by the SB with 0.88 mbar/mg (Figure 3.15). Increasing the number of geometries in the glass tube caused the respective values to equalise, due to the tube diameter as a limiting factor for the drag.

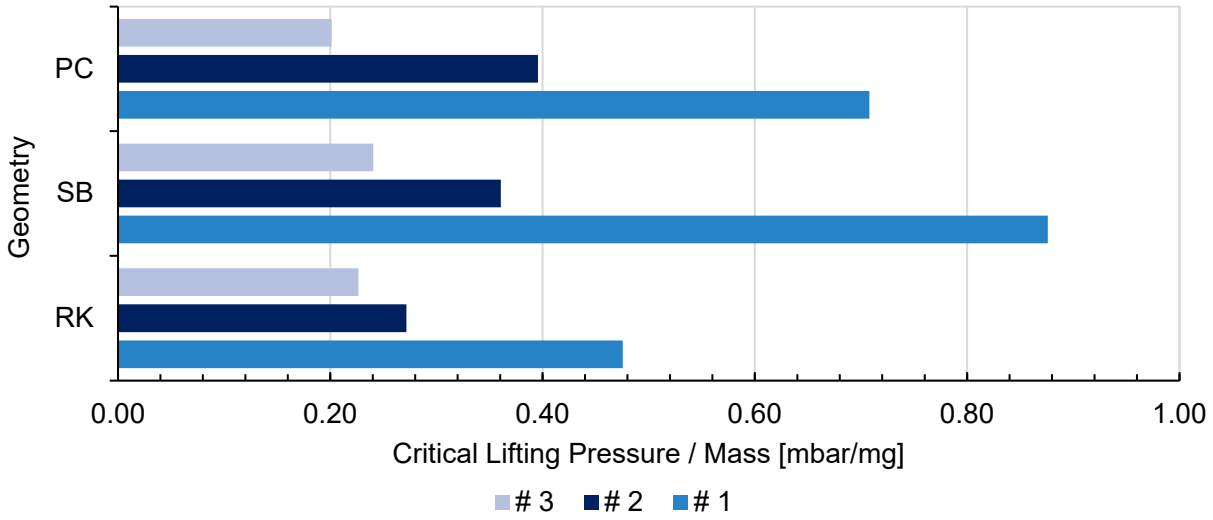

Figure 3.15: Critical lifting pressure to be applied to lift the respective objects (number of objects from top to bottom: 3, 2 and 1).

For describing a geometry-dependent motion pattern, the objects were labelled in colour in x-, y- and z-direction. In this observational study, it was found that the RK showed a comparably high tendency to irregular, tumbling behaviour in an air stream. This object showed heavy rotations, whereby a hovering state could not be reached, as it steadily oscillated in an upward and downward motion. The SB remained mostly on a straight vertical trajectory with rotations around a horizontal axis. On contact with the inner wall of the air tube, the behaviour deviated briefly, but returned to the previous pattern. Contrarily, the PC showed lateral movements in the air stream. A definite rotation pattern could not be detected. Intermittently, a fluctuating rotation axis in the horizontal axis was observed.

As an intermediate conclusion, remaining in levitation was not solely due to the total weight of the respective geometries but was also dependant on their individual shape. Once the object was lifted, the SB rotated around one axis, whereas the PC flew irregularly in the glass tube. Multiple PC geometries tended to form a closure of individual particles, forcing

the airflow to stream laterally along the glass wall. This diversion of the airflow resulted in increased drag causing a lift of the entangled geometries. Once the form-fitting bond loosened again, the geometries fell back to the ground because of gravitational forces. Entanglement of multiple RK geometries did not occur in this setting.

This study simplified the processes in the airflow of an inhaler. To conclude this study, the RK featured superior characteristics in terms of lifting and motion in an air stream. In comparison to the PC and SB, the RK showed a pronounced rotation and most irregularly motion pattern. Although the PC also showed tumbling motions, it tended to move rather laterally and to rotate less. Contrarily, the SB rotated extensively but only on a single axis with less pronounced irregularity. Considering the general purpose of DA in an inhaler device, irregular motion and low effort to lift were considered to be advantageous characteristics.

3.6 Assessment of DPI formulations with dispersing aids

Aerodynamic assessment was conducted as described in Chapter 2.3.4.1, except for the following methodological aspects. A dispersing aid was inserted into the device chamber of the Twister® before plugging the inhaler into the mouthpiece, which is mounted on the induction port of the NGI. In accordance with the requirements of the Ph. Eur., a pressure drop of 4 kPa resulted in an airflow rate of 55.0 L/min and thus a measuring time of 4.3 sec for each run (Table 2.4).

Inserting a DA into the chamber showed no effect on the airflow rate compared to the standard operation. After a testing run both the device and the DA were transferred into the same beaker, which was sealed with Parafilm® M (Bermis Company Inc., USA) after being rinsed with the appropriate volume of solvent. Hence, for the evaluation of the APSD, the amounts of API detected on the DA and in the device were not differentiated from each other but summed instead. The API residue on the capsule halves was quantified separately.

Depending on the respective analytes, different solutions served as solvents. For SBS, the solvent was $_{dd}H_2O$, whereas the respective mobile phase used for HPLC analysis served as the solvent for BUD, ISN and RIF (Table 3.3).

Table 3.3: Analytical parameters for quantification of the substrates via HPLC.

Substrate	Column type	Mobile phase	Flow [mL/min]	λ [nm]
BUD	RP-18	25 % $_{dd}H_2O$ + 75 Methanol	1.0	248

Substrate	Column type	Mobile phase	Flow [mL/min]	λ [nm]
ISN	RP-18	43 % Acetonitrile + 57 % buffer solution ($_{dd}H_2O$) Buffer: 0.16975 g/L Tetrabutylammonium hydrogen sulfate with a pH of 3.1 (0.0005 mol/L)	0.75	290
RIF	RP-8	55 % Acetonitrile + 45 % buffer solution ($_{dd}H_2O$) Buffer: 6.8045 g/L Phosphate buffer adjusted to pH 2.5 (0.05 mol/L)	1.0	254
SBS	RP-18	22 % Acetonitrile + 78 % buffer solution ($_{dd}H_2O$) Buffer: 2.87 g/l Sodium heptanosulfonate, 2.50 g/l Potassium dihydrogen phosphate. pH set to 3.65 by adding ortho-Phosphoric acid 85 %.	0.8	220

In this thesis, the geometries PC, SB and RK in different diameters served as model DAs (Figure 3.9, Figure 3.17 and Figure 3.34). The respective type and number of DAs was placed into the inner chamber of the Twister® device before a filled capsule was inserted. Triggering the NGI instrumentation induced an air stream (section 2.3.4.1), which caused both the DPI formulation and the DA to move inside the chamber. On the one hand, the powder particles partly dispersed and left the inhaler. On the other hand, the air stream led to random trajectories of the DAs inside of the inhaler, whereby these objects were too large to pass the grid of the mouthpiece (Figure 3.7, Figure 3.16).

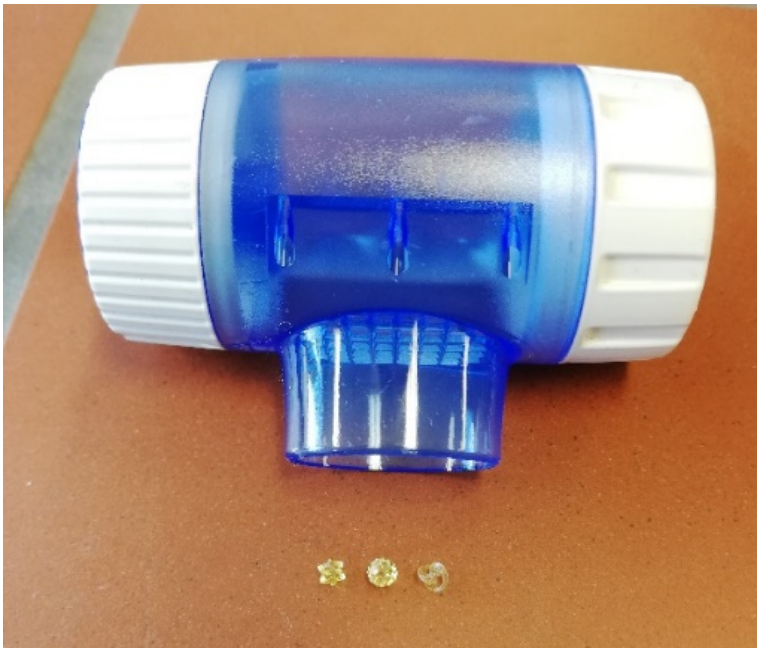

Figure 3.16: Image of the Twister® device and the DAs with a diameter of 3 mm (from left to right: PC, SB and RK).

In accordance with the findings described in section 3.5, the various DAs behaved differently in the inhaler device. Variation in DA movement were caused by differences in shape, volume and mass. Due to these different features including respective surface area,

inserting such objects was expected to offer additional contact areas for DPI particles to collide with. A higher collision probability in turn implies additional shear forces, which possibly promotes particle dispersion.

3.6.1 Dispersing aids in interactive blends

As described in Chapter 1.7.1, formulating interactive blends composed of carrier and micronised API particles ensures processability, fluidisation, and thus aerosolisation of the bulk powder. Efficient drug delivery depends on the dispersion of the carrier-drug agglomerate because API particles larger than 5 µm aerodynamic diameter predominantly impact in the upper airways (Chapter 1.2). To enhance the dispersion in the inhaler device during inhalation, inserting DAs is a promising approach.

Investigating the potential effects of DAs on aerodynamic performance, the following study considered the influence of

- carrier characteristics (1),
- API properties (2),
- drug content of the interactive blend (3),
- capsule infill (4) and
- number of DAs (5).

For the following study, the geometry RK served as the model DA. To fabricate this morphology in the required size range of 4 mm in diameter, SLA printing served as the manufacturing technology (section 3.4.2.3). The print used for this aerodynamic assessment and representatively shown in Figure 3.17 was produced by nobitec GmbH (Germany).

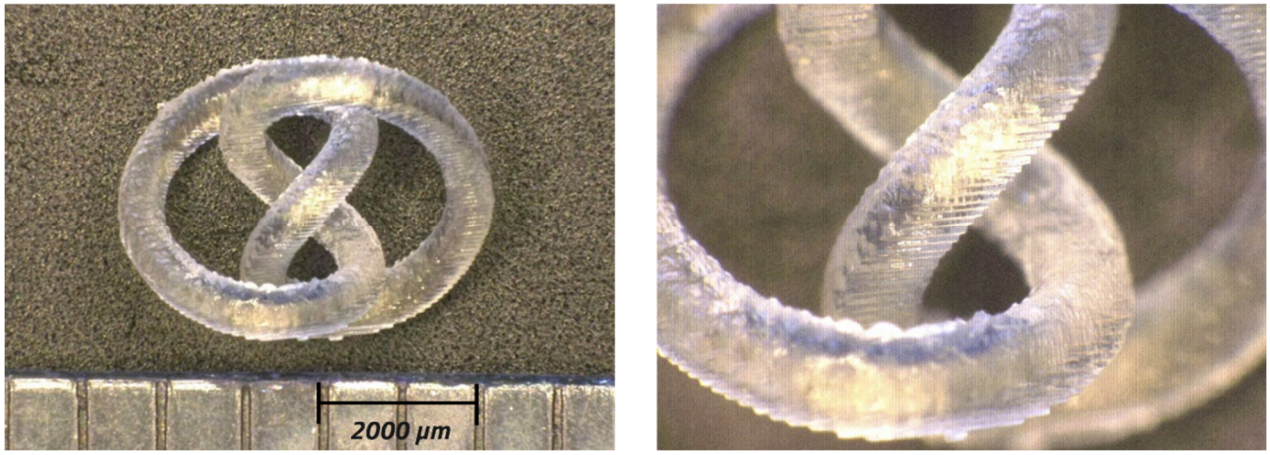

Figure 3.17: Representative image of the RK with a diameter of 4 mm made by SLA printing.

3.6.1.1 Preparation and characterisation of interactive blends

In this study, the utilised drug substances were common APIs for treating asthma and COPD, namely SBS and BUD (Section 3.3.2). These model drugs represent a variety of physico-chemical properties, in which SBS is hydrophilic and BUD lipophilic (Table 3.1). Both APIs were provided in micronised quality by the supplier, which was proven with laser diffraction measurements (Chapter 2.3.1.4).

As shown in Figure 3.18, the drug particles equalled in particle size distribution. SBS composed of particles that ranged from 0.77 µm ± 0.00 µm (x_{10}) to 3.46 µm ± 0.03 µm (x_{90}) with a median of 1.63 µm ± 0.00 µm (x_{50}). Likewise, BUD contained particles with a size between 0.45 µm ± 0.01 µm (x_{10}) and 2.67 µm ± 0.01 µm (x_{90}) with an x_{50} of 1.33 µm ± 0.01 µm.

Two different grades of lactose served as carrier material, namely InhaLac® 120 (IL120) and InhaLac® 251 (IL251). As displayed in Figure 3.18, these carrier materials differed in particle size distribution. IL120 contained particles with a size between 79.7 µm ± 0.56 µm (x_{10}) and 187 µm ± 0.62 µm (x_{90}) with an x_{50} of 129 µm ± 0.45 µm. In contrast, IL251 contained particles that ranged from 10.3 µm ± 0.12 µm (x_{10}) to 46.7 µm ± 0.36 µm (x_{90}) with a median of 91.5 µm ± 0.30 µm (x_{50}). Accordingly, IL120 consisted of carrier particles with on average larger diameter.

Each carrier material was blended with 2.0 %,4.0 % and 6.0 % (m/m) of micronised SBS and BUD, respectively, as described in section 2.3.3. To prove blend quality, the amount of API attached to each carrier material was quantified using HPLC analysis as described in section 2.3.3.1 and explained in section 2.5.2. Specifically, testing the blend quality comprised determining the API content (in m/m) and the respective RSD values for each sample (Table 3.4).

In this study, blending homogeneity was defined as drug content with less than 5 % RSD inter-sample deviation with a total API recovery of 90 – 110 %. The recovery value indicates the extent to which theoretically detectable API concentrations were actually quantified in the course of the process, e.g. during blending or aerodynamic assessment. As a quality attribute of a mixture, the recovery is calculated from the quantified API mass divided by the practically weighed and thus theoretically detectable API mass. The recovery value therefore indicates whether the procedure and analysis were carried out with sufficient care.

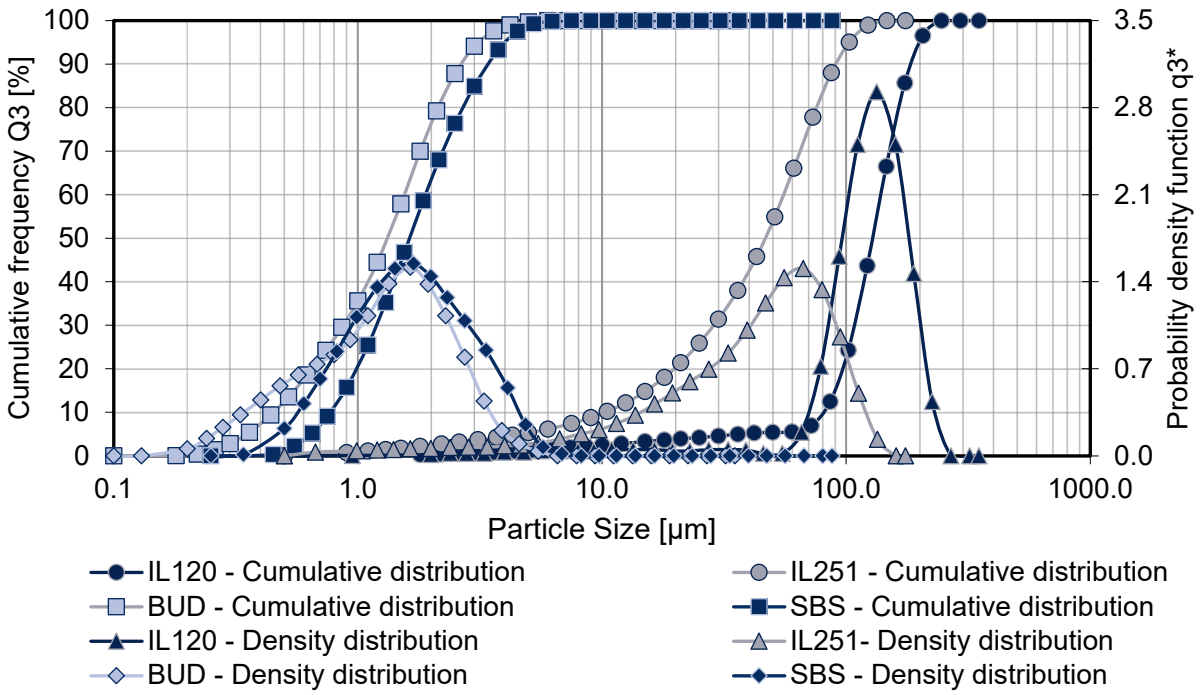

Figure 3.18: PSD measurements of the carrier material (IL120 and IL251) and the micronised drug particles (BUD and SBS); n = 3, error bars = SD.

Table 3.4 summarises the homogeneity values of the blends that based on IL120 or IL251. Although basing on identical blending processes, the homogeneity and recovery values varied from blend to blend. In summary, the batches were all within the specified limits.

Table 3.4: Blend homogeneity of blends composed of IL120 or IL251 as carrier material and SBS or BUD as model API; n = 10, deviation = RSD.

Blend + API content	SBS Content	BUD Content
IL120 + 2%	1.84 % ± 1.39 %	1.88 % ± 3.82 %
IL120 + 4%	3.71 % ± 3.12 %	3.67 % ± 1.10 %
IL120 + 6%	5.66 % ± 2.71 %	5.48 % ± 0.54 %
IL251 + 2%	1.89 % ± 1.78 %	1.92 % ± 1.42 %
IL251 + 4%	3.69 % ± 3.18 %	3.82 % ± 0.81 %
IL251 + 6%	5.78 % ± 1.53 %	5.88 % ± 1.84 %

Figure 3.19 and Figure 3.20 show representative images of the different interactive blends. Specifically, blends that contain micronised SBS are displayed in Figure 3.19. In turn, Figure 3.20 shows corresponding samples composed of BUD added to IL120 and Il251, respectively. Comparing the different carrier grades, APIs, and concentrations, the microscopic images shown in Figure 3.19 and Figure 3.20 indicated homogeneous particle distribution on the carrier surfaces for each blend. However, high drug concentrations favoured the formation of API agglomerates. On closer inspection, the images show that the

particles of the two different APIs accumulated differently. Compared to SBS particles, which partly adhered discretely to the surface of the carrier, BUD particles showed a higher tendency to form drug agglomerates. These differences in adhesion and cohesion could be attributed to chemical dissimilarities of the two model APIs.

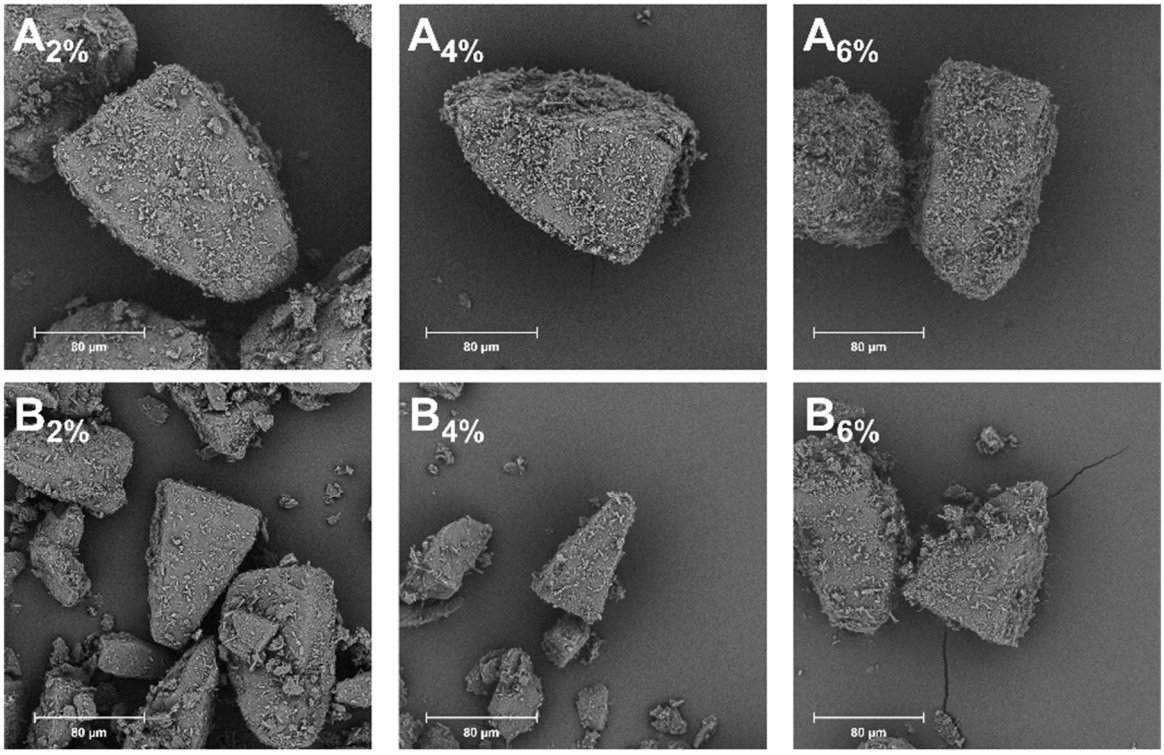

Figure 3.19: Representative images of IL120 (A) and IL251 (B) blended with different concentrations of SBS (from left to right: 2 %, 4 % and 6 %). Magnification: 1000x.

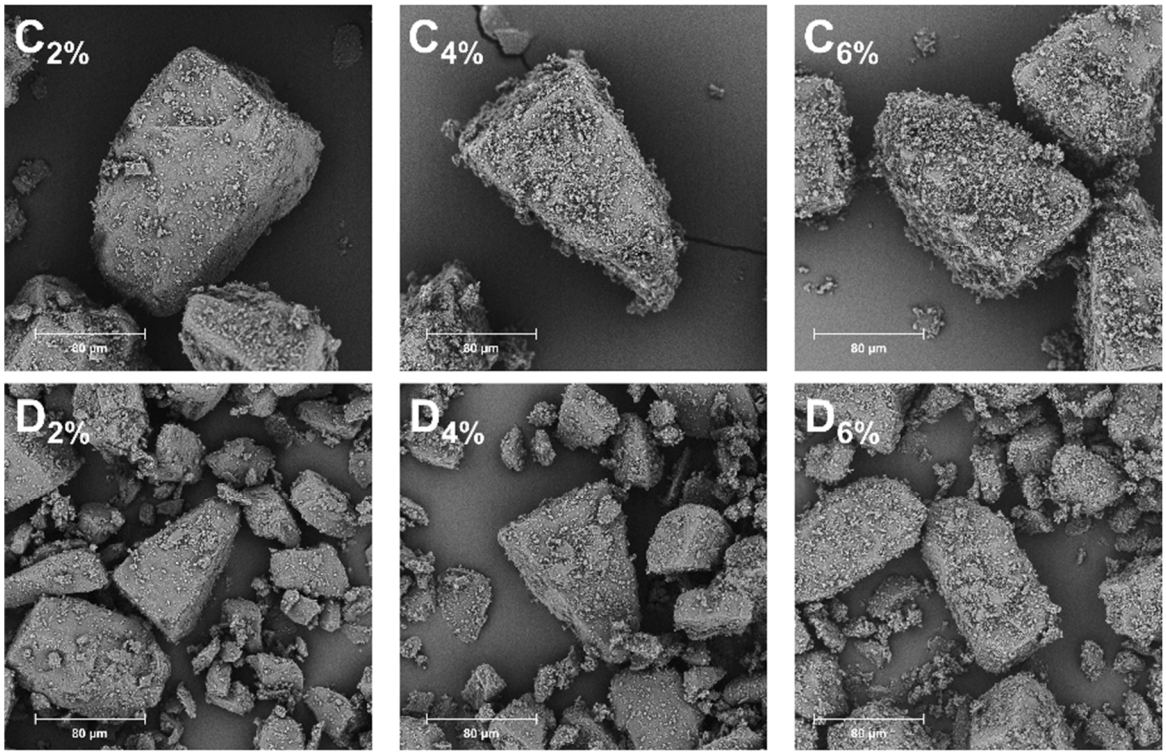

Figure 3.20: Representative images of IL120 (C) and IL251 (D) blended with different concentrations of BUD (from left to right: 2 %, 4 % and 6 %). Magnification: 1000x.

3.6.1.2 Aerodynamic assessment of interactive blends

To study the effect of inserting DAs into an inhaler on the aerodynamic performance of DPI formulations, aerodynamic assessments allowed for determining their APSD (Chapter 2.5.3). As a result of this aerodynamic particle sizing, the FPF values of API particles below 1, 3 and 5 µm aerodynamic diameter served as comparative measures.

As a representative evaluation of an APSD assessment, Figure 3.21 shows a deposition profile of IL120 blended with 2 % SBS as the model API. For this evaluation, no DA was inserted into the Twister® device (w/o DA). In this study, two different capsule fillings (20 mg and 60 mg) were tested.

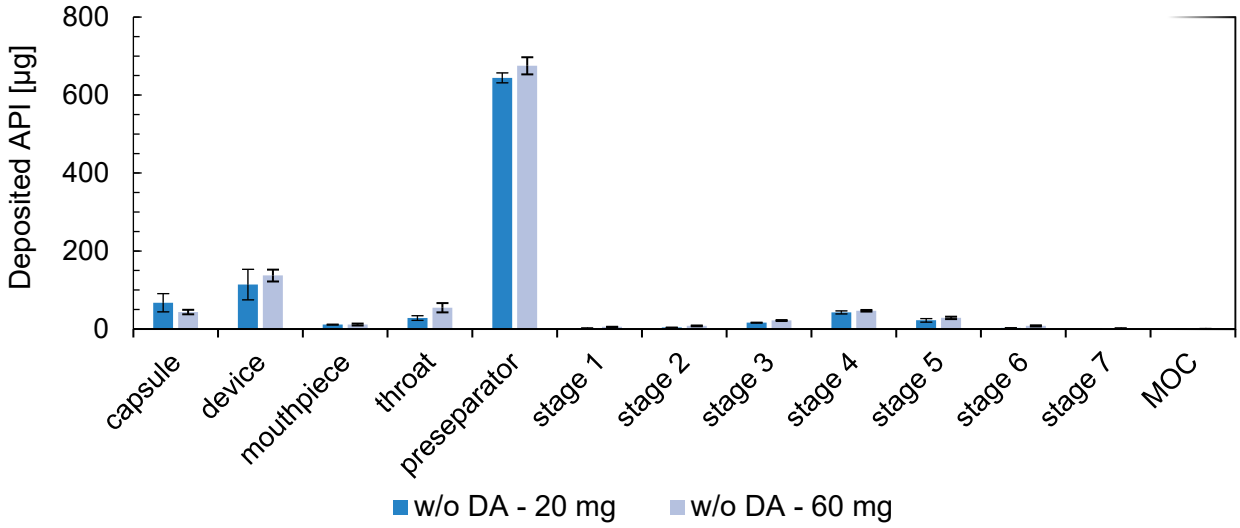

Figure 3.21: Deposition profile of interactive blends composed of IL120 as carrier material and 2.0 % SBS as a model API (Twister®; n = 3, error bars = SD).

The resultant FPF values are shown in Figure 3.22. Generally, the FPF < 5 µm values are comparably low, ranging from 10.9 % ± 1.49 % SD (20 mg) to 12.6 % ± 0.84 % SD (60 mg). Moreover, the data shows that the filling had no significant effect on the FPF values.

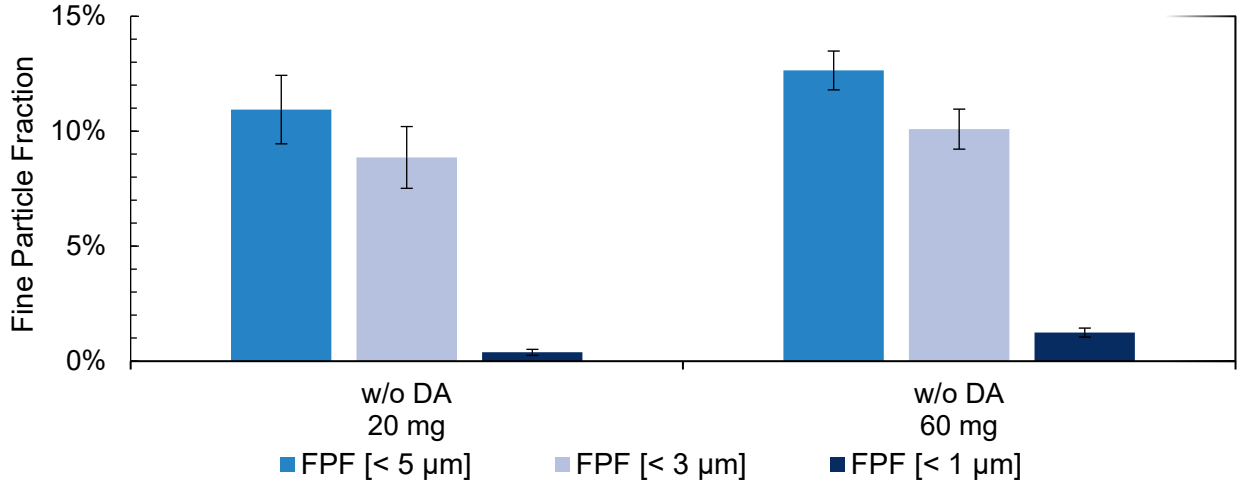

Figure 3.22: FPF values of interactive blends composed of IL120 and SBS without inserting an DA into the Twister® device (n = 3, error bars = SD).

The focus of the following study was on whether applying DAs caused a shift of the deposition profile towards stages with lower cut-offs. In principle, such a shift would lead to an increase in FPF values, which in turn would indicate an enhancement of aerodynamic performance.

To account for potential influencing factors besides the use of DAs (section 3.6.1), a three-factor study design was devised and applied to each interactive blend. As displayed in Figure 3.23, the fractional factorial design included eight corner points and one centre point. Specifically, this design covered a range of drug contents (2 %, 4 %, 6 %), different capsule infill masses (20 mg, 40 mg, 60 mg) and the number of DAs inserted into the inhaler device (1, 2, 3). In this study, SLA-printed RK geometries (section 3.3) with a diameter of 4 mm served as DAs.

In reference to the cube plot presented in Figure 3.23, Table 3.5 shows the description of the labelled corner and centre points. Referring to Table 3.5, sample A and sample B contained the lowest (2 % drug content, 20 mg capsule infill), whereas sample G and sample H contained the highest drug content (6 %) and capsule infill (60 mg). Complementing samples A and B, samples C and D had the same capsule infill (20 mg) but different drug content (6%). Conversely, sample E and sample F contained a drug content of 2 % in 60 mg of capsule filling.

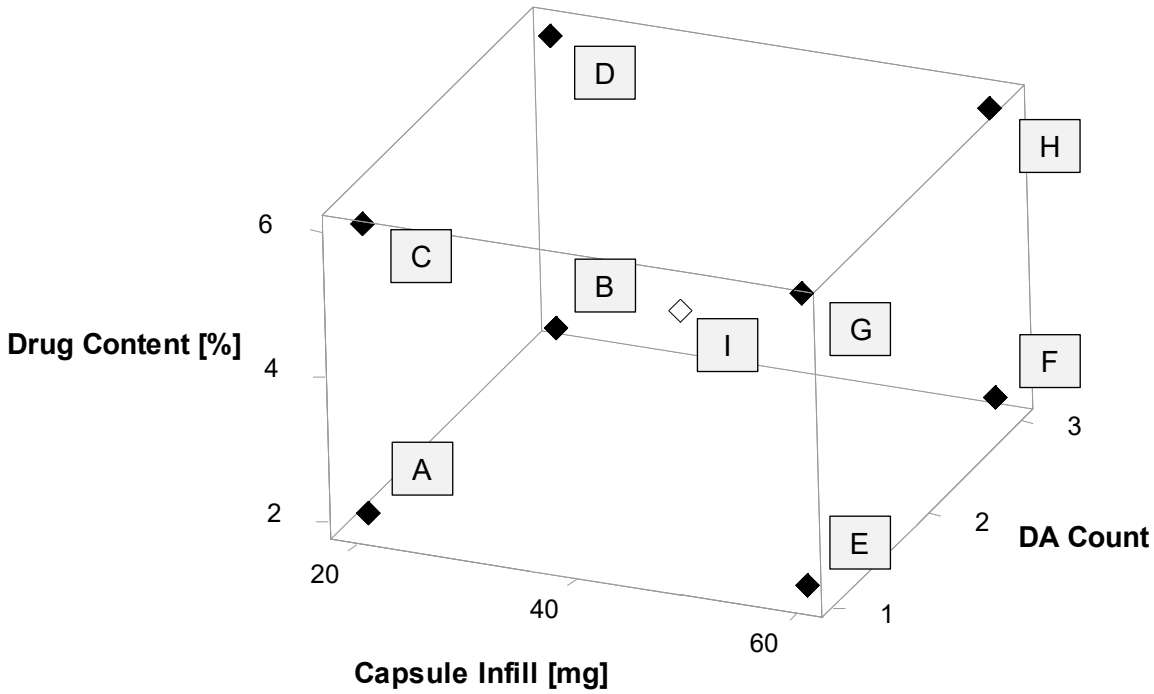

Figure 3.23: Study design to determine the effect of DAs on the aerodynamic performance of interactive blends. The factorial corner points are labelled A to H and the centre point is labelled I.

Table 3.5: Description of the labels with reference to Figure 3.23.

Label	Drug Content	DA Count	Capsule Infill	Capsules / Run
A	2 %	1	20 mg	3
B	2 %	3	20 mg	3
C	6 %	1	20 mg	3
D	6 %	3	20 mg	3
E	2 %	1	60 mg	1
F	2 %	3	60 mg	1
G	6 %	1	60 mg	1
H	6 %	3	60 mg	1
I	4 %	2	40 mg	2

To ensure drug concentrations above the detection limit of the respective API (Appendix G) in each NGI stage, conducting the assessments required a minimum formulation mass of 60 mg. Therefore, the centre point (sample I) was tested using two capsules with a total mass of 80 mg instead of 60 mg as for the corner points. Prior to conducting an NGI run, the corresponding number of DAs was inserted into the Twister® device (section 3.6). Depending on the capsule fillings, the corresponding number of capsules was then separately applied to the inhaler.

The aerodynamic assessments comprised determining comparative measures such as the inhaler device retention (DR) that is considered as the sum of the API masses that remained in the inhaler, in and on the capsule(s), and on the DAs inserted into the inhaler. This parameter is further expressed as a percentage of the total determined API mass thus representing the difference between the MD and the DD (Chapter 2.3.4.2). In the following evaluations, the determined total API concentration per run, defined as API recovery, generally ranged between 90 % and 110 %.

Resulting from the aerodynamic particle deposition profile, Figure 3.24 shows the MD and DD per capsule as well as calculated DR values for interactive blends composed of IL120 and SBS.

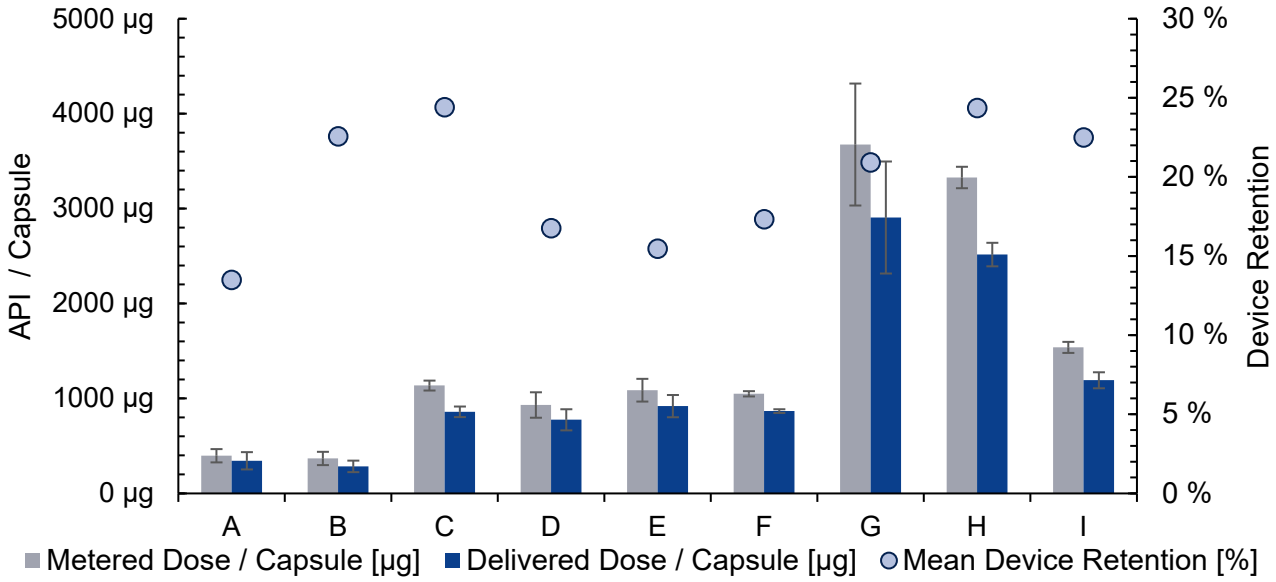

Figure 3.24: MD, DD and DR for interactive blends composed of IL120 and SBS (n = 3, error bars = SD). The labelling of the values corresponds to Figure 3.23 and Table 3.5.

The data presented in Figure 3.24 show that the MD values were in accordance with the corresponding capsule fillings and the individual drug concentrations. This finding is also evident for the corresponding DD values. Based on MD and DD, the resultant DR values ranged from 13.5 % (A) to 24.4 % (C). Figure 3.25 summarises the aerodynamic characteristics of each sample. Among all, sample A (2 % drug content and 20 mg capsule infill) had the lowest FPF < 5 µm (8.28 % ± 2.50 %), FPF < 3 µm (6.73 % ± 2.09 %) and FPF < 1 µm (0.45 % ± 0.18 %). In contrast, sample H (6 %; 60 mg) showed the highest FPF < 5 µm (21.4 % ± 1.31 %), FPF < 3 µm (16.9 % ± 1.01 %) and FPF < 1 µm (2.31 % ± 0.42 %). The MMAD showed no substantial difference among the sample set with an average of 2.27 µm.

Referring to the findings presented in Figure 3.22, the insertion of DAs into the inhaler caused in principle no significant effect on the aerodynamic performance of the respective formulation (Figure 3.25; A, B, E and F). Comparing the values of the individual samples, the aerodynamic performance primarily correlated with the SBS content of the respective blend. In contrast, neither the capsule filling nor the number of inserted DAs remarkably effected the FPF values (Figure 3.25). An exception of this finding were the 6% blends at 60 mg capsule filling (G and H). In these cases, the FPF increased with an increase in DA count.

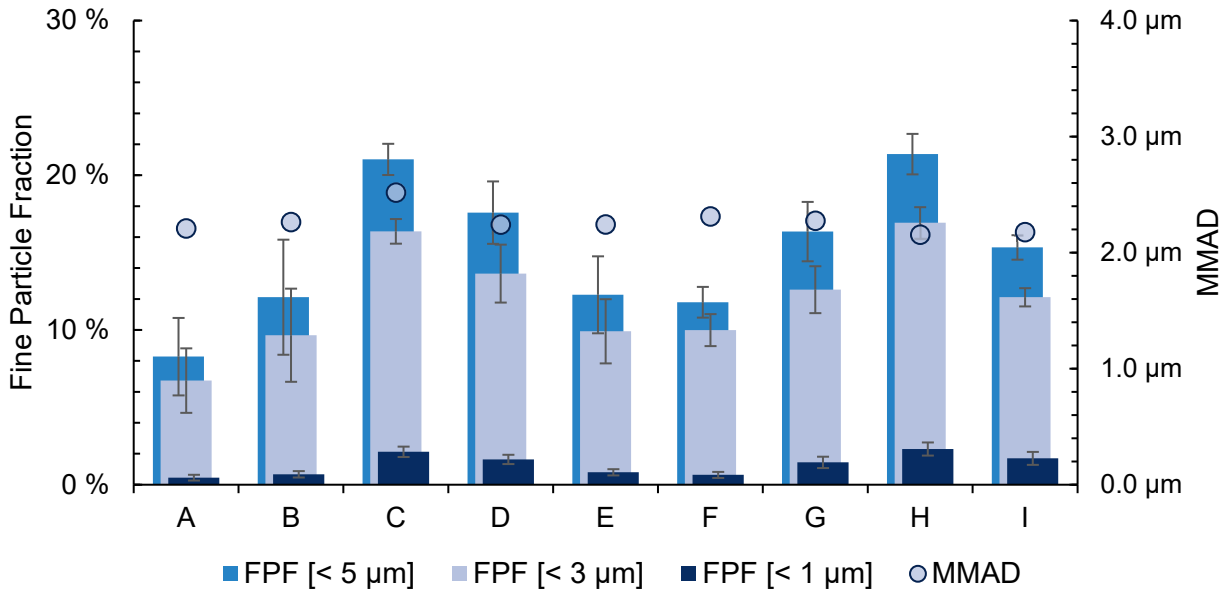

Figure 3.25: FPF and MMAD values of interactive blends composed of IL120 and SBS (n = 3, error bars = SD). The labelling of the values corresponds to Figure 3.23 and Table 3.5.

Figure 3.26 shows the MD, DD and DR values for interactive blends composed of IL251 and SBS. Similar to the results for the blends based on IL120 (Figure 3.24), the MD values matched the corresponding capsule fillings and drug concentrations. Based on the DD values of each sample, the DR values ranged between 19.8 % (E) and 30.1 % (C). This range is slightly higher compared to the blends based on IL251.

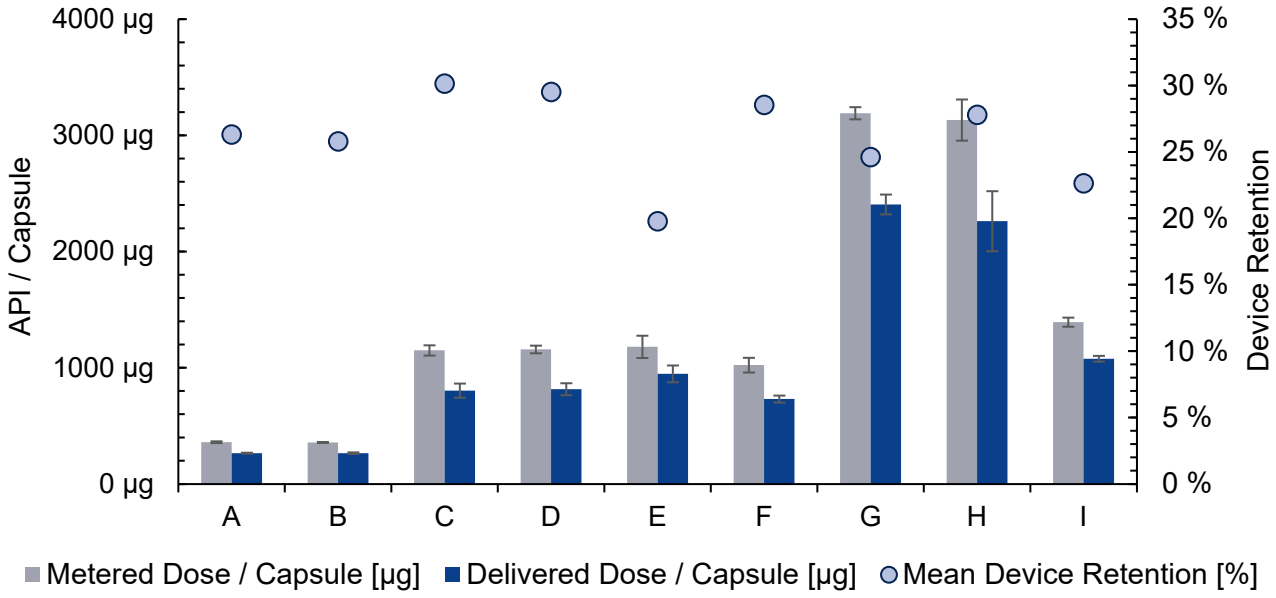

Figure 3.26: MD, DD and DR for interactive blends composed of IL251 and SBS (n = 3, error bars = SD). The labelling of the values corresponds to Figure 3.23 and Table 3.5.

Figure 3.27 shows the comparative measures for the blends containing IL251 an SBS. With an average of 2.29 µm, these blends had almost identical MMAD values compared to IL120 (Figure 3.25). Among all, sample F had the lowest FPF < 5 µm (19.9 % ± 4.75 %) and FPF < 3 µm (15.8 % ± 3.99 %) and sample B showed the lowest FPF < 1 µm

(1.58 % ± 0.08 %). In contrast, sample C showed the highest FPF < 5 µm (40.3 % ± 2.15 %), FPF < 3 µm (33.7 % ± 2.05 %) and FPF < 1 µm (4.95 % ± 0.89 %).

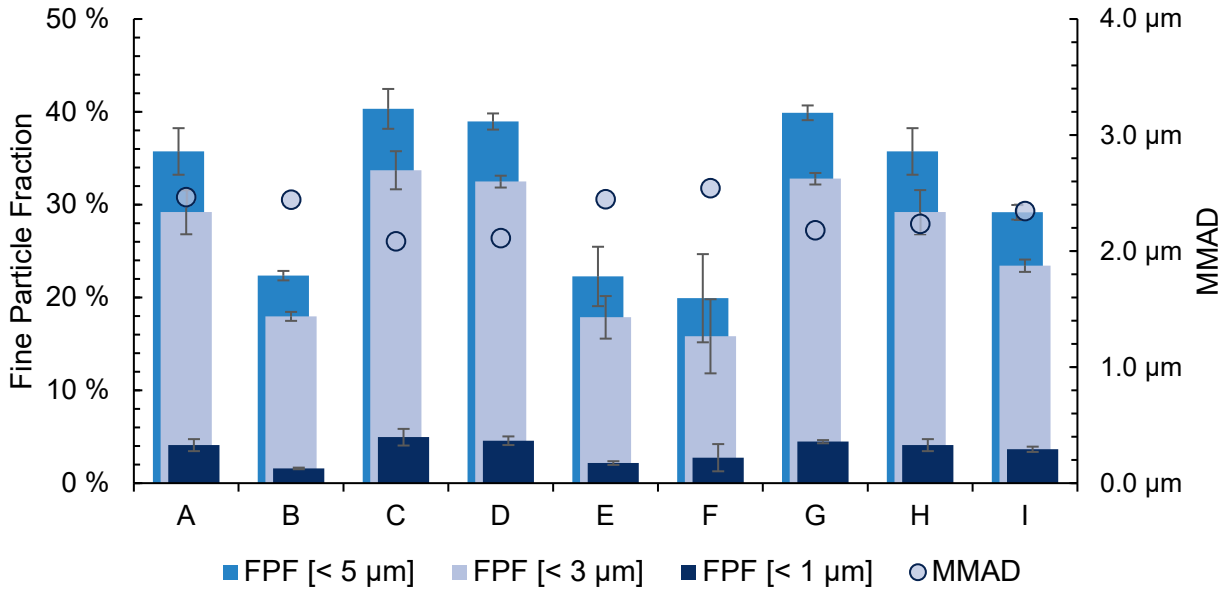

Figure 3.27: FPF and MMAD values of interactive blends composed of IL251 and SBS (n = 3, error bars = SD). The labelling of the values corresponds to Figure 3.23 and Table 3.5.

Similar to results of the IL120-based blends, the aerodynamic performance primarily correlated with the SBS content of the respective blend, except for sample A, which showed comparatively high FPF values. Moreover, neither the capsule filling nor the number of inserted DAs remarkably effected the FPF values.

A comparison of the APSD assessments of SBS blends shows that the use of IL120 as carrier material resulted in lower aerodynamic performance than using IL251 (Figure 3.28). Furthermore, the data faintly suggest that the higher the drug content, the higher the FPF values. Neither the capsule filling nor the number of inserted DAs influenced the aerodynamic performance of the SBS-containing formulations.

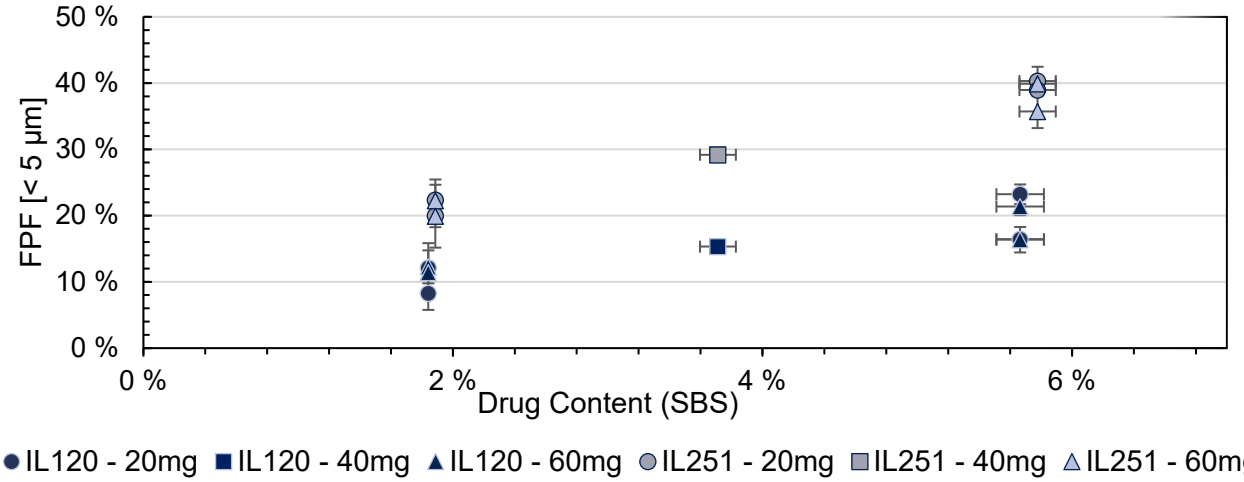

Figure 3.28: Summary of FPF < 5 µm values plotted against the actual SBS content in the interactive blends based on IL120 (dark labelled) and Il251 (light labelled).

For interactive blends composed of IL120 and BUD, Figure 3.29 presents the corresponding MD, DD and DR values. Similar to the results for the blends containing SBS (Figure 3.24), the MD values matched the corresponding capsule fillings and drug concentrations. The calculated DR values were between 11.8 % (F) and 20.4 % (C).

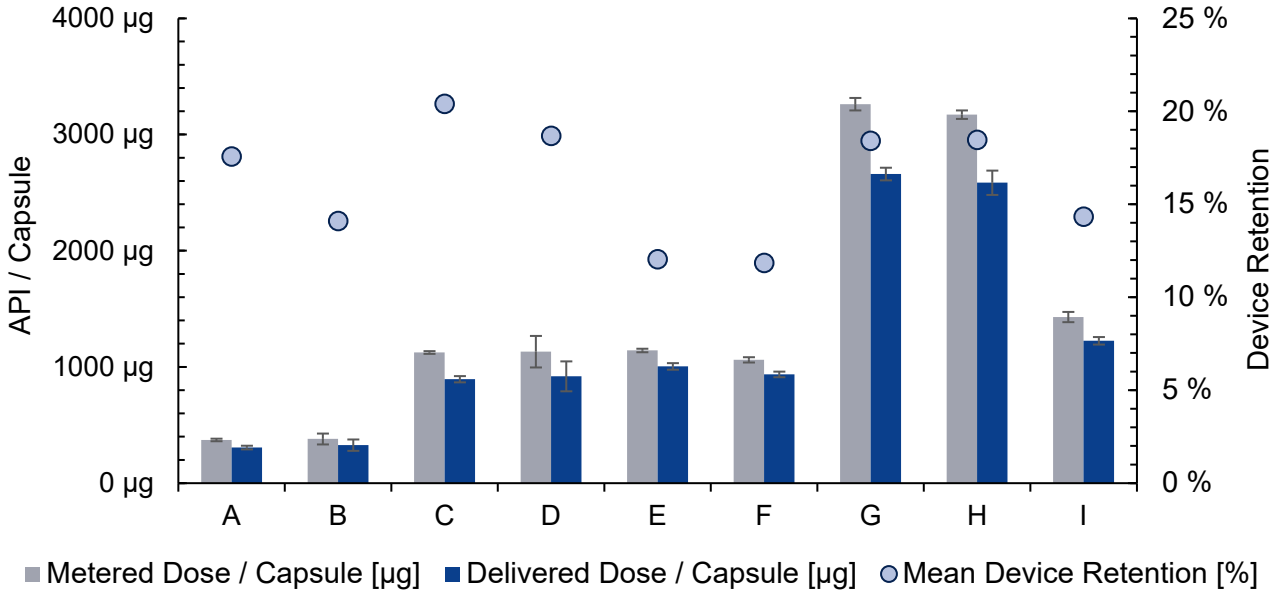

Figure 3.29: MD, DD and DR for interactive blends composed of IL120 and BUD (n = 3, error bars = SD). The labelling of the values corresponds to Figure 3.23 and Table 3.5.

Figure 3.30 summarises the aerodynamic characteristics of the samples based on IL120 and BUD. Sample B had the lowest FPF < 5 µm (3.93 % ± 0.82 %), FPF < 3 µm (2.38 % ± 0.56 %) and FPF < 1 µm (0.20 % ± 0.04 %). In contrast, sample G showed the highest FPF < 5 µm (12.9 % ± 1.87 %) and FPF < 3 µm (9.46 % ± 2.03 %), whereas sample D had the highest FPF < 1 µm (1.01 % ± 0.19 %).

Strikingly, the samples with a drug content of 6 % (C, D, G, H) had on average higher FPF values than the 2 % samples (A, B, E, F). Reversely, the latter subgroup of the sample set showed higher MMAD values (3.36 µm ± 0.09 µm) than the 6 % samples (2.48 µm ± 0.07 µm). Concluding this sample set based on IL120, the aerodynamic performance primarily correlated with the BUD content of the respective blend.

On closer inspection of the samples, the increase in FPF is reverse to the corresponding DR (Figure 3.29). In contrast, neither the capsule filling nor the number of inserted DAs remarkably effected the FPF values.

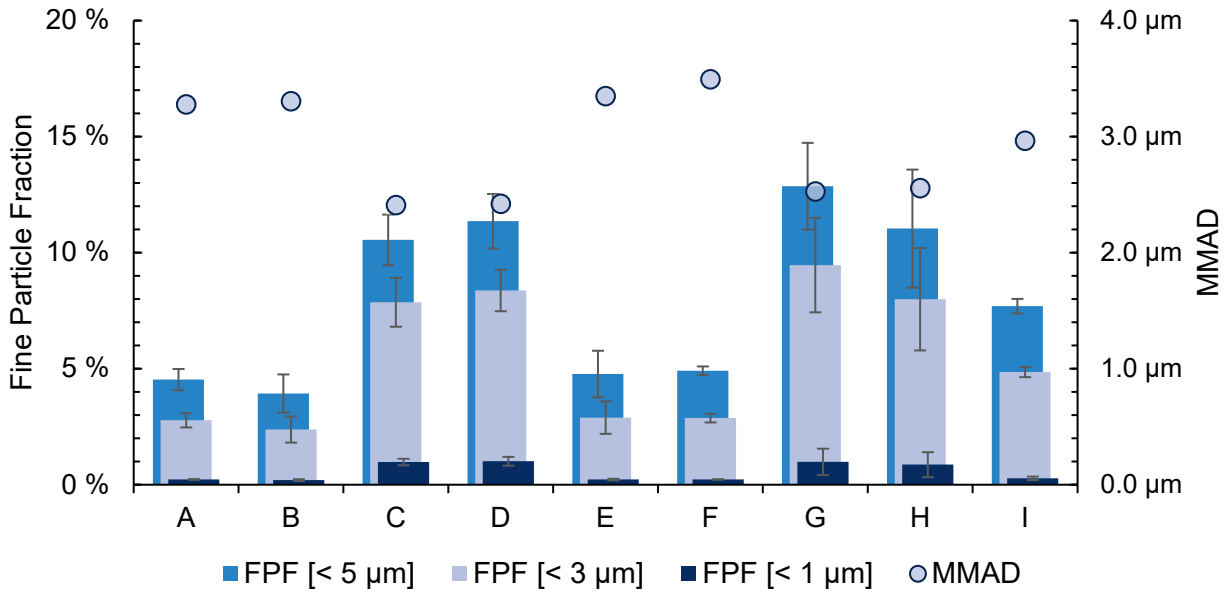

Figure 3.30: FPF and MMAD values of interactive blends composed of IL120 and BUD (n = 3, error bars = SD). The labelling of the values corresponds to Figure 3.23 and Table 3.5.

Figure 3.31 shows the MD, DD and DR values for interactive blends consisting of IL251 and BUD. Similar to the results for the previous interactive blends, the MD values of each sample corresponded to the respective capsule filling and drug concentrations. Based on the DD values of each sample, the DR values ranged between 26.6 % (A) and 30.6 % (E). For the BUD-containing formulations, comparing the use of IL120 and IL251 (Figure 3.29), a reduction in carrier particle size led to an increase in DR.

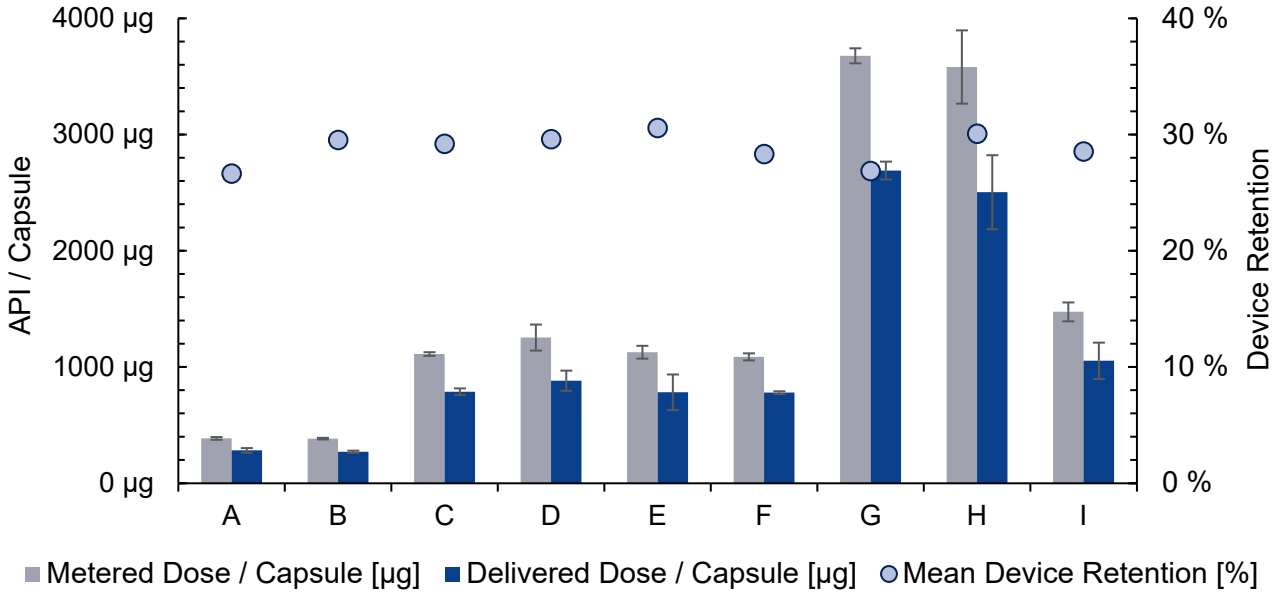

Figure 3.31: MD, DD and DR for interactive blends composed of IL251 and BUD (n = 3, error bars = SD). The labelling of the values corresponds to Figure 3.23 and Table 3.5.

Figure 3.32 shows the comparative measures for the blends containing IL251 an BUD. Sample C had the highest FPF < 5 µm (23.3 % ± 2.64 %), FPF < 3 µm (18.1 % ± 2.24 %) and FPF < 1 µm (2.68 % ± 0.75 %). The lowest FPF < 5 µm (11.4 % ± 2.55 %) and

FPF < 3 µm (7.89 % ± 1.93 %) were found for sample E, whereas sample F showed the lowest FPF < 1 µm (0.76 % ± 0.05 %). On average, the sample set had an MMAD of 3.29 µm.

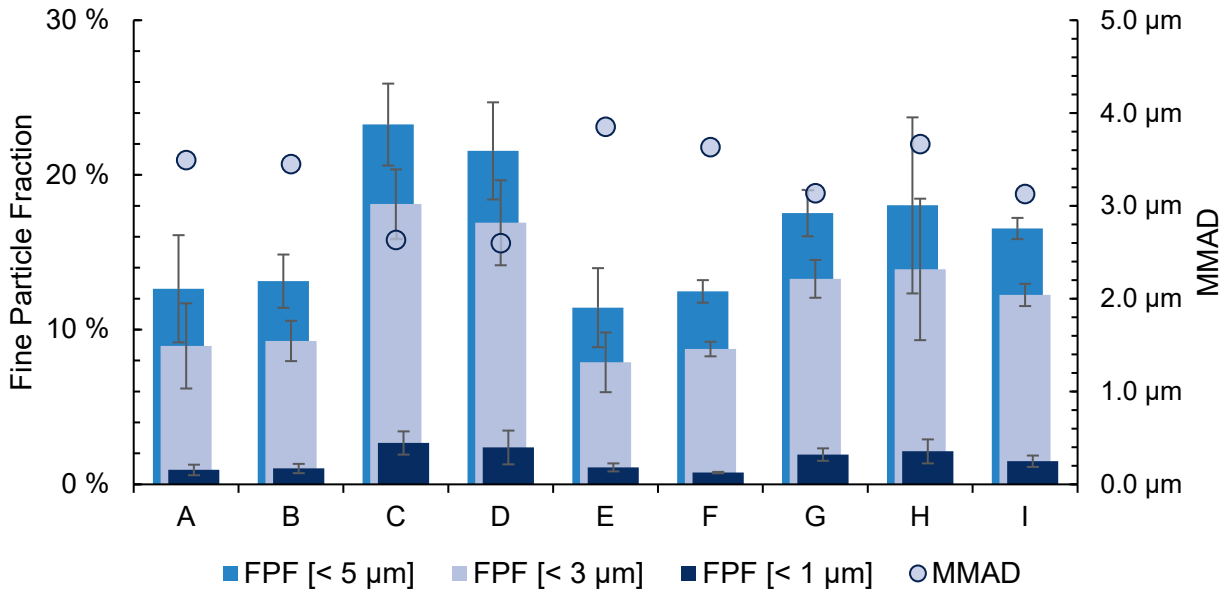

Figure 3.32: FPF and MMAD values of interactive blends composed of IL251 and BUD (n = 3, error bars = SD). The labelling of the values corresponds to Figure 3.23 and Table 3.5.

Figure 3.33 shows the actual BUD content plotted against the FPF < 5 µm values of each sample. As a concluding comparison of the APSD assessments of BUD blends, the use of IL120 resulted in lower aerodynamic performance than using IL251. In addition, the data suggest that the higher the drug content, the higher the FPF values. For IL251 blends with high drug content, low capsule filling was found to be slightly superior compared to high infills.

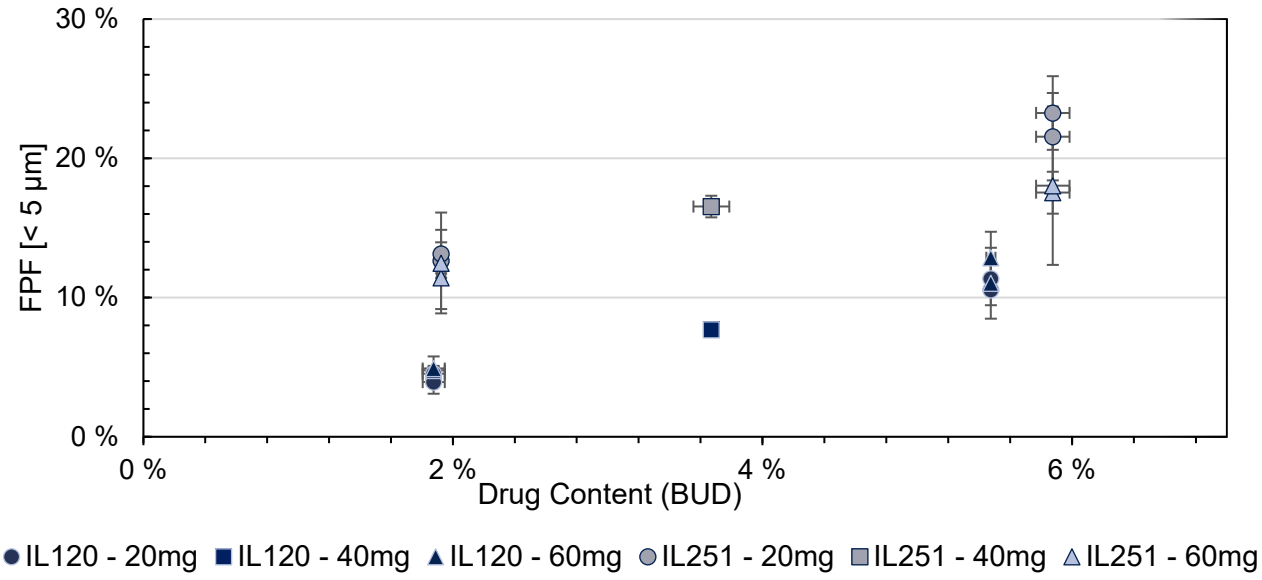

Figure 3.33: Summary of FPF < 5 µm values plotted against the actual BUD content in the interactive blends based on IL120 (dark labelled) and Il251 (light labelled).

This chapter has covered the investigation of carrier materials (1), API properties (2), drug contents (3), capsule filling (4), and number of DAs (5). As shown in Table 3.6, the findings allowed for numerous conclusions.

First, interactive powder blends with BUD and IL251 showed higher mean DR (Ø = 28.82%) compared to IL120 blends (Ø = 16.21%) across all concentrations. This effect was similarly evident for samples containing SBS for which the mean DR increased on average from IL120 (Ø = 19.25%) to IL251 (Ø = 26.13%).

Second, in the Twister® device, interactive powder blends composed of IL251 generally showed higher FPF values (< 5 µm, < 3 µm and < 1 µm) compared to IL120. This observation applied to both SBS and BUD. Comparing the same type of carrier material, the FPF values of these two APIs differed from each other. Despite identical assessment conditions such as capsule filling, number of DAs and drug content, the comparative measures of SBS showed higher values than the corresponding FPF values of BUD. As an additional finding for both APIs, the FPF values of IL120 were lower than IL251, even though a higher mass of the latter blend retained in the device (higher DR).

Third, throughout the APIs and carrier materials, the studies revealed evidence that the higher the drug content, the higher the FPF values.

Fourth, the influence of capsule filling on the aerodynamic performance was found to be carrier dependent for blends with high BUD content only. Thereby, low capsule filling was found to be slightly superior compared to high infills.

Fifth, the MMAD of SBS was lower than that of BUD, even though the PSDs of the APIs were similar. This finding could be related to the differences in particle shape or surface energies, which could result in a varying tendency to cohesion and agglomeration.

Lastly, the influence of inserting DAs into the inhaler on the aerodynamic performance remained unclear. The number of DAs were found to have no substantial effect on neither the DR nor the aerodynamic performance.

Table 3.6: Overview on preliminary results: Did the investigated attribute influence the aerodynamic performance (c.d. = carrier dependent)?

Attribute	API	DR	FPF < 5 µm	FPF < 3 µm	FPF < 1 µm	MMAD
Carrier material	**SBS**	yes	yes	yes	yes	no
	BUD					
Drug content	**SBS**	c.d.	yes	yes	yes	no
	BUD	c.d.				yes

Attribute	API	DR	FPF < 5 µm	FPF < 3 µm	FPF < 1 µm	MMAD
Capsule filling	**SBS**	no	no	no	no	no
	BUD		c.d.	c.d.		
Number of DAs	**SBS**	no	no	no	no	no
	BUD					

Build on the previous findings, this work considered the influence of the DA morphology (6) on the aerodynamic performance of interactive blends.

To study this effect, various DA morphologies in the required size range with appropriate resolution and quality were manufactured. Purchased from the company Nanoscribe GmbH & Co. KG (Germany), the DAs were fabricated using TPP (section 3.4.2.3). As shown in Figure 3.34, each of the tested DAs had a diameter of 3 mm. Despite the same size, the geometries had different volumes and surface areas due to their morphological differences (Table 3.7). The geometry SB had the largest calculated surface area and the highest volume, whereas the RK had the lowest values in each case.

Table 3.7: Surface area and volume of the studied DAs with a diameter of 3 mm.

Morphology	PC	RK	SB
Surface area	26.8 mm²	21.6 mm²	27.8 mm²
Volume	9.91 mm³	2.27 mm³	11.2 mm³

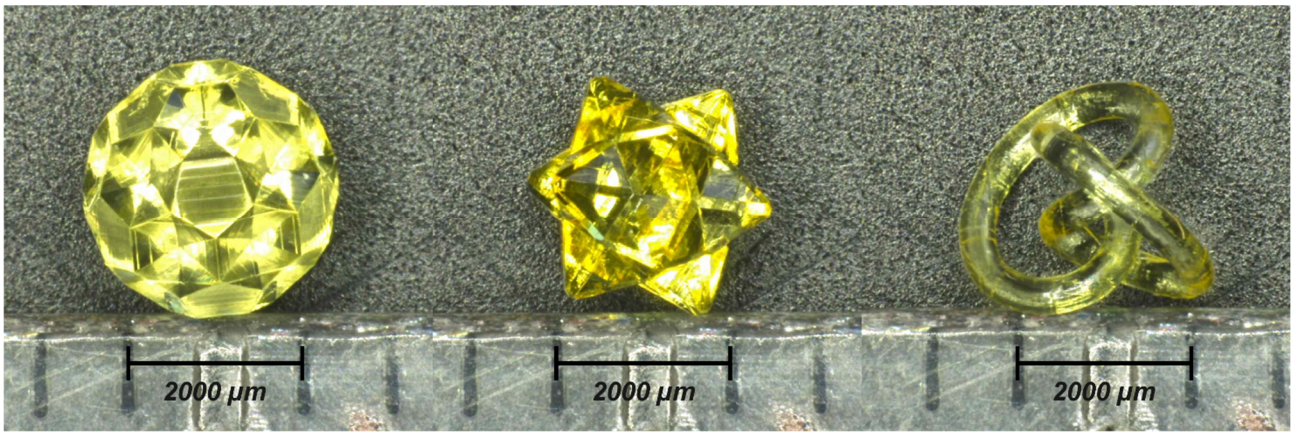

Figure 3.34: Representative image of the geometries SB, PC and RK (from left to right) made by TPP printing.

In the following aerodynamic assessments, each sample corresponds to a capsule filled with 60 mg of the respective blend, each containing 6 % SBS or BUD, respectively. The blends were tested either inserting no DA (w/o DA) or inserting an PC, RK or SB.

Figure 3.35 shows the MD, DD and DR values of the samples consisting of SBS blended with IL120 or IL251. The DR values ranged between 19.2 % (IL251 SBS w/o) and 24.7 % (IL251 SBS RK). These values indicate no significant deviation among each other.

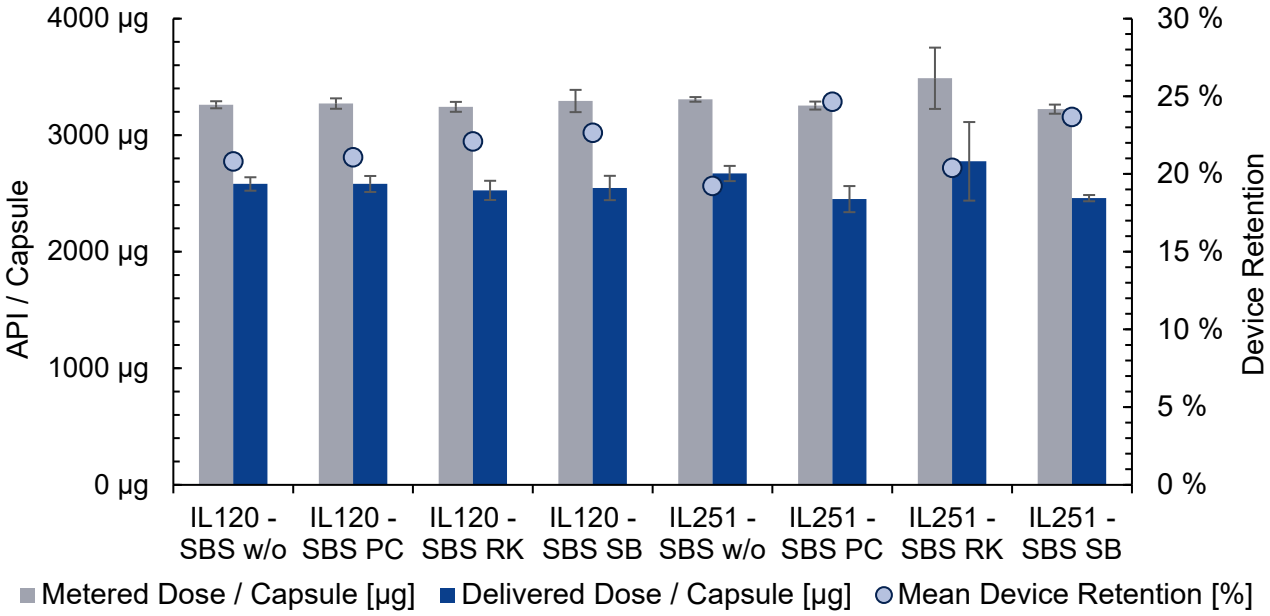

Figure 3.35: MD, DD and DR for SBS-containing interactive blends with no DA (w/o DA), PC, RK or SB been inserted into the inhaler device (n = 3, error bars = SD).

Figure 3.36 shows the FPF and MMAD values of the blends that contained SBS (see also Appendix B). For IL120, the FPF values ranged from 17.9 % ± 3.28 % to 21.4 % ± 3.39 % (FPF < 5 µm), from 14.1 % ± 2.88 % to 17.4 % ± 3.20 % (FPF < 3 µm) and from 1.87 % ± 0.69 % to 2.46 % ± 0.69 % (FPF < 1 µm), respectively. For IL251, the FPF values ranged from 36.7 % ± 1.39 % to 38.9 % ± 1.12 % (FPF < 5 µm), from 29.9 % ± 1.08 % to 32.0 % ± 1.13 % (FPF < 3 µm) and from 2.31 % ± 0.85 % to 4.97 % ± 2.24 % (FPF < 1 µm), respectively. On average, the sample set had an MMAD of 2.18 µm, with no substantial differences found between the different carrier materials.

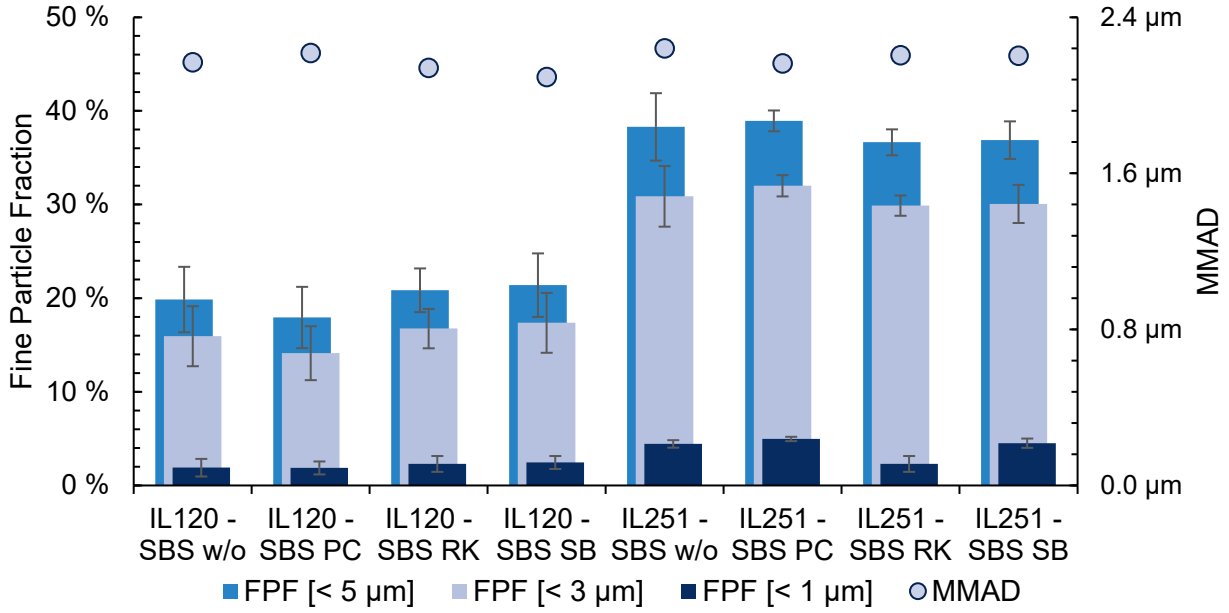

Figure 3.36: FPF and MMAD values of SBS-containing interactive blends with no DA (w/o DA), PC, RK or SB been inserted into the inhaler device (n = 3, error bars = SD).

Figure 3.37 shows the MD, DD and DR values of the samples consisting of BUD blended with IL120 or IL251. The DR values ranged between 14.7 % and 18.5 % for IL120 and from 22.3 % to 28.7 % for IL251. These values indicate no significant deviation caused by inserting a DA into the device. Instead, as the preceding data indicated (Table 3.6), the carrier material influenced the DR.

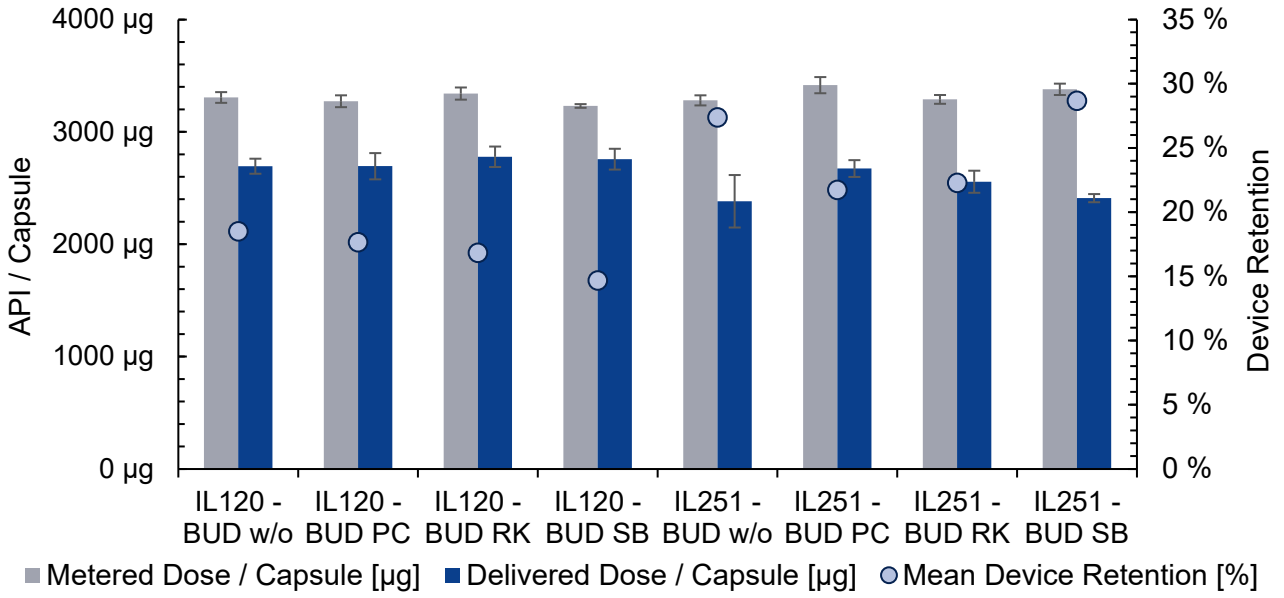

Figure 3.37: MD, DD and DR for BUD-containing interactive blends with no DA (w/o DA), PC, RK or SB been inserted into the inhaler device (n = 3, error bars = SD).

Figure 3.38 shows the FPF and MMAD values of the blends that contained BUD (Appendix B). For IL120, the FPF values ranged from 10.7 % ± 1.23 % to 13.2 % ± 1.34 % (FPF < 5 µm), from 7.43 % ± 1.17 % to 9.54 % ± 1.21 % (FPF < 3 µm) and from 0.75 % ± 0.38 % to 1.42 %± 0.15 % (FPF < 1 µm), respectively.

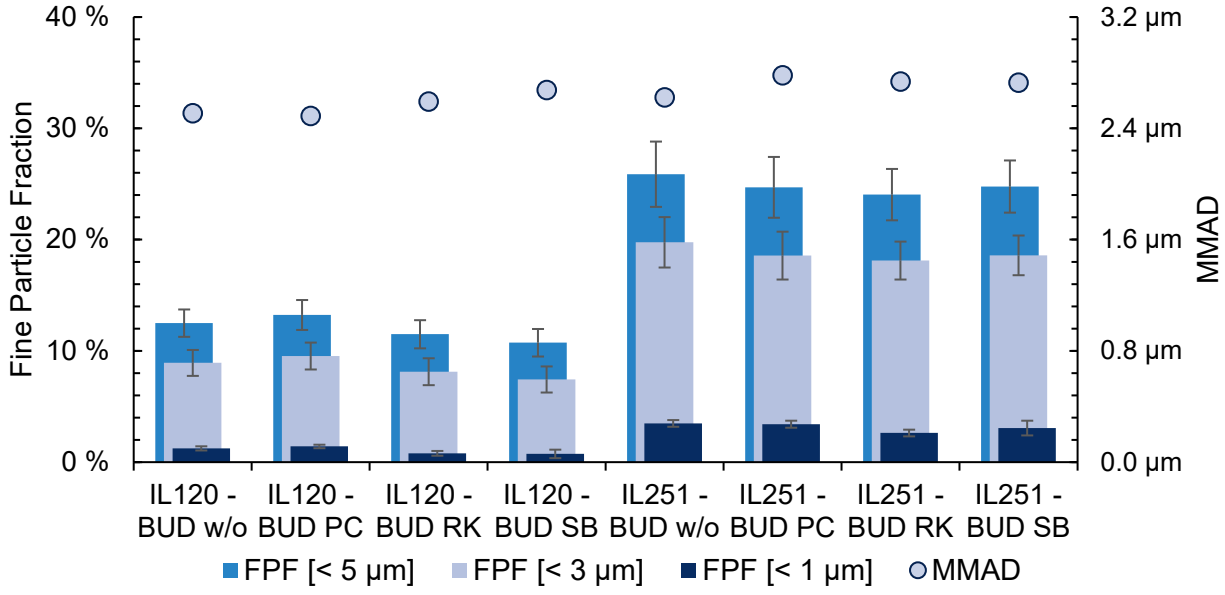

Figure 3.38: FPF and MMAD values of BUD-containing interactive blends with no DA (w/o DA), PC, RK or SB been inserted into the inhaler device (n = 3, error bars = SD).

For IL251, the FPF values ranged from 24.0 % ± 2.31 % to 29.3 % ± 1.98 % (FPF < 5 µm), from 18.1 % ± 1.70 % to 19.8 % ± 2.27 % (FPF < 3 µm) and from 2.63 % ± 0.30 % to 3.49 % ± 0.30 % (FPF < 1 µm), respectively.

For both carriers, the sample set had on average an MMAD of 2.64 µm. For both APIs, the use of IL251 resulted in higher aerodynamic performance compared to IL120. In general, comparatively low FPF values were found for BUD, despite lower API retention in the Twister®. Consequently, the MMAD of BUD was higher than that of SBS.

The data derived from assessing the analysed blends showed no significant influence of the insertion of any given DA into the inhaler device on the aerodynamic performance. The values for FPF < 5 µm and FPF < 3 µm were not substantially different among the samples with and without DA. On closer analysis of the blends with IL251, the FPF < 1 µm was lowest in the case of inserting the RK. This finding was evident for both APIs. Referring to Chapter 1, the difference of FPF < 5 µm and FPF < 1 µm is of particular interest because predominantly particles with the corresponding aerodynamic diameter deposit in the respiratory tract. Therefore, the data could indicate a beneficial effect when inserting a RK to an IL251-based blend.

For interactive blends, the use of DAs in a Twister® device
caused no substantial effect on aerodynamic performance
The performance of such DPI formulations
depended primarily on the choice of carrier material and the drug content.
A comprehensive discussion of the results of this section follows at the end of this chapter.

3.6.2 Dispersing aids in softpellet formulations

As described in Chapter 1.7.2, controlled agglomeration of micronised powder particles allows for formulating softpellets. Softpellet agglomerates as such are not inhalable as their size generally exceeds 5 µm in diameter, causing impaction in the upper airways (Chapter 1.2). Therefore, effective redispersion and aerosolisation of this formulation is a prerequisite for effective drug delivery to the lungs. To support softpellet dispersion in the inhaler device during inhalation, inserting DAs is a promising approach.

This section focusses on identifying the effects of DAs being inserted into an inhaler device on dispersion of softpellet formulations. Therefore, the following study considered the influence of:

- API properties (1) and
- morphology of DAs (2)

on the aerodynamic performance of softpellet formulations. Specifically, these investigations allowed for determining the influence of morphological features of an DA.

The following data and results have partly been collected within the a master project of Iwersen in 2022 [142]. Her work comprises detailed information on the preparation, the characterisation, and the assessment of different softpellet formulations. Furthermore, this master thesis addresses the influence of storage conditions on powder properties and thus on the resulting aerodynamic performance with and without using DAs.

3.6.2.1 Characterisation of the softpellet formulations

As described in section 3.4.1, the preparation of softpellets involves was a two-step procedure. First, the APIs, namely ISN and RIF (section 3.3.2), were milled with a jet mill. Second, the milled API particles formed spherical agglomerates due to a vibration process. To assess whether the used API materials had the desired particle size, HELOS® measurements (Chapter 2.3.1.4) of the micronised powder followed the initial milling process. For both APIs, the milling process provided the desired PSD with a target of an x_{90} less than 5 µm. Displayed in Table 3.8, the freshly micronised ISN had an x_{90} of 4.83 µm ± 0.03 µm and the x_{90} of RIF was 3.18 µm ± 0.01 µm after milling.

Table 3.8: Particle size distribution of freshly milled ISN and RIF particles; n=3.

API	x_{10}	x_{50}	x_{90}	Span
Isoniazid	0.48 µm ± 0.02 µm	1.99 µm ± 0.04 µm	4.83 µm ± 0.03 µm	2.19
Rifampicin	0.37 µm ± 0.02 µm	1.28 µm ± 0.00 µm	3.18 µm ± 0.01 µm	2.20

Figure 3.39 and Figure 3.40 show the appearance of the final softpellet agglomerates consisting of micronised ISN and RIF particles, respectively. Comparing the agglomerates visually, the RIF softpellets featured higher sphericity and a relatively smooth surface. In contrast, the ISN softpellets had a consistently frayed texture. Despite the morphological differences, the particle sizes were similar as the digital microscopy images indicated (Figure 3.39).

Figure 3.39: Softpellets consisting of ISN (left) and RIF (right), respectively. Images captured using digital microscopy with a magnification of 175x (adopted from Iwersen [142]).

SEM imaging provided detailed insights into particle shape and particulate arrangement of the softpellets. Imaging of softpellet formulations underwent the same procedure as mentioned in Chapter 2.3.1.1, except that the particles were applied on conductive carbon cement (Plano GmbH, Germany) instead of carbon sticker. As displayed in Figure 3.40, the primary particles featured different morphologies, with ISN having a comparably roundish shape. Moreover, the softpellets consisting of pure RIF show relatively dense packing compared to the ISN softpellets.

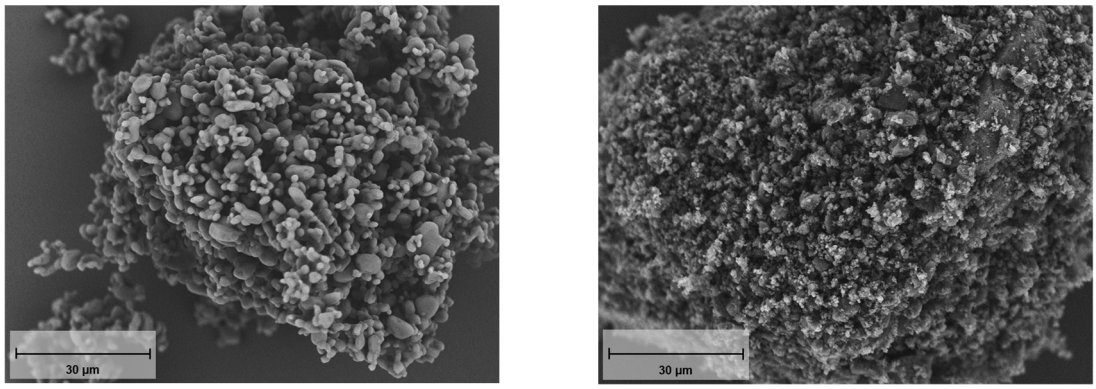

Figure 3.40: SEM images with a magnification of 2500x showing softpellets consisting of ISN (left) and RIF (right), respectively.

Iwersen could show that environmental conditions influence particle characteristics, especially of micronised ISN. The provided data demonstrated that the particle size increases with increasing humidity due to particle merging. Changes in particle properties caused by environmental storage conditions could not be specified conducting dynamic

vapour sorption or differential scanning calorimetry analysis. In contrast, comparable humidity-related effects were not observed for RIF agglomerates.

3.6.2.2 Aerodynamic assessment of softpellet formulations

To study the effect of inserting DA into an inhaler on the aerodynamic performance of the DPI formulation, impaction analyses allowed for aerodynamic particle sizing of the previously described softpellets (Chapter 2.5.3). As a result of this aerodynamic particle sizing, the FPF and FPD values of API particles below 1, 3 and 5 µm aerodynamic diameter served as comparative measures. For the aerodynamic assessment, the softpellet formulations were filled into a capsule (5.0 mg each), which was then inserted into the Twister® device (section 3.6). Then, one of the TPP-printed DAs with a diameter of 3 mm was inserted into the inhaler prior to the capsule (Figure 3.34).

Figure 3.41 summarises the deposition profiles of softpellets composed of RIF comparing the results of using no DA and using the DAs described in section 3.3. The highest amount of API deposited in the device, followed by the preseparator. Similar quantities of API remained in the device regardless of whether or which DA was used. However, the deposition profile shifted towards stages with lower aerodynamic cut-offs depending on the used DA. Generally, this shift derived from a decrease in API quantity in the preseparator and, in turn, an increase particularly in stage 4 to stage 7.

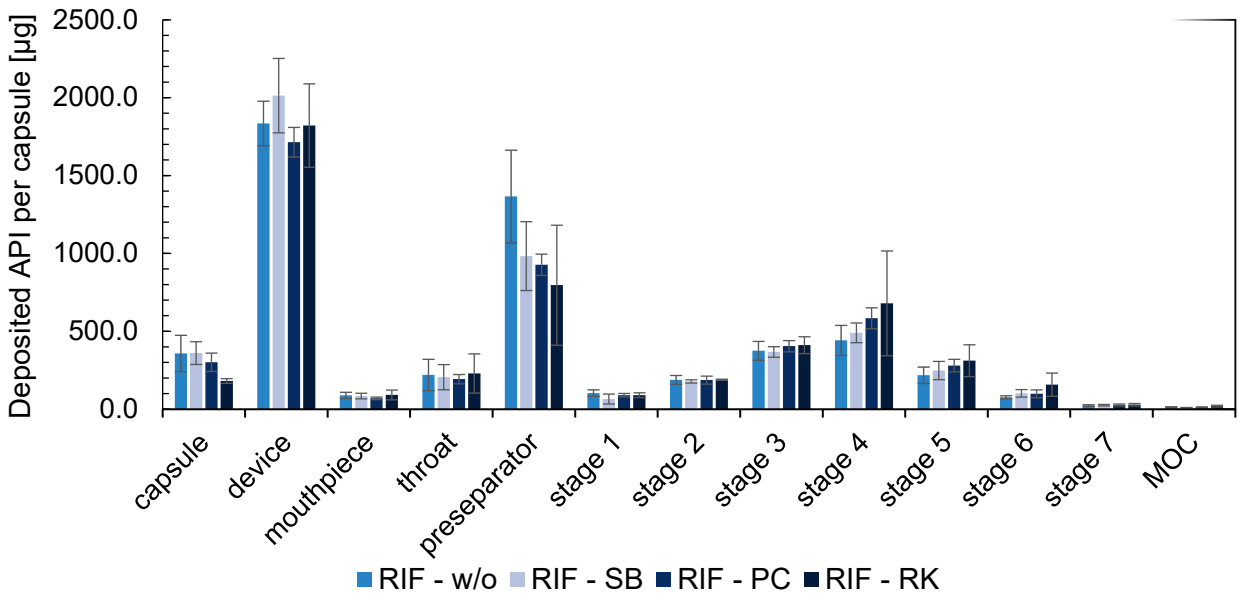

Figure 3.41: Aerodynamic particle size distribution of RIF-softpellets tested without DA (w/o), with Soccerball (SB), Pharmacone (PC) or Rollingknot (RK); n = 3, error bars = SD.

The data displayed in Figure 3.42 indicated that the MDs corresponded to the capsule infills, providing comparability of the results. Calculated from the aerodynamic particle sizing data and the MD, the DD and DR values showed no significant difference between the

samples. Overall, 41 to 48 % of the DPI formulation retained in the device independent on whether an DA was inserted or not. This indicated that the insertion had no effect on the DD. The data shown in Figure 3.41, however, indicated that the DA influenced the dispersion and thus the impaction of particles between preseparator and MOC.

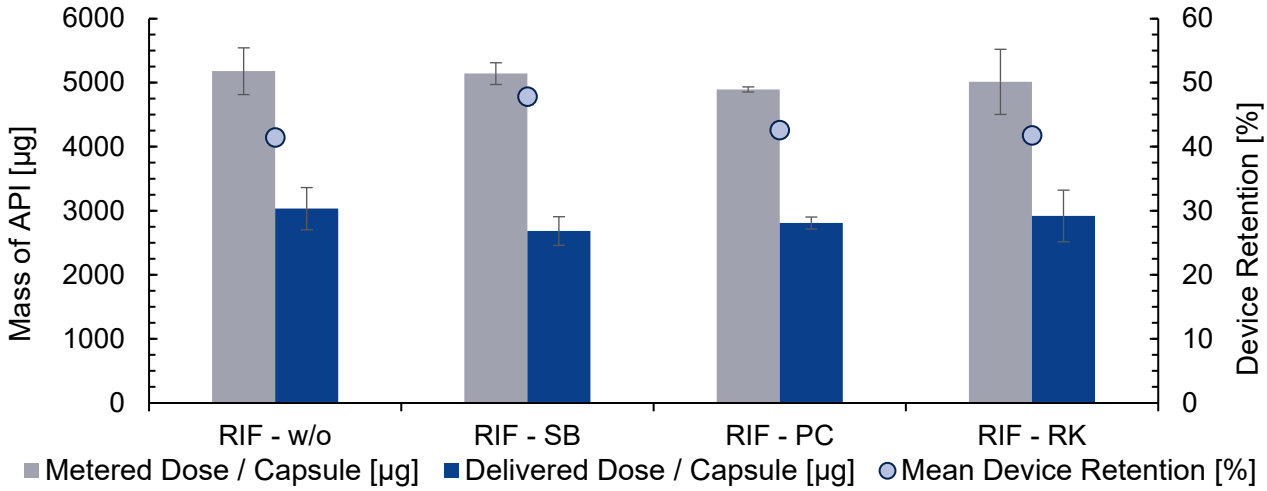

Figure 3.42: Comparison of Metered Dose, Delivered Dose and Device Retention of RIF-softpellets tested without DA (w/o), with Soccerball (SB), Pharmacone (PC) or Rollingknot (RK); n = 3, error bars = SD.

Resulting from the aerodynamic particle sizing, Figure 3.43 shows the FPF values for each sample (Appendix B). The sample without using a DA resulted in an FPF < 5 µm of 38.90 % ± 3.89 %, an FPF < 3 µm of 26.15 % ± 2.99 % and an FPF < 1 µm of 4.14 % ± 0.31 %. Generally, the use of DAs caused an increase in these values with the RK having the greatest effect on the FPF (< 5 µm: 55.88 % ± 14.47 %; < 3 µm: 41.34 % ± 13.66 %; < 1 µm: 7.31 % ± 1.97 %). Although the smallest effect, even the use of the SB led to an increase in FPF (< 5 µm: 47.79 % ± 5.54 %; < 3 µm: 33.56 % ± 4.83 %; < 1 µm: 5.57 % ± 1.10 %) compared to the sample without inserting a DA.

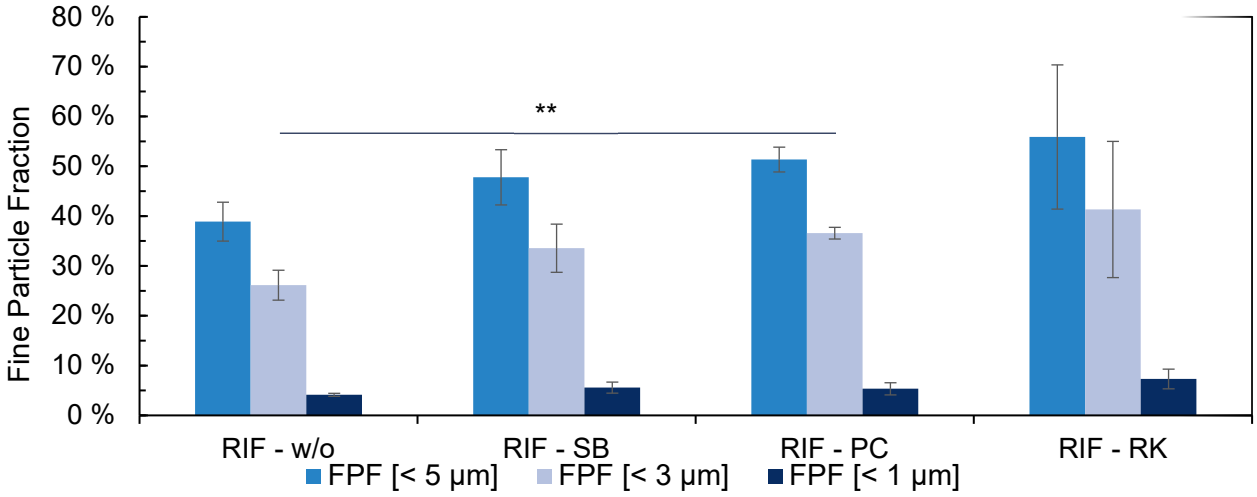

Figure 3.43: Comparison of FPF values of RIF-softpellets tested without DA (w/o), with Soccerball (SB), Pharmacone (PC) or Rollingknot (RK); n = 3, error bars = SD. Student's t-test: p = 0.006 (w/o – PC, FPF < 3 µm).

Comparing the values of the individual samples, the RK caused comparatively high standard deviations. Due to the high standard deviations and the small sample size, the statistical analysis only showed a significant difference between the FPF < 3 µm values of PC and w/o.

Inserting a DA into the Twister® device led to differences in FPD values. As shown in Figure 3.44 (see also Appendix B), the insertion provided on average comparably high FPD values, with SB having the lowest and RK having the greatest effect. The sample containing no DA resulted in an FPD < 5 µm of 1185 µg ± 221.7 µg, an FPD < 3 µm of 798.4 µg ± 165.7 µg and an FPD < 1 µm of 125.3 µg ± 15.65 µg. Inserting the SB into the device led to an FPD < 5 µm of 1282 µg ± 178.5 µg, an FPD < 3 µm of 900.8 µg ± 152.0 µg and an FPD < 1 µm of 149.4 µg ± 30.96 µg. The sample with adding an RK resulted in an FPD < 5 µm of 1645 µg ± 536.3 µg, an FPD < 3 µm of 1223 µg ± 485.5 µg and an FPD < 1 µm of 218.7 µg ± 83.16 µg.

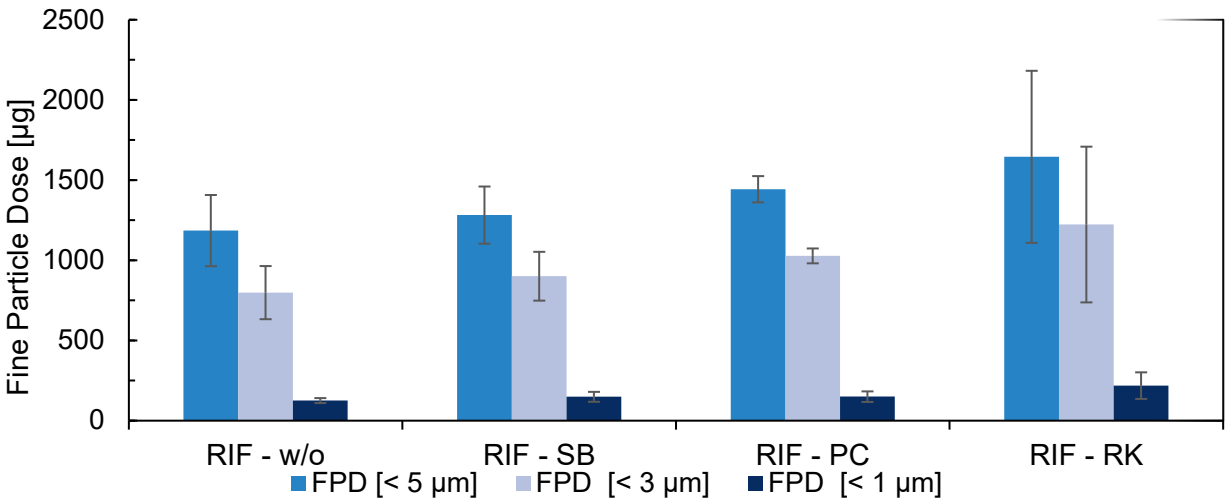

Figure 3.44: Comparison of FPD values of RIF-softpellets tested without DA (w/o), with Soccerball (SB), Pharmacone (PC) or Rollingknot (RK); n = 3, error bars = SD.

Determining the cumulative and density distributions also indicated an increase of the inhalable API fraction when inserting a DA (Figure 3.45). The distributions, which related to the DAs, shifted towards lower aerodynamic particle sizes. Accordingly, the MMAD of the RIF-softpellets decreased when inserting a DA (w/o: 2.79 µm ± 0.20 µm, PC: 2.55 µm ± 0.05 µm, RK: 2.49 µm ± 0.27 µm, SB: 2.56 µm ± 0.09 µm), indicating superior aerodynamic performance (Appendix B).

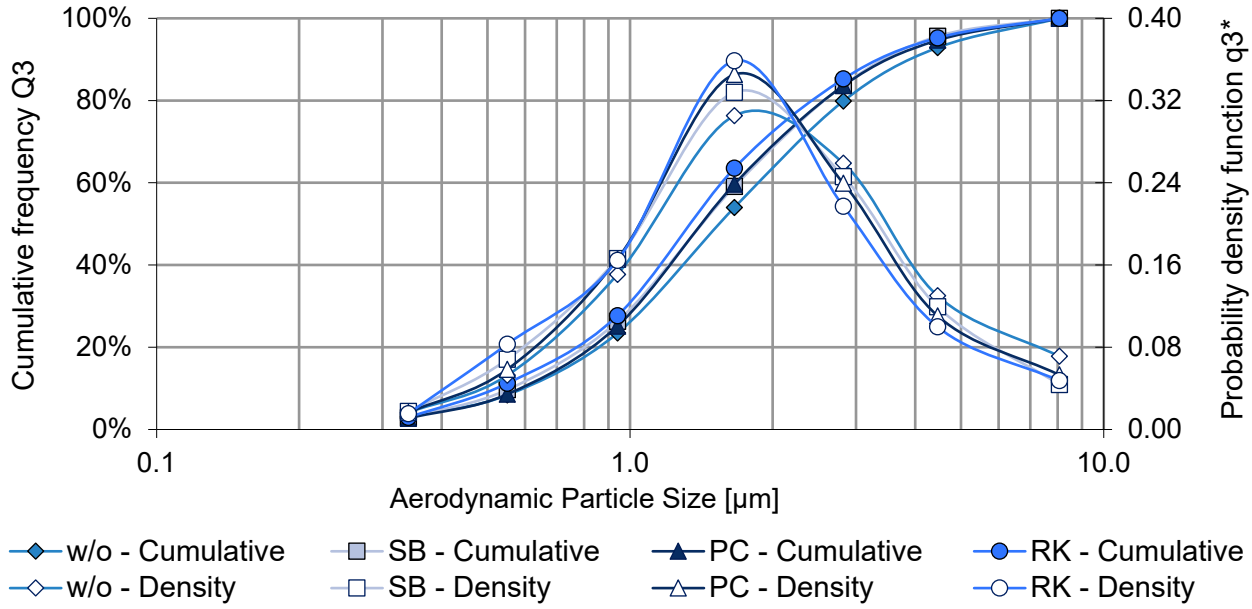

Figure 3.45: Cumulative frequency (left axis) and corresponding density distribution (right axis) of RIF-softpellets tested without DA (w/o), with SB, PC and RK.

Figure 3.46 summarises the aerodynamic particle sizing of softpellets composed of ISN comparing the results of using no DA and using the RK. In addition, the figure shows aerodynamic assessments of the softpellets stored at two different conditions (0 % and 12 %). The highest amount of API deposited in the preseparator, followed by the device. Regardless of the sample conditions and whether the RK was inserted, similar quantities of API remained in the preseparator and in the device, respectively. The deposition profile shifted towards stages with lower aerodynamic cut-offs when using the RK. This shift was due to an increase in API particularly in stage 2 to stage 4.

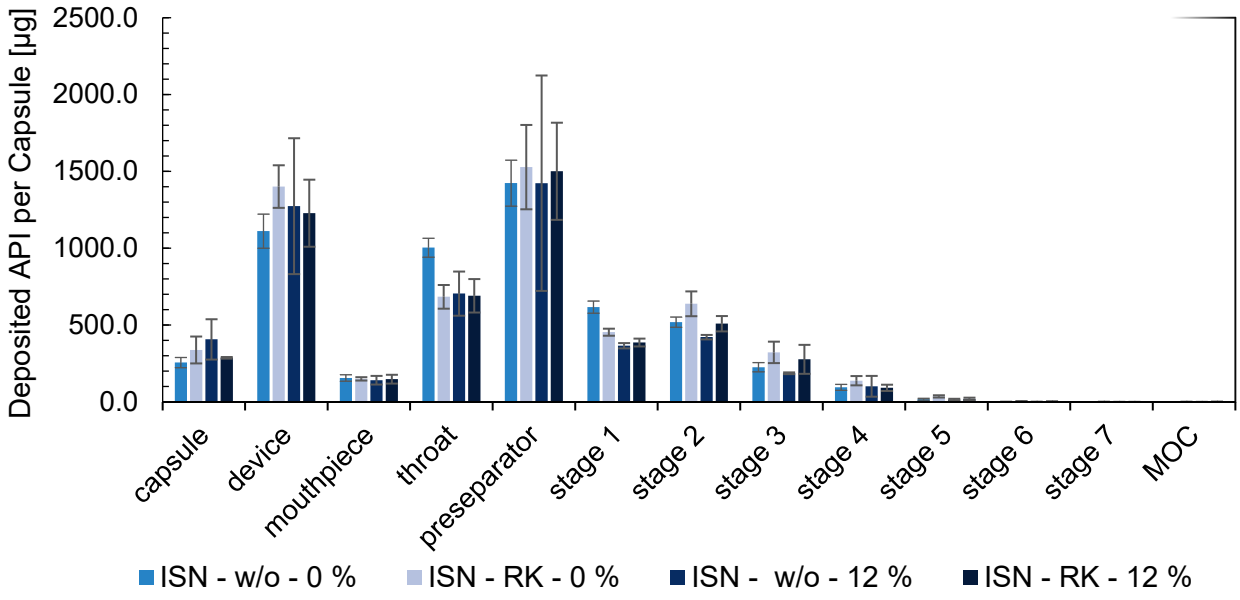

Figure 3.46: Deposition profiles of ISN-softpellets stored at 0 % and 12 % relative humidity, respectively (w/o = without DA; RK = Rollingknot); n = 3, error bars = SD.

The data shown in Figure 3.47 indicate that the MDs correspond to the previous capsule infills, providing comparability of the results. Calculated from the aerodynamic particle sizing data and the MD, the DD and DR values showed no significant difference between the samples. Overall, 28 to 35 % of the ISN-softpellets retained in the device independent on whether a DA was inserted or not. This indicated that the insertion had no effect on the DD. In contrast, the samples that were stored at 12 % rH showed comparably high standard deviation of the DD values.

Resulting from the aerodynamic particle sizing, Figure 3.48 shows the FPF < 5 µm and < 3 µm of each sample (Appendix B). No results were calculated for FPF < 1 µm because the quantities were below the limit of detection of the HPLC method. Testing the samples without using a DA resulted in an FPF < 5 µm of 10.1 % ± 1.60 % and an FPF < 3 µm of 3.12 % ± 0.70 % (0 % rH). In turn, the samples stored at 12 % rH resulted in FPF < 5 µm of 9.06 % ± 2.10 % and an FPF < 3 µm of 2.43 % ± 0.47 %. Inserting an RK resulted in an increase in FPF values for both storage conditions at 0 % rH (FPF < 5 µm: 15.1 % ± 3.10 %; FPF < 3 µm: 4.97 % ± 0.99 %) and 12 % rH (FPF < 5 µm: 12.9 % ± 2.86 %; FPF < 3 µm: 3.56 % ± 0.75 %).

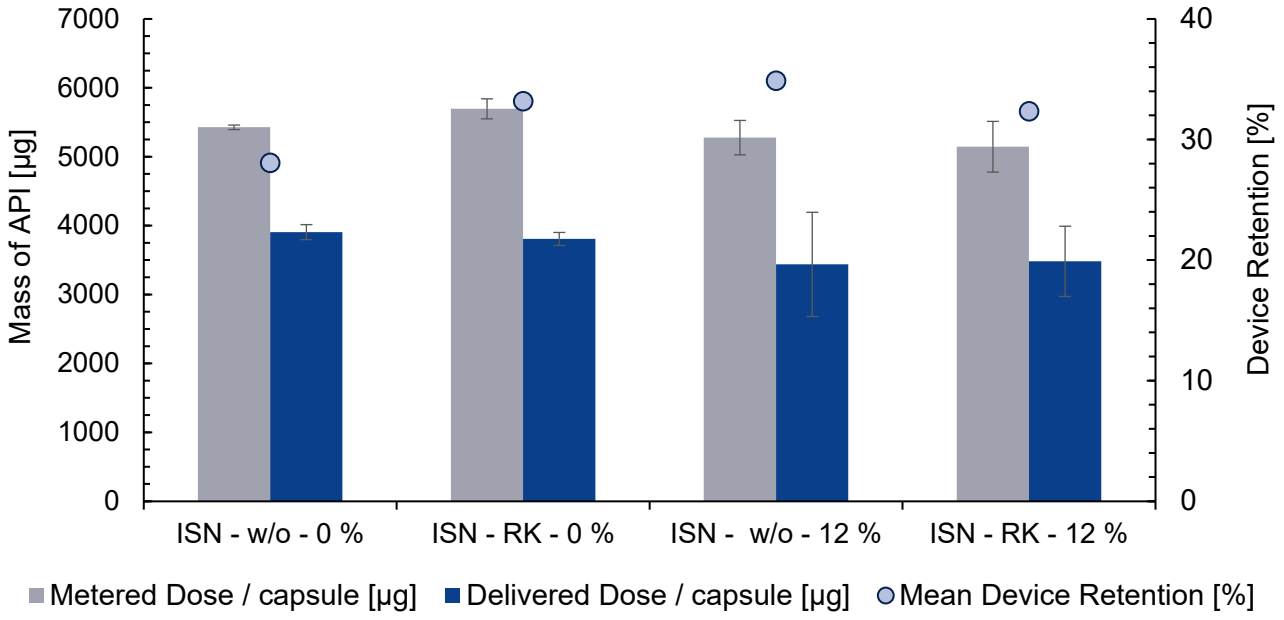

Figure 3.47: Comparison of Metered Dose, Delivered Dose and Device Retention of ISN-softpellets stored at 0 % and 12 % relative humidity, respectively (w/o = without DA; RK = Rollingknot); n = 3, error bars = SD).

Correspondingly, inserting a DA into the Twister® device led to differences in FPD (Appendix A) values. As shown in Figure 3.49, the insertion provided higher FPD values compared to the samples without inserting a DA. The FPD values of the latter samples decreased with increasing rH. Storage at 0 % rH led to an FPD < 5 µm of 393 µg ± 59.7 µg and an FPD < 3 µm of 121 µg ± 26.7 µg, whereby storage at 12 % rH resulted in an FPD

< 5 µm of 303 µg ± 40.0 µg and an FPD < 3 µm of 81.7 µg ± 2.20 µg. The samples, in which an RK was inserted, on the one hand resulted in an FPD < 5 µm of 573 µg ± 115 µg and an FPD < 3 µm of 189 µg ± 37.7 µg (0 % rH). For 12 % rH, aerodynamic assessment provided an FPD < 5 µm of 450 µg ± 132 µg and an FPD < 3 µm of 124 µg ± 32.4 µg.

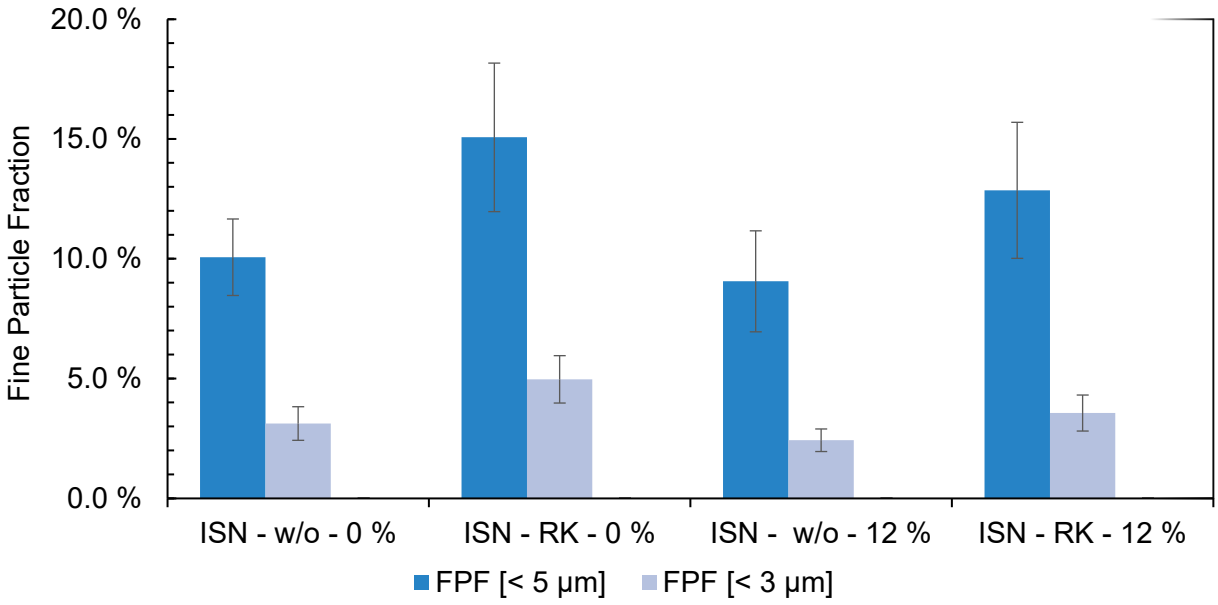

Figure 3.48: Comparison of FPF values of ISN-softpellets stored at 0 % and 12 % relative humidity, respectively (w/o = without DA; RK = Rollingknot); n = 3, error bars = SD).

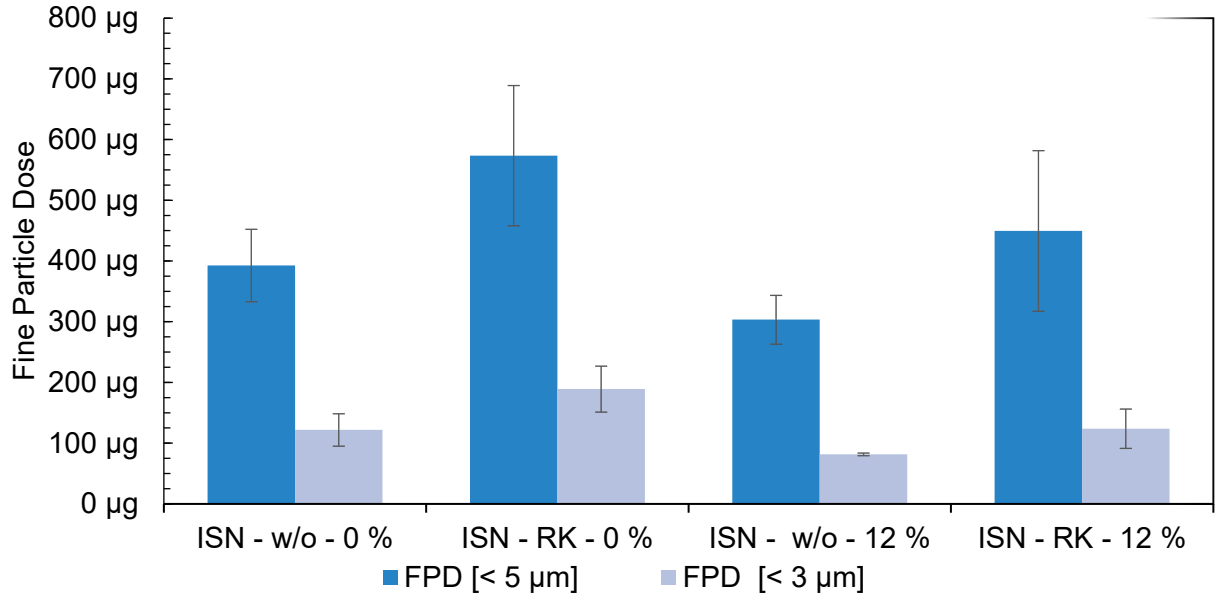

Figure 3.49: Comparison of FPD values of ISN-softpellets stored at 0 % and 12 % relative humidity, respectively (w/o = without DA; RK = Rollingknot); n = 3, error bars = SD

The aerodynamic performances of the ISN-softpellets were low compared to the samples composed of RIF-softpellets. For the ISN-softpellets, Iwersen measured that the particle size changed over time and that this change was dependent on the environmental conditions. Furthermore, Iwersen found evidence that the surfaces of the particles merged

forming chemical bonds and solid bridges. Forming of solid bonds decreased the softpellet dispersibility hampering the aerodynamic performance.

Results of APSD assessment principally change with the properties of the primary particles, such as size. In case of softpellet formulations, effective dispersion of the agglomerate correlates with aerodynamic particle size. Inserting a DA into the Twister® device led to enhanced dispersion of RIF-softpellets. The ISN-softpellets were principally susceptible to a DA, despite generally lower dispersibility. Reduced dispersibility potentially based on particle growth caused by environmental conditions.

Choice of the API and environmental conditions
affected the dispersion of softpellet formulations.
For such DPI formulations, complex geometries serving as DAs
enhanced the aerodynamic performance in a Twister® device.
The influence of the DA on particle dispersion
depended on the DA morphology.

3.7 Conclusion and discussion – Chapter 3

The focus of the studies in this chapter was on the assessment whether inserting free levitating objects with complex designs into a Twister® device would influence the dispersion of various DPI formulations. Two different DPI formulations were studied in this chapter, namely interactive blends and softpellets.

For studying the effect of DAs in interactive blends, two different carrier materials were processed with two different APIs. The carrier materials, namely IL120 and IL251, equalled in chemical composition but differed in PSD. In contrast, the micronised APIs, namely BUD and SBS, equalled in PSD but differed in particle shape and chemical properties.

Differences in the properties of the carrier and the API resulted in varying dispersibility in the Twister® device. In terms of FPF, FPD and MMAD values, IL251-based blends performed better than IL120-based formulations. Likewise, blends that contained SBS showed higher aerodynamic performance than those containing BUD.

A reason for the superior performance of IL251 could be the comparably low PSD and hence the presence of fines. As described in chapter 1.6, the addition of fines is well known to increase the FPF values. In addition, the IL251 carrier particles are less prone to impact on the inner surface of the device chamber compared to IL120 because of their differences in particle size and thus mass. However, the higher inertial forces of the IL120 particles do not indicate a corresponding favourable effect on deagglomeration as a potential result of particle-wall collisions.

Comparing BUD with SBS, the latter API shows a higher tendency to disperse, which could be explained by the differences in particle shape or chemistry. Accordingly, the APIs differ in their interaction with the carrier. These differences, in turn, could also explain the varying deagglomeration of the respective blends. Furthermore, being rather needle shaped, SBS particles could orient towards the direction of the airflow. Consequently, the orientation could lead to a smaller aerodynamic diameter than the roundish BUD particles. This in turn could lead to an increase in FPF values and aerodynamic performance, respectively.

The use of DAs was intended to promote dispersion of the API-carrier agglomerates by dynamic particle impaction. In the assessments of interactive blends, inserting DAs into the Twister® did not show any apparent effects on the aerodynamic performance. The results of this study showed no clear indication of increased dispersibility as a function of the number or the morphology of the DAs. Instead, the performance of the tested formulations depended

primarily on the choice of carrier material and the drug content. It was found that the higher the drug content, the higher the deagglomeration and thus performance.

In this study, the presented findings provide no indication of an influence of the capsule filling on the aerodynamic performance. The higher the filling, the more particles there are that need to be fluidised in the inhaler once an airflow is applied. However, fluidisation of more particles requires a higher energy input. Presuming a constant air flow and thus an equal energy input, a higher total number of particles in the inhaler could hinder the dispersion of the drug-carrier agglomerates. This hindrance could arise from the fact that the energy required for aerosolisation would have to be applied for fluidisation instead.

Based on the findings of this study, it can be concluded that capsule filling did not affect the deagglomeration. In turn, this conclusion could be overlaid by particle count dependent surface saturation of the inhaler chamber. As described by Etschmann, saturation phenomena could influence adhesion between particle agglomerates and the inhaler surface, which could affect the dispersion [63].

The second part of this chapter addressed the effect of DAs in softpellet formulations. For this, two different drugs for the treatment of tuberculosis served as model APIs. These APIs, namely RIF and ISN, equalled in initial particle size after milling but differed in chemical and thus physical properties. Differing properties resulted in varying dispersibility in the Twister® device, with RIF-softpellets generally performing better than ISN-softpellets in terms of FPF, FPD and MMAD values.

In aerodynamic assessments, inserting a DA into the Twister® device led to enhanced dispersion of RIF-softpellets. This enhancement was driven by the morphological structure of the inserted DA. In comparison, the RK proved to be most effective in increasing the FPF < 5 µm, whereas the SB showed the least effect on respective measures. Concurrently, the FPF < 1 µm increased only marginally in comparison to inserting no DA. As a result, the fraction of fine particles ranging from 1 µm to 5 µm, respectively, increased. This fraction is decisive for reaching the lungs, as explained in Chapter 1.

Principally, the ISN-softpellets were also susceptible to adding a DA, despite generally lower dispersibility. Reduced dispersibility potentially based on particle growth caused by environmental conditions. For ISN-softpellet formulations, the DAs did not compensate for environmental influences. Nevertheless, the insertion of DAs helped to counteract the effect of particle growth to a certain extent.

Overall, an effective use of DAs in DPI formulations depended on the physical and chemical properties of the involved components. As a main finding of this chapter, the usefulness and effectiveness of DAs is governed by the formulation strategy. On the one hand, their effect in interactive blends remained unclear. On the other hand, inserting DAs into softpellet formulations indicated beneficial effects. From these findings, it could be concluded that the morphology of the inserted DA might have an influence on dispersion. However, whether this insertion is beneficial depends largely on the particle properties of both the drug and the carrier.

As a general constraint, the findings of this study allow for conclusions to be drawn about the use of DAs in a Twister® device only. This constraint stems from the fact that the inhaler design principally influences the trajectories of the DA and the particles in the device. Potentially, a different device design could affect the trajectories in such a manner as to change the probability of collision and thus deagglomeration of the particles. Therefore, it remains questionable whether the Twister® is optimal for use with DAs or if it even masks their actual potential to aid dispersion. An optimal design would unleash the full potential of DAs, e.g. in terms of maximizing collisions.

To improve particle dispersion in inhaler devices by implementing free-levitating objects, the inhaler design must undergo concurrent adaptation. Adjusting the internal airflow in such a way that the DPI formulation is forced to pass the DA by the airflow could further improve dispersion efficiency. Optimally, the design of the inhaler and the DA would be mutually adapted. An investigation of the optimal inhaler would be a matter of iterative design thinking processes. Therefore, AM and numerical simulation could serve as a complementary methodology for prototyping of inhaler devices similar to what has been described in section 3.1.5.

The usefulness of DAs in influencing particle dispersion
depended on the formulation and its' components.
Applying a DA led to beneficial effects
in softpellet formulations unlike to an insertion to interactive blends.
The findings of this study are limited to the use of a Twister® device.
Future research should investigate the optimal device and DA design.

Chapter 4 Numerical simulation of DPI carrier particles

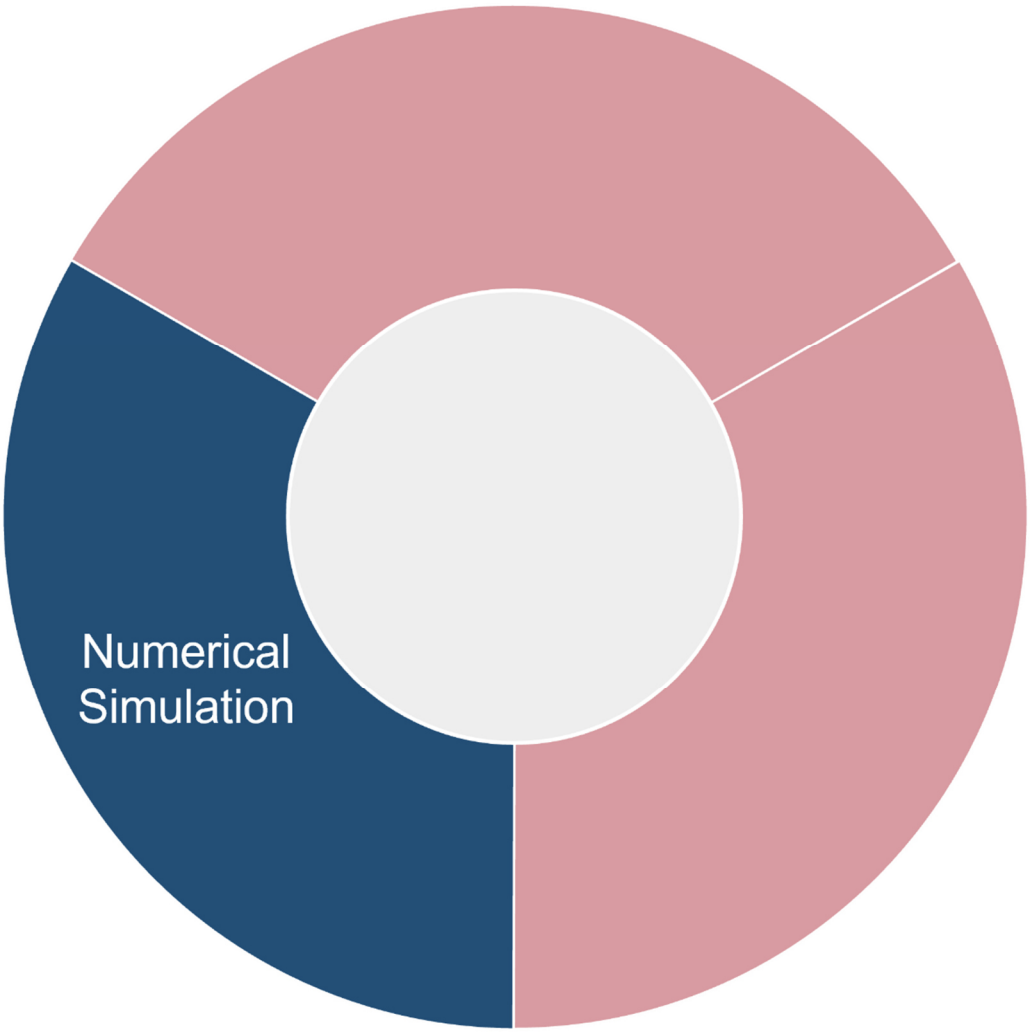

4.1 Numerical simulation in respiratory sciences

Experimental data from *in vitro* or *in vivo* studies generally provide an understanding of how various factors influence aerosol deposition. The properties of the individual particles that compose the aerosol determine its fate in the upper airways, the tracheobronchial tract and finally in the alveolar region. In addition to aerosol properties, inter-subject variability due to individual anatomy, physiology and constitution leads to many uncertainties in drug deposition (as discussed in Chapter 1).

Applying *in silico* methods is a complementary strategy for the development of novel pharmaceutical products and accessories. *In silico* modelling and numerical simulation, respectively, is a computational approach to predict the behaviour of materials based on the laws of physics and chemistry. The use of numerical simulation techniques intends to reduce the use of material resources by relying on rational, i.e., predictable and potentially extrapolatable, factors. It is further anticipated that applying numerical models could reduce the need for human subject testing and thus accelerate the approval process for generic inhalation devices and formulations [143]. Due to such reasoning, the techniques used for simulation purposes such as CFD [143,144] and DEM [122,122,145] increasingly attract attention. In the following sections, the principles of these techniques are briefly described, with a focus on the DEM methodology, which has been used in this thesis.

On a theoretical basis, there are three key factors for making statements about the performance of formulations for pulmonary applications. First, the droplet or particle properties in the transition from static bulk to fluidised and aerosolised state. Second, the size change through condensation. Third, the particle impaction behaviour in both the device and the airway system. Since the overall behaviour is highly dependent on the individual anatomic and physiological conditions, it appears to be most challenging to mimic the interdependency of environmental parameters and inter-patient variability in a specific model. To decipher these complex processes of respiratory drug delivery, a variety of simulation approaches have been conducted. Basically, three main application areas in respiratory sciences have been identified: (i) liquid and powder aerosol formation, (ii) device design and performance, and (iii) airway deposition modelling [143].

Initially, semi-empirical and one-dimensional models were used to predict aerosol deposition in the airways, as reviewed by Longest and Holbrook [146]. These relatively simple models were inferred from analyses of aerosol deposition in simplistic geometries resembling the respiratory tract. Recognisably, these led to outcomes of limited accuracy

and applicability. Applying CFD and DEM instead promises to provide methodological improvements and thus more insightful results.

4.1.1 Computational fluid dynamics

CFD is a technique that calculates the motion of fluids by numerically solving mathematical partial differential equations governing mass, momentum and energy transport. An extensive number of applications based on CFD exists, ranging from aerospace industry over process engineering to automotive design.

In respiratory drug delivery, mathematical models were initially applied to simulate aerosol deposition and air flow resistance in the lungs [147]. Then, particle deposition patterns were determined numerically both under inspiratory [148] and expiratory [149] flow conditions within airway-like structures. As remarked by Finlay et al. in 1996, the modelling was primarily conducted with computational limitations and under the assumption of physical boundaries [150]. In order to depict the naturally highly complex airways as realistically as possible, the available computer models have been continuously refined and extended [143,146,151]. However, CFD models alone are generally unsuitable for adequately simulating the complexity of aerosol generation and particle fate in the branching airways.

As recently summarised by Longest et al., the modelling of fluid dynamics in the respiratory tract is therefore confined to the areas from the oral cavity to approximately the sixth generation of the airways (Chapter 1) [143]. Nevertheless, the influence of morphological variabilities in the upper airways on airflow patterns and thus the local particle deposition can be effectively determined using CFD models [152,153]. The dependency of the deposition characteristics on different inhalation patterns for both MDI and DPI devices has been computationally investigated [154]. The individual, multifactorial and disparate health condition is the reason for differences in inspiration patterns.

For prediction of particle deposition and, on the long run, for *in silico* diagnosis as well as personalised treatment, the implementation of models that represent the entire respiratory tract is required [152]. For the time being, lack of applicability on diseased airways is one of the most severe limitations of deposition prediction [155]. Furthermore, validation of numerical results with extended experimental data is needed, since the CFD model specifications and input parameters are partly user-dependent and can vary widely [143,152,156]. Considering these challenges, De Backer et al. presented patient specific CFD simulations that were consistent with computer tomography scan data [157].

Apart from the effort to mirror the particle flow in the human respiratory tract, CFD has emerged as a scientific tool for the engineering and characterisation of inhalation devices

[123,144,144]. Modifications in the design of an inhaler affect internal flow patterns as well as specific device resistance and thus aerosolisation performance. The thereby emerging differences can be computed and subsequently correlated to *in vitro* data [40,125,126,158–164]. Mostly, such correlations are based on data derived from aerodynamic particle sizing. In a series of publications, Coates et al. have investigated different design aspects of DPI devices. In particular, the research group emphasised the impact of the size of the air inlet [161], the grid structure [125], the length and geometry of the mouthpiece [125,162,162] and the effect of a spinning capsule [160] analysing the flow motion and structure numerically at steady-state conditions.

The use of CFD coupled with *in vitro* drug deposition studies provided deeper insight into aerosol behaviour. Accordingly, the influence of physical properties of carrier particles was investigated to assess their impact on aerosol deposition [163]. The importance of the respective dispersion principle for the different inhalers as well as the size and morphology of the carrier particles has been conclusively recognised.

For dispersion and thus drug release of large carrier particles with micronised API and fines attached to them, different mechanisms of interaction are conceivable (Figure 4.1): First, particle-particle collision, which could lead to both API detachment and API transfer from one carrier to another. Second, interaction of the particles with the surrounding fluid medium (air), causing shear stresses and thus API blow-off. Third, particle-wall collisions, in which API particles are knocked off once the carrier hits a wall. This could also induce press-on forces on the contact area between the carrier and the wall. As a result, drug particles may show strengthened attachment to the carrier or stick to the wall, due to the adhesive nature of the micronised particles. In addition, when the large particles move through the surrounding medium, reattachment of the previously dispersed fine particles may occur [122].

Due to the massive complexity of predicting how a dispersion of polyform particles behaves, simulations without assumptions and simplification are currently not feasible. This is especially true when considering different sizes and densities, inhomogeneous surface energy distribution and potential deformations of the individual particles. CFD analysis only accounts for the patterns of a fluid medium (gas, liquid) and conceptually cannot accommodate the interactions between particles. Subsequently, other methods that can in turn incorporate such interplay is of utmost relevance. By coupling CFD models with DEM, a more comprehensive representation of the effects generated by both fluids and particle interactions is achieved [122,123,127,128,165–167].

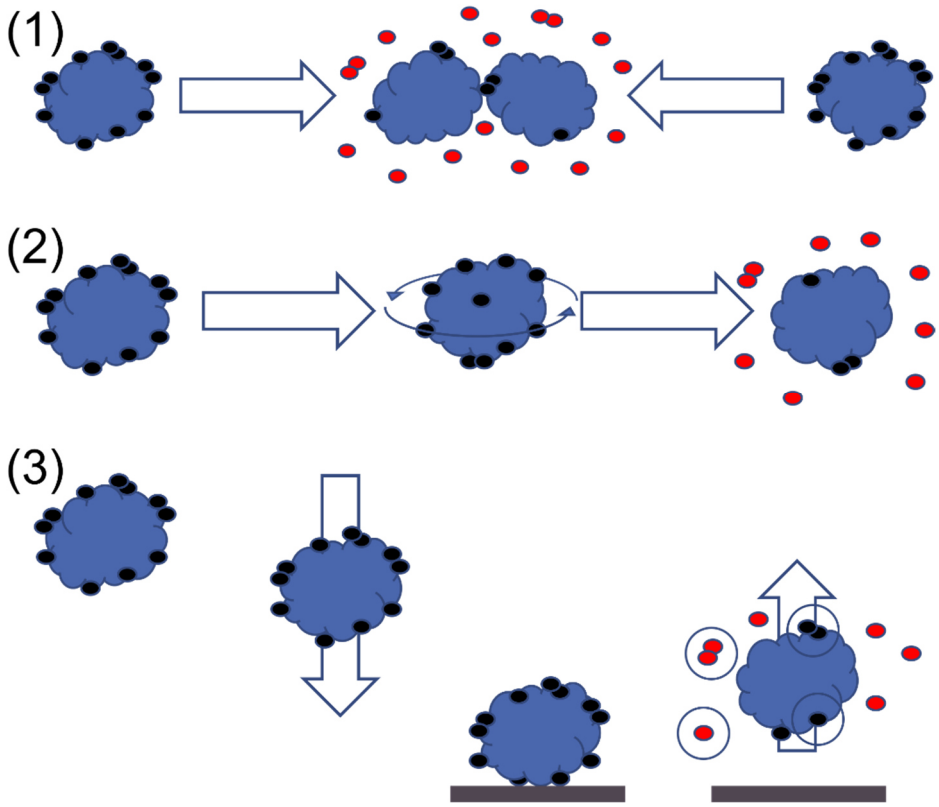

Figure 4.1: Dispersion mechanisms: particle-to-particle collision (1), velocity gradients caused by shear stress (2) and particle-to-wall collision (3). Particles detach as individual particles or agglomerates (red), while some remain on the surface or are even pressed onto it (black).

4.1.2 Discrete element method

Computational modelling provides a general understanding of a certain process and can therefore reduce experimental efforts. Mechanical behaviour and interaction of solid particles with different shapes and sizes can be simulated numerically using DEM. This method involves a computational calculation of the equations of motion for a set of particles integrated over time. The core assumption of DEM is that the observed matter consists of distinct objects. For every object, all contact forces arising e.g. from particle-particle collisions or particle-boundary interactions as well as the body forces acting on the object (e.g. gravity, electrostatic, electromagnetic) are calculated. The occurring forces are then induced into Newton's second law of motion resulting in a change of momentum for the particle.

Several models exist that numerically describe the forces acting on and between particles. These range from simplified models that do not account for adhesion forces to highly complex contact mechanics simulations that include a variety of factors [168]. To compute the interactions and resulting forces, two main approaches are basically used, namely hard-sphere and soft-sphere models. In the hard-sphere approach the boundary of the particle is impenetrable. Therefore, momentum transfer between two colliding particles

is the only result of a collision. Contrarily, determining the interaction forces as a result of particle overlap is referred to as the soft-sphere approach, which was first described by Cundall and Strack [169].

To initiate a DEM simulation run, a system of objects must be specified. Specifying the objects involves a careful selection of their individual characteristics and attributes. In addition, the interactions between the objects in the system must be defined and a reasonable choice of the composition of the system is required. This choice includes e.g. the number of different objects to be included in the simulation, the initial state, and the time step of the simulation.

The DEM software then calculates the sum of all momentums, contact and body forces acting on each object at a certain time point. Considering the current particle locations, their momenta, and all boundary information, the software determines the new locations of all objects and their status at the end of the next simulation time step. This discrete procedure is repeated until the simulation is terminated, or pre-defined criteria are reached.

4.1.3 Discrete element method in respiratory sciences

As mentioned above, CFD models provide important information about particle movement in inhalers. Although particle-wall collision was identified as a predominant dispersion mechanism [170], scientific publications that focus primarily on DEM simulation are less numerous than CFD publications. Simulating particle impact on a wall has initially been restricted to two-dimensional monodisperse agglomerates [171]. A complementary study, also published by Thornton et al., showed the influence of different impact velocities on polydisperse agglomerates [172]. These studies laid the foundation for following DEM simulations of fracture and agglomerate break-up. Tong et al. observed that the impact angle is also relevant to realistically describe these events in the simulated system [173]. In this study, optimal breakage performance of agglomerates, consisting of particles with approximately the same size, was obtained at an angle of 45°. On this basis, Yang et al. transferred the DEM approach to interactive blends, for which particles with different sizes were considered. The authors studied the dispersion performance at different impact velocities and angles. They found in numerical simulations that the detachment of APIs from the carrier increases particularly with the translational velocity [174]. Moreover, they identified the impact and adhesion energy as key parameters for adequately modelling the behaviour of carrier-based blends.

With a focus on the interactions between particles, Ariane et al. provided a simplified DEM model simulating the collision between an API-carrier agglomerate and a plane wall. This

DEM model, which describes the effects of impact velocity, angle of impact and angular velocity on the API detachment from a spherical carrier, was considered to be implemented into further CFD studies [145]. As ternary interactive blends contain excipient fines, Nguyen et al. simulated the transfer of such particles between colliding carriers. The fines were found to be redistributed between the carriers as well as restructured among themselves with different patterns depending on their kinetic and surface energy [175]. Their finding additionally indicated the complexity of simulating the mechanistic of interactive blends.

The effect of differences in adhesion energy, namely in the Hamaker constant describing the van der Waals energy between two bodies (see Chapter 1), were simulated in a multi-scale approach by van Wachem et al. Their approach consisted of three distinct levels of simulation set-ups: micro- (interactions of the APIs with larger carrier particles), meso- (interactions of carrier particles) and macro- (particle-wall interactions) scale. By coupling DEM with CFD, the authors investigated the effect of realistic airflow profiles on particle dispersion in a prototype inhaler. This simulation demonstrated the importance of implementing particle properties into numerical models to depict inhaler performances more accurately [122].

As concluded by Longest et al., a correlation between powder dispersion and turbulence exposure, inducing kinetic energy and shear stress, can be derived from both CFD simulations and *in vitro* experiments [126]. Previously, Tong et al. developed a combination of CFD and DEM to investigate the additional influence of particle size and particle size distribution on the dispersion of mannitol agglomerates [167]. In their model different flow velocities were adjusted by CFD, while particle size and particle size distribution were controlled by DEM. The forces acting on an agglomerate were then simulated by DEM-CFD coupling. As a result, agglomerates consisting of smaller particles were found to be more difficult to disperse under low flow velocities. Conversely, the dispersion performance has been shown to improve with increasing velocity.

Research carried out with DEM models led to the conclusion that particle properties and size distributions have a major influence on dispersion performance. In studies based on CFD models, particle impact velocity was considered to be indicative of the resulting deagglomeration of multiparticulate systems [158,159,161]. By coupling DEM with CFD, a proportionality of particle-wall impact energy and particle-particle cohesion energy to dispersion efficiency was observed. However, in contrast to analyses with only CFD modelling, internal shearing by airflow was considered less important for powder dispersion [167]. The findings by Zhou et al. furthermore emphasise the necessity to couple DEM with

CFD in order to comprehensively investigate the aerosolisation mechanisms in an inhaler. This study underpins that air velocity and turbulence kinetic energy are critical for drug detachment from carrier particles [165]. A similar approach quantified the energy generated by particle-particle collisions and particle-wall impacts. It was shown by Tong et al. that the energy of particle collision with an immobile wall was the predominant factor for particle dispersion [170]. Since in the latter computations particle-device collisions occurred mainly in the inhaler chamber, this unit was identified as the critical point in device design [165,170]. Corresponding practical findings for the influence of air inlet, grid structure and mouthpiece generally match the results based on CFD simulations performed earlier by Coates et al. [125,161,162,176,177].

Previous models are essentially based on simulating the behaviour of spherical particles. To minimise the computational effort, spherical bodies serve as simplified carriers. Some simplifying models are even entirely unsuitable for the simulation of aspherical bodies. However, this simplification does not represent the variety of particle morphologies present in conventional interactive mixtures. With increasing computing capacities and progress in the mechanistic description of particle-particle interactions, the variety of morphologies should be taken into account. To explore the effect of carrier morphology on API loading and detachment, the following sections elaborate on the implementation of aspherical bodies in DEM simulations. In addition, these studies are intended to allow for defining optimised carrier morphologies for DPI formulations.

This chapter explores the application of numerical simulation to assess the effect of DPI carrier morphology on drug loading capacity and particle detachment following particle-wall collision. DEM modelling is used to investigate these phenomena and to computationally evaluate the most suitable particle morphology and size.

4.2 Experimental simulations with Rocky DEM®

With the technical capabilities offered by TPP (3.4.2.3), an evaluation of the most appropriate carrier shape and size was sought by applying numerical simulations. To investigate the effects of particle morphology and size, a mathematical simulation software has been used in this thesis. The following section gives a general overview of the experimental set-up and the corresponding mathematical basics of the numerical methods applied.

Numerical simulations in this work were conducted with the software Rocky DEM® (version number 4.7, ESSS Rocky S.L., Argentina). This software allows an implementation of real particle geometries (derived from CAD-files) as well as to simulation and analysis of complex phenomena such as particle breakage, rotation and stickiness. In this thesis, two separate numerical simulation set-ups using Rocky DEM® are presented. The first setting covers the simulation of carrier particles to be loaded with spherical API particles (section 4.2.2). Loading the carrier with API particles with a diameter of 1 µm, 3 µm and 5 µm, respectively, artificially mirrors the blending step in a production process of interactive blends. Secondly, Rocky DEM® was used to simulate the behaviour of resultant API-carrier agglomerates during particle-wall collision (section 4.2.3).

Rocky DEM® is based on solving the equations of contact forces numerically. These contact forces consist of normal-to-contact-plane and tangential-to-contact-plane forces. Determining a contact-plane is dependent on the particle shape. Essentially, the respective algorithm calculates the closest points of two approaching bodies and the maximum overlap distance in case of a physical contact, respectively. The following sections provide descriptions for the calculation of the normal and tangential forces, as well as the corresponding models used in this thesis.

4.2.1 Normal, tangential and adhesive forces

Models that incorporate repulsive forces and allow energy dissipation on contact are denoted as normal force models. First proposed by Walton and Braun, the hysteretic linear spring model allows simulating both repulsive elastic and dissipative contact forces [178]. The simple spring model represents a linear relationship between particle displacement σ and force F considering the material constant K_n(Equation 4.1).

$$F_n = K_n * \sigma_n \qquad \text{Equation 4.1}$$

F_n: Normal contact forces

K_n: Normal contact stiffness

σ : Displacement

A typical cycle of normal force-overlap response for the extended, hysteretic linear model is depicted in Figure 4.2. Between points A and B, the normal force increases linearly with the overlap. When reaching the maximum overlap and the colliding particles reverse their directions of motion, a steeper decline of the repulsive forces follows, as illustrated between points B and C. When the contact force has decreased to zero (point C), there is still some remaining overlap σ_{Res}. Plastic deformation occurs during contact, which leads to energy dissipation. The energy dissipated during impact corresponds numerically to the enclosed area in the hysteretic force-deformation diagram of Figure 4.2. For further simulation steps, any residual deformation is ignored after the contact ceases.

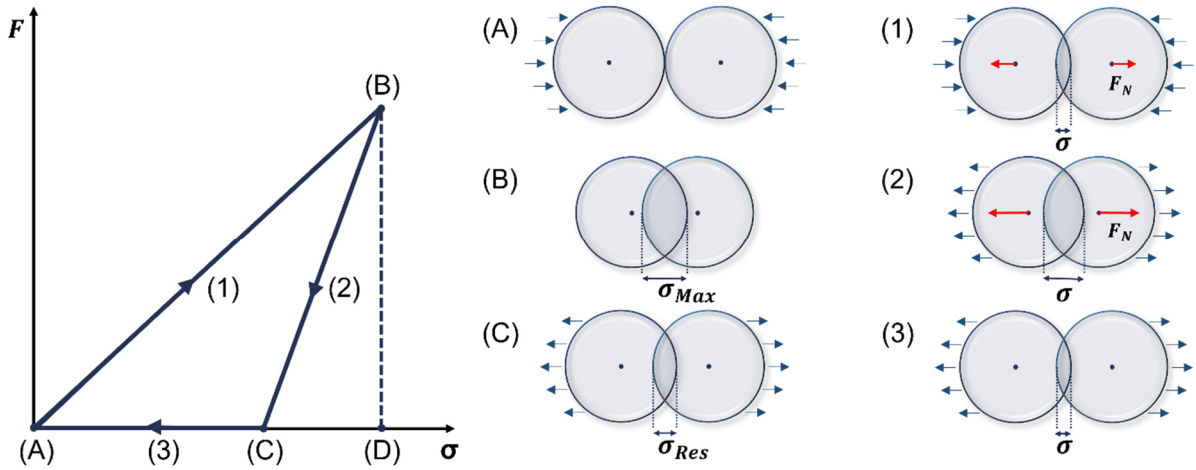

Figure 4.2: Schematics of a typical force-deformation for the hysteretic linear spring model with F_n defined as normal force, σ_{Max} defined as maximal overlap and σ_{Res} defined as residual overlap. The red arrows indicate the direction of forces whereas blue arrows represent direction of movement.

From the linear spring model, which was first proposed by Cundall and Strack, derives the Hertzian spring-dashpot model [169]. They introduced a model, whose normal contact force is composed of a linear elastic repulsive and a damping force (Equation 4.2):

$$F_{n,Hertz} = K_n * s_n + C_n * \check{s}_n \qquad \text{Equation 4.2}$$

$\boldsymbol{F_{n,Hertz}}$: Normal elastic-plastic contact forces

$\boldsymbol{s_n}$: Contact normal overlap

$\boldsymbol{C_n}$: Normal damping coefficient

$\check{s}_n$: Time derivative of the contact normal overlap

From this linear model, the so-called Hertzian spring dashpot model has been derived, in which both the elastic and the damping components of the normal force are nonlinear functions of the overlap. The elastic part is based in the classical contact theory developed by Hertz [179]. Overall, this refined model describes the contact of two perfectly spherical, smooth bodies in a simplifying approach, taking into account elastic overlap and energy dissipating plastic deformations.

For calculating tangential-to-contact-plane forces in Rocky DEM®, the Mindlin-Deresiewicz model was applied. This model considers a nonlinear relationship between force and displacement [180]. A combined model based on the Hertz theory for the contact forces between two bodies in the normal direction and the Mindlin and Deresiewicz theory for the contact between two bodies in the tangential direction (Figure 4.3, 2) has already been applied to simulate pharmaceutical processes (e.g. milling, blending and coating) [181]. In this Hertz-Mindlin model, material properties such as Young's modulus (E), size and shear modulus are taken into account to calculate the respective forces. The Young's modulus describes the stiffness indicating how easily a solid surface deforms. To what extent a given body changes its shape when a load is applied determines the contact area that results when two bodies meet. In turn, the contact area, and so the initial surface roughness, effects the corresponding adhesion.

Adhesive forces affect material-to-material interactions and thus energy dissipation. Therefore, the JKR model, which was proposed by Johnson, Kendall and Roberts based on the Hertz theory, introduces adhesion into the contact model considering a balance between stored elastic energy and loss of surface energy γ (Equation 4.3) [182]. Surface energy defines the interaction between two bodies in dependency on the physico-chemical attributes such as chemical composition, crystallinity and shape, expressed as the work per area unit. JKR bases on a nonlinear relationship between force and displacement (Figure 4.3, 3), which allows to simulate cohesive particles. Modelling cohesiveness of particles makes this model useful for the simulation of API-to-carrier interactions.

$$F_{JKR\,,adh} = \sqrt{8\pi a^3 \Delta\gamma E_{eq}} \qquad \text{Equation 4.3}$$

a: Contact area of two bodies

$\Delta\gamma$: Difference in surface energy of two bodies

E_{eq}: Equivalent Young's modulus of two bodies

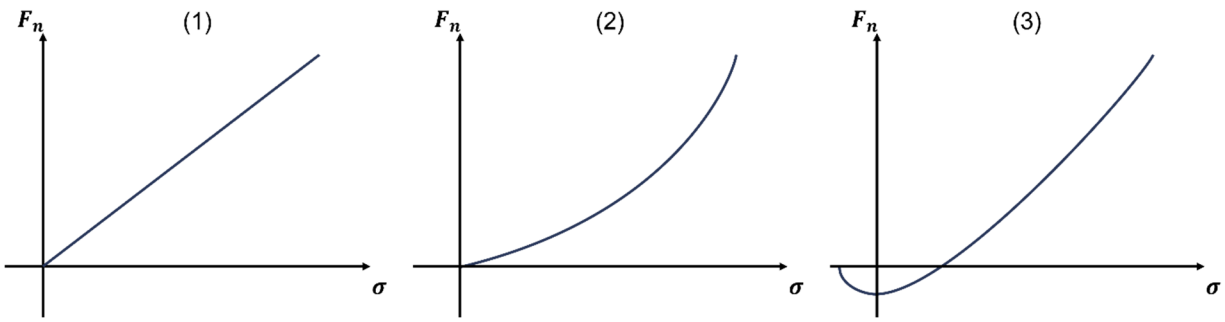

Figure 4.3: Schematic illustration of the relationship between force (F_n) and displacement (σ): (1) linear spring model, (2) Hertz-Mindlin model and (3) Hertz-Mindlin-JKR model (adopted from [181]).

Elasto-plastic-adhesive behaviour was partly simulated in this thesis with the help of a simplified linear model, namely Leeds contact model [183]. As schematically shown in Figure 4.4, the normal force defined in the Leeds model equals the sum of a repulsive, hysteretic force $F_{n,rep}$ (in blue), and an adhesive force $F_{n,adh}$ (in red). In simple terms, the Leeds model is a linearised version of Hertz-Mindlin-JKR force response comprising a composition of repulsive and adhesive forces.

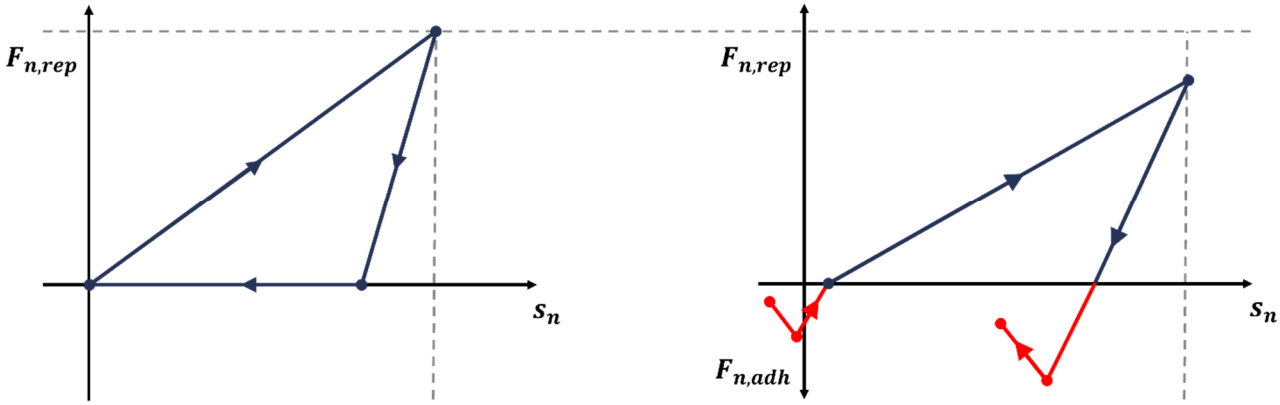

Figure 4.4: Schematic comparison Schematic comparison: hysteretic linear spring model (left) and Leeds model (right).

The previously described models were used for the following numerical simulations, namely carrier loading and particle-wall collision. Specific differences in the applied models between these simulations are listed in Table 4.1.

Table 4.1 Differences in simulation models applied for carrier loading and particle-wall collision, respectively.

Carrier loading		**Particle-wall collision**	
Factor	**Model**	**Factor**	**Model**
Normal force	Leeds contact model	Normal force	Hertzian spring
		Tangential force	Mindlin-Deresiewicz
		Adhesive force	JKR

4.2.2 Carrier loading

This section explains a simplified simulation of loading a carrier with API particles by using the software Rocky DEM®. The simulation was intended to mirror the blending of such particles, as it is a common manufacturing step in the preparation of interactive blends.

Given a mass of 1 mg, which consists of 2% (m/m) of spherical API with 1 µm in diameter and 98 % (m/m) of spherical carrier particles with 50 µm in diameter, both having a density of 1 g/cm³, would require the simulation of 38197186 API and 14973 carrier particles in total. Changing the diameters to 5 µm (API) and 200 µm (carrier), respectively, would still demand to numerically model 305577 API and 234 carrier particles. To solve the equations of motion for each particle, massive computational power would be needed. Yet, 1 mg is not even an adequate amount that depicts a practical mixing process. In addition, an interactive powder mixture is realistically composed of particles with different physicochemical properties, morphologies and size distributions. Therefore, simulating the process conditions for particle blending are poorly documented regarding the preparation of DPI formulations.

To minimise the computational effort, the loading of carrier with API particles was simplified by reducing it to a single carrier particle. The shapes illustrated in served as carrier particles and were compared to a sphere. As shown in Chapter 3, the selected geometries differ in their morphological and physical properties such as edges, indentations, surface area, fluidisation behaviour and intrinsic flowability.

Each simulation scenario based on a single carrier particle with a longitudinal dimension of 50 µm or 100 µm in reference to the particle sizes in commercial lactose grades. In analogy to micronised API particles in DPI formulations, spherical API particles with three different sizes (1, 3 and 5 µm diameter) served as input objects. To model the physical conditions most accurately, the respective particle properties corresponded to empirical values reported in the literature (Table 4.2). To mimic the blending process in Rocky DEM®, the carrier particle was surrounded by a total of 14 input entities, each of which was directed towards the centralised carrier (Figure 4.5, i-ii).

An API particle input with a defined mass flow was implemented in the simulation scenario, defining the number of particles and their velocity. Different mass flows generated three different cases for each carrier morphology in the respective size to cover a variety of drug-carrier ratios. The mass flow consistently composed of the three different API particle sizes in equal mass proportions. Accordingly, the total number of inlet API particles was defined as the total count (Table 4.3).

Table 4.2: Carrier loading simulations: physical and simulation parameter.

Parameters	API particle	Carrier particle
Particle diameter	1, 3 and 5 µm	50 or 100 µm
Particle density	1000 kg/m³	800 kg/m³ [184]
Young's modulus	1 GPa [185]	5 GPa
Poisson ratio	0.3 [145]	0.24 [145]
Surface energy API-API	$1*10^{-06}$ mJ/m²	
Damping ratio API-API	0	
Surface energy API-carrier	1 mJ/m²	
Damping ratio API-carrier	0.1	

Table 4.3: Carrier loading simulations: particle inlet values.

Carrier diameter	Case	API particle inlet (mass/time)	Total API particle inlet (total count)
50 µm	1	0.5e-08 g/h	1550
	2	1.0e-08 g/h	3100
	3	1.5e-08 g/h	4650
100 µm	4	0.5e-08 g/s	5600
	5	1.0e-08 g/s	11200
	6	1.5e-08 g/s	16800

In this part of the work, the deposition of API particles on the carrier was modelled using the Leeds contact model (Table 4.1). The simulation scenario, covering a period of 2.5 seconds with an output frequency of 0.0001 seconds, comprised three steps. In a first step, the API particles moved towards the central carrier at a relatively low velocity, with no gravitational forces acting. After a time step of 2.0 seconds, which ensured every API particle to have touched the carrier, the gravity was turned on. With the gravity acting on the particles, every single body fell in y-direction. A concave grid that was inserted below the central object prevented both the carrier and the API particles, whose contact forces were sufficiently strong to stick to the carrier, from exiting the bounding box (Figure 4.5, iii). The other particle that detached, fell through the grid and were eliminated from the bounding box.

The final state of a carrier-API agglomerate is illustrated in Figure 4.5 (iv) and is regarded as the state at with as much APIs as possible attached to the carrier for the specific setting. For each case, the number of particles that remained attached and their size distribution were evaluated depending on the size/mass/volume/surface area of the respective carrier (section 4.3.1). This simulation scenario allowed for identifying specific morphological features that are favouring API particle adhesion. Furthermore, the loaded carriers and agglomerates, respectively, served as the initial state for further studies on particle-wall collision.

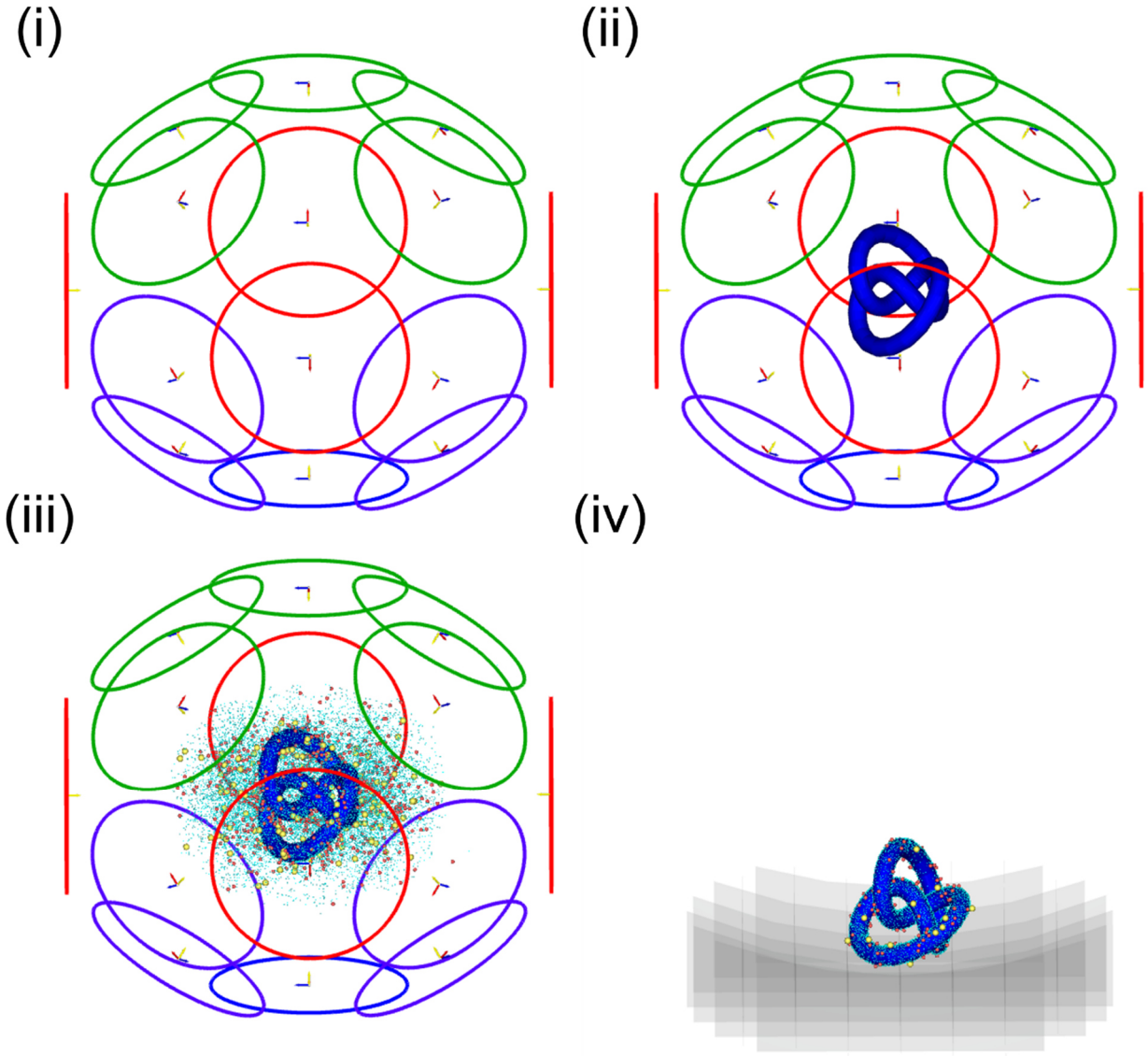

Figure 4.5: From the initial scenario setup to the final state of the carrier loading. (i) Overall, 14 input entities release API particles, bottom (blue), side (yellow) and top (red), each directed towards the carrier particle in the centre (ii, iii). Final state of the agglomerate on the grid (iv).

For each case, evaluation of the carrier loading included a calculation of the relative mass of API particles that attached to the carrier (Equation 4.4), the drug/API loading capacity in

relation to the carrier volume (Equation 4.5) and in relation to the carrier surface area (Equation 4.6).

1. Drug content of agglomerate after carrier loading:

$$DC_{agglomerate} = \frac{m_{API_{total}}}{m_{total}} = \frac{m_{total} - m_{carrier}}{m_{total}} \qquad \text{Equation 4.4}$$

2. Volume-specific drug loading capacity:

$$DLC_V = \frac{m_{API_{total}}}{V_{carrier}} \qquad \text{Equation 4.5}$$

3. Surface-specific drug loading capacity:

$$DLC_{SA} = \frac{m_{API_{total}}}{Surface\ Area_{carrier}} \qquad \text{Equation 4.6}$$

4.2.3 Particle-wall collision

This section explains a simplified simulation of particle-wall collision using Rocky DEM®. The simulation addressed the interaction and rearrangement of API particles and carrier once the respective agglomerate hits a wall. It is scientifically relevant to simulate the mechanistic processes of a collision, as a significant contribution to particle dispersion in an inhaler is attributed to this event (Chapter 3). Each simulation scenario based on the API-carrier agglomerates derived from the previous carrier loading model (section 4.2.2). Thus, the final state of the latter model corresponded to the initial step in the collision simulation scenario. In this scenario, the grid on which the agglomerate lay accelerated in the y-direction towards a plane wall. As a result, the carried agglomerate accelerated in the same direction. Three different terminal velocities (5, 10 and 15 m/s) were simulated in reference to the velocities that occur in common inhaler devices [122,145,165,176].

In this work, the particle-wall collision was simulated with a combination of different models, which allow for focused modelling of adhesion mechanics (Table 4.1). Adequate modelling of adhesion requires defining material interactions, namely friction and restitution, as well as the respective surface energies (Table 4.4).

Table 4.4: Material interactions - particle-wall collision.

Parameters	API-API	API-carrier	API-wall	Carrier-wall
Static friction coefficient	0.2	0.8	0.3	0.3
Dynamic friction coefficient	0.2	0.8	0.3	0.3
Restitution coefficient	0.1	0.1	0.3	0.4
Surface energy	10 mJ/m²	1 mJ/m²	1 mJ/m²	0.1 mJ/m²

Further physical and simulation parameters were set to the values shown in Table 4.5. To mimic the interactions as accurately as possible, these values originated from direct physical measurements or from previously published simulation models.

Table 4.5: Physical and simulation parameter – particle-wall collision.

Parameters	API particle	Carrier particle	Wall
Diameter	1, 3 and 5 µm	50 or 100 µm	n/a
Density	1000 kg/m³	800 kg/m³ [184]	1000 kg/m³
Young's modulus	1 GPa [185]	3.45 GPa [186]	2 GPa [187]
Poisson ratio	0.3 [145]	0.24 [145]	0.43 [188]

Figure 4.6 exemplifies the temporal course of the collision and the change in the agglomerate structure and particle dispersion, respectively. The carrier is directed towards a plate with a certain velocity (i). Once the carrier hit the plate, the API particles partly detach from the carrier and distribute into the surrounding space (i-ii). Particles detach mono- or polydispersely, while some remain on the surface of the carrier or are even pressed onto it. In addition, some particles adhere to the plate (iii-iv) due to the respective settings of API-wall interaction.

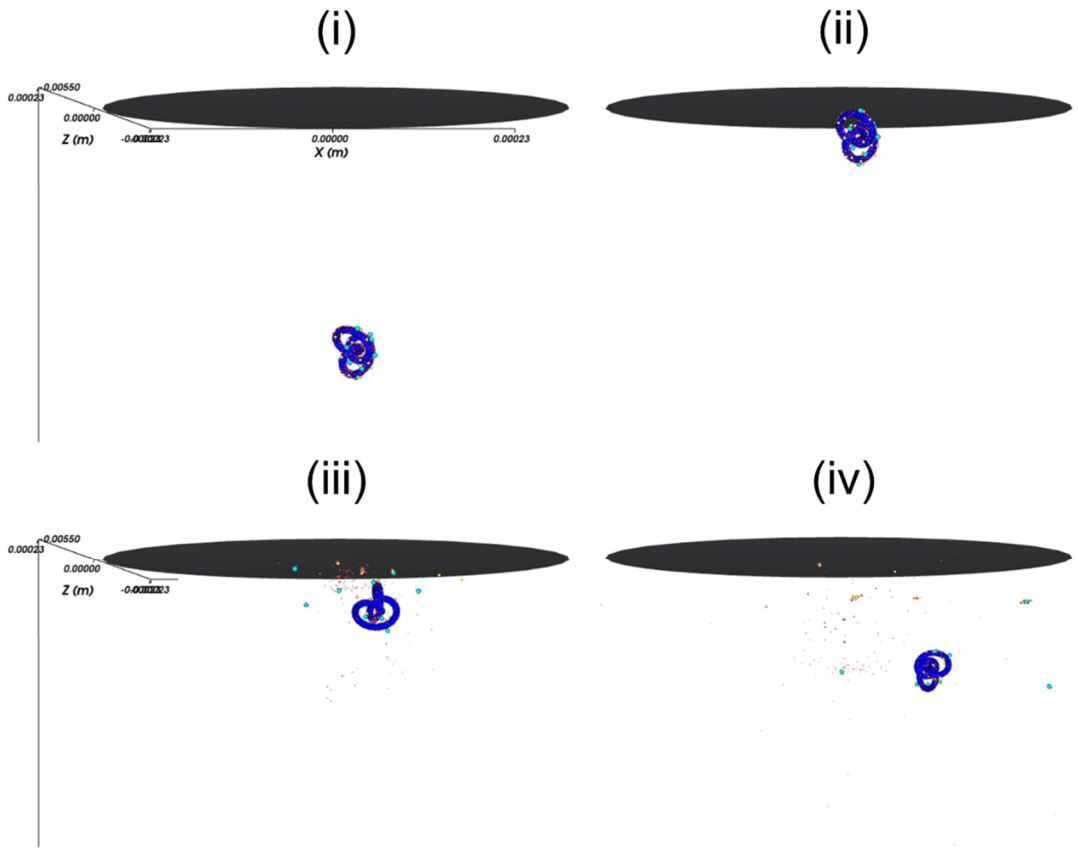

Figure 4.6: Temporal course of the particle-wall collision: Agglomerate formation immediately before (i-ii) and after the collision (iii-iv).

The collision studies provided information on the particle detachment from the carrier in dependence on the carrier morphology, size and loading as well as collision velocity. For each case, evaluation of the detachment behaviour included a calculation of the number of API particles that remained attached on the carrier after the collision (Equation 4.7).

1. Detachment rate:

$$DR = \frac{m_{API_{detached}}}{m_{API_{total}}} = \frac{m_{API_{total}} - m_{attached\ after\ collision}}{m_{API_{total}}} \qquad \text{Equation 4.7}$$

2. Carrier adherence:

$$CA = \frac{m_{attached\ after\ collision}}{m_{API_{total}}} \qquad \text{Equation 4.8}$$

4.3 Results and Discussion – Chapter 4

Different carrier morphologies with a diameter of 50 µm and 100 µm were computationally loaded with spherical API particles with a diameter of 1 µm, 3 µm and 5 µm in equal mass proportions (section 4.2.2). After computational loading, the resulting agglomerates were accelerated towards a plate forcing a particle-wall collision at different velocities (5 m/s, 10 m/s and 15 m/s). The morphologies studied in this thesis included a perfect sphere and the geometries displayed in Figure 3.9, namely pharmacone (PC), rollingknot (RK) and soccerball (SB). Three different mass inputs resulted in different terminal quantities of API particles in each simulation model (case 1 to 3, Table 4.3). Every model calculated with Rocky DEM® based on the same simulation parameters and physics, respectively (Table 4.2).

4.3.1 Drug content and loading capacity

Differences in morphology and size influenced carrier mass ($m_{carrier}$), volume ($V_{carrier}$) and surface area ($SA_{carrier}$), as shown in Table 4.6. In both size categories, the spherical object featured the largest surface area and the highest mass as a result of the highest volume. Next lower values resulted for the SB and subsequently for the PC. The geometry RK featured the lowest values for each attribute.

Table 4.6: Differences in mass, volume and surface area between different carriers and sizes.

	Parameter	PC	RK	SB	Sphere
50 µm	$\boldsymbol{m_{carrier}}$ [µg]	0.03669	0.00841	0.04142	0.05236
	$\boldsymbol{V_{carrier}}$ [µm³]	45858.7	10510.6	51773.1	65449.8
	$\boldsymbol{SA_{carrier}}$[µm²]	7449.01	5992.33	7732.00	7853.98

	Parameter	PC	RK	SB	Sphere
100 µm	$m_{carrier}$ [µg]	0.29350	0.06727	0.33135	0.41888
	$V_{carrier}$ [µm³]	366869	84085.0	414185	523599
	$SA_{carrier}$[µm²]	2979.60	2397.90	3092.80	3141.60

In the presented simulation model, attachment of API particles onto the carrier depended on the respective mass input as well as on the carrier morphology and size (Table 4.7, Table 4.8, Table 4.9). To compare the loading efficiencies in these simulations for each geometry and size, the drug content of the entire agglomerate ($DC_{agglomerate}$, Equation 4.4) served as a mass-dependent attribute. In addition, the drug loading capacity in relation to the volume (DLC_V, Equation 4.5) and the surface area (DLC_{SA}. Equation 4.6) provided information about morphological influences on the simplified API-carrier blending simulation.

Table 4.7 summarises the drug content for each API-carrier-agglomerate ($DC_{agglomerate}$) as an output parameter of the respective simulations. Generally, higher mass input corresponded to higher results for both carrier sizes (see Table 4.3). Comparing the different morphologies among each other, the drug-RK-agglomerate consistently showed the highest drug content values for every carrier size and API input (50 µm - case 1: 7.79 %, case 2: 8.97 %, case 3: 13.37 %; 100 µm - case 4: 4.31 %, case 5: 5.93 %, case 6: 7.94 %). Contrarily, the drug-SB-agglomerate had the lowest values for both sizes (50 µm, case 1: 1.03 %, case 2: 2.98 %, case 3: 3.41 %; 100 µm, case 4: 0.71 %, case 5: 1.33 %, case 6: 1.72 %).

Table 4.7: Influence of carrier geometry and size on API content of agglomerate after loading.

$DC_{agglomerate}$, %		PC	RK	SB	Sphere
50 µm	case 1	2.18	7.79	1.03	1.62
	case 2	3.31	8.97	2.98	2.20
	case 3	3.61	13.37	3.41	2.84
100 µm	case 4	1.12	4.31	0.71	1.14
	case 5	1.26	5.93	1.33	1.56
	case 6	1.88	7.94	1.72	1.97

At first glance, the $DC_{agglomerate}$ values decreased with increasing carrier diameter (Table 4.7) despite a higher API mass input (Table 4.3). The carrier mass, as a reference parameter in the calculation of $DC_{agglomerate}$, however, increases with increasing carrier diameter.

Therefore, a direct comparison of the values of both sizes with each other is not appropriate since this would also require consideration of the change in carrier mass. Nevertheless, the data revealed that an increase in carrier size from 50 µm to 100 µm had different effects on the drug loading for each morphology (Table 4.7). For carrier with a diameter of 50 µm, the mass input of simulation case 1 (1550 API particles, Table 4.3) resulted in an $DC_{agglomerate}$ of 7.79 % (RK), 2.18 % (PC), 1.62 % (Sphere) and 1.03 % (SB), respectively. Likewise, for carrier with 100 µm in diameter, the mass input of simulation case 4 (5600 API particles, Table 4.3) resulted in $DC_{agglomerate}$ of 4.31 % (RK), 1.14 % (Sphere), 1.12 % (PC) and 0.71 % (SB), respectively. This order changed with size insofar as the Sphere with 100 µm diameter showed higher values than the PC (Table 4.7).

According to the API content of the entire agglomerate, the volume-specific drug loading capacity changed as a function of both the carrier size and the API mass input (Table 4.8).

Table 4.8: Influence of carrier geometry and size on volume-specific drug loading capacity.

DLC_V, µg/mm³		PC	RK	SB	Sphere
50 µm	case 1	17.9	67.6	9.42	13.1
	case 2	27.4	78.9	24.6	18.0
	case 3	30.0	123	28.3	23.4
100 µm	case 4	9.08	36.0	5.73	9.21
	case 5	10.2	50.4	10.8	12.7
	case 6	15.3	69.0	14.0	16.1

The API-RK-agglomerate consistently showed the highest values, indicating that the RK is capable of loading a relatively high mass of API per volume. For a carrier with a diameter of 50 µm, a mass input of 4650 API particles (case 3, Table 4.3) resulted in an DLC_v of 123 µg/mm³ (RK), 30.0 µg/mm³ (PC), 28.3 µg/mm³ (SB) and 23.4 µg/mm³ (Sphere), respectively. Noteworthy, the DLC_v of the RK is approximately three (50 µm, case 2; RK vs. PC) to seven (50 µm, case 1; RK vs. SB) times higher than the other geometries. Moreover, the drug loading capacities of 50 µm PC (case 1: 17.9 µg/mm³, case 2: 27.4 µg/mm³, case 3: 30.0 µg/mm³) and SB (case 1: 9.42 µg/mm³, case 2: 24.6 µg/mm³, case 3: 28.3 µg/mm³) were higher than of the Sphere (case 1: 13.1 µg/mm³, case 2: 18.0 µg/mm³, case 3: 23.4 µg/mm³) in the same carrier diameter. However, this order changed with an increase in particle size to 100 µm. In this size and subgroup without the RK, the SB geometry showed the lowest (case 4: 5.73 µg/mm³, case 5: 10.8 µg/mm³, case 6: 14.0 µg/mm³), whereas the

Sphere had the highest values (case 4: 9.21 µg/mm³, case 5: 12.7 µg/mm³, case 6: 16.1 µg/mm³).

Considering the values in Table 4.6, the RK has the highest surface area to volume ratio ($\frac{SA}{V}$; 50 µm: 0.57 µm²/µm³; 100 µm: 0.029 µm²/µm³) due to its morphological characteristics. In contrast, the Sphere without edges or recesses has the lowest ratio (50 µm: 0.12 µm²/µm³; 100 µm: 0.006 µm²/µm³). Given the same mass of API attached to each of these different morphologies, the Sphere would show a higher API mass per surface area to volume ratio compared to RK. API particle loading capacity as a function of the surface area without considering the volume levels out the influence of surface features such as edges and indentations (DLC_{SA} ,Table 4.9). Although the surface area was different, the DLC_{SA} values for both sizes ranged between 0.06 and 0.27 µg/mm². Being virtually identical, the parameter was unsuitable for comparing the geometries with each other. Overall, the results simply indicated that maximising the surface area correlated with the mass of API to be attached, regardless of the carrier geometry.

Table 4.9: Influence of geometry and size on surface area-specific drug loading capacity.

DLC_{SA}, µg/mm²		PC	RK	SB	Sphere
50 µm	case 1	0.11	0.12	0.06	0.11
	case 2	0.17	0.14	0.16	0.15
	case 3	0.18	0.22	0.19	0.20
100 µm	case 4	0.11	0.13	0.08	0.15
	case 5	0.13	0.18	0.14	0.21
	case 6	0.19	0.24	0.19	0.27

Figure 4.7 and Figure 4.8 illustrate the size distribution of the adhering API particles as a function of carrier morphology, carrier size and case (Appendix C). In accordance with previously presented results, higher mass input corresponded to higher values in each carrier size category. In case of both the 50 µm (Figure 4.7) and the 100 µm (Figure 4.8) carriers, higher mass inputs progressively increased the number of 1 µm API particles adhering to the carrier particle. The simulations indicated a comparatively small increment for adherent particles with a diameter of 3 µm with increasing mass input. In contrast, the number of adherent API particles with a diameter of 5 µm reached a maximum value for every carrier morphology. Reaching a maximum value implicates that no further particles of

this size attached to the carrier, despite increasing mass input and offered amount, respectively.

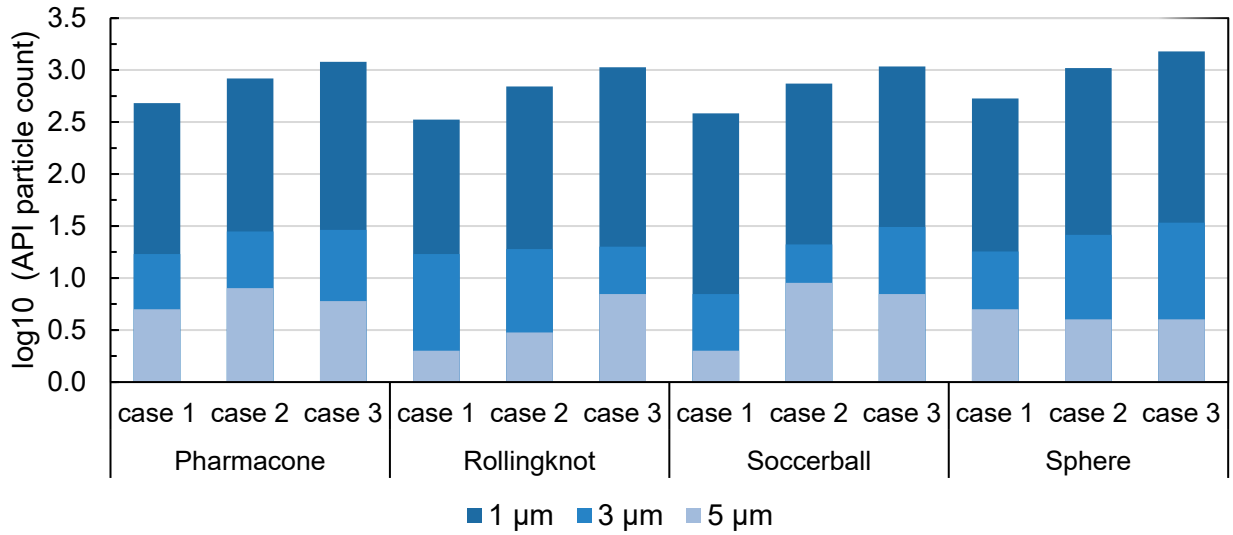

Figure 4.7: Size distribution of API particles adhering to carrier with a diameter of 50 µm as a function of carrier morphology and case (expressed as the log10 of the API particle count).

The particle size distributions derived from the present simulation model indicate that the smaller the API particle, the higher the probability of attachment. This finding is in accordance with the physics of adhesion, as the smaller the particle, the higher the relative adhesive forces acting on it (Chapter 1.6).

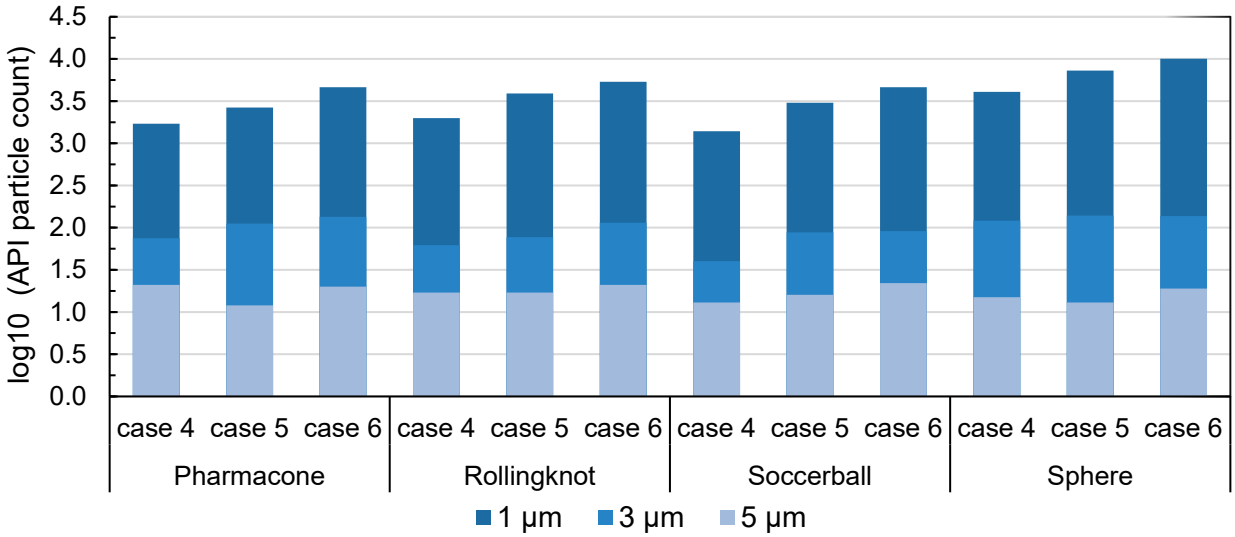

Figure 4.8: Size distribution of API particles adhering to carrier with a diameter of 100 µm as a function of carrier morphology and case (expressed as the log10 of the API particle count).

In the simulation models, an increase in mass flow primarily concerned the adhesion of API particles in the size of 1 µm. Those API particles that cover the free areas on the carrier surface first thereby prevent other particles from contacting the carrier. An increase in the total mass input implied the presence of considerably more particles with smaller sizes,

which is due to the predefined constant mass proportion of the input particles. This is because a defined mass equals a higher number of smaller particles compared to large ones because of their volume ratio. However, the probability of adhesion to the carrier also increases with the number of particles involved. Thus, the number of 1 µm API particles influenced the attachment behaviour of API particles with a diameter of 3 µm and 5 µm because they were comparably numerous. This relation explains why only a limited number of larger particles adhere to the carriers when increasing the total mass input. Further, saturation of the surface due to limited surface area explains why a continued increase in mass input partly led to a decrease in the number of larger particles (Figure 4.7 and Figure 4.8).

Comparing the numerical results of the different carrier with each other, the composition of API particles differed from morphology to morphology. A difference in particle count was calculated particularly for particles with 1 µm in diameter (Figure 4.7 and Figure 4.8, Appendix C). In the exemplary comparison of case 3 simulations with 50 µm carriers (Figure 4.9, upper row), the number of such particles was 1197 (PC), 1063 (RK), 1083 (SB) and 1509 (Sphere), respectively. Thus, most particles of this size adhered to the Sphere. Similarly, the absolute number of API particles with 3 µm in diameter differed from 29 (PC), 20 (RK), 31 (SB) and 34 (Sphere). Complementarily, 6 (PC), 7 (RK), 7 (PC) and 4 (Sphere) API particles with 5 µm in diameter adhered to the respective carrier morphology. The difference in the particle composition increased with the carrier size (Figure 4.9, Appendix C). 4625 (PC), 5371 (RK), 4610 (SB) and 10036 (Sphere) API particles with a diameter of 1 µm adhered to 100 µm carrier. Derived from these simulation data, the number of this particle type was 1.9 to 2.2 times higher on a Sphere than on the other morphologies. Corresponding values for 3 µm API particles did not indicate a substantial difference between the sphere (137) and the PC (134), but to the RK (114) and SB (91). The respective carrier loading simulations resulted in similar particle counts for API particles with a diameter of 5 µm (PC: 20, RK: 21, SB: 22, Sphere: 19).

Referring to the API particle size distributions for both carrier sizes (Figure 4.7 and Figure 4.8), in absolute numbers most particles adhere to the sphere. Considering the mere number of particles, the Sphere supposedly shows a superior drug loading capacity. Nevertheless, the $DC_{agglomerate}$ values of the sphere are comparatively low because its high volume and mass. Conversely, even though in numbers the fewest API particles adhere, the RK had high $DC_{agglomerate}$ values because of its low volume. It should be noted that the adhesion was mathematically calculated with the help of the adhesion models described in Chapter

4.2.1, which are fundamentally based on spherical geometries. This implies that the overlap leading to the simulated adhesion may not have been calculated accurately for the complex, partly angular geometries. This could explain why the drug loading between the Sphere and the other geometries was apparently so different in numbers. Noteworthy, the drug loading differed most between Sphere and SB, despite their relatively similar appearance regarding sphericity and volume. Depicting realistic particulate adhesion requires models that allow for lifelike simulation. The present models included simplifications and approximations. Therefore, practical API-to-carrier interactions may differ from what was numerically simulated in this study.

Moreover, the physical parameters listed in Table 4.2 factor the actual properties in a simplified manner. Owing to the simulation settings, the model largely excluded API-API interactions. Consequently, no pure API agglomerates formed in the course of the simulations. The absence of API-API interactions contradicts realistic particle blending processes. Nevertheless, simulating a carrier loading process with the present model aimed at creating comparable API-carrier agglomerates for further studies. Figure 4.9 displays the corresponding agglomerates of every morphology, each derived from case 3 simulations. Noticeably, the particles distributed randomly and heterogeneously on the carrier surface.

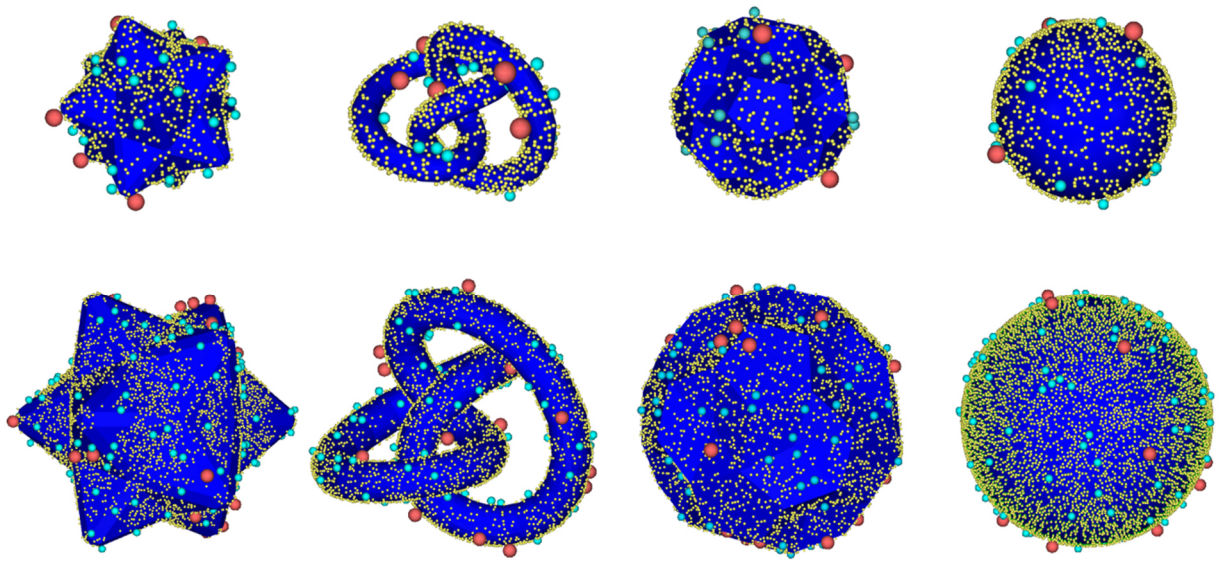

Figure 4.9: Representative images of agglomerates based on various carrier morphologies with 50 µm (upper row) and 100 µm (lower row) in diameter.

The carrier loading simulation presented in this thesis revealed that the choice of particle morphology impacts on numerical simulation data. Modelling the mechanisms of particle-particle interactions requires detailed consideration on the particle morphologies. In the recent past, numerical modelling of DPI formulations mainly based on spherical particles

(Section 4.1.3). Contrarily, common formulations consist of particles with a broad variety of morphologies, sizes and surface characteristics (Chapter 2.1). The explained simulation model accounts for the presence of particles with edges, protrusions and indentations. With these morphological features, the geometries PC, RK and SB represent further idealised geometries next to the Sphere. Consequently, these geometries merely idealise particles as they are actually utilised in the formulation of OIP. However, the results of this study show that variations in morphology considerably influence the simulation outcome. Therefore, the author of this thesis considers that simulating the behaviour of DPI formulations in a realistic manner would include an implementation of actual morphologies as well as their characteristics.

In case that idealised particles will be manufacturable in the future (Chapter 6), this study provides a digital approach to develop optimised carrier shapes. Regarding the morphologies studied with the presented model, especially the Rollingknot resulted in a relatively high volume-specific drug loading capacity. For the development of DPI formulations, high $DC_{agglomerate}$ and DLC_v values would be particularly beneficial in terms of dosing and thus drug delivery (Chapter 1.5). In contrast, the surface-area-specific drug loading capacity was considered unsuitable as a comparative measure for carrier loading performance. Moreover, determining the size distribution of the adhering particles provided indications of size-dependent interactions. As an interim conclusion, the carrier loading simulation provided insights into morphological relationships of API-carrier agglomeration, albeit excluding API-API interactions.

Numerical simulation of carrier loading allows for
modelling API-carrier agglomerates.
The variation range in drug loading capacity
apparently depends on the carrier morphology and particle size.

4.3.2 Detachment rate and carrier adherence

To describe the suitability of a certain morphology as a carrier geometry, numerical simulation was also utilised for evaluating the corresponding dispersion performance. By comparing the API particles that detach off the carrier after collision with a wall, the resulting detachment rate (DR, Equation 4.7) served as a comparative measure for *in-silico* evaluation of dispersion efficiency. Conversely, the carrier adherence (CA, Equation 4.8) corresponds to the morphological property to impede detachment. To calculate these parameters, each agglomerate that derived from previous carrier loading simulations (Section 4.3.1) was accelerated onto a plate at different terminal velocities (5 m/s, 10 m/s, 15 m/s). In contrast to the drug loading model, the simulation of particle-wall collision involved API-to-API interactions to factor cohesion (Table 4.4). Once the agglomerate hit the plate, the API particles partly detached from the carrier. The cohesive and adhesive interaction caused some of these particles to adhere to the plate, whereby other particles formed API-agglomerates or re-attached to the respective carrier (Figure 4.6, Figure 4.10). Simulation parameter settings prevented unrealistic sliding or rolling movements along the carrier surface.

Figure 4.10 representatively shows the appearance of API-carrier agglomerates after particle-wall collision. In comparison to Figure 4.9, less API particles adhered to the surface of each carrier. The collision resulted in the particles detaching mainly from the side facing and hitting the wall but also from the opposite side. Nevertheless, the wall-facing side shows sporadic particles of different sizes, which detached in the event of the collision and then adhered again. The particle-wall collision led to a change in particle count adhered to the carrier surface, as displayed in Figure 4.10 (see also Appendix C). Differences in carrier topography resulted in differences in post-collision particle coverage and thus carrier adherence or detachment rate, respectively.

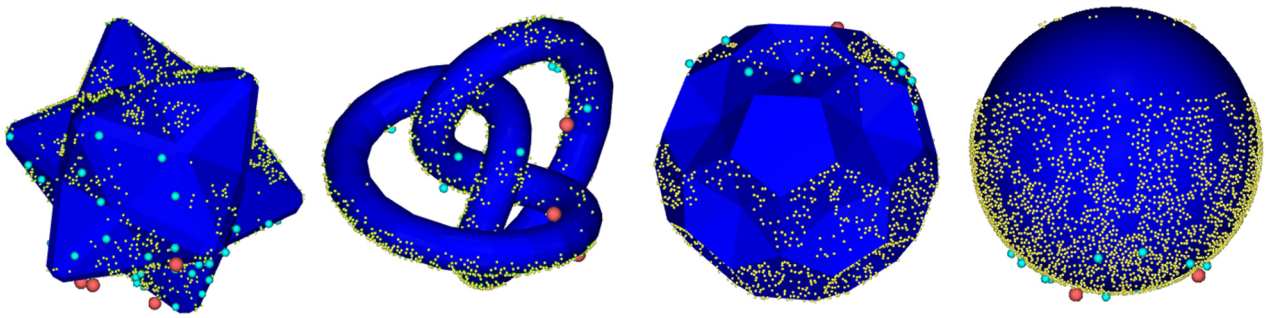

Figure 4.10: Representative images of API-carrier agglomerates (case 3) based on morphologies with 100 µm in diameter after particle-wall at a speed of 15 m/s.

For the drug-PC agglomerate, increasing velocity was not necessarily tantamount to increasing the likelihood of API particles to detach (50 µm: Figure 4.11; 100 µm: Figure 4.12). This observation was made for both modelled sizes of the PC. After detachment, the API particles encountered the protrusions of the carrier again, thus adhering to it. The protrusions and indentations of the carrier geometry spatially restricted potential trajectories of the API particles, which prevented a dispersion in every direction. Accordingly, the higher the impact velocity of the entire agglomerate, the higher the interparticle collision velocity of the detached APIs towards the carrier surfaces, which in turn favoured particle overlap and adhesion, respectively. In addition, the high velocities caused API particles to be pressed onto the opposite side of the carrier relative to the wall. Consequently, the detachment rate reached a maximum that could not be raised any further by higher collision speeds.

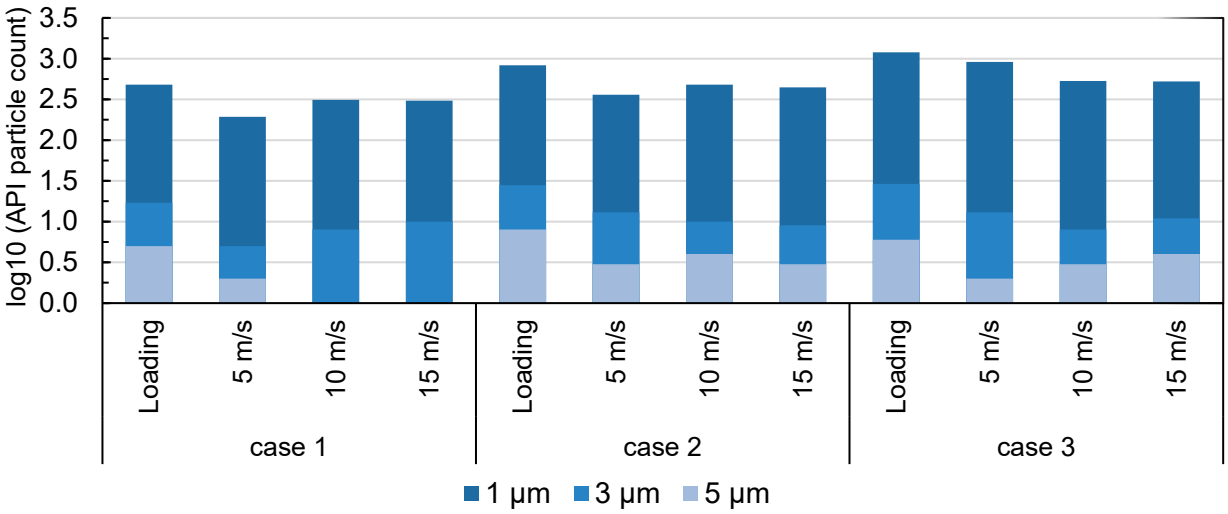

Figure 4.11: PSD of API particles adhering to the PC with 50 µm in diameter after particle-wall collision with different carrier loading and at different collision velocities (expressed as the log10 of the API particle count).

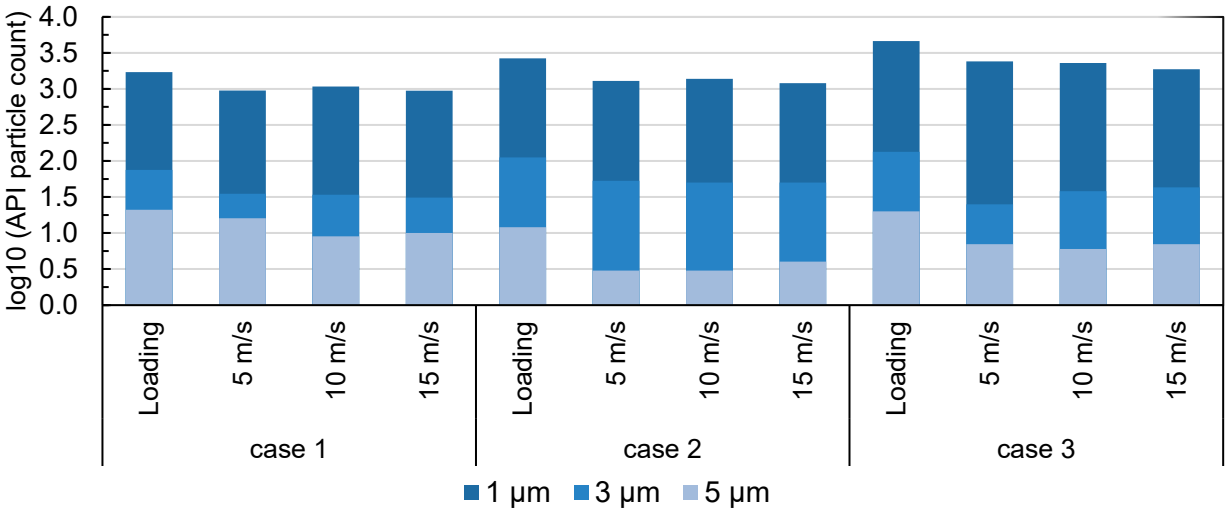

Figure 4.12: PSD of API particles adhering to the PC with 100 µm in diameter after particle-wall collision with different carrier loading and at different collision velocities (expressed as the log10 of the API particle count).

For every API size, collision simulations with drug-RK agglomerates showed that the probability of detachment increased with higher velocities. Once the agglomerate hit the plate, this carrier geometry rotated randomly causing a widespread dispersion of detached API particles. For both studied carrier sizes, the higher the collision velocity, the higher the overall probability of particles to detach (50 µm: Figure 4.13; 100 µm: Figure 4.14). At a collision speed of 5 m/s, every API particle with 5 µm in size already detached from the RK-carrier with a diameter of 50 µm. While API with 1 µm and 3 µm in diameter increasingly detached even at higher velocities, 5 µm APIs adhered to the 100 µm diameter carrier again. This finding was attributed to the relatively high volume and surface of the carrier as well as to the rotational movement, which increased the likelihood of interparticle contact.

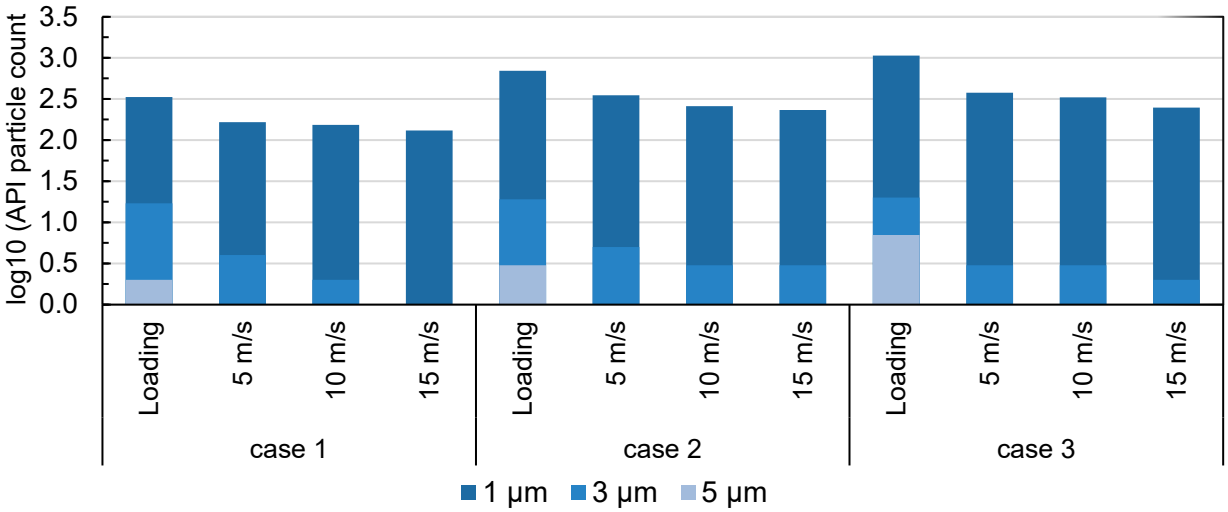

Figure 4.13: PSD of API particles adhering to the RK with 50 µm in diameter after particle-wall collision with different carrier loading and at different collision velocities (expressed as the log10 of the API particle count).

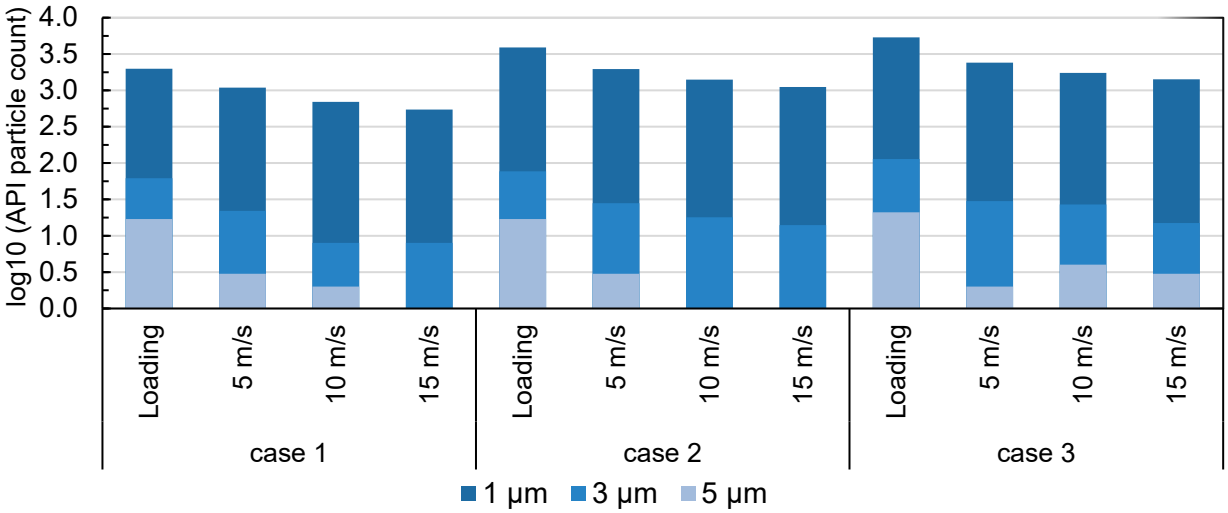

Figure 4.14: PSD of API particles adhering to the RK with 100 µm in diameter after particle-wall collision with different carrier loading and at different collision velocities (expressed as the log10 of the API particle count).

Simulating SB agglomerates, an increase in collision velocity did not promote further particle detachment beyond a certain threshold. For both carrier sizes, the number of API

particles with 1 µm in diameter decreases with increasing collision velocity. Contrarily, a minimum count of 3 µm and 5 µm API particles remained onto the carrier surface (50 µm: Figure 4.15; 100 µm: Figure 4.16). A similar phenomenon as occurring for the PC carrier explains the high probability of re-attaching after the event of collision, despite the absence of protrusions. In turn, the indentations on the carrier surface served as catch basins for previously detached API particles.

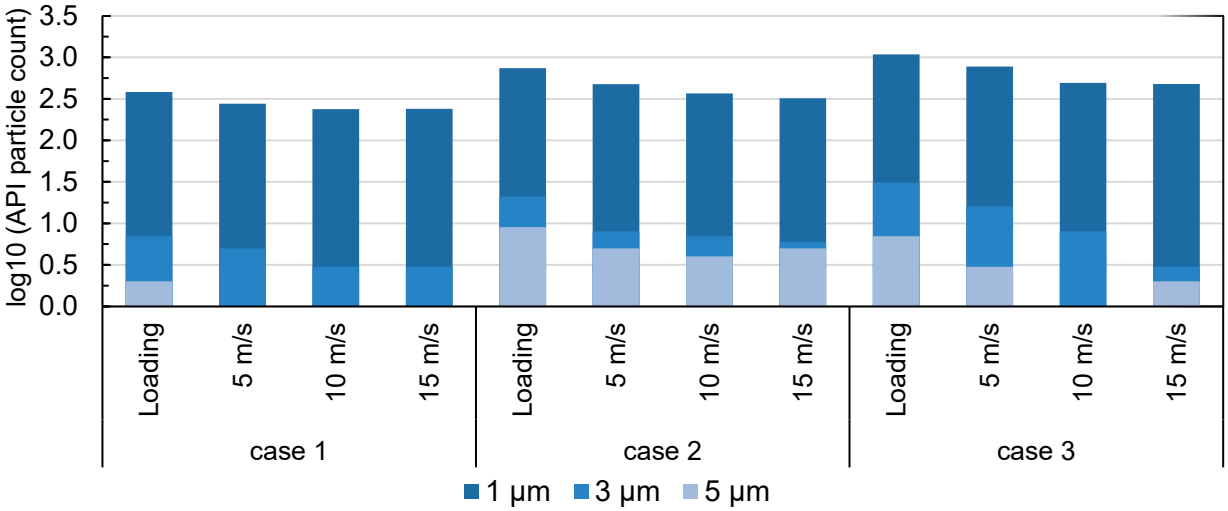

Figure 4.15: PSD of API particles adhering to the SB with 50 µm in diameter after particle-wall collision with different carrier loading and at different collision velocities (expressed as the $\log_{10}$ of the API particle count).

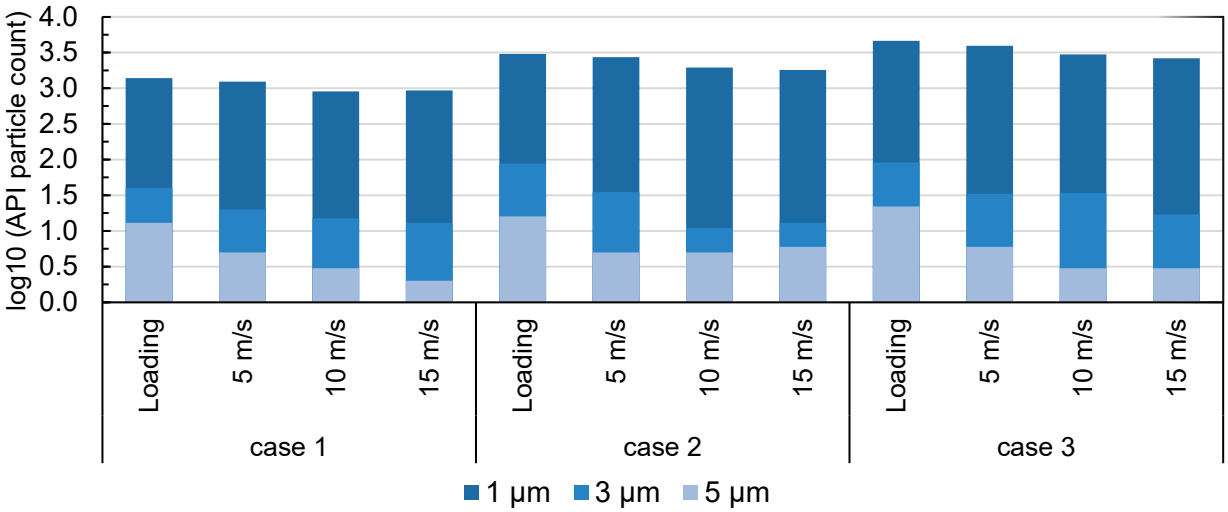

Figure 4.16: PSD of API particles adhering to the SB with 100 µm in diameter after particle-wall collision with different carrier loading and at different collision velocities (expressed as the $\log_{10}$ of the API particle count).

Spherical carrier geometries lack of edges, protrusions and indentations, explaining the absence of carrier rotation or change of direction after wall-collision. In turn, the Sphere bounced off the wall at the same angle as it collided with it. By contrast, the other geometries rotate or change direction to different degrees once they hit the wall because of their shape.

An increase in collision velocity led to press-on phenomena on the opposite hemisphere of the carrier relative to the wall which hampered particle detachment on this side. As a result of the trajectory and the press-on phenomena, the count of API particles with 3 µm and 5 µm in diameter reached a minimum threshold for both sizes of the Sphere. Further increase of the impact velocity did not necessarily increase the detachment of these particle sizes. In contrast, increasing carrier velocity caused progressively more 1 µm API particles to detach, which is attributed to their relative low surface area and thus contact overlap with the carrier particle (50 µm: Figure 4.17; 100 µm: Figure 4.18).

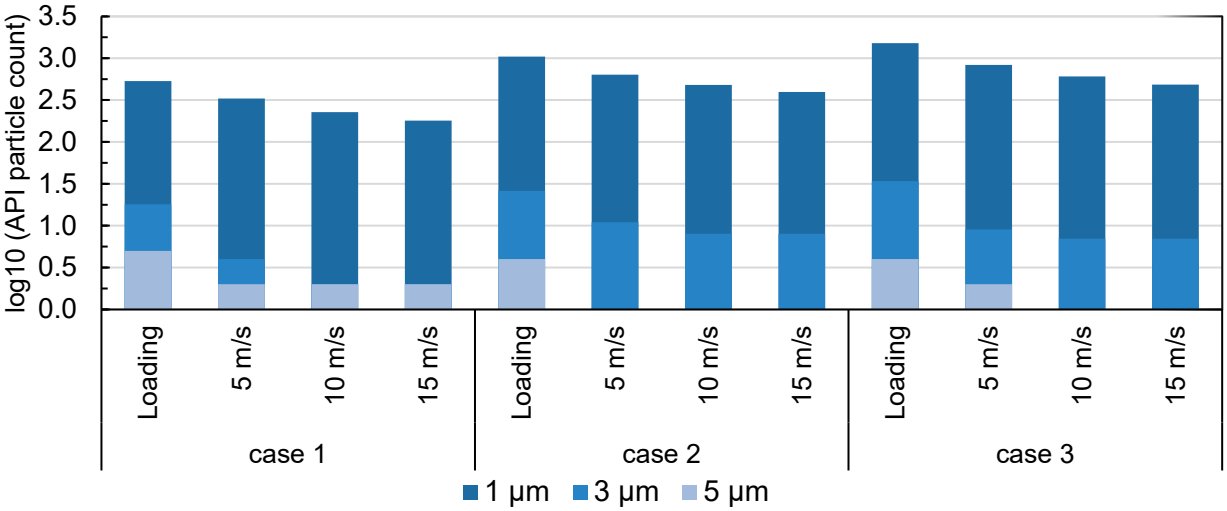

Figure 4.17: PSD of API particles adhering to the Sphere with 50 µm in diameter after particle-wall collision with different carrier loading and at different collision velocities (expressed as the $\log_{10}$ of the API particle count).

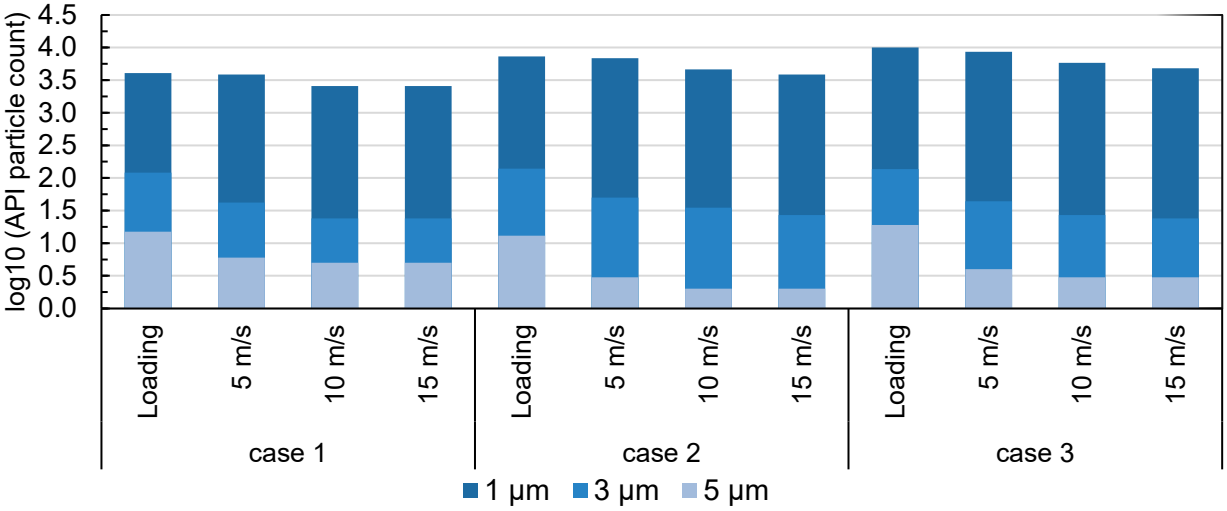

Figure 4.18: PSD of API particles adhering to the Sphere with 100 µm in diameter after particle-wall collision with different carrier loading and at different collision velocities (expressed as the $\log_{10}$ of the API particle count).

For carriers with 50 µm in size, Figure 4.19 shows the DR and CA values at each velocity and for each drug-carrier-agglomerate. For this carrier size, the simulation results indicated

morphology-, velocity- and loading-dependent drug detachment patterns. The DR of the RK, SB and Sphere increased in varying extents with increasing collision velocity and $DC_{agglomerate}$. This correlation was not found for the drug-PC agglomerate. The CA values gave inverse results, due to their mathematical correlation with the corresponding DR value.

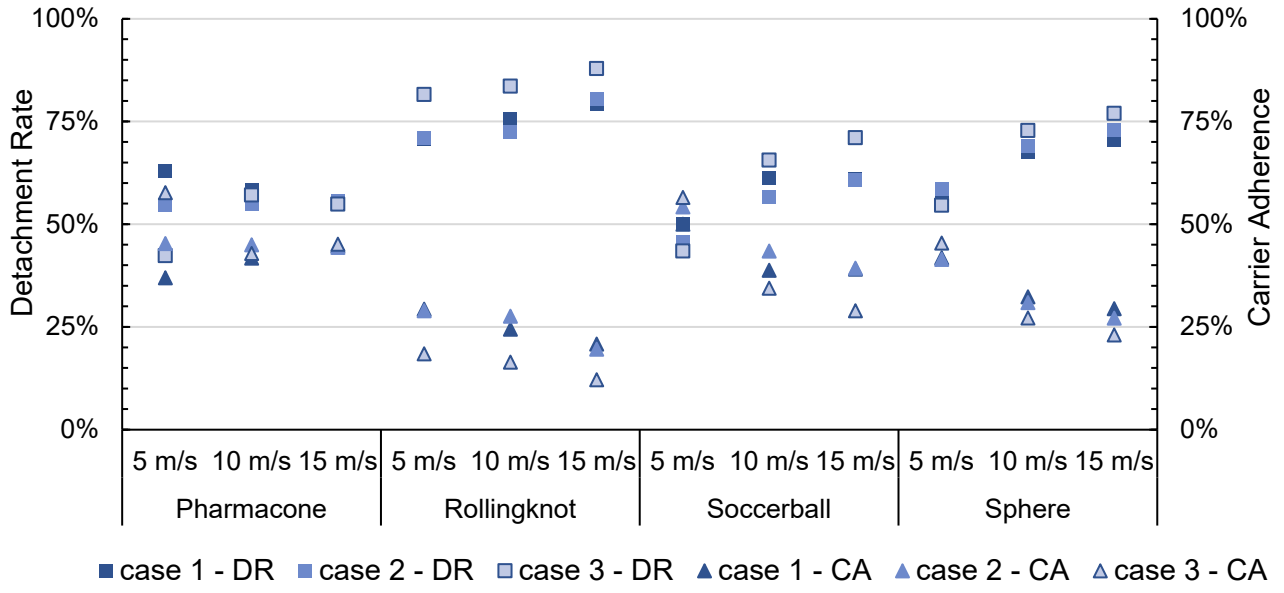

Figure 4.19: Overview on particle detachment rates (DR) and carrier adherence (CA) values after particle-wall-collisions with a velocity of 5 m/s, 10 m/s and 15 m/s for carrier with 50 µm in size.

As displayed in Table 4.10, the drug-RK agglomerate consistently showed the highest DR values when comparing every case and velocity among each other (5 m/s – case 1: 70.7 %, case 2: 71.1 %, case 3: 81.6 %; 10 m/s - case 1: 75.5 %, case 2: 72.4 %, case 3: 83.6 %; 15 m/s – case 1: 79.1 %, case 2: 80.4 %, case 3: 87.9 %). Contrarily, the API-SB agglomerate had the lowest values at a velocity of 5 m/s (case 1: 50.0 %, case 2: 45.8 %, case 3: 43.5 %). At a velocity of 10 m/s and 15 m/s, in turn, the API-PC agglomerate showed the lowest values (case 1: 58.2 %, case 2: 55.0 %, case 3: 57.1 %; 15 m/s - case 1: 55.2 %, case 2: 55.7 %, case 3: 54.9 %).

Table 4.10: Particle detachment rates (DR) after particle-wall collision at different velocities (carrier diameter: 50 µm).

DR, % [50 µm]		PC	RK	SB	Sphere
5 m/s	case 1	63.0	70.7	50.0	58.2
	case 2	54.7	71.1	45.8	58.6
	case 3	42.3	81.6	43.5	54.6
10 m/s	case 1	58.2	75.5	61.2	67.7
	case 2	55.0	72.4	56.5	69.1
	case 3	57.1	83.6	65.6	72.8

DR, % [50 µm]		PC	RK	SB	Sphere
15 m/s	case 1	55.2	79.1	61.0	70.5
	case 2	55.7	80.4	60.7	72.9
	case 3	54.9	87.9	71.1	77.0

Table 4.11 summarises the findings derived from the data presented in Figure 4.19 and Table 4.10. Despite identical simulation settings, each carrier morphology resulted in different findings.

Table 4.11: Findings derived from simulating particle-wall collisions (carrier: 50 µm in diameter).

Carrier	Findings
PC	- $\boldsymbol{DC_{agglomerate}}$had an influence on $\boldsymbol{DR}$ and $\boldsymbol{CA}$, respectively, only at low collision velocities. At 5 m/s, the higher the $\boldsymbol{DC_{agglomerate}}$, the lower the $\boldsymbol{DR}$. - High collision velocities levelled out the influence of $\boldsymbol{DC_{agglomerate}}$on $\boldsymbol{DR}$.
RK	- Highest $\boldsymbol{DR}$ in every case and at every collision velocity among the carriers. - The higher the $\boldsymbol{DC_{agglomerate}}$, the higher the $\boldsymbol{DR}$. - The higher the collision velocity, the higher the $\boldsymbol{DR}$.
SB	- At 5 m/s, the higher the $\boldsymbol{DC_{agglomerate}}$, the lower the $\boldsymbol{DR}$. - Higher collision velocities levelled out the influence of $\boldsymbol{DC_{agglomerate}}$on $\boldsymbol{DR}$ for low and medium $\boldsymbol{DC_{agglomerate}}$; high $\boldsymbol{DC_{agglomerate}}$ resulted in highest $\boldsymbol{DR}$.
Sphere	- At 5 m/s, low $\boldsymbol{DC_{agglomerate}}$ resulted in comparably high $\boldsymbol{DR}$. - Low $\boldsymbol{DC_{agglomerate}}$ resulted in relatively low $\boldsymbol{DR}$ at high collision velocities (15 m/s).

For carrier with 100 µm in size, Figure 4.20 shows the DR and CA values at each velocity and for each API-carrier-agglomerate indicating morphology- and velocity-dependant API detachment patterns.

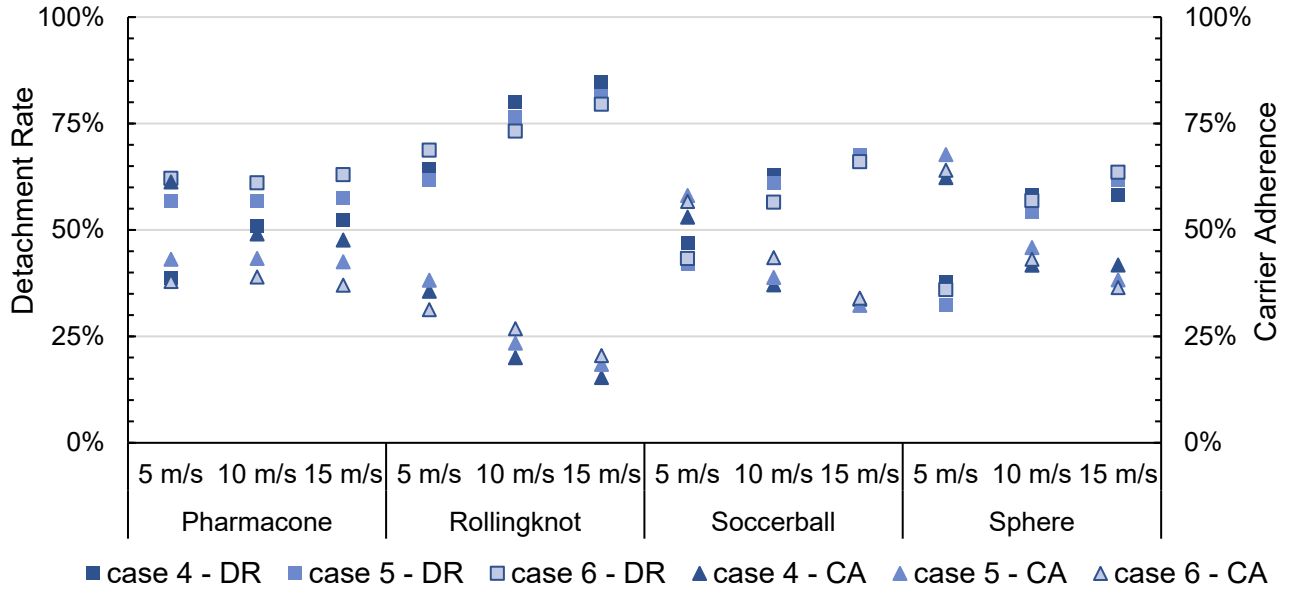

Figure 4.20: Overview on particle detachment rates (DR) and carrier adherence (CA) values after particle-wall-collisions with a velocity of 5 m/s, 10 m/s and 15 m/s for carrier with 100 µm in size.

As shown in Figure 4.20, the DR of the RK, SB and Sphere correlated in varying extents to the collision velocity. This correlation was not found for the API-PC agglomerate, whereby the $DC_{agglomerate}$ influenced the detachment of API particles from the carrier.

As shown in Table 4.12, the API-RK agglomerate consistently showed the highest DR values among each case and at every velocity (5 m/s – case 4: 64.4 %, case 5: 61.8 %, case 6: 68.7 %; 10 m/s - case 4: 80.0 %, case 5: 76.6 %, case 6: 73.2 %; 15 m/s – case 4: 84.7 %, case 5: 81.6 %, case 6: 79.5 %). Contrarily, the API-Sphere agglomerate had the lowest values at a velocity of 5 m/s (case 4: 37.7 %, case 5: 32.3 %, case 6: 36.0 %) and at 10 m/s (case 4: 58.3 %, case 5: 54.1 %, case 6: 56.9 %). At a velocity of 15 m/s, the API-PC agglomerate showed lowest DR values (case 4: 52.3 %, case 5: 57.5 %, case 6: 63.0 %). Table 4.13 summarises the findings derived from the data presented in Figure 4.12 and Table 4.12.

Table 4.12: Detachment rates (DR) after particle-wall collision at different velocities (carrier diameter: 100 µm).

DR, % [100 µm]		PC	RK	SB	Sphere
5 m/s	case 4	38.7	64.4	47.0	37.7
	case 5	56.9	61.8	41.9	32.3
	case 6	63.1	68.7	43.3	36.0
10 m/s	case 4	50.9	80.0	62.9	58.3
	case 5	56.7	76.6	61.2	54.1
	case 6	62.1	73.2	56.5	56.9
15 m/s	case 4	52.3	84.7	66.3	58.2
	case 5	57.5	81.6	67.3	61.7
	case 6	63.0	79.5	66.0	63.5

Table 4.13: Findings derived from simulating particle-wall collisions (carrier: 100 µm in diameter).

Carrier	Findings
PC	- The higher the $DC_{agglomerate}$, the higher the DR and the lower the CA, respectively. - Increase in collision velocity caused increase of DR for low/medium $DC_{agglomerate}$.
RK	- Highest DR in every case and at every collision velocity among the carriers. - The higher the collision velocity, the higher the DR (velocity-dependency). - At 10 m/s and 15 m/s, the higher the $DC_{agglomerate}$, the lower the DR.
SB	- At 5 m/s and 10 m/s, the higher the $DC_{agglomerate}$, the lower the DR. - Higher collision velocities levelled out the influence of $DC_{agglomerate}$on DR.
Sphere	- The higher the collision velocity, the higher the DR. - Change in DR due to the collision velocity partly depended on the $DC_{agglomerate}$. High $DC_{agglomerate}$ resulted in relatively high DR at 15 m/s.

Considering the $DC_{agglomerate}$ next to the collision velocity and the DR for both carrier sizes allowed for insights in optimal detachment characteristics. The carrier with 50 µm in diameter had comparably higher $DC_{agglomerate}$ values and, in most cases, higher detachment rates than 100 µm carrier. Overall, the detachment pattern and rate depended on the carrier morphology, size and collision velocity.

The simulations performed in this thesis revealed that the choice of particle morphology affected the results derived from numerical simulations of particle-wall collision. Modelling the mechanisms of particle detachment and rearrangement requires detailed consideration of the particle morphologies. In the recent past, spherical particles (Section 4.1.3) served as model carriers for simulating the properties of DPI formulations, although inaccurately depicting the morphologies, sizes, and surface characteristics of actual carriers (Chapter 2.1). The presented simulation model accounts for the presence of carriers with edges, indentations and recesses. Based on the findings of this thesis, the RK geometry would be most promising as a carrier particle, due to:

- its capability of loading a relatively high mass of API per volume resulting in a high $DC_{agglomerate}$ value and
- the highest DR in every case and at every collision velocity among the numerically studied carrier morphologies.

As previously concluded, the tested geometries still represent idealised morphologies that are presently not existent in OIPs. Nevertheless, the collision studies show that variations in morphology considerably influence the simulation results. In this thesis, differences in API detachment and rearrangement after collision were ascribed to the morphological features of the respective carriers. Therefore, it is considered that simulating API-carrier agglomerates in a realistic manner requires accounting for the actual morphologies as well as their properties.

Detailed insights into the relation of carrier morphology, carrier size and particle detachment require further quantitative and qualitative refinements of the simulation models presented in this work. On the one hand, carrier sizes between 50 µm and 100 µm, but also larger or smaller than the specified sizes should be investigated. On the other hand, to determine the optimal carrier geometry, the morphological variations should be parameterised and studied. The selected simulation settings still represent a simplification of the physical and chemical properties of excipients used in interactive blends. To account

for variations in these properties, physical and chemical attributes should also be parameterised and simulated in the future.

Representing realistic particle size distributions and shapes includes the implementation of micronised API particles as those are actually contained in interactive blends. To implement realistic particulate properties, future simulation models could base on three-dimensional scans of commonly used carrier and API materials. Numerical assessment of all details of carrier and API characteristics requires adequate computing power and speed. In summary, the numerical simulation of DPI formulations requires appropriate consideration of the multitude of particle properties.

Control of particle characteristics in terms of size, morphology, and physicochemical properties would enable validation of the simulation data. The diversity and complexity of excipient properties complicate a realistic representation in numerical simulations. Nevertheless, the proof of resulting computational findings fundamentally requires practical validation. Validating the results of this thesis would accordingly comprise fabricating and assessing the simulated morphologies.

Computational modelling of particle wall collision allows for insights in dispersion of API and carrier particles. Numerical detachment pattern and rate depends on the carrier morphology, particle size, collision velocity and simulation settings.

Chapter 5 Next level DPI carrier engineering

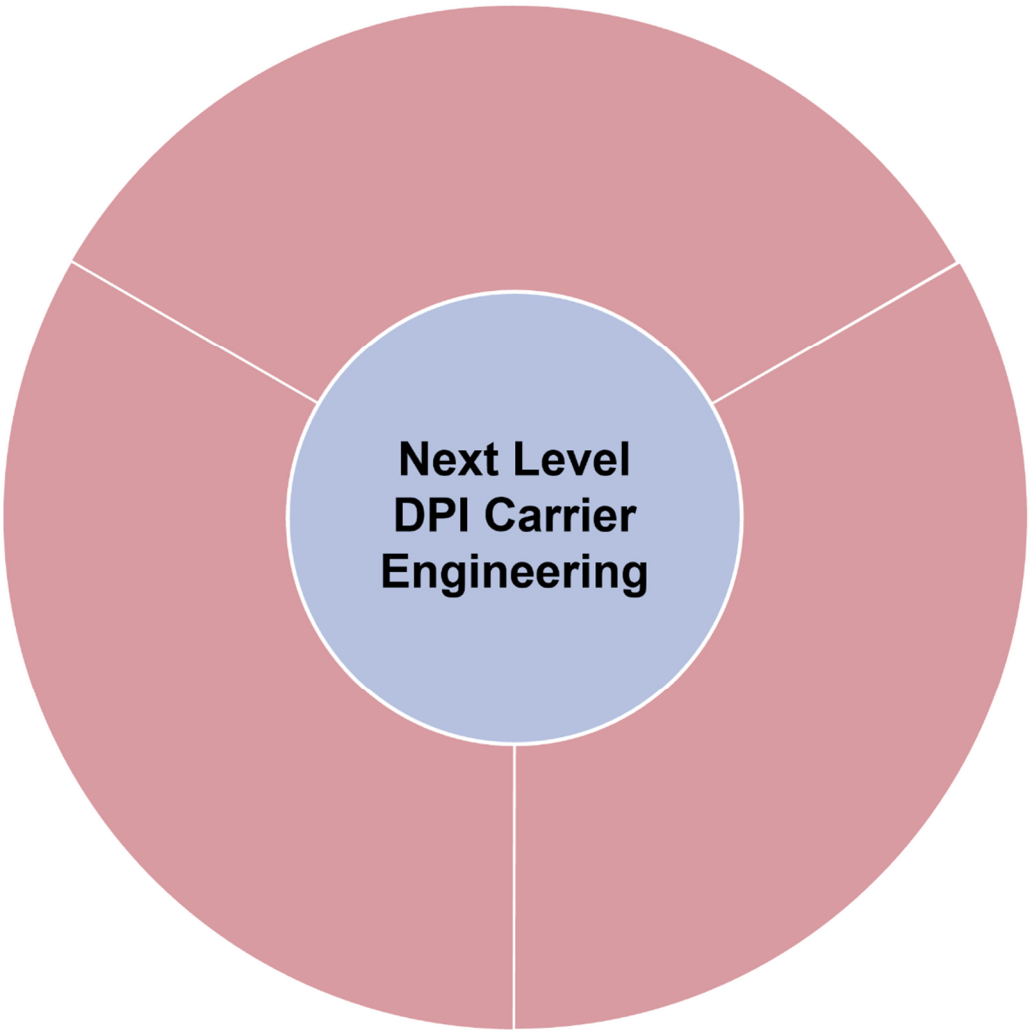

The following sections 5.1 - 5.5 were published as a part of the review named *Particle Engineering in dry powders for inhalation* in *European Journal of Pharmaceutical Sciences, Volume 172,* by Regina Scherließ, Simon Bock, Nicholas Bungert, Lena Valentin and Anna Neustock in May 2022 [64].

5.1 Considerations on next level carrier attributes

As previously described, characteristics of a DPI formulation derive from an interplay of various, mutually influential factors. To modify a specific parameter without influencing others is one of the main challenges in particle engineering. In the absence of technical capabilities, the influence of a single property such as particle shape on carrier-API interactions has not been systematically investigated. To date, lactose and mannitol serve as standard carrier excipients. Lactose crystals are considered to resemble tomahawks whereas mannitol particles show a raspberry-like appearance. The production processes of the standard, irregularly shaped carriers imply a high degree of inter-particle variability, which potentially leads to dose-to-dose variations. This variability primarily applies to particle characteristics such as morphology but also to size distribution, roughness and surface energy. To investigate the effects of isolated properties, uniform particles with constant qualities would be required. In this respect, the conventional production methods appear unsuitable because of their limited capacity to counter the variability whilst manufacturing.

5.2 Considerations on particle shape

In a conceptional setting, spherical glass beads with narrow size distribution and low morphological heterogeneity served as tangible entities to investigate particle roughness [189]. This work provided explanations for the interaction between particles on the micron scale. However, the study can be classified as fundamental research because the nature of glass beads precludes their suitability as carriers for DPI formulations. As a subsidiary outcome, this investigation posed the question of which carrier geometry and corresponding size would be most suitable. This question relates the entire process flow from production of the DPI formulation to API detachment during inhalation. The process includes proper filling of the formulation into a suitable dosage form as well as dosing while administration and the particle behaviour during inhalation. In each phase of this process, different particle properties are of particular relevance, which partly contradict each other. On the one hand, spherical shapes appear advantageous because of their intrinsic tendency to roll or flow, which facilitates processing and metering. On the other hand, irregularly shaped particles

with clefts and cavities show a relatively high surface area. Therefore, such particle shapes are associated with a high drug loading capacity [190].

5.3 Balance of particle interactions

The number of contact points between API and carrier determines the magnitude of interactions. An increase of interparticle contact area strengthens the adhesion. Despite the need for stable adhesive interactions, a particular precondition for pulmonary drug delivery using DPI blends is the detachment of the micronised drug from the carrier. Optimal as balanced adhesion ensures both the attachment during processing and the detachment of the particles during inhalation. While the contact surface area is defined by the particle morphology, the adhesion forces are largely governed by chemical interactions. Therefore, both the morphology and the chemical characteristics of the formulation components affect adhesion. Consequently, given a constant composition of the carrier material, its shape determines the adhesiveness to an API and vice versa. On this basis, balanced adhesion might similarly be achieved through optimised carrier morphology.

5.4 Particle motion and trajectories

The efficiency of DPI formulations and thus the pulmonary drug delivery is inextricably linked to the device that is used [38]. Corresponding device design determines the internal airflow and thus the dispersion of the primary drug particles in the airstream. In the transition phase from fluidisation to aerosolisation, particular importance is assigned to the trajectories of the carrier. Its physical and morphological attributes are considered to affect particle detachment, because particle motion in the surrounding airflow is generally influenced by its density, size and shape. Specifically, the morphology is a decisive factor in whether rather turbulent or laminar particle trajectories result. A turbulent motion profile, characterised by irregular and intermittent movements, potentially favours deagglomeration due to relatively high momentum transfer. On the contrary, a particle with a laminar trajectory profile remains relatively rigid with comparatively little energy diffusion and thus less probability of particle detachment [163]. Still, it is currently uncertain to what extent the morphology influences carrier turbulences, API detachment and the general aerosolisability of DPI formulations.

In conclusion, optimal carrier attributes for interactive blends are still unclear. An ideal carrier is expected to feature characteristics that are complementary to the physical and chemical properties of any given API: I) absence of chemical and morphological heterogeneity, II) good processability ensuring bulk handling and dose metering, III) tailor-

made adhesion and cohesion properties, IV) customisable drug loading capacity and V) particle trajectories in the airflow favouring API detachment off the carrier (Figure 5.1).

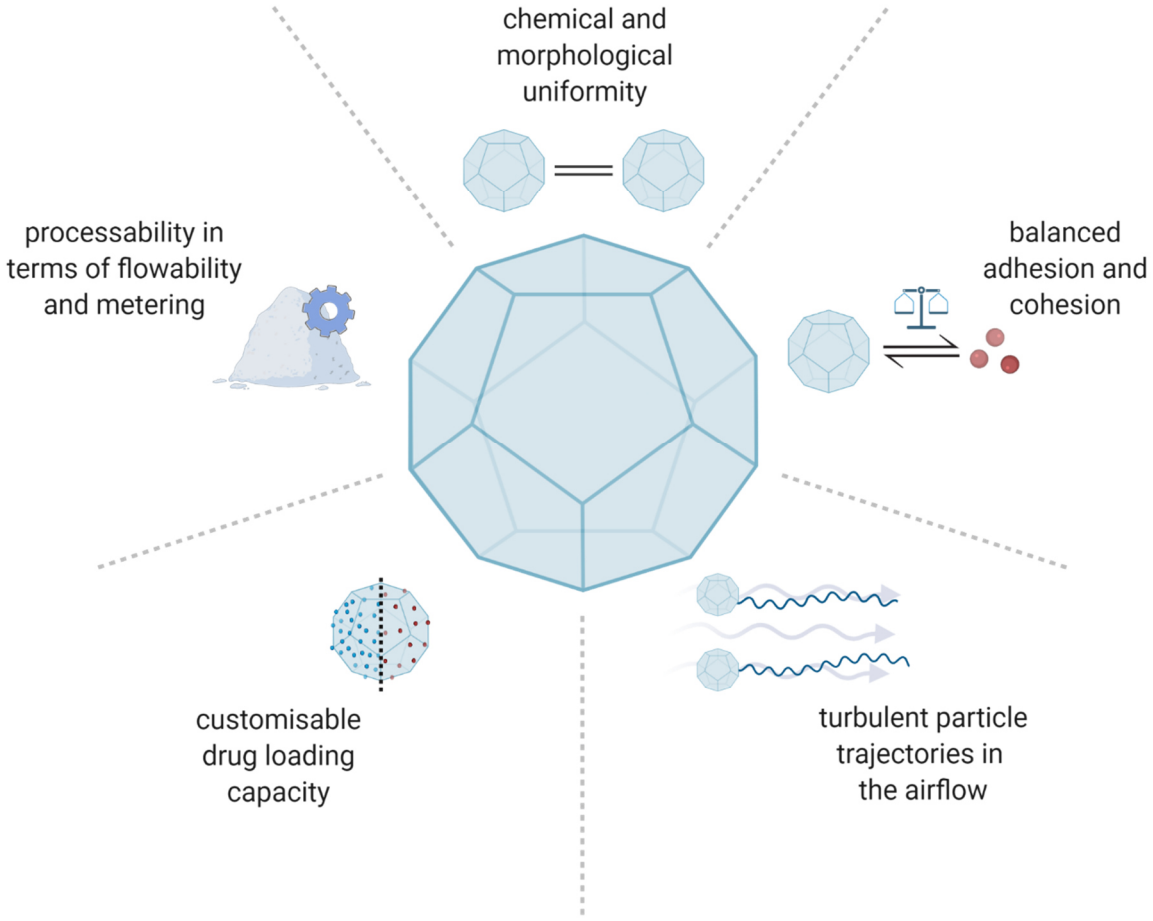

Figure 5.1: Next generation carrier engineering (adopted from [64]).

5.5 Novel approaches to manufacture microparticles

To address these fundamental issues of carrier characteristics, control of particle morphology, size and chemistry is considered an inevitable prerequisite. Novel techniques that in principle meet these requirements by replicating precisely defined structures come to the fore. However, to manufacture small objects with minute details in the sub-micrometre range is still a great challenge. Recently, various approaches reported technological feasibility of particle replication in the micron range. Such methods differ widely but are generally grouped under the umbrella term AM [106]. Despite recent technical progress in such manufacturing techniques, as elucidated by Hahn et al, production speed and capacity are still far too low compared to conventional processes. Although the fabrication of microstructures is principally feasible, these obstacles impede an implementation in pharmaceutical sciences to date. In addition, the materials applied in the described techniques are not recognised as safe for pharmaceutical purposes. Biocompatibility and

toxicity need to be investigated, because the development of dosage forms ultimately intends for human application. This is especially true for DPI formulations, as the lung is a particularly sensitive and vulnerable entry point for drugs and other airborne agents. However, such AM processes promise technical potential for systematic investigation of fundamental influences of particle morphology, size and chemical composition in the near future. One time, this technology may also be used to design and manufacture tailored carrier materials for DPI formulations.

5.6 Additive Manufacturing of particles

Particle design and manufacturing of next level carrier generations require enhanced process capabilities. To date, the manufacturing of tailor-made particles in the sense of AM currently lacks technological possibilities. Future AM processes should consequently enable the rapid production of feature-rich particles in high volumes and at low cost. As shown in Figure 5.2, manufacturing of complex geometries is within reach because of technological refinements. However, limitations in material choice and printing speed currently hamper practical application.

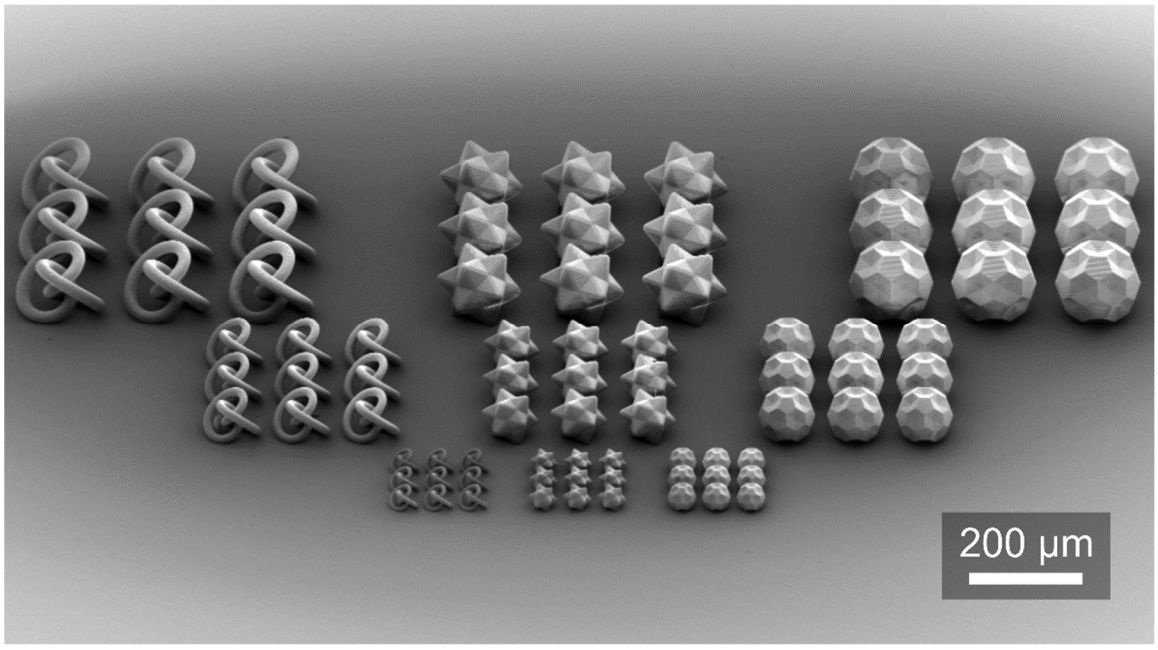

Figure 5.2: Nanoscale precision of advanced AM technologies allow intricate details for next level particle engineering (adopted from [92]).

Once thorough control over particle composition, morphology, and size becomes possible, a whole new field of research could emerge. Manufacturing of customised particles at large scales would allow to fine-tune bulk properties and thus dispersion behaviour. With such an AM-assisted particle engineering approach, researchers will have the ability to verify particle-related hypotheses experimentally. Further, researchers will explore fundamental

mechanisms of respiratory drug delivery. In-depth knowledge on the mechanisms of drug delivery would in turn allow for optimising DPI formulations (Figure 5.3).

Figure 5.3: In the future, application of AM methodologies will allow to fabricate customised particles for enhanced respiratory drug delivery.

As future options, innovative and disruptive concepts can be envisioned such as designing and manufacturing particles that feature relatively high elasticity or that change their characteristics due to external stimuli. For DPI carrier particles, it would be highly valuable if the tendency to form agglomerates with API particles changes during the inhalation phase. In this case, the stimuli could comprise particle specific or environmental parameters such as acceleration, moisture, or temperature. Optimally, a corresponding decrease of adhesion would lead to higher detachment rates and thus enhanced deposition of API particles in the respiratory tract. However, to manufacture particles that change their properties in response to a certain stimulus, namely four-dimensional particles, still remains an inscrutable endeavour.

At the particle level, an ideal DPI carrier features characteristics
that are complementary to the properties of any given API.
Current engineering approaches lack control over such properties.
Although limitations in speed and choice of materials,
novel approaches enable the manufacturing of tailored particles.

Chapter 6 Overall discussion and conclusion

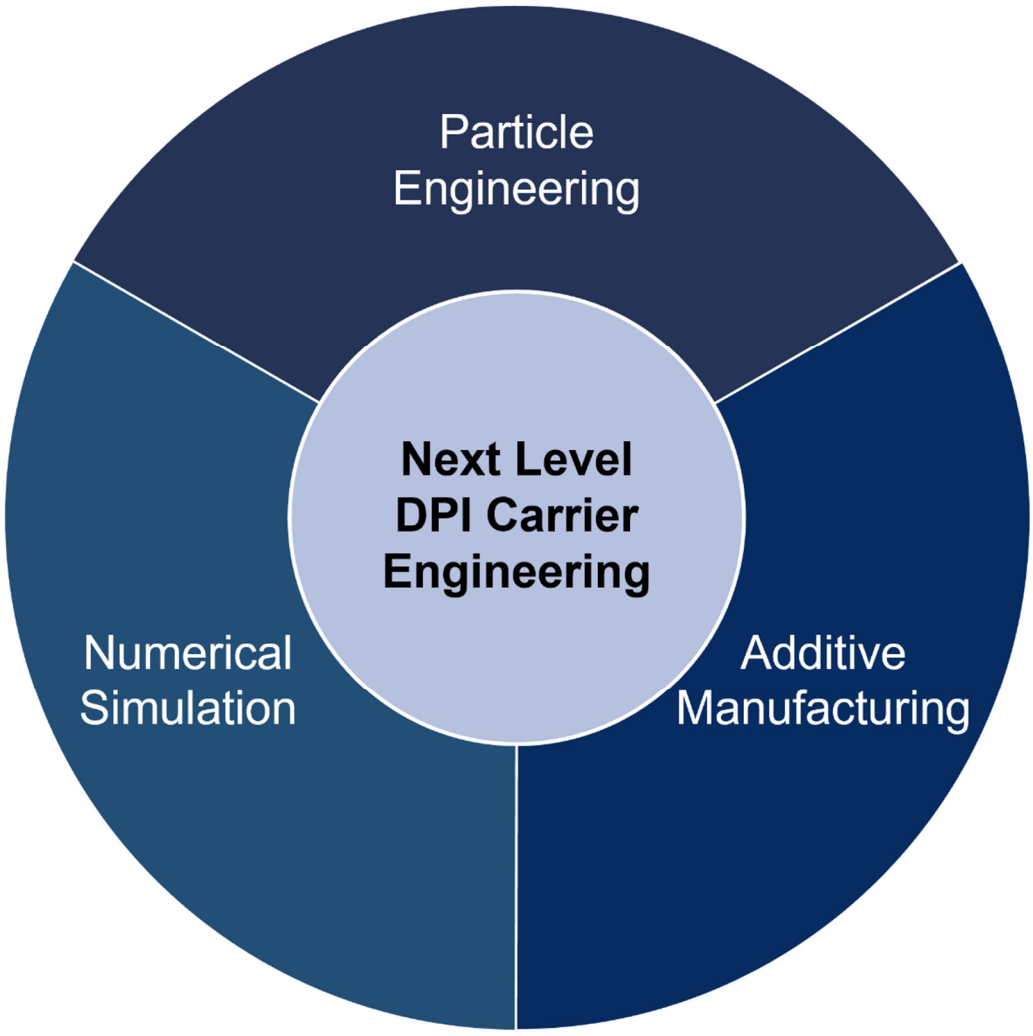

6.1 Comprehensive discussion on the preceding chapters

The pulmonary route is a well-established way to treat both local and systemic diseases. For treatments via the pulmonary route, a variety of dosage forms exist. Chapter 1 introduced fundamental mechanisms of respiratory drug delivery. In addition, it described formulation strategies that currently exist for powder based OIPs, namely interactive blends, softpellets and engineered powders. Describing different influencing factors on aerodynamic performance, this chapter outlined the complexity of formulating DPI formulations.

In chapter 2, spherical MCC particles were presented as model carrier material for interactive blends. These particles served as carrier because of their relatively uniform shape in comparison to commonly used lactose or mannitol carriers, eliminating the effect of heterogeneity in size and morphology. This uniformity was postulated as a prerequisite for drawing conclusions about the influence of morphological characteristics on aerodynamic performance. Aerodynamic assessments revealed evidence of the general suitability of MCC spheres as carrier particles. As an additional finding, the dispersion efficiency of respective blends depended on the type of inhaler. In comparison to a capsule-based HandiHaler®, the reservoir-based Novolizer® device led to a superior aerodynamic performance. Dispersing efficiency was proven to be a function of the device design, with a cyclone-based dispersing system proving advantageous when using MCC pellets as carrier particles. Dispersing efficiency was also indicated to be influenced by the carrier size. The studies showed that the smaller the MCC pellets, the higher the aerodynamic performance.

Besides the investigation of the influence of carrier morphology and size, this chapter dealt with how alternating the carrier surface influences the aerodynamic performance. To modify the chemical composition of the carriers' surface, the respective particles were coated with various aromatic amino acids. In a Novolizer® device, coated carriers resulted in superior aerodynamic performance compared to uncoated MCC particles. This superiority was evident with carriers of different PSDs.

Previous research on surface modification of carrier particles has involved the addition of specific agents, e.g. magnesium stearate or leucine, to conventional carrier particles. One limitation of such processing approaches is the lack of control over particle size and uniformity, which logically precludes examining isolated carrier properties. By coating spherical and more uniform material with amino acids which have not been examined previously, this work presented a novel approach to investigate the effect of particle chemistry on aerodynamic performance.

The approach described provided relatively tight control of carrier size and morphology compared to previous research. Despite this control, the findings of this chapter revealed that aerodynamic performance was not directly related to these specific properties. Thus, the fundamental challenge of relating formulation properties to performance could not be fully solved with this approach. A limitation of this study was that the deployed processes lack of sufficient control on coating quantity and quality. In addition, the carrier particles were still not strictly equal in terms of particle size and morphology. In summary, investigating the effect of isolated properties was confirmed to be highly challenging. The findings emphasised the necessity to closely match formulation and device for achieving high aerodynamic performance.

The studies in chapter 3 aim at enhancing aerodynamic performance of DPI formulations by applying AM. This chapter introduced the use of additively manufactured objects, namely DAs, with interactive blends and softpellet formulations.

To study the effect of DAs on aerodynamic performance of interactive blends, a fractional factorial design was employed for investigating various influencing factors. Thus, various blends with different APIs, drug contents, capsule filling, carrier materials and DA morphologies were tested in a Twister® device. The results revealed that the performance was primarily affected by the choice of carrier material and the drug content of the blend, rather than by carrier filling or DA morphology. Furthermore, the dispersion efficiency was driven by the chemical properties of the API.

Chemical properties of the API and environmental conditions also affected the dispersion of softpellet formulations. For this type of DPI formulation, the complex geometries serving as DAs enhanced the aerodynamic performance in a Twister® device. The data indicated that the influence of the DA on particle dispersion depended on the DA morphology. Future studies at this application level should aim at fathoming the rationale for this dependency finding the optimal fit of DA size and shape.

In total, these studies provided evidence of the usefulness of DAs in influencing the dispersion of powder formulations for inhalation. The studies showed that the dispersion efficiency is governed by the formulation and the particle characteristics, respectively. A limitation of this study was that it comprised the examination of a single inhaler only. Varying the device design implies a variation in fluidic patterns, which in turn results in deviating trajectories of particles and DAs. Consequently, future research should involve the investigation of different device designs on the dispersion.

In summary, the findings of this chapter do not allow a general statement about the usefulness of DAs. Such a statement would require an investigation DAs of different shapes and sizes in several devices. Further research on this application level should aim at a systematic investigation of complementary and thus optimal device and DA designs. Furthermore, such a systematic approach should account for the interplay of formulation and device.

Chapter 4 covered numerical simulation studies on particle interactions. Using DEM modelling, these studies described the formation and the dispersion of drug-carrier agglomerates as they relate to interactive blends.

Modelling the particle behaviour was shown to provide insights into morphological influences on carrier loading and detachment. Specifically, simulating the loading of various carrier morphologies in different sizes with API particles revealed that the drug loading capacity depended on both carrier size and shape. Likewise, carrier morphology and size influenced the numerically evaluated detachment patterns after particle-wall collision. In this study, the detachment was further shown to be a function of collision speed.

A general limitation of simulations studies was that the selected simulation settings still represent a simplification of the physical and chemical properties of the ingredients used in interactive blends. Experimental validation of the results would inevitably require the fabrication of the investigated carrier designs and thus corresponding technologies, which are under development and will be available in near future.

Chapter 5 covered considerations on optimal carrier attributes and recent advances in manufacturing and engineering to obtain such particles. To conclude, an ideal DPI carrier would feature characteristics that are complementary to the properties of any given API and would take into account inhaler- and patient-specific needs. However, current engineering techniques lack control over such properties.

Despite limitations in speed of manufacture and choice of materials still prevail, novel approaches principally enable the manufacturing of geometries with desired shape in the micrometre range. With recent refinements in AM technologies, creating tailored particles is considered within reach. Chapter 5 introduced Two-Photon-Polymerisation (TPP) as a promising technology to create carrier particles with any desired design. Despite current technological capacities, a considerable refinement would still be needed to enable the manufacturing of such particles in sufficient quantities for practical testing and validation.

6.2 Conclusion and outlook

The overarching objective of this thesis was to identify gaps in research on respiratory drug delivery that could potentially be bridged with the help of AM and NS.

Specifically, this thesis introduces the use of AM at two levels of application. First, at a level between device design and formulation development. Inserting additively manufactured objects with complex geometrical structures is a novel strategy to promote particle deagglomeration (Figure 6.1).

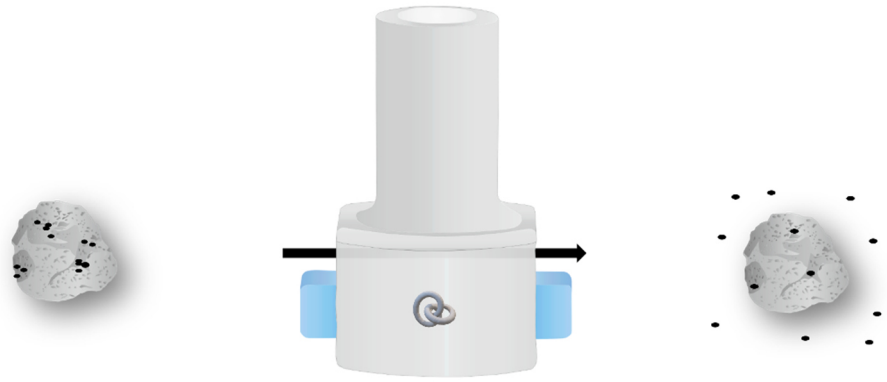

Figure 6.1: Schematic illustration of free levitating objects inserted into an inhaler device promoting deagglomeration of particles.

Second, at the particle level. This thesis presents a vision for a synthesis of AM technologies and *in silico* methods to develop and create optimised DPI carrier particles (Figure 6.2).

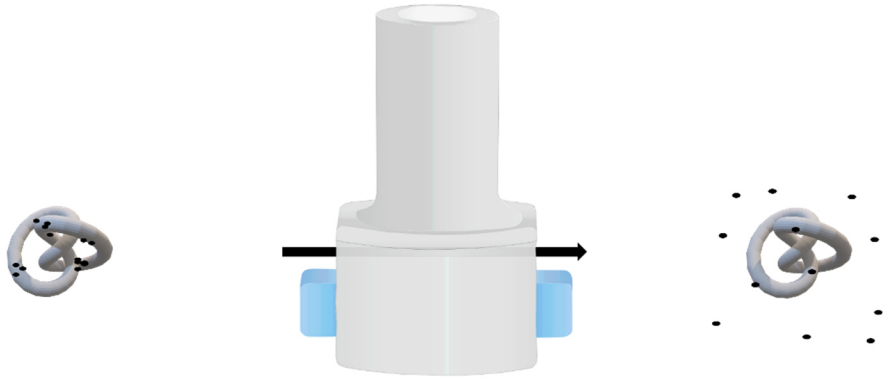

Figure 6.2: Schematic illustration of optimised carrier particles in terms of deagglomeration.

Implementing AM in the development of DPI formulations currently lacks technological capabilities in terms of process speed, accuracy, and capacity. It is therefore inevitable to research on novel materials that are applicable in advanced AM processes with outstanding resolution. Once the technical prerequisites for printing any object in any size in high

quantities are in place, the question arises which morphology should be optimally created. In turn, optimising the morphology of DPI carrier particles requires the analysis of all influencing factors. Specifically, these factors include API, excipient, device, and patient characteristics.

As an additional input for particle design thinking processes, numerical simulations provide valuable insights in the mechanisms of particle dispersion. Simulating the behaviour of API and excipient particles in the device during inspiration complements the findings that result from practical investigations. Prior to a manufacturing procedure, simulations can be conducted to pre-evaluate the most suitable particle design. Hence, analysing and combining practical with numerical datasets close the loop of iterative particle optimisation (Figure 6.3).

In the best-case scenario, *in silico* and *in vitro* methods will converge with *in vivo* studies, whereby each method would complement the other. On the one hand, such holistic approaches will help expanding the current knowledge on drug delivery to the lungs. On the other hand, comprehensive understanding of particle behaviour will provide a rationale for optimising particles. Ultimately, such a methodology paves the way for developing and manufacturing customised particles and thus novel high-performance DPI formulations.

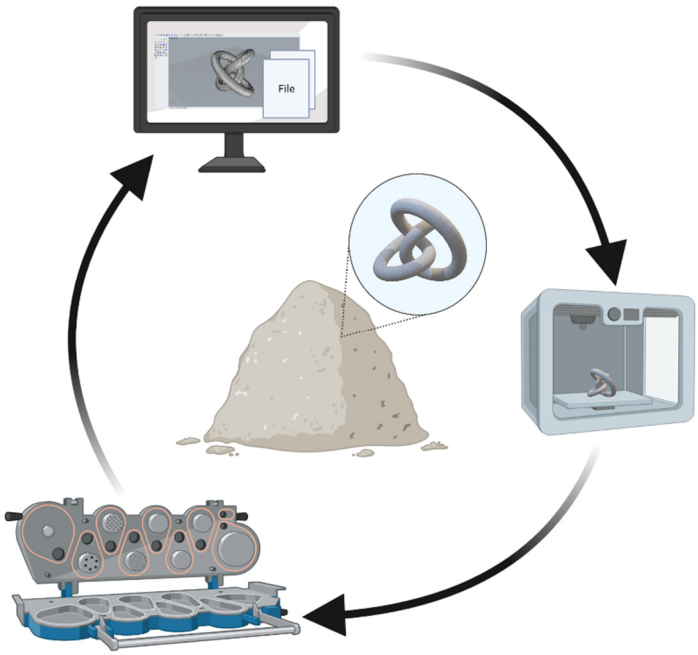

Figure 6.3: Iterative loop of particle design, manufacturing, and in vitro evaluation. Particle designs deriving from numerical studies will be fabricated using AM techniques. The particles created in bulk will then be evaluated using standardised procedures (e.g. impaction analysis). In turn, resulting *in vitro* data will enable to optimise the particle design and thus performance.

Overall, this thesis anticipates AM and NS as novel strategies to engineer and evaluate particles for use in DPI formulations. The results point to the need of further refinements in manufacturing and simulation capabilities. Future researchers should consider a combination of these techniques to enable optimisation and customisation of particles.

Focussing on the patients' unmet needs in respiratory drug delivery, a pharmaceutical should be effective but also affordable. Therefore, developing DPI formulations based on a particle customisation approach is also an economic issue. From an economic point of view, customisation on a particle level is expected to be very costly due to the complexity of the corresponding process. In turn, complexity and costs of creating customised particles impede an implementation in healthcare in the near future.

A more tangible concept in the medium term would be the use of numerically evaluated and additively manufactured DAs into an inhaler. Principally, this thesis has shown the impact of such auxiliaries on the deagglomeration of different DPI formulations. Depending on the formulation, the use of an DA affects the dispersion and thus the drug delivery to the lungs. In the future, a holistic view on formulation characteristics, DA and device design will enable an increase of respirable drug particles. Similar to the design thinking process of particles, the optimal design of DAs could be accessible by using numerical simulations in combination with *in vitro* and in *in-vivo* studies.

Appendices

Appendix A – Results of Chapter 2

Particle size distribution of processed MCC spheres

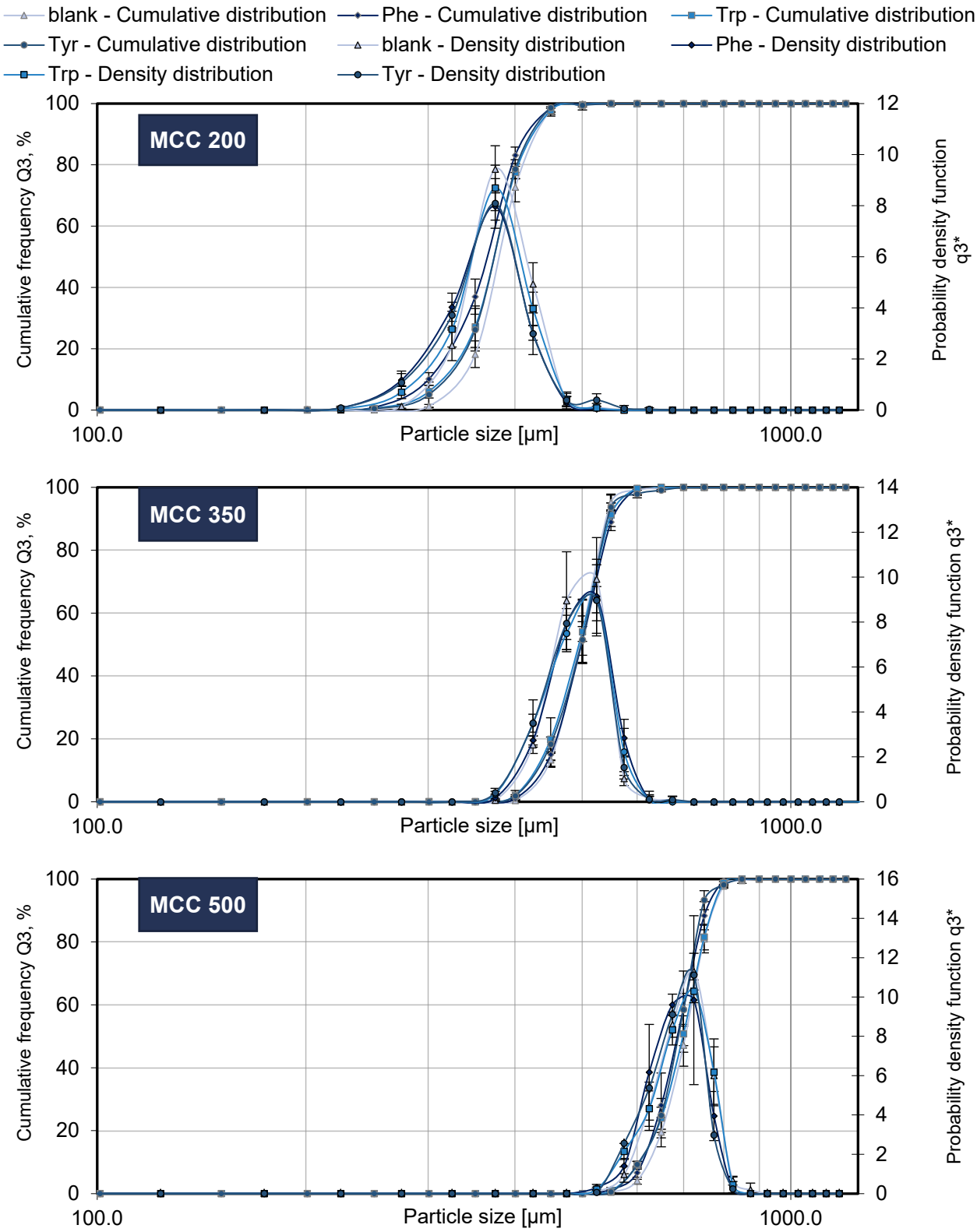

Figure App.1: Graphical illustration of PSD for uncoated and coated MCC spheres; n = 3.

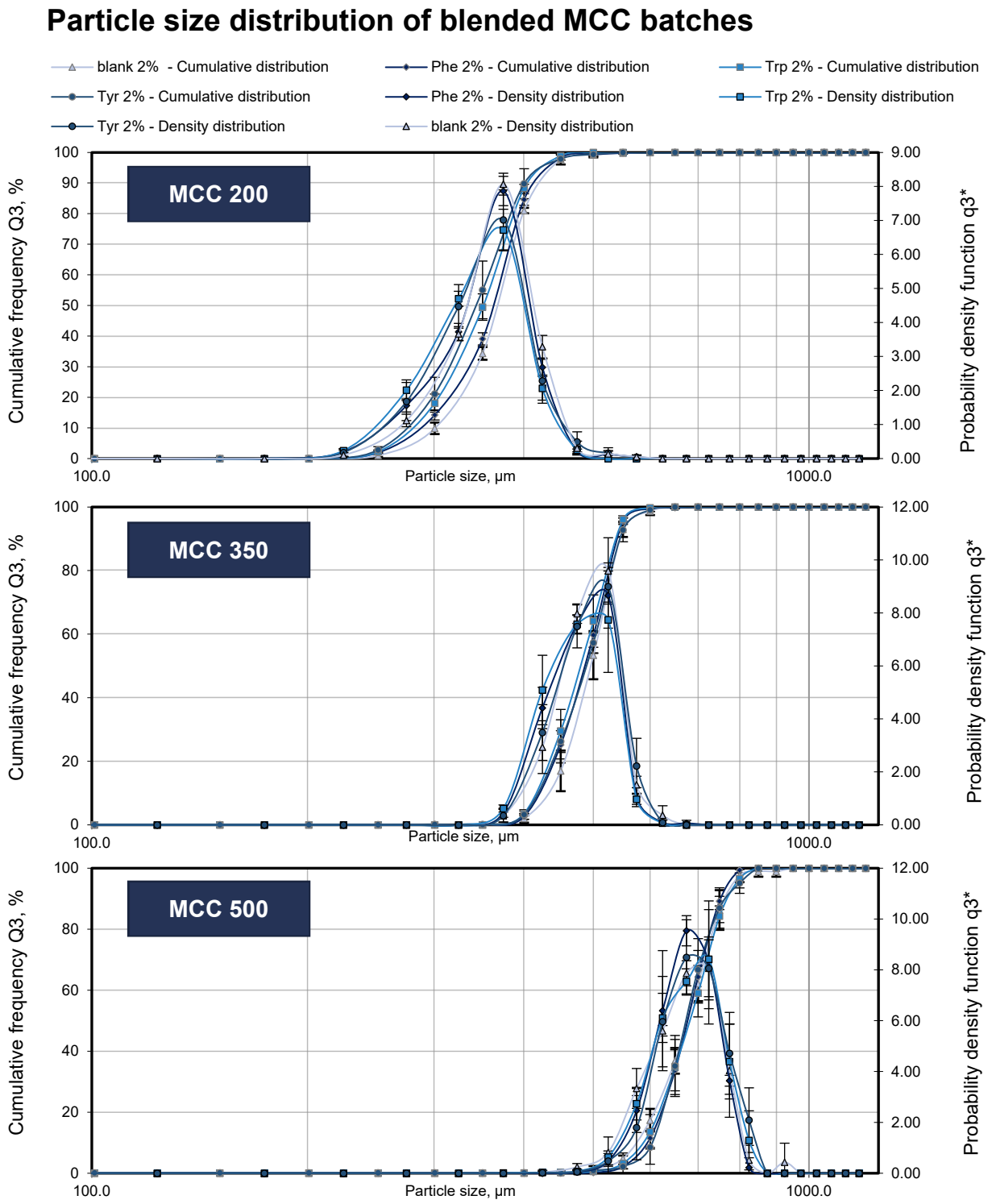

Figure App.2: Graphical illustration of PSD for blended MCC spheres; n = 3.

Aerodynamic particle sizing of interactive blends – Handihaler®

Table App.1: FPF, FPD and MMAD of the uncoated and coated MCC spheres; HandiHaler®; n = 3.

Batch	MCC 200$_{uncoated}$	MCC 350$_{uncoated}$	MCC 500$_{uncoated}$
FPF < 5 µm	5.25 % ± 4.66 %	8.96 % ± 6.26 %	7.49 % ± 7.22 %
FPF < 3 µm	4.14 % ± 1.29 %	5.60 % ± 2.21 %	6.03 % ± 0.28 %
FPF < 1 µm	0.80 % ± 0.52 %	1.26 % ± 0.81 %	1.68 % ± 0.09 %
FPD < 5 µm	20.8 µg ± 5.12 µg	21.5 µg ± 5.58 µg	29.6 µg ± 1.76 µg
FPD < 3 µm	18.4 µg ± 4.68 µg	19.2 µg ± 5.17 µg	24.7 µg ± 1.50 µg
FPD < 1 µm	3.47 µg ± 2.15 µg	4.21 µg ± 2.19 µg	6.88 µg ± 0.46 µg
MMAD	1.73 µm ± 0.12 µm	1.65 µm ± 0.09 µm	1.88 µm ± 0.03 µm

Aerodynamic particle sizing of interactive blends – Novolizer®

Table App.2: FPF values of the uncoated and coated MCC spheres; Novolizer®; n = 3.

Batch	FPF < 5 µm	FPF < 3 µm	FPF < 1 µm
MCC $200_{uncoated}$	35.5 % ± 2.12 %	33.0 % ± 2.35 %	8.55 % ± 0.80 %
MCC 200_{Phe}	45.1 % ± 2.58 %	42.4 % ± 2.49 %	11.8 % ± 0.77 %
MCC 200_{Trp}	46.6 % ± 3.72 %	43.2 % ± 3.40 %	11.3 % ± 0.96 %
MCC 200_{Tyr}	46.2 % ± 7.29 %	42.7 % ± 7.43 %	12.2 % ± 2.45 %
MCC $350_{uncoated}$	11.9 % ± 1.42 %	11.0 % ± 1.32 %	2.56 % ± 0.30 %
MCC 350_{Phe}	34.5 % ± 2.71 %	32.1 % ± 2.53 %	9.40 % ± 1.62 %
MCC 350_{Trp}	27.0 % ± 2.14 %	25.1 % ± 2.01 %	7.03 % ± 0.42 %
MCC 350_{Tyr}	44.6 % ± 1.53 %	41.3 % ± 1.30 %	12.5 % ± 0.12 %
MCC $500_{uncoated}$	12.6 % ± 1.84 %	11.5 % ± 1.67 %	2.70 % ± 0.50 %
MCC 500_{Phe}	27.1 % ± 0.59 %	24.7 % ± 0.61 %	6.87 % ± 0.24 %
MCC 500_{Trp}	24.9 % ± 2.56 %	22.8 % ± 2.35 %	6.88 % ± 0.58 %
MCC 500_{Tyr}	25.1 % ± 2.19 %	22.9 % ± 1.97 %	6.55 % ± 0.59 %

Table App.3: Fine Particle Dose (FPD) of the uncoated and coated MCC spheres; Novolizer®; n = 3.

Batch	FPD < 5 µm	FPD < 3 µm	FPD < 1 µm
MCC $200_{uncoated}$	77.2 µg ± 3.28 µg	71.8 µg ± 3.21 µg	18.6 µg ± 0.92 µg
MCC 200_{Phe}	93.8 µg ± 17.6 µg	88.2 µg ± 16.4 µg	24.6 µg ± 4.19 µg
MCC 200_{Trp}	96.1 µg ± 6.80 µg	89.2 µg ± 6.25 µg	23.4 µg ± 2.29 µg
MCC 200_{Tyr}	97.5 µg ± 17.8 µg	90.2 µg ± 18.0 µg	25.8 µg ± 5.56 µg
MCC $350_{uncoated}$	21.6 µg ± 3.89 µg	19.9 µg ± 3.59 µg	4.63 µg ± 0.74 µg
MCC 350_{Phe}	58.3 µg ± 4.11 µg	54.2 µg ± 3.86 µg	15.8 µg ± 2.59 µg
MCC 350_{Trp}	40.7 µg ± 5.02 µg	37.7 µg ± 4.59 µg	10.6 µg ± 1.25 µg
MCC 350_{Tyr}	71.5 µg ± 0.12 µg	66.3 µg ± 0.10 µg	20.1 µg ± 0.47 µg
MCC $500_{uncoated}$	21.0 µg ± 4.11 µg	19.3 µg ± 3.74 µg	4.53 µg ± 1.09 µg
MCC 500_{Phe}	68.5 µg ± 7.56 µg	62.5 µg ± 6.78 µg	17.3 µg ± 1.40 µg
MCC 500_{Trp}	40.3 µg ± 7.04 µg	36.9 µg ± 6.26 µg	11.1 µg ± 1.57 µg
MCC 500_{Tyr}	49.0 µg ± 11.3 µg	44.6 µg ± 10.1 µg	12.8 µg ± 2.97 µg

Appendix B – Results of Chapter 3

Aerodynamic particle sizing of interactive blends

Table App.4: FPF and MMAD of interactive blends composed of IL120 and SBS; n = 3.

Batch	FPF < 5 µm	FPF < 3 µm	FPF < 1 µm	MMAD
A	8.28 % ± 2.5 %	6.73 % ± 2.09 %	0.45 % ± 0.18 %	2.21 µm ± 0.03 µm
B	12.1 % ± 3.72 %	9.66 % ± 3.01 %	0.67 % ± 0.21 %	2.26 µm ± 0.02 µm
C	21.0 % ± 1.01 %	16.4 % ± 0.79 %	2.12 % ± 0.34 %	2.52 µm ± 0.50 µm
D	17.6 % ± 2.01 %	13.7 % ± 1.88 %	1.63 % ± 0.3 %	2.24 µm ± 0.07 µm
E	12.3 % ± 2.49 %	9.92 % ± 2.07 %	0.80 % ± 0.2 %	2.24 µm ± 0.03 µm
F	11.8 % ± 0.99 %	9.99 % ± 1.03 %	0.63 % ± 0.2 %	2.31 µm ± 0.16 µm
G	16.4 % ± 1.92 %	12.6 % ± 1.51 %	1.44 % ± 0.37 %	2.28 µm ± 0.03 µm
H	21.4 % ± 1.31 %	16.9 % ± 1.01 %	2.31 % ± 0.42 %	2.16 µm ± 0.02 µm
I	15.3 % ± 0.79 %	12.1 % ± 0.59 %	1.70 % ± 0.42 %	2.18 µm ± 0.05 µm

Table App.5: FPF and MMAD of interactive blends composed of IL251 and SBS; n = 3.

Batch	FPF < 5 µm	FPF < 3 µm	FPF < 1 µm	MMAD
A	35.7 % ± 2.51 %	29.2 % ± 2.38 %	4.10 % ± 0.64 %	2.46 µm ± 0.12 µm
B	22.4 % ± 0.51 %	18.0 % ± 0.48 %	1.58 % ± 0.08 %	2.44 µm ± 0.03 µm
C	40.3 % ± 2.15 %	33.7 % ± 2.05 %	4.95 % ± 0.89 %	2.08 µm ± 0.06 µm
D	39.0 % ± 0.88 %	32.5 % ± 0.64 %	4.56 % ± 0.46 %	2.11 µm ± 0.02 µm
E	22.3 % ± 3.21 %	17.9 % ± 2.3 %	2.16 % ± 0.19 %	2.45 µm ± 0.09 µm
F	19.9 % ± 4.75 %	15.8 % ± 3.99 %	2.74 % ± 1.46 %	2.54 µm ± 0.12 µm
G	39.9 % ± 0.8 %	32.8 % ± 0.62 %	4.47 % ± 0.18 %	2.18 µm ± 0.04 µm
H	35.7 % ± 2.51 %	29.2 % ± 2.38 %	4.10 % ± 0.64 %	2.24 µm ± 0.07 µm
I	29.2 % ± 0.78 %	23.4 % ± 0.67 %	3.65 % ± 0.29 %	2.34 µm ± 0.02 µm

Table App.6: FPF and MMAD of interactive blends composed of IL120 and BUD; n = 3.

Batch	FPF < 5 µm	FPF < 3 µm	FPF < 1 µm	MMAD
A	4.53 % ± 0.46 %	2.78 % ± 0.31 %	0.23 % ± 0.02 %	3.28 µm ± 0.11 µm
B	3.93 % ± 0.82 %	2.38 % ± 0.56 %	0.2 % ± 0.04 %	3.3 µm ± 0.12 µm
C	10.5 % ± 1.09 %	7.86 % ± 1.05 %	0.98 % ± 0.14 %	2.41 µm ± 0.08 µm
D	11.4 % ± 1.17 %	8.37 % ± 0.89 %	1.01 % ± 0.19 %	2.42 µm ± 0.03 µm
E	4.77 % ± 1.00 %	2.89 % ± 0.70 %	0.22 % ± 0.03 %	3.35 µm ± 0.15 µm
F	4.91 % ± 0.19 %	2.87 % ± 0.19 %	0.23 % ± 0.01 %	3.49 µm ± 0.09 µm
G	12.9 % ± 1.87 %	9.46 % ± 2.03 %	0.98 % ± 0.57 %	2.53 µm ± 0.31 µm
H	11.0 % ± 2.54 %	7.99 % ± 2.21 %	0.86 % ± 0.54 %	2.56 µm ± 0.17 µm
I	7.69 % ± 0.31 %	4.85 % ± 0.21 %	0.28 % ± 0.08 %	2.96 µm ± 0.06 µm

Table App.7: FPF and MMAD of interactive blends composed of IL251 and BUD; n = 3.

Batch	FPF < 5 µm	FPF < 3 µm	FPF < 1 µm	MMAD
A	12.64 % ± 3.46 %	8.95 % ± 2.76 %	0.93 % ± 0.34 %	3.49 µm ± 0.45 µm
B	13.14 % ± 1.72 %	9.27 % ± 1.3 %	1.02 % ± 0.30 %	3.45 µm ± 0.16 µm
C	23.26 % ± 2.64 %	18.1 % ± 2.24 %	2.68 % ± 0.75 %	2.63 µm ± 0.10 µm
D	21.55 % ± 3.14 %	16.9 % ± 2.74 %	2.38 % ± 1.10 %	2.60 µm ± 0.14 µm
E	11.42 % ± 2.55 %	7.89 % ± 1.93 %	1.10 % ± 0.26 %	3.85 µm ± 0.31 µm
F	12.47 % ± 0.73 %	8.75 % ± 0.47 %	0.76 % ± 0.05 %	3.63 µm ± 0.11 µm
G	17.53 % ± 1.5 %	13.3 % ± 1.22 %	1.92 % ± 0.40 %	3.14 µm ± 0.10 µm
H	18.03 % ± 5.69 %	13.9 % ± 4.57 %	2.13 % ± 0.77 %	3.67 µm ± 1.18 µm
I	16.54 % ± 0.69 %	12.2 % ± 0.72 %	1.49 % ± 0.37 %	3.13 µm ± 0.20 µm

Table App.8: FPF and MMAD values of SBS-containing interactive blends with no DA (w/o DA), PC, RK or SB been inserted into the inhaler device (n = 3).

Batch	FPF < 5 µm	FPF < 3 µm	FPF < 1 µm	MMAD
IL120 SBS w/o	19.9 % ± 3.50 %	15.9 % ± 3.20 %	1.9 % ± 0.94 %	2.17 µm ± 0.12 µm
IL120 SBS PC	17.9 % ± 3.28 %	14.1 % ± 2.88 %	1.9 % ± 0.69 %	2.22 µm ± 0.09 µm
IL120 SBS RK	20.8 % ± 2.33 %	16.8 % ± 2.10 %	2.3 % ± 0.85 %	2.14 µm ± 0.09 µm
IL120 SBS SB	21.4 % ± 3.39 %	17.4 % ± 3.20 %	2.5 % ± 0.69 %	2.09 µm ± 0.09 µm
IL251 SBS w/o	38.3 % ± 3.60 %	30.9 % ± 3.24 %	4.4 % ± 0.40 %	2.24 µm ± 0.05 µm
IL251 SBS PC	38.9 % ± 1.12 %	32 % ± 1.13 %	5.00 % ± 0.22 %	2.16 µm ± 0.05 µm
IL251 SBS RK	36.7 % ± 1.39 %	29.9 % ± 1.08 %	2.3 % ± 0.85 %	2.21 µm ± 0.06 µm
IL251 SBS SB	36.9 % ± 2.00 %	30.1 % ± 2.03 %	4.50 % ± 0.50 %	2.2 µm ± 0.07 µm

Table App.9: FPF and MMAD values of BUD-containing interactive blends with no DA (w/o DA), PC, RK or SB been inserted into the inhaler device (n = 3).

Batch	FPF < 5 µm	FPF < 3 µm	FPF < 1 µm	MMAD
IL120 BUD w/o	12.5 % ± 1.23 %	8.90 % ± 1.17 %	1.24 % ± 0.19 %	2.51 µm ± 0.10 µm
IL120 BUD PC	13.2 % ± 1.34 %	9.50 % ± 1.21 %	1.42 % ± 0.15 %	2.49 µm ± 0.10 µm
IL120 BUD RK	11.5 % ± 1.27 %	8.10 % ± 1.21 %	0.80 % ± 0.22 %	2.59 µm ± 0.10 µm
IL120 BUD SB	10.7 % ± 1.23 %	7.40 % ± 1.17 %	0.75 % ± 0.38 %	2.68 µm ± 0.18 µm
IL251 BUD w/o	25.9 % ± 2.93 %	19.8 % ± 2.27 %	3.49 % ± 0.30 %	2.62 µm ± 0.02 µm
IL251 BUD PC	24.7 % ± 2.73 %	18.6 % ± 2.15 %	3.41 % ± 0.31 %	2.78 µm ± 0.10 µm
IL251 BUD RK	24.0 % ± 2.31 %	18.1 % ± 1.70 %	2.63 % ± 0.30 %	2.74 µm ± 0.03 µm
IL251 BUD SB	24.8 % ± 2.35 %	18.6 % ± 1.78 %	3.06 % ± 0.66 %	2.73 µm ± 0.14 µm

Aerodynamic particle sizing of softpellets

Table App.10: Values of FPF, FPD and MMAD of softpellets composed of RIF inserting no DA (w/o DA) or a specific DA into the Twister®, respectively (n = 3).

Batch - RIF	w/o DA	PC	RK	SB
FPF < 5 µm	38.9 % ± 3.89 %	51.4 % ± 2.48 %	55.9 % ± 14.6 %	47.8 % ± 5.54 %
FPF < 3 µm	26.1 % ± 2.99 %	36.6 % ± 1.17 %	41.3 % ± 13.7 %	33.6 % ± 4.83 %
FPF < 1 µm	4.14 % ± 0.31 %	5.35 % ± 1.22 %	7.31 % ± 1.97 %	5.57 % ± 1.10 %
FPD < 5 µm	1185 µg ± 221.7 µg	1443 µg ± 82.02 µg	1645 µg ± 536.3 µg	1282 µg ± 178.5 µg
FPD < 3 µm	798.4 µg ± 165.7 µg	1027 µg ± 46.06 µg	1223 µg ± 485.5 µg	900.8 µg ± 152.0 µg
FPD < 1 µm	125.3 µg ± 15.65 µg	150.0 µg ± 33.19 µg	218.7 µg ± 83.16 µg	149.4 µg ± 30.96 µg
MMAD	2.79 µm ± 0.20 µm	2.55 µm ± 0.05 µm	2.49 µm ± 0.27 µm	2.56 µm ± 0.09 µm

Table App.11: Values of FPF, FPD and MMAD of softpellets composed of ISO inserting no DA (w/o DA) or a specific DA into the Twister®, respectively (n = 3).

Batch - ISN	w/o DA, 0 %	RK, 0 %	w/o DA, 12 %	RK, 12 %
FPF < 5 µm	10.1 % ± 1.60 %	15.1 % ± 3.10 %	9.06 % ± 2.10 %	12.9 % ± 2.86 %
FPF < 3 µm	3.12 % ± 0.70 %	4.97 % ± 0.99 %	2.43 % ± 0.47 %	3.56 % ± 0.75 %
FPF < 1 µm	below LOD	below LOD	below LOD	below LOD
FPD < 5 µm	393 µg ± 59.7 µg	573 µg ± 115 µg	303 µg ± 40.0 µg	450 µg ± 132 µg
FPD < 3 µm	122 µg ± 26.7 µg	189 µg ± 37.7 µg	81.7 µg ± 2.20 µg	124 µg ± 32.4 µg
FPD < 1 µm	below LOD	below LOD	below LOD	below LOD
MMAD	7.42 µm ± 0.15 µm	6.15 µm ± 0.23 µm	6.84 µm ± 0.12 µm	6.29 µm ± 0.49 µm

Appendix C – Results of Chapter 4

Carrier loading

Table App.12: Values of carrier specific properties (size, mass, volume and surface area) and corresponding parameters after simulation of carrier loading (e.g. $DC_{agglomerate}$, DLC_V, DLC_{SA}).

Carrier loading

carrier size [µm]	parameter		Pharmacone			RollingKnot			Soccerball			Sphere		
			case 1	case 2	case 3	case 1	case 2	case 3	case 1	case 2	case 3	case 1	case 2	case 3
50	m_{total}	[µg]	0.03751	0.03794	0.03806	0.00912	0.00924	0.00971	0.04185	0.04269	0.04288	0.05322	0.05354	0.05389
	$m_{carrier}$	[µg]	0.03669			0.00841			0.04142			0.05236		
	$V_{carrier}$	[µm³]	45858.7			10510.6			51773.1			65449.8		
	$SA_{carrier}$	[µm²]	7449.01			5992.33			7732			7853.98		
	$m_{API-total}$	[µg]	0.0008188	0.0012551	0.0013734	0.0007106	0.0008289	0.0012975	0.0004304	0.0012723	0.0014634	0.0008603	0.0011766	0.0015327
	DC		2.18%	3.31%	3.61%	7.79%	8.97%	13.37%	1.03%	2.98%	3.41%	1.62%	2.20%	2.84%
	DLC-V	[µg/mm³]	17.86	27.37	29.95	67.61	78.86	123.45	8.31	24.57	28.27	13.14	17.98	23.42
	DLC-SA	[µg/mm²]	0.11	0.17	0.18	0.12	0.14	0.22	0.06	0.16	0.19	0.11	0.15	0.20
100	m_{total}	[µg]	0.29683	0.29725	0.29912	0.0703	0.07151	0.07307	0.33372	0.33522	0.33649	0.42370	0.42551	0.42731
	$m_{carrier}$	[µg]	0.29350			0.06727			0.33135			0.41888		
	$V_{carrier}$	[µm³]	366869			84085			414185			523599		
	$SA_{carrier}$	[mm²]	0.029796			0.023969			0.030928			0.031416		
	$m_{API-total}$	[µg]	0.0033305	0.0037585	0.0056255	0.0030306	0.0042375	0.0057983	0.002373	0.003872	0.00514	0.0048218	0.0066298	0.0084348
	DC		1.12%	1.26%	1.88%	4.31%	5.93%	7.94%	0.71%	1.16%	1.53%	1.14%	1.56%	1.97%
	DLC-V	[µg/mm³]	9.08	10.2	15.3	36.0	50.4	69.0	5.73	9.3	12.4	9.21	12.7	16.1
	DLC-SA	[µg/mm²]	0.11	0.13	0.19	0.13	0.18	0.24	0.08	0.13	0.17	0.15	0.21	0.27

Particle size distribution after loading

Table App.13: Values of carrier and case specific API particle count (1 µm, 3 µm, 5µm) after simulation of carrier loading.

Carrier loading - PSD

carrier size [µm]	particle count	Pharmacone			Rollingknot			Soccerball			Sphere		
		case 1	case 2	case 3	case 1	case 2	case 3	case 1	case 2	case 3	case 1	case 2	case 3
50	$n_{API-1\mu m}$	480	830	1197	333	695	1063	383	740	1083	532	1045	1509
	$n_{API-3\mu m}$	17	28	29	17	19	20	7	21	31	18	26	34
	$n_{API-5\mu m}$	5	8	6	2	3	7	2	9	7	5	4	4
	log10 1 µm	2.68	2.92	3.08	2.52	2.84	3.03	2.58	2.87	3.03	2.73	3.02	3.18
	log10 3 µm	1.23	1.45	1.46	1.23	1.28	1.30	0.85	1.32	1.49	1.26	1.41	1.53
	log10 5 µm	0.70	0.90	0.78	0.30	0.48	0.85	0.30	0.95	0.85	0.70	0.60	0.60
carrier size [µm]	particle count	Pharmacone			Rollingknot			Soccerball			Sphere		
		case 4	case 5	case 6	case 4	case 5	case 6	case 4	case 5	case 6	case 4	case 5	case 6
100	$n_{API-1\mu m}$	1710	2653	4625	1989	3889	5371	1387	3019	4610	4067	7285	10036
	$n_{API-3\mu m}$	75	112	134	62	77	114	40	88	91	121	139	137
	$n_{API-5\mu m}$	21	12	20	17	17	21	13	16	22	15	13	19
	log10 1 µm	3.23	3.42	3.67	3.30	3.59	3.73	3.14	3.48	3.66	3.61	3.86	4.00
	log10 3 µm	1.88	2.05	2.13	1.79	1.89	2.06	1.60	1.94	1.96	2.08	2.14	2.14
	log10 5 µm	1.32	1.08	1.30	1.23	1.23	1.32	1.11	1.20	1.34	1.18	1.11	1.28

Drug detachment after collision

Table App.14: Values of carrier (type and size) and case specific parameters of API detachment (DR and CA) after simulation of collision with different velocities (5 m/s, 10 m/s and 15 m/s).

Collision - 50 µm

velocity	parameter	Pharmacone			Rollingknot			Soccerball			Sphere		
		case 1	case 2	case 3	case 1	case 2	case 3	case 1	case 2	case 3	case 1	case 2	case 3
	$m_{API-total}$ [µg]	0.000082	0.00126	0.00137	0.000071	0.00083	0.00130	0.00043	0.00127	0.00146	0.00086	0.00118	0.00153
5 m/s	$m_{attached}$ [µg]	0.00030	0.0005686	0.0007922	0.0002084	0.00024	0.0002393	0.0002152	0.0006896	0.0008273	0.0003597	0.0004875	0.0006932
	$m_{detached}$	0.00051621	0.000686442	0.000581195	0.000502208	0.000589072	0.0010582215	0.000215221	0.00058274	0.000636134	0.000500588	0.00068909	0.000833655
	DR [%]	63.0%	54.7%	42.3%	70.7%	71.1%	81.6%	50.0%	45.8%	43.5%	58.2%	58.6%	54.6%
	CA [%]	37.0%	45.3%	57.7%	29.3%	28.9%	18.4%	50.0%	54.2%	56.5%	41.8%	41.4%	45.4%
10 m/s	$m_{attached}$	0.0003419	0.0005645	0.000589	0.0001738	0.0002288	0.0002131	0.000167	0.0005529	0.0005037	0.000278	0.0003639	0.0004152
	$m_{detached}$	0.00047694	0.000690572	0.000784351	0.000536765	0.000600067	0.001084395	0.000263392	0.0007194	0.000959718	0.000582269	0.000812659	0.001111686
	DR [%]	58.2%	55.0%	57.1%	75.5%	72.4%	83.6%	61.2%	56.5%	65.6%	67.7%	69.1%	72.8%
	CA [%]	41.8%	45.0%	42.9%	24.5%	27.6%	16.4%	38.8%	43.5%	34.4%	32.3%	30.9%	27.2%
15 m/s	$m_{attached}$	0.0003665	0.0005566	0.0006199	0.0001482	0.0001623	0.0001576	0.0001681	0.0005	0.0004236	0.0002534	0.0003194	0.0003519
	$m_{detached}$	0.000452331	0.000698485	0.000753459	0.000562422	0.000666564	0.001139897	0.000262345	0.000772283	0.001039829	0.000606878	0.000857165	0.001175042
	DR [%]	55.2%	55.7%	54.9%	79.1%	80.4%	87.9%	61.0%	60.7%	71.1%	70.5%	72.9%	77.0%
	CA [%]	44.8%	44.3%	45.1%	20.9%	19.6%	12.1%	39.0%	39.3%	28.9%	29.5%	27.1%	23.0%

Collision - 100 µm

velocity	parameter	Pharmacone			Rollingknot			Soccerball			Sphere		
		case 4	case 5	case 6	case 4	case 5	case 6	case 4	case 5	case 6	case 4	case 5	case 6
	$m_{API-total}$ [µg]	0.00333	0.00376	0.00547	0.00303	0.00424	0.00580	0.00237	0.00387	0.00514	0.00482	0.00663	0.00843
5 m/s	$m_{attached}$ [µg]	0.00204	0.0016211	0.0020745	0.00108	0.00162	0.0018127	0.0012577	0.0022489	0.0029149	0.0030034	0.0044888	0.0053999
	$m_{detached}$	0.00128951	0.00213744	0.00339868	0.00195199	0.00261906	0.0039856	0.00111532	0.00162314	0.00222513	0.00181844	0.00214099	0.00303493
	DR [%]	38.7%	56.9%	62.1%	64.4%	61.8%	68.7%	47.0%	41.9%	43.3%	37.7%	32.3%	36.0%
	CA [%]	61.3%	43.1%	37.9%	35.6%	38.2%	31.3%	53.0%	58.1%	56.7%	62.3%	67.7%	64.0%
10 m/s	$m_{attached}$	0.00163	0.00163	0.0021321	0.00061	0.00099	0.00155	0.0008802	0.0015038	0.0022358	0.00201	0.00304	0.0036359
	$m_{detached}$	0.00169582	0.00213116	0.00334109	0.002424273	0.00324528	0.00424426	0.00149283	0.00236822	0.00290423	0.00280961	0.00358874	0.00479893
	DR [%]	50.9%	56.7%	61.0%	80.0%	76.6%	73.2%	62.9%	61.2%	56.5%	58.3%	54.1%	56.9%
	CA [%]	49.1%	43.3%	39.0%	20.0%	23.4%	26.8%	37.1%	38.8%	43.5%	41.7%	45.9%	43.1%
15 m/s	$m_{attached}$	0.00159	0.00160	0.0020269	0.00046	0.00078	0.00119	0.0008006	0.0012505	0.0017473	0.00201	0.00254	0.0030751
	$m_{detached}$	0.00174347	0.002161	0.00344633	0.002566168	0.003457338	0.00461025	0.001572417	0.00262147	0.00339275	0.00280752	0.00409296	0.0053597
	DR [%]	52.3%	57.5%	63.0%	84.7%	81.6%	79.5%	66.3%	67.7%	66.0%	58.2%	61.7%	63.5%
	CA [%]	47.7%	42.5%	37.0%	15.3%	18.4%	20.5%	33.7%	32.3%	34.0%	41.8%	38.3%	36.5%

Particle size distribution after collision

Table App.15: Comparison of carrier (type and size) and case specific API particle count (1 µm, 3 µm, 5µm) before and after simulation of collision with different velocities (5 m/s, 10 m/s and 15 m/s).

carrier size	particle count	Pharmacone											
		case 1				case 2				case 3			
		Loading	5 m/s	10 m/s	15 m/s	Loading	5 m/s	10 m/s	15 m/s	Loading	5 m/s	10 m/s	15 m/s
50 µm	$n_{API-1\mu m}$	480	193	312	305	830	360	480	445	1197	911	533	524
	$n_{API-3\mu m}$	17	5	8	10	28	13	10	9	29	13	8	11
	$n_{API-5\mu m}$	5	2	1	1	8	3	4	3	6	2	3	4
	log10 1 µm	2.68	2.29	2.49	2.48	2.92	2.56	2.68	2.65	3.08	2.96	2.73	2.72
	log10 3 µm	1.23	0.70	0.90	1.00	1.45	1.11	1.00	0.95	1.46	1.11	0.90	1.04
	log10 5 µm	0.70	0.30	0.00	0.00	0.90	0.48	0.60	0.48	0.78	0.30	0.48	0.60
		case 4				case 5				case 6			
100 µm	$n_{API-1\mu m}$	1710	952	1079	944	2653	1290	1383	1201	4625	2412	2296	1881
	$n_{API-3\mu m}$	75	35	34	31	112	53	50	50	134	25	38	43
	$n_{API-5\mu m}$	21	16	9	10	12	3	3	4	20	7	6	7
	log10 1 µm	3.23	2.98	3.03	2.97	3.42	3.11	3.14	3.08	3.67	3.38	3.36	3.27
	log10 3 µm	1.88	1.54	1.53	1.49	2.05	1.72	1.70	1.70	2.13	1.40	1.58	1.63
	log10 5 µm	1.32	1.20	0.95	1.00	1.08	0.48	0.48	0.60	1.30	0.85	0.78	0.85

carrier size	particle count	Rollingknot											
		case 1				case 2				case 3			
		Loading	5 m/s	10 m/s	15 m/s	Loading	5 m/s	10 m/s	15 m/s	Loading	5 m/s	10 m/s	15 m/s
50 µm	$n_{API-1\mu m}$	333	165	153	131	695	350	258	232	1063	376	330	248
	$n_{API-3\mu m}$	17	4	2	1	19	5	3	3	20	3	3	2
	$n_{API-5\mu m}$	2	1	1	1	3	1	1	0	7	0	0	0
	log10 1 µm	2.52	2.22	2.18	2.12	2.84	2.54	2.41	2.37	3.03	2.58	2.52	2.39
	log10 3 µm	1.23	0.60	0.30	0.00	1.28	0.70	0.48	0.48	1.30	0.48	0.48	0.30
	log10 5 µm	0.30	0.00	0.00	0.00	0.48	0.00	0.00		0.85			
		case 4				case 5				case 6			
100 µm	$n_{API-1\mu m}$	1989	1091	694	546	3889	1960	1409	1112	5371	2402	1739	1422
	$n_{API-3\mu m}$	62	22	8	8	77	28	18	14	114	30	27	15
	$n_{API-5\mu m}$	17	3	2	1	17	3	0	0	21	2	4	3
	log10 1 µm	3.30	3.04	2.84	2.74	3.59	3.29	3.15	3.05	3.73	3.38	3.24	3.15
	log10 3 µm	1.79	1.34	0.90	0.90	1.89	1.45	1.26	1.15	2.06	1.48	1.43	1.18
	log10 5 µm	1.23	0.48	0.30	0.00	1.23	0.48	n.a.	n.a.	1.32	0.30	0.60	0.48

carrier size	particle count	Soccerball											
		case 1				case 2				case 3			
		Loading	5 m/s	10 m/s	15 m/s	Loading	5 m/s	10 m/s	15 m/s	Loading	5 m/s	10 m/s	15 m/s
50 µm	$n_{API-1\mu m}$	383	276	238	240	740	476	367	322	1083	773	493	478
	$n_{API-3\mu m}$	7	5	3	3	21	8	7	6	31	16	8	3
	$n_{API-5\mu m}$	2	0	0	0	9	5	4	5	7	3	1	2
	log10 1 µm	2.58	2.44	2.38	2.38	2.87	2.68	2.56	2.51	3.03	2.89	2.69	2.68
	log10 3 µm	0.85	0.70	0.48	0.48	1.32	0.90	0.85	0.78	1.49	1.20	0.90	0.48
	log10 5 µm	0.30				0.95	0.70	0.60	0.70	0.85	0.48	0.00	0.30
		case 4				case 5				case 6			
100 µm	$n_{API-1\mu m}$	1387	1237	901	928	3019	2725	1950	1803	4610	3926	2977	2629
	$n_{API-3\mu m}$	40	20	15	13	88	35	11	13	91	33	34	17
	$n_{API-5\mu m}$	13	5	3	2	16	5	5	6	22	6	3	3
	log10 1 µm	3.14	3.09	2.95	2.97	3.48	3.44	3.29	3.26	3.66	3.59	3.47	3.42
	log10 3 µm	1.60	1.30	1.18	1.11	1.94	1.54	1.04	1.11	1.96	1.52	1.53	1.23
	log10 5 µm	1.11	0.70	0.48	0.30	1.20	0.70	0.70	0.78	1.34	0.78	0.48	0.48

carrier size	particle count	Sphere											
		case 1				case 2				case 3			
		Loading	5 m/s	10 m/s	15 m/s	Loading	5 m/s	10 m/s	15 m/s	Loading	5 m/s	10 m/s	15 m/s
50 µm	$n_{API-1\mu m}$	532	329	227	180	1045	634	479	394	1509	831	604	483
	$n_{API-3\mu m}$	18	4	2	2	26	11	8	8	34	9	7	7
	$n_{API-5\mu m}$	5	2	2	2	4	0	0	0	4	2	0	0
	log10 1 µm	2.73	2.52	2.36	2.26	3.02	2.80	2.68	2.60	3.18	2.92	2.78	2.68
	log10 3 µm	1.26	0.60	0.30	0.30	1.41	1.04	0.90	0.90	1.53	0.95	0.85	0.85
	log10 5 µm	0.70	0.30	0.30	0.30	0.60				0.60	0.30		
		case 4				case 5				case 6			
100 µm	$n_{API-1\mu m}$	4067	3852	2570	2574	7285	6848	4613	3866	10036	8611	5840	4814
	$n_{API-3\mu m}$	121	42	24	24	139	50	35	27	137	44	27	24
	$n_{API-5\mu m}$	15	6	5	5	13	3	2	2	19	4	3	3
	log10 1 µm	3.61	3.59	3.41	3.41	3.86	3.84	3.66	3.59	4.00	3.94	3.77	3.68
	log10 3 µm	2.08	1.62	1.38	1.38	2.14	1.70	1.54	1.43	2.14	1.64	1.43	1.38
	log10 5 µm	1.18	0.78	0.70	0.70	1.11	0.48	0.30	0.30	1.28	0.60	0.48	0.48

Appendix D – List of abbreviations

µg	Microgram
µm	Micrometre
AM	Additive manufacturing
API	Active pharmaceutical ingredient
APSD	Aerodynamic particle size distribution
BUD	Budesonide
CA	Carrier adherence
CFD	Computational fluid dynamics
cLP	Critical lifting pressure
COPD	Chronical obstructive pulmonal disease
DA	Dispersing aid
DD	Delivered dose
$_{dd}H_2O$	Double distilled water
DEM	Discrete element method
DLP	Drug loading capacity
DPI	Dry powder inhaler
DR	Device retention
ED	Emitted dose
FCAs	Force control agents
FDM	Fused deposition modeling
FPD	Fine particle dose
FPF	Fine particle fraction
h	Hour
HPLC	High performance liquid chromatography
IL	InhaLac®
ISN	Isoniazid
m/m	Mass divided by mass
mbar	Millibar
MD	Metered Dose
MDI	Metered dose inhaler
mg	Milligram
mJ	Millijoule
mm	Millimetre
MMAD	Mass median aerodynamic diameter
NGI	Next generation pharmaceutical impactor

NS	Numerical Simulation
OINDP	Orally inhaled and nasal drug products
OIP	Orally inhaled drug products
PSD	Particle size distribution
rH	Relative humidity
RIF	Rifampicin
RSD	Relative standard deviation
s	Second
SBS	Salbutamol sulfate
SD	Standard deviation
SEM	Scanning electron microscopy
SLA	Selective Laser Sintering
TPP	Two-Photo-Polymerisation

Appendix E – Formula symbols

Contact area of two bodies	a
Contact normal overlap	s_n
Density	ρ
Diameter	d
Displacement	σ
Normal contact forces	F_n
Normal contact stiffness	K_n
Normal damping coefficient	C_n
Normal elastic-plastic contact forces	$F_{n,Hertz}$
Radius	r
Stokes number	Stk
Surface energy	γ
Time derivative of the contact normal overlap	$\check{s}_n$
Viscosity	η
Young's modulus	E
Drug content of agglomerate	$DC_{agglomerate}$
Drug loading capacity (volume-specific)	DLC_V
Drug loading capacity (surface-area-specific)	DLC_{SA}
Detachment rate	DR
Carrier adherence	CA
Mass	m
Volume	V
Surface area	SA

Appendix F – Materials

Accura 60®	3D Systems Inc., USA
Acetonitrile (HPLC grade)	Honeywell Riedel-de Häen, Germany
Brij® 35	Carl Roth GmbH & Co. KG, Germany
Budesonide	Farmabios S.p.A., Italy
$_{dd}H_2O$	Bi-distilled water produced with Finn Aqua 75, San-Asalo-Sohlberg Corp., Finland
Ethanol	Sigma-Aldrich (Merck KGaA), Germany
Ethanol (HPLC grade)	Avantor Performance Materials S.A., Poland
Formiga-P 100®	EOS GmbH, Germany
Glycerol	Sigma-Aldrich (Merck KGaA), Germany
Helium 5.0	Linde AG, Germany
InhaLac®	Meggle GmbH & Co. KG, Germany
IP-Q®	Nanoscribe GmbH & Co. KG, Germany
Isoniazid	Sigma-Aldrich (Merck KGaA), Germany
Methanol (HPLC grade)	Avantor Performance Materials S.A., Poland
Nitrogen 5.0	Linde AG, Germany
ortho-Phosphoric acid	Sigma-Aldrich (Merck KGaA), Germany
Phenylalanine	Sigma-Aldrich (Merck KGaA), Germany
PLA black	Ultimaker B.V., The Netherlands
Potassium dihydrogen phosphate	Sigma-Aldrich (Merck KGaA), Germany
PVA natural	Ultimaker B.V., The Netherlands
Rifampicin	Caesar & Loretz GmbH, Germany
Salbutamol sulfate	Lusochimica S.p.A., Italy
Sodium heptanosulfonate	Carl Roth GmbH & Co. KG, Germany
Sodium hydroxide	Sigma-Aldrich (Merck KGaA), Germany
Tetrabutylammonium hydrogensulfate	Sigma-Aldrich (Merck KGaA), Germany
Tryptophan	Sigma-Aldrich (Merck KGaA), Germany
Tyrosine	Sigma-Aldrich (Merck KGaA), Germany
Vivapur® MCC Spheres	JRS Pharma GmbH & Co. KG, Germany

Appendix G – HPLC-Methods

Quantification of the respective substance was carried out using HPLC equipment from Waters (Waters Corp., USA). For evaluation, the peak area of the respective substance was identified with an external standard and integrated with the Empower® 3 software (Waters Corp., Milford, USA) in the pre-set time limits.

Budesonide

Column: LiChroCART® 125-4, LiChrospher® 100 RP-18 (5 µm; Merck KGaA, Germany)
Pre-Column: LiChroCART® 4-4, LiChrospher® 100 RP-18 (5 µm; Merck KGaA, Germany)

Mobile phase: A: 75 % Methanol (MeOH)
B: 25 % $_{dd}H_2O$

Elution Type:	isocratic
Flow rate:	1 ml/min
Detection wavelength:	248 nm
Column temperature:	25 °C
Sample temperature:	15 °C
Injection volume:	10 µl

Isoniazid

Column: LiChroCART® 125-4, LiChrospher® 100 RP-18 (5 µm; Merck KGaA, Germany)
Pre-Column: LiChroCART® 4-4, LiChrospher® 100 RP-18 (5 µm; Merck KGaA, Germany)

Mobile phase: A: 57 % t-Butylammonium hydrogen sulfate (C16H37NO4S) in $_{dd}H_2O$
B: 43 % Acetonitrile (ACN)

Elution Type:	isocratic
Flow rate:	1.0 ml/min
Detection wavelength:	284 nm
Column temperature:	25 °C
Sample temperature:	15 °C
Injection volume:	100 µl

Phenylalanine-Tryptophan-Tyrosine

Column: LiChroCART® 125-4, LiChrospher® 100 RP-18 (5 µm; Merck KGaA, Germany)

Pre-Column: LiChroCART® 4-4, LiChrospher® 100 RP-18 (5 µm; Merck KGaA, Germany)

Mobile phase: A: 90 % Buffer (3,4 g/L KH2PO4; $_{dd}H_2O$; pH 3.0)

B: 10 % Acetonitrile (ACN)

Elution Type: isocratic

Flow rate: 0.8 ml/min and 1.0 ml/min (Tryptophan)

Detection wavelength: 210 nm (Tryptophan) and 274 nm

Column temperature: 20 °C

Sample temperature: 15 °C

Injection volume: 10 µl

Retention time for peak:

Tyrosine: 2.3 min

Phenylalanine: 3.1 min

Tryptophan: 6.1 min

Rifampicin

Column: LiChroCART® 125-4, LiChrospher® 100 RP-8 (5 µm; Merck KGaA, Germany)

Pre-Column: LiChroCART® 4-4, LiChrospher® 100 RP-8 (5 µm; Merck KGaA, Germany)

Mobile phase: A: 65 % Buffer (5.9 g/L $C_6H_8O_7$, 2.50 g/L KH_2PO_4, 1.9 g/L $NaClO_4$; $_{dd}H_2O$ pH set to 3.6 with phosphoric acid 85 %)

B: 35 % Acetonitrile (ACN)

Elution Type: isocratic

Flow rate: 1.0 ml/min

Detection wavelength: 254 nm

Column temperature: 25 °C

Sample temperature: 15 °C

Injection volume: 20 µl

Samples were dissolved in 55 % (v/v) Acetonitrile, 45 % (v/v) KH_2PO_4-buffer (0.05 mol/L; pH 2.50) and 0.5 mg/ml ascorbic acid as an antioxidant prior to the HPLC-analysis.

Salbutamol sulfate

Column: LiChroCART® 125-4, LiChrospher® 100 RP-18 (5 µm; Merck KGaA, Germany)

Pre-Column: LiChroCART® 4-4, LiChrospher® 100 RP-18 (5 µm; Merck KGaA, Germany)

Mobile phase: A: 78 % Buffer (2.87 g/L $C_7H_{15}O_3SNa$, 2.50 g/L KH_2PO_4; $_{dd}H_2O$; pH set to 3.65 with phosphoric acid 85 %)

B: 22 % Acetonitrile (ACN)

Elution Type:	isocratic
Flow rate:	0.8 ml/min
Detection wavelength:	220 nm
Column temperature:	25 °C
Sample temperature:	15 °C
Injection volume:	10 µl

References

[1] A.B. Lumb, Functional Anatomy of the Respiratory Tract, Elsevier, 2017.

[2] E.R. Weibel, Morphometry of the Human Lung, Springer Berlin Heidelberg, Berlin, Heidelberg, 1963.

[3] W.G. Kreyling, M. Semmler-Behnke, S. Takenaka, W. Möller, Differences in the biokinetics of inhaled nano- versus micrometer-sized particles, Acc. Chem. Res. 46 (3) (2013) 714–722. https://doi.org/10.1021/ar300043r.

[4] O.S. Usmani, M.F. Biddiscombe, P.J. Barnes, Regional lung deposition and bronchodilator response as a function of beta2-agonist particle size, Am. J. Respir. Crit. Care Med. 172 (12) (2005) 1497–1504. https://doi.org/10.1164/rccm.200410-1414OC.

[5] X.M. Zeng, G.P. Martin, C. Marriott, Particulate Interactions in Dry Powder Formulation for Inhalation, CRC Press, 2000.

[6] T.C. Carvalho, J.I. Peters, R.O. Williams, Influence of particle size on regional lung deposition--what evidence is there? Int. J. Pharm. 406 (1-2) (2011) 1–10. https://doi.org/10.1016/j.ijpharm.2010.12.040.

[7] J.S. Patton, Mechanisms of macromolecule absorption by the lungs, Adv. Drug Deliv. Rev. 19 (1) (1996) 3–36. https://doi.org/10.1016/0169-409X(95)00113-L.

[8] S. Buist, C. Mapp, Respiratory Diseases in Women, European Respiratory Society Journals, Sheffield, 2003.

[9] International Commission on Radiological Protection (Ed.), Guide for the practical application of the ICRP human respiratory tract model, 66th ed., Pergamon Press, Oxford, 2003.

[10] M.J. Morris, R.G. Madgwick, I. Collyer, F. Denby, D.J. Lane, Analysis of expiratory tidal flow patterns as a diagnostic tool in airflow obstruction, Eur. Respir. J. 12 (5) (1998) 1113–1117. https://doi.org/10.1183/09031936.98.12051113.

[11] M.J. Morris, D.J. Lane, Tidal expiratory flow patterns in airflow obstruction, Thorax 36 (2) (1981) 135–142. https://doi.org/10.1136/thx.36.2.135.

[12] S. Stanojevic, A. Wade, J. Stocks, J. Hankinson, A.L. Coates, H. Pan, M. Rosenthal, M. Corey, P. Lebecque, T.J. Cole, Reference ranges for spirometry across all ages: A new approach, Am. J. Respir. Crit. Care Med. 177 (3) (2008) 253–260. https://doi.org/10.1164/rccm.200708-1248OC.

[13] Á. Farkas, F. Lizal, J. Jedelsky, J. Elcner, A. Horváth, M. Jicha, Simulation of Airway Deposition of an Aerosol Drug in COPD Patients, Pharmaceutics 11 (4) (2019). https://doi.org/10.3390/pharmaceutics11040153.

[14] A.R. Clark, J.G. Weers, R. Dhand, The Confusing World of Dry Powder Inhalers: It Is All About Inspiratory Pressures, Not Inspiratory Flow Rates, J. Aerosol Med. Pulm. Drug Deliv. 33 (1) (2020) 1–11. https://doi.org/10.1089/jamp.2019.1556.

[15] S.L. James, Global, regional, and national incidence, prevalence, and years lived with disability for 354 diseases and injuries for 195 countries and territories, 1990–2017: A systematic analysis for the Global Burden of Disease Study 2017, The Lancet 392 (10159) (2018) 1789–1858. https://doi.org/10.1016/S0140-6736(18)32279-7.

[16] W.W. Labaki, M.K. Han, Chronic respiratory diseases: A global view, The Lancet Respiratory Medicine 8 (6) (2020) 531–533. https://doi.org/10.1016/S2213-2600(20)30157-0.

[17] J.B. Soriano, P.J. Kendrick, K.R. Paulson, Prevalence and attributable health burden of chronic respiratory diseases, 1990–2017: A systematic analysis for the Global Burden of Disease Study 2017, The Lancet Respiratory Medicine 8 (6) (2020) 585–596. https://doi.org/10.1016/S2213-2600(20)30105-3.

[18] World Health Organisation, From burden to “best buys”: Reducing the economic impact of non-communicable disease in low- and middle-income countries, 2011. http://www.who.int/nmh/publications/best_buys_summary/en/.

[19] A.J. Hickey, Emerging trends in inhaled drug delivery, Adv. Drug Deliv. Rev. (2020). https://doi.org/10.1016/j.addr.2020.07.006.

[20] D.A. Edwards, A. Ben-Jebria, R. Langer, Recent advances in pulmonary drug delivery using large, porous inhaled particles, J. Appl. Physiol. 85 (2) (1998) 379–385. https://doi.org/10.1152/jappl.1998.85.2.379.

[21] T.R. Sosnowski, Selected Engineering and Physicochemical Aspects of Systemic Drug Delivery by Inhalation, Curr. Pharm. Des. 22 (17) (2016) 2453–2462. https://doi.org/10.2174/1381612822666160128145644.

[22] M. Hellfritzsch, R. Scherließ, Mucosal Vaccination via the Respiratory Tract, Pharmaceutics 11 (8) (2019). https://doi.org/10.3390/pharmaceutics11080375.

[23] Q.T. Zhou, S.S.Y. Leung, P. Tang, T. Parumasivam, Z.H. Loh, H.-K. Chan, Inhaled formulations and pulmonary drug delivery systems for respiratory infections, Adv. Drug Deliv. Rev. 85 (2015) 83–99. https://doi.org/10.1016/j.addr.2014.10.022.

[24] N.R. Labiris, M.B. Dolovich, Pulmonary drug delivery. Part I: Physiological factors affecting therapeutic effectiveness of aerosolized medications, Br. J. Clin. Pharmacol. 56 (6) (2003) 588–599. https://doi.org/10.1046/j.1365-2125.2003.01892.x.

[25] S. Hou, J. Wu, X. Li, H. Shu, Practical, regulatory and clinical considerations for development of inhalation drug products, Asian Journal of Pharmaceutical Sciences 10 (6) (2015) 490–500. https://doi.org/10.1016/j.ajps.2015.08.008.

[26] A. Ari, J.B. Fink, Recent advances in aerosol devices for the delivery of inhaled medications, Expert Opin. Drug Deliv. 17 (2) (2020) 133–144. https://doi.org/10.1080/17425247.2020.1712356.

[27] W. Hofmann, Regional Deposition: Deposition Models, J. Aerosol Med. Pulm. Drug Deliv. 33 (5) (2020) 239–248. https://doi.org/10.1089/jamp.2020.29031.wh.

[28] T.R. Gerrity, P.S. Lee, F.J. Hass, A. Marinelli, P. Werner, R.V. Lourenço, Calculated deposition of inhaled particles in the airway generations of normal subjects, J. Appl. Physiol. Respir. Environ. Exerc. Physiol. 47 (4) (1979) 867–873. https://doi.org/10.1152/jappl.1979.47.4.867.

[29] J. Heyder, J. Gebhart, G. Rudolf, C.F. Schiller, W. Stahlhofen, Deposition of particles in the human respiratory tract in the size range 0.005–15 µm, Journal of Aerosol Science 17 (5) (1986) 811–825. https://doi.org/10.1016/0021-8502(86)90035-2.

[30] W. Stahlhofen, G. Rudolf, A.C. JAMES, Intercomparison of Experimental Regional Aerosol Deposition Data, Journal of Aerosol Medicine 2 (3) (1989) 285–308. https://doi.org/10.1089/jam.1989.2.285.

[31] G. Rudolf, R. Köbrich, W. Stahlhofen, Modelling and algebraic formulation of regional aerosol deposition in man, Journal of Aerosol Science 21 (1990) S403-S406. https://doi.org/10.1016/0021-8502(90)90266-Z.

[32] S.P. Newman, H.-K. Chan, In vitro/in vivo comparisons in pulmonary drug delivery, J. Aerosol Med. Pulm. Drug Deliv. 21 (1) (2008) 77–84. https://doi.org/10.1089/jamp.2007.0643.

[33] S.P. Newman, H.-K. Chan, In vitro-in vivo correlations (IVIVCs) of deposition for drugs given by oral inhalation, Adv. Drug Deliv. Rev. 167 (2020) 135–147. https://doi.org/10.1016/j.addr.2020.06.023.

[34] A.H. de Boer, D. Gjaltema, P. Hagedoorn, H.W. Frijlink, Can 'extrafine' dry powder aerosols improve lung deposition? Eur. J. Pharm. Biopharm. 96 (2015) 143–151. https://doi.org/10.1016/j.ejpb.2015.07.016.

[35] European Pharmacopoeia, 10th edition 2020, English: Subscription to Supplement 3 + Supplement 4 + Supplement 5, 1st ed., Deutscher Apotheker Verlag, Stuttgart, 2020.

[36] M.J. Telko, A.J. Hickey, Dry powder inhaler formulation, Respir. Care 50 (9) (2005) 1209–1227.

[37] G. Pilcer, K. Amighi, Formulation strategy and use of excipients in pulmonary drug delivery, Int. J. Pharm. 392 (1-2) (2010) 1–19. https://doi.org/10.1016/j.ijpharm.2010.03.017.

[38] A.J. Hickey, Complexity in Pharmaceutical Powders for Inhalation: A perspective, KONA 35 (0) (2018) 3–13. https://doi.org/10.14356/kona.2018007.

[39] D. Brocklebank, F. Ram, J. Wright, P. Barry, C. Cates, L. Davies, G. Douglas, M. Muers, D. Smith, J. White, Comparison of the effectiveness of inhaler devices in asthma and chronic obstructive airways disease: A systematic review of the literature, Health Technol. Assess. 5 (26) (2001) 1–149. https://doi.org/10.3310/hta5260.

[40] A.H. de Boer, P. Hagedoorn, R. Woolhouse, E. Wynn, Computational fluid dynamics (CFD) assisted performance evaluation of the Twincer™ disposable high-dose dry powder inhaler, J. Pharm. Pharmacol. 64 (9) (2012) 1316–1325. https://doi.org/10.1111/j.2042-7158.2012.01511.x.

[41] A.H. de Boer, P. Hagedoorn, M. Hoppentocht, F. Buttini, F. Grasmeijer, H.W. Frijlink, Dry powder inhalation: Past, present and future, Expert Opin. Drug Deliv. 14 (4) (2017) 499–512. https://doi.org/10.1080/17425247.2016.1224846.

[42] N. Islam, M.J. Cleary, Developing an efficient and reliable dry powder inhaler for pulmonary drug delivery--a review for multidisciplinary researchers, Med. Eng. Phys. 34 (4) (2012) 409–427. https://doi.org/10.1016/j.medengphy.2011.12.025.

[43] P.B. Myrdal, P. Sheth, S.W. Stein, Advances in metered dose inhaler technology: Formulation development, AAPS PharmSciTech 15 (2) (2014) 434–455. https://doi.org/10.1208/s12249-013-0063-x.

[44] S.W. Stein, P.B. Myrdal, The Relative Influence of Atomization and Evaporation on Metered Dose Inhaler Drug Delivery Efficiency, Aerosol Science and Technology 40 (5) (2006) 335–347. https://doi.org/10.1080/02786820600612268.

[45] S.W. Stein, P.B. Myrdal, A theoretical and experimental analysis of formulation and device parameters affecting solution MDI size distributions, Journal of pharmaceutical sciences 93 (8) (2004) 2158–2175. https://doi.org/10.1002/jps.20116.

[46] M. Hoppentocht, P. Hagedoorn, H.W. Frijlink, A.H. de Boer, Technological and practical challenges of dry powder inhalers and formulations, Adv. Drug Deliv. Rev. 75 (2014) 18–31. https://doi.org/10.1016/j.addr.2014.04.004.

[47] P.P. Mehta, Dry powder inhalers: A brief overview of the drug detachment techniques, Ther. Deliv. 11 (3) (2020) 139–143. https://doi.org/10.4155/tde-2019-0087.

[48] R. Scherließ, C. Etschmann, DPI formulations for high dose applications - Challenges and opportunities, Int. J. Pharm. 548 (1) (2018) 49–53. https://doi.org/10.1016/j.ijpharm.2018.06.038.

[49] A.J. Hickey, S. Giovagnoli, Pharmaceutical Powder and Particles, Springer International Publishing, Cham, 2018.

[50] M.S. Hassan, R.W.M. Lau, Effect of particle shape on dry particle inhalation: Study of flowability, aerosolization, and deposition properties, AAPS PharmSciTech 10 (4) (2009) 1252–1262. https://doi.org/10.1208/s12249-009-9313-3.

[51] D.A. Edwards, J. Hanes, G. Caponetti, J. Hrkach, A. Ben-Jebria, M.L. Eskew, J. Mintzes, D. Deaver, N. Lotan, R. Langer, Large porous particles for pulmonary drug delivery, Science 276 (5320) (1997) 1868–1871. https://doi.org/10.1126/science.276.5320.1868.

[52] A.J. Hickey, T.B. Martonen, Behavior of hygroscopic pharmaceutical aerosols and the influence of hydrophobic additives, Pharm. Res. 10 (1) (1993) 1–7. https://doi.org/10.1023/A:1018952425107.

[53] B. Chaurasiya, Y.-Y. Zhao, Dry Powder for Pulmonary Delivery: A Comprehensive Review, Pharmaceutics 13 (1) (2020). https://doi.org/10.3390/pharmaceutics13010031.

[54] J.A. Hersey, Ordered mixing: A new concept in powder mixing practice, Powder Technology 11 (1) (1975) 41–44. https://doi.org/10.1016/0032-5910(75)80021-0.

[55] J.N. Staniforth, British Pharmaceutical Conference Science Award lecture 1986. Order out of chaos, J. Pharm. Pharmacol. 39 (5) (1987) 329–334. https://doi.org/10.1111/j.2042-7158.1987.tb03393.x.

[56] N. Islam, P. Stewart, I. Larson, P. Hartley, Effect of carrier size on the dispersion of salmeterol xinafoate from interactive mixtures, Journal of pharmaceutical sciences 93 (4) (2004) 1030–1038. https://doi.org/10.1002/jps.10583.

[57] P. Mehta, Imagine the Superiority of Dry Powder Inhalers from Carrier Engineering, J. Drug Deliv. 2018 (2018) 5635010. https://doi.org/10.1155/2018/5635010.

[58] M.D. Louey, P.J. Stewart, Particle interactions involved in aerosol dispersion of ternary interactive mixtures, Pharm. Res. 19 (10) (2002) 1524–1531. https://doi.org/10.1023/A:1020464801786.

[59] M.D. Jones, R. Price, The influence of fine excipient particles on the performance of carrier-based dry powder inhalation formulations, Pharm. Res. 23 (8) (2006) 1665–1674. https://doi.org/10.1007/s11095-006-9012-7.

[60] B.H.J. Dickhoff, A.H. de Boer, D. Lambregts, H.W. Frijlink, The effect of carrier surface treatment on drug particle detachment from crystalline carriers in adhesive mixtures for inhalation, Int. J. Pharm. 327 (1-2) (2006) 17–25. https://doi.org/10.1016/j.ijpharm.2006.07.017.

[61] J. Shur, H. Harris, M.D. Jones, J.S. Kaerger, R. Price, The role of fines in the modification of the fluidization and dispersion mechanism within dry powder inhaler formulations, Pharm. Res. 25 (7) (2008) 1631–1640. https://doi.org/10.1007/s11095-008-9538-y.

[62] F. Grasmeijer, A.J. Lexmond, M. van den Noort, P. Hagedoorn, A.J. Hickey, H.W. Frijlink, A.H. de Boer, New mechanisms to explain the effects of added lactose fines on the dispersion performance of adhesive mixtures for inhalation, PLoS One 9 (1) (2014) e87825. https://doi.org/10.1371/journal.pone.0087825.

[63] C. Etschmann, Development of a Softpellet Formulation for Inhaled High-Dose Therapy. PhD thesis, Kiel, Germany, 2021.

[64] R. Scherließ, S. Bock, N. Bungert, A. Neustock, L. Valentin, Particle engineering in dry powders for inhalation, Eur. J. Pharm. Sci. 172 (2022) 106158. https://doi.org/10.1016/j.ejps.2022.106158.

[65] J.G. Weers, D.P. Miller, Formulation Design of Dry Powders for Inhalation, Journal of pharmaceutical sciences 104 (10) (2015) 3259–3288. https://doi.org/10.1002/jps.24574.

[66] T. Santos Cavaiola, S. Edelman, Inhaled insulin: A breath of fresh air? A review of inhaled insulin, Clin. Ther. 36 (8) (2014) 1275–1289. https://doi.org/10.1016/j.clinthera.2014.06.025.

[67] J. Weers, T. Tarara, The PulmoSphere™ platform for pulmonary drug delivery, Ther. Deliv. 5 (3) (2014) 277–295. https://doi.org/10.4155/tde.14.3.

[68] M. Rendell, Technosphere inhaled insulin (Afrezza), Drugs Today (Barc) 50 (12) (2014) 813–827. https://doi.org/10.1358/dot.2014.50.12.2233894.

[69] L. Wu, X. Miao, Z. Shan, Y. Huang, L. Li, X. Pan, Q. Yao, G. Li, C. Wu, Studies on the spray dried lactose as carrier for dry powder inhalation, Asian Journal of Pharmaceutical Sciences 9 (6) (2014) 336–341. https://doi.org/10.1016/j.ajps.2014.07.006.

[70] W. Kaialy, M. Ticehurst, A. Nokhodchi, Dry powder inhalers: Mechanistic evaluation of lactose formulations containing salbutamol sulphate, Int. J. Pharm. 423 (2) (2012) 184–194. https://doi.org/10.1016/j.ijpharm.2011.12.018.

[71] N. Hertel, Mannitol als alternativer Träger in interaktiven Pulvermischungen zur Inhalation. PhD thesis, Kiel, Germany, 2020.

[72] M. Mönckedieck, J. Kamplade, P. Fakner, N.A. Urbanetz, P. Walzel, H. Steckel, R. Scherließ, Spray drying of mannitol carrier particles with defined morphology and flow characteristics for dry powder inhalation, Drying Technology 35 (15) (2017) 1843–1857. https://doi.org/10.1080/07373937.2017.1281291.

[73] K. Iida, H. Todo, H. Okamoto, K. Danjo, H. Leuenberger, Preparation of dry powder inhalation with lactose carrier particles surface-coated using a Wurster fluidized bed, Chem. Pharm. Bull. (Tokyo) 53 (4) (2005) 431–434. https://doi.org/10.1248/cpb.53.431.

[74] D. Traini, S. Scalia, H. Adi, E. Marangoni, P.M. Young, Polymer coating of carrier excipients modify aerosol performance of adhered drugs used in dry powder inhalation therapy, Int. J. Pharm. 438 (1-2) (2012) 150–159. https://doi.org/10.1016/j.ijpharm.2012.08.036.

[75] P. Bareschino, A. Marzocchella, P. Salatino, Fluidised bed drying of powdered materials: Effects of operating conditions, Powder Technology 308 (2) (2017) 158–164. https://doi.org/10.1016/j.powtec.2016.11.069.

[76] T.M. Chitu, D. Oulahna, M. Hemati, Rheology, granule growth and granule strength: Application to the wet granulation of lactose–MCC mixtures, Powder Technology 208 (2) (2011) 441–453. https://doi.org/10.1016/j.powtec.2010.08.041.

[77] H. Steckel, N. Bolzen, Alternative sugars as potential carriers for dry powder inhalations, Int. J. Pharm. 270 (1-2) (2004) 297–306. https://doi.org/10.1016/j.ijpharm.2003.10.039.

[78] R. Jawad, G.P. Martin, P.G. Royall, Chemical and Compositional Characterisation of Lactose as a Carrier in Dry Powder Inhalers (2015). https://doi.org/10.1002/9781118799536.ch7.

[79] S.K. Tee, C. Marriott, X.M. Zeng, G.P. Martin, The use of different sugars as fine and coarse carriers for aerosolised salbutamol sulphate, Int. J. Pharm. 208 (1-2) (2000) 111–123. https://doi.org/10.1016/s0378-5173(00)00553-6.

[80] US Food and Drug Administration, Mannitol. Generally recognized as safe (GRAS), 2021. https://www.accessdata.fda.gov/scripts/cdrh/cfdocs/cfCFR/CFRSearch.cfm?fr=582.5470 (accessed 1 January 2022).

[81] F.R. Fronczek, H.N. Kamel, M. Slattery, Three polymorphs (alpha, beta, and delta) of D-mannitol at 100 K, Acta Crystallogr. C 59 (Pt 10) (2003) O567-70. https://doi.org/10.1107/s0108270103018961.

[82] Y. Rahimpour, M. Kouhsoltani, H. Hamishehkar, Alternative carriers in dry powder inhaler formulations, Drug Discov. Today 19 (5) (2014) 618–626. https://doi.org/10.1016/j.drudis.2013.11.013.

[83] G. Thoorens, F. Krier, B. Leclercq, B. Carlin, B. Evrard, Microcrystalline cellulose, a direct compression binder in a quality by design environment--a review, Int. J. Pharm. 473 (1-2) (2014) 64–72. https://doi.org/10.1016/j.ijpharm.2014.06.055.

[84] C.A. Murphy, M.N. Collins, Microcrystalline cellulose reinforced polylactic acid biocomposite filaments for 3D printing, Polym. Compos. 39 (4) (2018) 1311–1320. https://doi.org/10.1002/pc.24069.

[85] D.S. Wishart, C. Knox, A.C. Guo, S. Shrivastava, M. Hassanali, P. Stothard, Z. Chang, J. Woolsey, DrugBank: A comprehensive resource for in silico drug discovery and exploration, Nucleic Acids Res. 34 (Database issue) (2006) D668-72. https://doi.org/10.1093/nar/gkj067.

[86] Drugbank, Budesonide: https://go.drugbank.com/drugs/DB01222, 2022.

[87] Drugbank, Salbutamol: https://www.drugbank.ca/drugs/DB01001, 2022.

[88] G.B. McGaughey, M. Gagné, A.K. Rappé, pi-Stacking interactions. Alive and well in proteins, J. Biol. Chem. 273 (25) (1998) 15458–15463. https://doi.org/10.1074/jbc.273.25.15458.

[89] H. Faghihi, A. Vatanara, A.R. Najafabadi, V. Ramezani, K. Gilani, The use of amino acids to prepare physically and conformationally stable spray-dried IgG with enhanced aerosol performance, Int. J. Pharm. 466 (1-2) (2014) 163–171. https://doi.org/10.1016/j.ijpharm.2014.03.020.

[90] M.M. Pop, H.S. Mulder, M. Lamkadmi (Boehringer Ingelheim Int.) EP1881980B1, 2012.

[91] A.H. de Boer, D. Gjaltema, P. Hagedoorn, H.W. Frijlink, Comparative in vitro performance evaluation of the Novopulmon 200 Novolizer and Budesonid-ratiopharm Jethaler: Two novel budesonide dry powder inhalers, Pharmazie 59 (9) (2004) 692–699.

[92] S. Bock, T. Rades, J. Rantanen, R. Scherließ, Additive manufacturing in respiratory sciences - Current applications and future prospects, Adv. Drug Deliv. Rev. 186 (2022) 114341. https://doi.org/10.1016/j.addr.2022.114341.

[93] W. Jamróz, J. Szafraniec, M. Kurek, R. Jachowicz, 3D Printing in Pharmaceutical and Medical Applications - Recent Achievements and Challenges, Pharm. Res. 35 (9) (2018) 176. https://doi.org/10.1007/s11095-018-2454-x.

[94] I. Seoane-Viaño, S.J. Trenfield, A.W. Basit, A. Goyanes, Translating 3D printed pharmaceuticals: From hype to real-world clinical applications, Adv. Drug Deliv. Rev. 174 (2021) 553–575. https://doi.org/10.1016/j.addr.2021.05.003.

[95] J. Norman, R.D. Madurawe, C.M.V. Moore, M.A. Khan, A. Khairuzzaman, A new chapter in pharmaceutical manufacturing: 3D-printed drug products, Adv. Drug Deliv. Rev. 108 (2017) 39–50. https://doi.org/10.1016/j.addr.2016.03.001.

[96] E.S. Bishop, S. Mostafa, M. Pakvasa, H.H. Luu, M.J. Lee, J.M. Wolf, G.A. Ameer, T.-C. He, R.R. Reid, 3-D bioprinting technologies in tissue engineering and regenerative medicine: Current and future trends, Genes Dis. 4 (4) (2017) 185–195. https://doi.org/10.1016/j.gendis.2017.10.002.

[97] Z. Gu, J. Fu, H. Lin, Y. He, Development of 3D bioprinting: From printing methods to biomedical applications, Asian Journal of Pharmaceutical Sciences 15 (5) (2020) 529–557. https://doi.org/10.1016/j.ajps.2019.11.003.

[98] G.K. Eleftheriadis, N. Genina, J. Boetker, J. Rantanen, Modular design principle based on compartmental drug delivery systems, Adv. Drug Deliv. Rev. 178 (2021) 113921. https://doi.org/10.1016/j.addr.2021.113921.

[99] R. Govender, S. Abrahmsén-Alami, A. Larsson, A. Borde, A. Liljeblad, S. Folestad, Independent Tailoring of Dose and Drug Release via a Modularized Product Design Concept for Mass Customization, Pharmaceutics 12 (8) (2020). https://doi.org/10.3390/pharmaceutics12080771.

[100] R. Govender, S. Abrahmsén-Alami, A. Larsson, S. Folestad, Therapy for the individual: Towards patient integration into the manufacturing and provision of pharmaceuticals, Eur. J. Pharm. Biopharm. 149 (2020) 58–76. https://doi.org/10.1016/j.ejpb.2020.01.001.

[101] US Food and Drug Administration, Technical Considerations for Additive Manufactured Medical Devices: Guidance for Industry and Food and Drug Administration Staff, 2017. https://www.fda.gov/media/97633/download (accessed 13 September 2021).

[102] Aprecia Pharmaceuticals, Zipdose® technology: 12/3/2015, 2015. https://www.aprecia.com/technology/zipdose.

[103] Triastek Inc., MED™ 3D-Printing, 2021. https://www.triastek.com/.

[104] R. Ge, M. Ghadiri, T. Bonakdar, K. Hapgood, 3D printed agglomerates for granule breakage tests, Powder Technology 306 (3) (2017) 103–112. https://doi.org/10.1016/j.powtec.2016.10.070.

[105] E. Walsh, J.H. ter Horst, D. Markl, Development of 3D printed rapid tooling for micro-injection moulding, Chemical Engineering Science 235 (2021) 116498. https://doi.org/10.1016/j.ces.2021.116498.

[106] V. Hahn, P. Kiefer, T. Frenzel, J. Qu, E. Blasco, C. Barner-Kowollik, M. Wegener, Rapid Assembly of Small Materials Building Blocks (Voxels) into Large Functional 3D Metamaterials, Adv. Funct. Mater. 30 (26) (2020) 1907795. https://doi.org/10.1002/adfm.201907795.

[107] G.E. Marsh, Utilising micron-scale 3D printing to investigate particulate interactions for respiratory applications. Thesis, Nottingham, UK, 2018.

[108] C. López-Iglesias, A.M. Casielles, A. Altay, R. Bettini, C. Alvarez-Lorenzo, C.A. García-González, From the printer to the lungs: Inkjet-printed aerogel particles for pulmonary delivery, Chemical Engineering Journal 357 (2018) 559–566. https://doi.org/10.1016/j.cej.2018.09.159.

[109] K.J. McHugh, T.D. Nguyen, A.R. Linehan, D. Yang, A.M. Behrens, S. Rose, Z.L. Tochka, S.Y. Tzeng, J.J. Norman, A.C. Anselmo, X. Xu, S. Tomasic, M.A. Taylor, J. Lu, R. Guarecuco, R. Langer, A. Jaklenec, Fabrication of fillable microparticles and other complex 3D microstructures, Science 357 (6356) (2017) 1138–1142. https://doi.org/10.1126/science.aaf7447.

[110] A. Torge, G. Pavone, M. Jurisic, K. Lima-Engelmann, M. Schneider, A comparison of spherical and cylindrical microparticles composed of nanoparticles for pulmonary application, Aerosol Science and Technology 53 (1) (2019) 53–62. https://doi.org/10.1080/02786826.2018.1542484.

[111] J. Xu, D.H.C. Wong, J.D. Byrne, K. Chen, C. Bowerman, J.M. DeSimone, Future of the particle replication in nonwetting templates (PRINT) technology, Angew. Chem. Int. Ed Engl. 52 (26) (2013) 6580–6589. https://doi.org/10.1002/anie.201209145.

[112] A. Garcia, P. Mack, S. Williams, C. Fromen, T. Shen, J. Tully, J. Pillai, P. Kuehl, M. Napier, J.M. DeSimone, B.W. Maynor, Microfabricated engineered particle systems for respiratory drug delivery and other pharmaceutical applications, J. Drug Deliv. 2012 (2012) 941243. https://doi.org/10.1155/2012/941243.

[113] C.A. Fromen, T.W. Shen, A.E. Larus, P. Mack, B.W. Maynor, J.C. Luft, J.M. DeSimone, Synthesis and characterization of monodisperse uniformly shaped respirable aerosols, AIChE J. 59 (9) (2013) 3184–3194. https://doi.org/10.1002/AIC.14157.

[114] Z. Gu, S. Li, F. Zhang, S. Wang, Understanding Surface Adhesion in Nature: A Peeling Model, Adv. Sci. (Weinh) 3 (7) (2016) 1500327. https://doi.org/10.1002/advs.201500327.

[115] S. Bock, R. Scherließ, Artificial dispersing aids and carriers for DPI formulations – Proof of Principle, Drug Delivery to the Lungs Conference, 2019. https://aerosol-soc.com/abstracts/artificial-dispersing-aids-and-carriers-for-dpi-formulations-proof-of-principle/ (accessed 7 January 2022).

[116] F. Buttini, J. Hannon, K. Saavedra, I. Rossi, A.G. Balducci, H. Smyth, A. Clark, P. Colombo, Accessorized DPI: A Shortcut towards Flexibility and Patient Adaptability in Dry Powder Inhalation, Pharm. Res. 33 (12) (2016) 3012–3020. https://doi.org/10.1007/s11095-016-2023-0.

[117] Y.-J. Son, P.W. Longest, G. Tian, M. Hindle, Evaluation and modification of commercial dry powder inhalers for the aerosolization of a submicrometer excipient enhanced growth (EEG) formulation, Eur. J. Pharm. Sci. 49 (3) (2013) 390–399. https://doi.org/10.1016/j.ejps.2013.04.011.

[118] S.R.B. Behara, D.R. Farkas, M. Hindle, P.W. Longest, Development of a high efficiency dry powder inhaler: Effects of capsule chamber design and inhaler surface modifications, Pharm. Res. 31 (2) (2014) 360–372. https://doi.org/10.1007/s11095-013-1165-6.

[119] W. Wong, D.F. Fletcher, D. Traini, H.-K. Chan, J. Crapper, P.M. Young, Particle aerosolisation and break-up in dry powder inhalers: Evaluation and modelling of the influence

of grid structures for agglomerated systems, Journal of pharmaceutical sciences 100 (11) (2011) 4710–4721. https://doi.org/10.1002/jps.22663.

[120] P.W. Longest, M. Hindle, Quantitative analysis and design of a spray aerosol inhaler. Part 1: Effects of dilution air inlets and flow paths, J. Aerosol Med. Pulm. Drug Deliv. 22 (3) (2009) 271–283. https://doi.org/10.1089/jamp.2008.0739.

[121] M. Hindle, P.W. Longest, Quantitative analysis and design of a spray aerosol inhaler. Part 2: Improvements in mouthpiece performance, J. Aerosol Med. Pulm. Drug Deliv. 26 (5) (2013) 237–247. https://doi.org/10.1089/jamp.2012.0995.

[122] B. van Wachem, K. Thalberg, J. Remmelgas, I. Niklasson-Björn, Simulation of dry powder inhalers: Combining micro-scale, meso-scale and macro-scale modeling, AIChE J. 63 (2) (2017) 501–516. https://doi.org/10.1002/aic.15424.

[123] W. Wong, D.F. Fletcher, D. Traini, H.-K. Chan, P.M. Young, The use of computational approaches in inhaler development, Adv. Drug Deliv. Rev. 64 (4) (2012) 312–322. https://doi.org/10.1016/j.addr.2011.10.004.

[124] H.K. Versteeg, G. Hargrave, L. Harrington, I. Shrubb, D. Hodson, The use of computational fluid dynamics (CFD) to predict pMDI air flows and aerosol plume formation, Respiratory Drug Delivery VII (1) (2000) 257–264.

[125] M.S. Coates, D.F. Fletcher, H.-K. Chan, J.A. Raper, Effect of design on the performance of a dry powder inhaler using computational fluid dynamics. Part 1: Grid structure and mouthpiece length, Journal of pharmaceutical sciences 93 (11) (2004) 2863–2876. https://doi.org/10.1002/jps.20201.

[126] W. Longest, D. Farkas, Development of a New Inhaler for High-Efficiency Dispersion of Spray-Dried Powders Using Computational Fluid Dynamics (CFD) Modeling, AAPS J. 21 (2) (2019) 25. https://doi.org/10.1208/s12248-018-0281-y.

[127] Z. Tong, A. Yu, H.-K. Chan, R. Yang, Discrete Modelling of Powder Dispersion in Dry Powder Inhalers - A Brief Review, Curr. Pharm. Des. 21 (27) (2015) 3966–3973. https://doi.org/10.2174/1381612821666150820110958.

[128] Z. Tong, W. Zhong, A. Yu, H.-K. Chan, R. Yang, CFD–DEM investigation of the effect of agglomerate–agglomerate collision on dry powder aerosolisation, Journal of Aerosol Science 92 (2016) 109–121. https://doi.org/10.1016/j.jaerosci.2015.11.005.

[129] E. Hoerlin - WO1995/003846A1, 1994.

[130] A.W. Gieschen, M. Ligotke, J. Chen, C. Gamen, B. Greenspan - US2001/0027790A1, 2001.

[131] Drugbank, Isoniazid: https://go.drugbank.com/drugs/DB00951, 2022.

[132] Drugbank, Rifampicin: https://go.drugbank.com/drugs/DB01045, 2022.

[133] K. Giry, J.M. Péan, L. Giraud, S. Marsas, H. Rolland, P. Wüthrich, Drug/lactose co-micronization by jet milling to improve aerosolization properties of a powder for inhalation, Int. J. Pharm. 321 (1-2) (2006) 162–166. https://doi.org/10.1016/j.ijpharm.2006.05.009.

[134] A. Chamayou, J.A. Dodds, Chapter 8 Air Jet Milling, in: A.D. Salman, M. Ghadiri, M.J. Hounslow (Eds.), Particle breakage, Elsevier, Amsterdam, 2007, pp. 421–435.

[135] K. Wetterlin, Turbuhaler: A new powder inhaler for administration of drugs to the airways, Pharm. Res. 5 (8) (1988) 506–508. https://doi.org/10.1023/A:1015969324799.

[136] A.H. Jones, C.G. Langdon, P.S. Lee, S.A. Lingham, J.P. Nankani, R.M. Follows, U. Tollemar, P.D. Richardson, Pulmicort Turbohaler once daily as initial prophylactic therapy for asthma, Respir. Med. 88 (4) (1994) 293–299. https://doi.org/10.1016/0954-6111(94)90059-0.

[137] S. Bock, R. Scherließ - WO2021115877A1, 2019.

[138] C.W. Hull, The birth of 3D printing: IRI achievement award address, Research technology management RTM 58 (6) (2015) 25–29.

[139] M. Göppert-Mayer, Über Elementarakte mit zwei Quantensprüngen, Ann. Phys. 401 (3) (1931) 273–294. https://doi.org/10.1002/andp.19314010303.

[140] W. Denk, J.H. Strickler, W.W. Webb, Two-photon laser scanning fluorescence microscopy, Science 248 (4951) (1990) 73–76. https://doi.org/10.1126/SCIENCE.2321027.

[141] A. Spangenberg, N. Hobeika, F. Stehlin, J. Pierre Malval, F. Wieder, P. Prabhakaran, P. Baldeck, O. Sopper, Recent Advances in Two-Photon Stereolithography, in: S. Hosaka (Ed.), Updates in Advanced Lithography, InTech, 2013.

[142] L. Iwersen, The influence of artificial dispersing aids on the deagglomeration of softpellet formulations for inhalation, Kiel, Germany, 2022.

[143] P.W. Longest, K. Bass, R. Dutta, V. Rani, M.L. Thomas, A. El-Achwah, M. Hindle, Use of computational fluid dynamics deposition modeling in respiratory drug delivery, Expert Opin. Drug Deliv. 16 (1) (2019) 7–26. https://doi.org/10.1080/17425247.2019.1551875.

[144] C.A. Ruzycki, E. Javaheri, W.H. Finlay, The use of computational fluid dynamics in inhaler design, Expert Opin. Drug Deliv. 10 (3) (2013) 307–323. https://doi.org/10.1517/17425247.2013.753053.

[145] M. Ariane, M. Sommerfeld, A. Alexiadis, Wall collision and drug-carrier detachment in dry powder inhalers: Using DEM to devise a sub-scale model for CFD calculations, Powder Technology 334 (2018) 65–75. https://doi.org/10.1016/j.powtec.2018.04.051.

[146] P.W. Longest, L.T. Holbrook, In silico models of aerosol delivery to the respiratory tract - development and applications, Adv. Drug Deliv. Rev. 64 (4) (2012) 296–311. https://doi.org/10.1016/j.addr.2011.05.009.

[147] C.S. Kim, L.K. Brown, G.G. Lewars, M.A. Sackner, Deposition of aerosol particles and flow resistance in mathematical and experimental airway models, J. Appl. Physiol. Respir. Environ. Exerc. Physiol. 55 (1 Pt 1) (1983) 154–163. https://doi.org/10.1152/jappl.1983.55.1.154.

[148] I. Balásházy, W. Hofmann, Particle deposition in airway bifurcations—I. Inspiratory flow, Journal of Aerosol Science 24 (6) (1993) 745–772. https://doi.org/10.1016/0021-8502(93)90044-A.

[149] I. Balásházy, W. Hofmann, Particle deposition in airway bifurcations–II. Expiratory flow, Journal of Aerosol Science 24 (6) (1993) 773–786. https://doi.org/10.1016/0021-8502(93)90045-B.

[150] W.H. Finlay, K.W. Stapleton, J. Yokota, On the Use of Computational Fluid Dynamics for Simulating Flow and Particle Deposition in the Human Respiratory Tract, Journal of Aerosol Medicine 9 (3) (1996) 329–341. https://doi.org/10.1089/jam.1996.9.329.

[151] J.K. Comer, C. Kleinstreuer, S. Hyun, C.S. Kim, Aerosol transport and deposition in sequentially bifurcating airways, J. Biomech. Eng. 122 (2) (2000) 152–158. https://doi.org/10.1115/1.429636.

[152] Y. Feng, J. Zhao, C. Kleinstreuer, Q. Wang, J. Wang, D.H. Wu, J. Lin, An in silico inter-subject variability study of extra-thoracic morphology effects on inhaled particle transport and deposition, Journal of Aerosol Science 123 (2018) 185–207. https://doi.org/10.1016/j.jaerosci.2018.05.010.

[153] P. Koullapis, L. Nicolaou, S.C. Kassinos, The effect of mouth-throat geometry on regional deposition in the tracheobronchial tree. The effect of mouth-throat geometry, in: P. Nithiarasu, A.M. Robertson (Eds.), CMBE17: 5th International Conference on Computational & Mathematical Biomedical Engineering 10th-12th April 2017, The University Club, University of Pittsburgh, Pittsburgh, PA, United States, CMBE, Swansea, United Kingdom, 2017, pp. 942–945.

[154] P.W. Longest, G. Tian, R.L. Walenga, M. Hindle, Comparing MDI and DPI aerosol deposition using in vitro experiments and a new stochastic individual path (SIP) model of the conducting airways, Pharmaceutical Research An Official Journal of the American Association of

Pharmaceutical Scientists 29 (6) (2012) 1670–1688. https://doi.org/10.1007/s11095-012-0691-y.

[155] W.H. Finlay, The mechanics of inhaled pharmaceutical aerosols: An introduction, Academic Press, London, England, 2019.

[156] P. Koullapis, S.C. Kassinos, J. Muela, C. Perez-Segarra, J. Rigola, O. Lehmkuhl, Y. Cui, M. Sommerfeld, J. Elcner, M. Jicha, I. Saveljic, N. Filipovic, F. Lizal, L. Nicolaou, Regional aerosol deposition in the human airways: The SimInhale benchmark case and a critical assessment of in silico methods, Eur. J. Pharm. Sci. 113 (2018) 77–94. https://doi.org/10.1016/j.ejps.2017.09.003.

[157] J.W. de Backer, W.G. Vos, S.C. Vinchurkar, R. Claes, A. Drollmann, D. Wulfrank, P.M. Parizel, P. Germonpré, W. de Backer, Validation of computational fluid dynamics in CT-based airway models with SPECT/CT, Radiology 257 (3) (2010) 854–862. https://doi.org/10.1148/radiol.10100322.

[158] J. Shur, S. Lee, W. Adams, R. Lionberger, J. Tibbatts, R. Price, Effect of device design on the in vitro performance and comparability for capsule-based dry powder inhalers, AAPS J. 14 (4) (2012) 667–676. https://doi.org/10.1208/s12248-012-9379-9.

[159] J. Shur, B. Saluja, S. Lee, J. Tibbatts, R. Price, Effect of Device Design and Formulation on the In Vitro Comparability for Multi-Unit Dose Dry Powder Inhalers, AAPS J. 17 (5) (2015) 1105–1116. https://doi.org/10.1208/s12248-015-9775-z.

[160] M.S. Coates, D.F. Fletcher, H.-K. Chan, J.A. Raper, The role of capsule on the performance of a dry powder inhaler using computational and experimental analyses, Pharm. Res. 22 (6) (2005) 923–932. https://doi.org/10.1007/s11095-005-4587-y.

[161] M.S. Coates, H.-K. Chan, D.F. Fletcher, J.A. Raper, Effect of design on the performance of a dry powder inhaler using computational fluid dynamics. Part 2: Air inlet size, Journal of pharmaceutical sciences 95 (6) (2006) 1382–1392. https://doi.org/10.1002/jps.20603.

[162] S. Coates, H.-K. Chan, F. Fletcher, H. Chiou, Influence of Mouthpiece Geometry on the Aerosol Delivery Performance of a Dry Powder Inhaler, Pharmaceutical Research An Official Journal of the American Association of Pharmaceutical Scientists 24 (8) (2007) 1450–1456. https://doi.org/10.1007/s11095-007-9262-z.

[163] M.J. Donovan, S.H. Kim, V. Raman, H.D. Smyth, Dry powder inhaler device influence on carrier particle performance, Journal of pharmaceutical sciences 101 (3) (2012) 1097–1107. https://doi.org/10.1002/jps.22824.

[164] S.R.B. Behara, P.W. Longest, D.R. Farkas, M. Hindle, Development and comparison of new high-efficiency dry powder inhalers for carrier-free formulations, Journal of pharmaceutical sciences 103 (2) (2014) 465–477. https://doi.org/10.1002/jps.23775.

[165] Q.T. Zhou, Z. Tong, P. Tang, M. Citterio, R. Yang, H.-K. Chan, Effect of device design on the aerosolization of a carrier-based dry powder inhaler--a case study on Aerolizer(®) Foradile (®), AAPS J. 15 (2) (2013) 511–522. https://doi.org/10.1208/s12248-013-9458-6.

[166] Z.B. Tong, B. Zheng, R.Y. Yang, A.B. Yu, H.K. Chan, CFD-DEM investigation of the dispersion mechanisms in commercial dry powder inhalers, Powder Technology 240 (2013) 19–24. https://doi.org/10.1016/j.powtec.2012.07.012.

[167] Z.B. Tong, R.Y. Yang, K.W. Chu, A.B. Yu, S. Adi, H.K. Chan, Numerical study of the effects of particle size and polydispersity on the agglomerate dispersion in a cyclonic flow, Chemical Engineering Journal 164 (2-3) (2010) 432–441. https://doi.org/10.1016/j.cej.2009.11.027.

[168] K.L. Mittal, R. Jaiswal, Particle Adhesion and Removal, John Wiley & Sons, Inc, Hoboken, NJ, USA, 2015.

[169] P.A. Cundall, O.D.L. Strack, A discrete numerical model for granular assemblies, Géotechnique 29 (1) (1979) 47–65. https://doi.org/10.1680/geot.1979.29.1.47.

[170] Z. Tong, H. Kamiya, A. Yu, H.-K. Chan, R. Yang, Multi-scale modelling of powder dispersion in a carrier-based inhalation system, Pharm. Res. 32 (6) (2015) 2086–2096. https://doi.org/10.1007/s11095-014-1601-2.

[171] C. Thornton, K.K. Yin, M.J. Adams, Numerical simulation of the impact fracture and fragmentation of agglomerates, J. Phys. D: Appl. Phys. 29 (2) (1996) 424–435. https://doi.org/10.1088/0022-3727/29/2/021.

[172] C. Thornton, M.T. Ciomocos, M.J. Adams, Numerical simulations of agglomerate impact breakage, Powder Technology 105 (1-3) (1999) 74–82. https://doi.org/10.1016/S0032-5910(99)00120-5.

[173] Z.B. Tong, R.Y. Yang, A.B. Yu, S. Adi, H.K. Chan, Numerical modelling of the breakage of loose agglomerates of fine particles, Powder Technology 196 (2) (2009) 213–221. https://doi.org/10.1016/j.powtec.2009.08.001.

[174] J. Yang, C.-Y. Wu, M. Adams, DEM analysis of the effect of particle-wall impact on the dispersion performance in carrier-based dry powder inhalers, Int. J. Pharm. 487 (1-2) (2015) 32–38. https://doi.org/10.1016/j.ijpharm.2015.04.006.

[175] D. Nguyen, A. Rasmuson, K. Thalberg, I.N. Björn, The exchange of fines between carriers in adhesive particle mixing: A study using DEM simulation, Powder Technology 288 (2016) 266–278. https://doi.org/10.1016/j.powtec.2015.10.048.

[176] M.S. Coates, H.-K. Chan, D.F. Fletcher, J.A. Raper, Influence of air flow on the performance of a dry powder inhaler using computational and experimental analyses, Pharm. Res. 22 (9) (2005) 1445–1453. https://doi.org/10.1007/s11095-005-6155-x.

[177] C. Friebel, Rationale Entwicklung eines Inhalationssystems. PhD thesis, Kiel, Germany, 2010.

[178] O.R. Walton, R.L. Braun, Viscosity, granular-temperature, and stress calculations for shearing assemblies of inelastic, frictional disks, Journal of Rheology 30 (5) (1986) 949–980. https://doi.org/10.1122/1.549893.

[179] H. Hertz, Ueber die Berührung fester elastischer Körper, Journal für die reine und angewandte Mathematik (Crelles Journal) 1882 (92) (1882) 156–171. https://doi.org/10.1515/crll.1882.92.156.

[180] R.D. Mindlin, H. Deresiewicz, Elastic Spheres in Contact Under Varying Oblique Forces, Journal of Applied Mechanics 20 (3) (1953) 327–344. https://doi.org/10.1115/1.4010702.

[181] S.B. Yeom, E.-S. Ha, M.-S. Kim, S.H. Jeong, S.-J. Hwang, H. Du Choi, Application of the Discrete Element Method for Manufacturing Process Simulation in the Pharmaceutical Industry, Pharmaceutics 11 (8) (2019). https://doi.org/10.3390/pharmaceutics11080414.

[182] K.L. Johnson, K. Kendall, A.D. Roberts, Surface energy and the contact of elastic solids, Proc. R. Soc. Lond. A 324 (1558) (1971) 301–313. https://doi.org/10.1098/rspa.1971.0141.

[183] M. Pasha, S. Dogbe, C. Hare, A. Hassanpour, M. Ghadiri, A linear model of elasto-plastic and adhesive contact deformation, Granular Matter 16 (1) (2014) 151–162. https://doi.org/10.1007/s10035-013-0476-y.

[184] MEGGLE Excipients & Technology, Technical brochure InhaLac®: Dry powder inhaler: InhaLac®, 2021. https://www.meggle-pharma.com/en/downloads.html (accessed 1 January 2022).

[185] H.A. Kubavat, J. Shur, G. Ruecroft, D. Hipkiss, R. Price, Influence of primary crystallisation conditions on the mechanical and interfacial properties of micronised budesonide for dry powder inhalation, Int. J. Pharm. 430 (1-2) (2012) 26–33. https://doi.org/10.1016/j.ijpharm.2012.03.020.

[186] M. Perkins, S.J. Ebbens, S. Hayes, C.J. Roberts, C.E. Madden, S.Y. Luk, N. Patel, Elastic modulus measurements from individual lactose particles using atomic force microscopy, Int. J. Pharm. 332 (1-2) (2007) 168–175. https://doi.org/10.1016/j.ijpharm.2006.09.032.

[187] Engineering ToolBox, Young's Modulus, Tensile Strength and Yield Strength Values for some Materials, 2003. https://www.engineeringtoolbox.com/young-modulus-d_417.html (accessed 1 January 2022).

[188] Chemical Retrieval on the Web, Typical Poisson's ratios of polymers at room temperature, 2021. http://www.polymerdatabase.com/polymer%20physics/Poisson%20Table2.html (accessed 1 January 2022).

[189] S. Zellnitz, N. Renner, Y. Cui, R. Scherließ, M. Sommerfeld, H. Steckel, N. Urbanetz, The Importance of Interactions Between Carrier and Drug Particles for the Application in Dry Powder Inhalers, in: S. Antonyuk (Ed.), Particles in Contact, Springer Nature, 2019, pp. 458–517.

[190] Rhein Nancy, R. Scherließ, Influence of drug concentration on Dry Powder Inhaler formulations based on a mannitol and a lactose carrier system, Respiratory Drug Delivery (2) (2018) 349–354.

Abstract

Administration of drugs via the respiratory tract lacks efficiency despite the variety of inhalers and formulations available. In the case of dry powder inhaler (DPI) formulations, scientists attribute this lack of efficiency to the variety of properties of the powder particles and the devices. Matching these interdependent properties is complex, making it difficult to determine the effect of any single influencing factor. With the aim of resolving this complexity and enhancing the aerodynamic performance, this thesis presents novel strategies for the development of DPI formulations.

Heterogeneity of particle properties is a crucial factor affecting the efficiency of a DPI formulation. To eliminate the heterogeneity of carrier particles in interactive blends in terms of size and morphology, this thesis investigates the use of relatively uniform and spherical pellets of microcrystalline cellulose (MCC). Moreover, this thesis describes the effects of coating the carrier surface with three different amino acids in a fluidised bed, namely phenylalanine, tryptophan and tyrosine, on the aerodynamic performance. Although an influence of carrier size and the coating on performance in a Novolizer® inhaler is shown, a direct correlation with any of the carrier properties cannot be demonstrated.

For the purpose of controlling the properties of individual particles and investigating them isolated from each other, this thesis presents the use of Additive Manufacturing (AM). As a technique that enables the production of customised objects with specific properties, AM is shown to allow applications at the DPI particle level and at a level between device and formulation. The latter level of application involves the manufacturing of structurally complex objects that are inserted in inhaler devices as free levitating dispersing aids (DAs). Investigation of their use in interactive blends and softpellets shows the influence of DAs on the aerodynamic performance of DPI formulations.

In addition, this thesis explores manufacturing of tailored microstructures as a novel particle engineering approach. AM is presented as a technical solution for controlling and adjusting particle size, design and chemical composition, which can be used to decipher the complexities of developing enhanced DPI formulations.

For particle design thinking and engineering processes, this thesis presents the use of Numerical Simulation (NS) as a complementary tool. Applying Discrete Element Method (DEM) modelling allows for simulating the formation and dispersion of drug-carrier agglomerates. On the one hand, this work describes the simulation of a loading non-

spherical carrier with spherical API particles. On the other hand, it presents a model for simulating the detachment of API particles from the carrier after a collision with a wall. Simulating corresponding patterns provides insights into the influence of particle morphology on carrier loading and particle detachment. The simulations show that both events depend on the size as well as the morphology of the carrier.

In summary, this thesis presents AM and NS as novel strategies to engineer and evaluate particles for use in DPI formulations. With further refinements in manufacturing and simulation capabilities, a combination of these techniques is anticipated to enable optimisation and mass customisation of particles in the future.

Zusammenfassung

Der Verabreichung von Arzneimitteln über die Atemwege mangelt es trotz der Vielfalt der zurzeit vorhandenen Inhalatoren und Formulierungen an Effizienz. Bei Pulvern zur Inhalation wird die mangelnde Effizienz auf die Vielzahl von Eigenschaften der Pulverpartikel und der Inhalatoren zurückgeführt. Die Abstimmung dieser voneinander abhängigen Eigenschaften ist komplex und macht es schwierig, die Wirkung eines einzelnen Einflussfaktors zu bestimmen. Mit dem Ziel, diese Komplexität aufzulösen und die aerodynamische Leistung von Pulvern zu Inhalation zu verbessern, werden in dieser Arbeit neue Strategien für die Entwicklung von derartigen Formulierungen vorgestellt.

Die Heterogenität der Partikeleigenschaften ist ein entscheidender Faktor, der die Effizienz einer Pulver Formulierung beeinflusst. Um die Heterogenität der Trägerpartikel in interaktiven Mischungen in Bezug auf Größe und Morphologie zu eliminieren, wird in dieser Arbeit die Verwendung von relativ einheitlichen und kugelförmigen Pellets aus mikrokristalliner Cellulose (MCC) untersucht. Darüber hinaus zeigt diese Arbeit die Auswirkungen einer Beschichtung der Trägeroberfläche von MCC Pellets mit drei verschiedenen Aminosäuren auf die aerodynamische Leistung auf. Für die Beschichtung kommen ein Wirbelschichtverfahren und die aromatischen Aminosäuren Phenylalanin, Tryptophan und Tyrosin zum Einsatz. Obwohl der Einfluss der Trägergröße und deren Beschichtung auf die Leistung in einem Novolizer®-Inhalator gezeigt werden kann, lässt sich kein direkter Zusammenhang mit einer der Trägereigenschaften darstellen.

Um die Eigenschaften einzelner Partikel zu kontrollieren und zu voneinander isoliert untersuchen, wird in dieser Arbeit der Einsatz von Additiven Fertigungsverfahren vorgestellt. Mit diesen Verfahren, die die Herstellung maßgeschneiderter Objekte mit spezifischen Eigenschaften ermöglichen, ergeben sich Anwendungsmöglichkeiten auf der Partikel-Ebene und auf einer Ebene zwischen Gerät und Formulierung. Die letztgenannte Anwendungsebene umfasst die Herstellung strukturell komplexer Objekte, die als freischwebende Dispergierhilfen (DAs) in Inhalationsgeräte eingesetzt werden. Die Untersuchung ihrer Verwendung in interaktiven Mischungen und Softpellets zeigt den Einfluss der DAs auf die aerodynamische Leistung von Pulverformulierungen zur Inhalation.

Darüber hinaus wird in dieser Arbeit die Herstellung von maßgeschneiderten Mikrostrukturen als neuartiger Ansatz für die Partikeltechnik präsentiert. Der Einsatz Additiver Fertigungsverfahren wird als technische Lösung zur Kontrolle und Anpassung der Partikelgröße, der Morphologie und der chemischen Zusammensetzung vorgestellt,

die zur Entschlüsselung der Komplexität der Entwicklung verbesserter DPI-Formulierungen genutzt werden kann.

In dieser Arbeit wird die Numerische Simulation als ergänzendes Werkzeug für das Entwickeln von Partikeldesigns eingesetzt. Die Anwendung der Diskrete-Elemente-Methode (DEM) ermöglicht die Simulation der Bildung und Dispersion von Agglomeraten bestehend aus Wirkstoff und Träger. Diese Arbeit beschreibt einerseits die Simulation einer Beladung von nicht-sphärischen Trägerpartikel mit sphärischen Wirkstoffpartikeln. Andererseits präsentiert sie ein Modell zur Simulation der Ablösung von Wirkstoffpartikeln von den Träger nach einer Kollision mit einer Wand. Die Simulation entsprechender Muster gibt Aufschluss über den Einfluss der Partikelmorphologie auf die Ladung der Träger und die Ablösung der Partikel. Die Simulationen zeigen, dass beide Ereignisse sowohl von der Größe als auch von der Form des Trägers abhängen.

Zusammenfassend werden in dieser Arbeit Additive Fertigungsverfahren und Numerische Simulationen als neue Strategien zur Entwicklung und Bewertung von Partikeln für die Verwendung in Pulverformulierungen zur Inhalation dargelegt. Mit zukünftigen Erweiterungen der Fertigungs- und Simulationsmöglichkeiten wird eine Kombination dieser Techniken die Optimierung und maßgefertigte Anpassung von Partikeln ermöglichen.

Acknowledgments

Many people have guided, supported and inspired me in this work and during my PhD. Besides financial support, various individuals and companies provided advice and assistance at different stages of the PhD project. I would like to express my gratitude to all of them. This thesis would not have been possible without their help.

At first, I would like to thank Professor Regina Scherließ for her expert advice, encouragement, and personal trust throughout my period as a PhD student. She made me realise my own ideas and develop both professionally and personally. With her instinct for building networks and starting collaborations across disciplinary and national boundaries, she has helped me as a researcher in numerous ways. I thank her very much.

Many sincere thanks go to the staff and former colleagues of the Department of Pharmaceutics and Biopharmaceutics at Kiel University for the kind, manifold and countless support, which ultimately led to this thesis: Karl Willi Bock, Dirk Böhme, Denissa Gummels, Dr. Kirsten Seidel, Simone Diekjobst, Hanna Göttsche, Maren Greve, Regina Krehl, Ann-Kathrin Muhs and Rüdiger Smal. Special thanks go to Karl Willi, Hanna and Regina!

Thankfully, some good friendships have developed during my time at Kiel University with other PhD student. Many thanks to all colleagues and clever minds for their skilled and creative support. Office 106 (+ all the regular guests) had such a great impact on my life that I will never forget.

In addition to the staff, some of the students I had the privilege of supervising and teaching during my PhD also conducted valuable studies. Partly, these studies have been included in this thesis. In this regard, a special thanks go to Laura Iwersen, Laura Rossodivita and Fabian Schefe.

I am very grateful for the enriching, instructive, and friendly collaboration with Professor Jukka Rantanen and Professor Thomas Rades from University of Copenhagen. Working with them has taught me to think outside the box of science throughout my entire life.

Some of the studies in this thesis were partly funded by NordForsk. Funding for the Nordic University Hub project #85352 (Nordic POP, Patient Oriented Products) allowed to cooperate on Additive Manufacturing with the University of Oslo. In this regard, a special thanks goes to Professor Ingunn Tho who made this cooperation possible. Being

awarded with the DDL Career Development Grant in 2021 by the Aerosol Society also provided me with further financial leeway to put the initiated project idea into reality. Thank you for this award.

A special thanks goes to Tobias Möckel from Wissenschaftszentrum Kiel and MakerCube© e.V. for the operational and technical support on Additive Manufacturing. I would also like to acknowledge Armin Reimers from the Institute of Materials Science at Kiel University for his support in creating some of the designs described in this thesis. Moreover, I am grateful to Pascal Kiefer and Professor Martin Wegener from the Karlsruhe Institute of Technology (KIT) for stimulating discussions and collaboration on particle printing. The exchange with Jörg Smolenski (Nanoscribe GmbH & Co. KG) was equally stimulating - thank you for your support.

The Numerical Simulations described in this thesis were thankfully conducted in close cooperation with Dr. Jan-Philipp Fürstenau from CADFEM Germany GmbH. In this regard, I would also like to thank Professor Nora Urbanetz, Dr. Srikanth Gopireddy and Tigran Kharatyan from Daiichi Sankyo Europe GmbH for stimulating conversations and for setting up an initial simulation model.

The professional journey I have chosen is partly thanks to the initiative of Dr. Mathias Mönckedieck, who contributed to me starting my PhD at Kiel University.

Finally, I would like to thank my family for always having confidence in my ability to succeed and in always being supportive whenever I needed them. Without their optimism, good heart and unconditional support I would not be the person I am today.

Thank you very much.

Statement in lieu of an oath

Erklärung nach § 8 der Promotionsordnung

Hiermit erkläre ich gemäß § 8 der Promotionsordnung der Mathematisch-Naturwissenschaftlichen Fakultät der Christian-Albrechts-Universität zu Kiel, dass ich die vorliegende Arbeit, abgesehen von der Beratung durch meinen Betreuer, selbstständig und ohne fremde Hilfe verfasst habe. Weiterhin habe ich keine anderen als die angegeben Quellen oder Hilfsmittel benutzt und die den benutzten Werken wörtlich oder inhaltlich entnommenen Stellen als solche kenntlich gemacht. Die vorliegende Arbeit ist unter Einhaltung der Regeln guter wissenschaftlicher Praxis der Deutschen Forschungsgemeinschaft entstanden. Sie wurde weder ganz noch in Teilen an einer anderen Stelle im Rahmen eines Prüfungsverfahrens vorgelegt, veröffentlicht oder zur Veröffentlichung eingereicht. Außerdem versichere ich, dass mir noch kein akademischer Grad entzogen wurde, noch habe ich an dieser oder einer anderen Fakultät einen früheren Promotionsversuch unternommen.

_____

Simon Bock